Multi-Wavelength Observations of the High-Mass Star Forming Complexes W33 and DR 21

Dissertation

zur

Erlangung des Doktorgrades (Dr. rer. nat.)

der

Mathematisch−Naturwissenschaftlichen Fakultät

der

Rheinischen Friedrich−Wilhelms−Universität Bonn

vorgelegt von

Katharina Immer

aus

Berlin, Deutschland

Bonn, August 2013

Angefertigt mit Genehmigung der Mathematisch-Naturwissenschaftlichen Fakultät der
Rheinischen Friedrich-Wilhelms-Universität Bonn

1. Gutachter: Prof. Dr. Karl M. Menten
2. Gutachter: Prof. Dr. Uli Klein
Tag der Promotion: 13.11.2013

Summary

High-mass stars play a key role in shaping the Universe. Stars with masses above 8 $M_\odot$ have a huge impact on the energy budget of galaxies, through their stellar winds, expanding H II regions, outflows, and supernova explosions. Although insight into the formation of stars is gained from low-mass star forming regions, the knowledge about high-mass star formation is still incomplete and has to be increased through new observations and theories. Observationally, different stages of star formation are distinguished. A cold molecular cloud collapses and fragments into smaller entities ("clumps" and "cores"). The cores contract further and slowly start to warm up their center where a protostar is formed. The protostar grows through accretion of material while at a certain point, hydrogen burning sets in. The evolving protostar starts to heat up its birth cloud, changing the chemistry in different layers around the star (hot core phase). An H II region is formed once the radiation of the protostar is energetic enough to ionize the surrounding material. With time, the radiation of the protostar destroys the birth cloud and the star becomes observable at optical wavelengths.

In the course of this dissertation, the formation of high-mass stars was studied along the described evolutionary sequence on the basis of multi-wavelength observations of the high-mass star forming complexes W33 and DR 21. In W33, molecular clouds in several stages of star formation are detected, from quiescent cold clouds to highly active H II regions. Two radial velocity components with a difference of ~20 km s^{-1} were detected towards different parts of the complex. For a long time, this raised the question if W33 is a physically connected star forming complex or if the star forming regions with different radial velocities are located at different distances along the line-of-sight. Due to this peculiar velocity structure, the distance to W33 was not well known. As part of the dissertation, the trigonometric parallax distance of

W33 was determined with Very Long Baseline Interferometry observations of water masers in the complex, yielding a distance of 2.4 kpc. Since the star forming regions with the different radial velocity components are located at similar distances, we conclude that W33 is physically connected. Furthermore, these observations yield the proper motions of the water masers from which we inferred the internal motions of the star forming regions and the motions of these regions within the W33 complex.

Since the clouds in the W33 complex are physically linked and are in different stages of star formation, we conducted a chemical study of these clouds with single dish and interferometer observations at submillimeter wavelengths to gather information about the chemical composition on different scales along the evolutionary sequence. On larger scales, the number of detected molecules and their complexity increases from the prestellar phase to the H II region phase. On smaller scales, the clouds in the hot core phase show the highest chemical complexity and diversity. The observed molecules, some of them quite complex, were generated on the dust grains and then released into the gas phase as primary molecules or produced in the gas phase by the evaporated molecules as secondary molecules. In the H II region phase, almost no complex molecules are detected anymore and the spectrum resembles the spectra of the clouds in the protostellar phase before the excitation of a hot core. The complex molecules are either destroyed by photo-dissociation or their emission is not compact enough to be detected by the interferometer.

With interferometer observations at radio wavelengths, we looked for hypercompact and ultracompact H II regions in the W33 Main cloud. We detected an ultracompact H II region and inferred the spectral type of the dominating star which ionizes the surrounding material. The ultracompact H II region has an arc-shape similar to cometary H II regions. Furthermore, water masers and a Class I methanol maser are detected in the W33 Main cloud. While the water masers are probably associated with an outflow in W33 Main, the methanol maser is located offset from any dust or molecular line emission and it is not clear what powers it.

DR 21 contains two cometary H II regions, whose sizes classify them as ultracompact and compact H II regions. To study the velocity field of the two H II regions, we analyzed archival radio recombination line observations of DR 21. We detected two velocity components in the tails of both H II regions which indicate the presence of stellar winds. Stellar winds clear cavities around the stars and confine the ionized gas in thin shells around these cavities. The two velocity components probably originate from ionized gas at the near and the far side of these shells. The velocity distribution of both H II regions is best explained with a combination of bow shock and champagne flow models. The moving star produces a bow shock at the head of the cometary H II regions, increasing the velocity of the ionized gas compared to the systemic velocity of the

neutral material. Increasing velocities of the ionized gas down both tails indicate the presence of a density gradient in the surrounding neutral material (champagne flow model). The density gradient in the southern H II region has been tentatively shown in molecular line observations of DR 21 but has to be confirmed with observations at higher spatial resolution.

Contents

List of Figures

List of Tables

1 Introduction

1.1 High-Mass Star Formation

Stars are the building blocks of the Universe. High-mass stars ($M > 8\ M_{\odot}$) shape the galaxies through their stellar winds, powerful outflows, H II regions, and supernova explosions. They are the main source for the production of heavy elements. However, despite their importance, the formation of high-mass stars is still poorly understood. Some of the reasons for this are their rareness and large distances (> 1 kpc), requiring high angular resolution observations. The star formation processes take place while the protostars are still deeply embedded in their birth clouds, preventing the new born stars to be directly observed at optical or near-infrared wavelengths due to high extinction. The surrounding dust is heated by the protostar and reradiates the light at mid- and far-infrared wavelengths. Light at these wavelengths is less affected by extinction and thus is a good signpost for ongoing star formation. Furthermore, the formation process of high-mass stars is very fast, making it difficult to detect them in different stages of evolution. High-mass stars are also mostly formed in clusters where they affect each others' evolution through their stellar winds, outflows, and expanding H II regions. Over the past decades, many observational and theoretical studies have greatly improved the knowledge about the formation of high-mass stars (for detailed reviews, see, for example, McKee & Ostriker 2007; Shu et al. 1987; Zinnecker & Yorke 2007; Beuther et al. 2007, and references therein). However, open questions remain.

What do we know about low-mass star formation?

Since low-mass stars are much more abundant than high-mass stars (e.g. Salpeter 1955; Kroupa 2001) and several low-mass star forming regions are located close to the Sun, the formation of

Figure 1.1: Evolutionary sequence of low-mass star formation. The phases are a) cloud collapse, b) protostar with rotating accretion disk and outflow, c) star with protoplanetary disk, and d) mature star system (Images after Lada 1987; Andre et al. 1993).

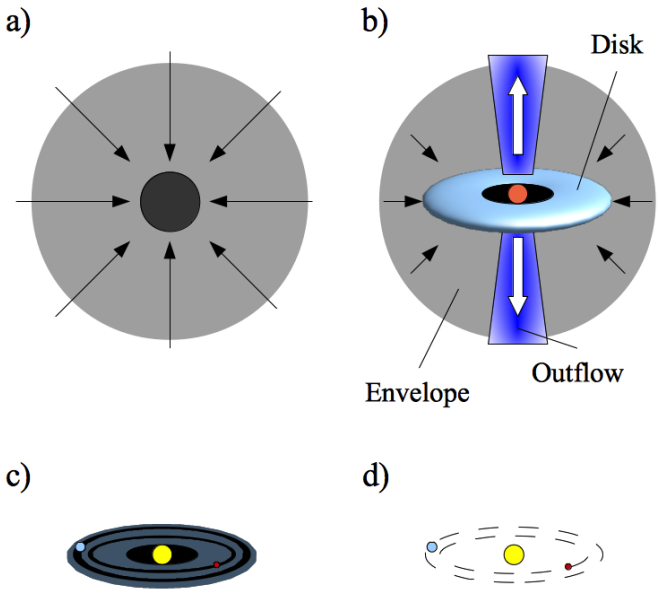

low-mass stars has been studied in greater detail and is better understood than the formation of high-mass stars. In this subsection, the formation stages of low-mass stars (Fig. 1.1) will be shortly described as an introduction for the observed evolutionary stages of high-mass stars.

From the spectral energy distributions (SEDs) of the continuum emission, observed in low-mass star forming regions, Lada (1987) and Andre et al. (1993) divided the sources in four classes, 0–III. The formation of a low-mass protostar begins with the gravitational collapse of a molecular core (for the description of cores, see Section 1.2.1; panel a) in Fig. 1.1), known as class 0. Once a protostar is formed, it keeps accreting material through a rotating accretion disk (sizes < 1000 AU) which itself accretes material from the surrounding envelope. To allow for the infall of material onto the protostar, the system has to loose the angular momentum of the infalling material by launching collimated jets and outflows perpendicular to the disk (panel b), class I). Stellar winds will stop the infall of material and thus the accretion process. Eventually, protoplanets start to form in the disk (panel c), class II). In the last stage, the mature star system becomes detectable at optical wavelengths (panel d), class III).

1.2 Observed Evolutionary Sequence of High-Mass Star Formation

As low-mass protostars, high-mass protostars grow through accretion of matter. However, Kahn (1974) and Shu et al. (1987) showed that the radiation pressure acting on the infalling material around stars more massive than ~7 $M_\odot$ can stop the accretion for spherical infall. However, many stars with masses above this limit have been observed. Wolfire & Cassinelli (1987) suggest that spherical infall is possible with high accretion rates of $> 10^{-3}$ $M_\odot$ yr^{-1}. Another possibility is nonspherical infall, allowing the material to accumulate in an accretion disk (Shu et al. 1987).

Due to the large distances of high-mass star forming regions and the small sizes of accretion disks (< 1000 AU), accretion disks around high-mass protostars are difficult to resolve. An example for a high-mass protostar with an accretion disk is IRAS13481−6124, which was observed by Kraus et al. (2010) at near-infrared wavelengths. Indirect evidence for the presence of accretion disks has been gathered through observations of outflows in high-mass star forming regions (see, e.g. Beuther et al. 2002).

Figure 1.2: Observed evolutionary sequence of high-mass star formation.

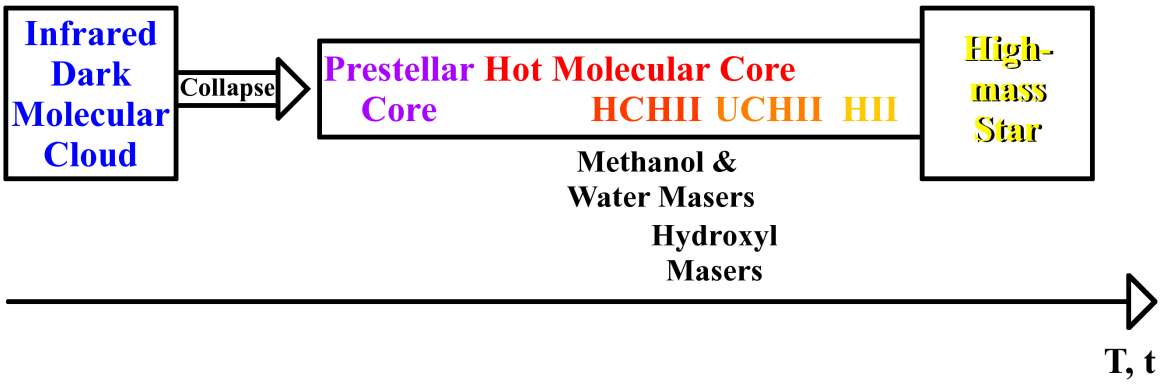

However, high-mass star formation is not a scaled-up version of low-mass star formation (Zinnecker & Yorke 2007). Since the Kelvin-Helmholtz timescale (contraction timescale before the start of hydrogen burning) for high-mass stars is much shorter than the infall timescale, high-mass stars end up on the main sequence while still accreting material. Compared to low-mass stars, high-mass stars produce large amounts of ionizing photons that photo-evaporate the accretion disk as well as the surrounding envelope, eventually stopping the infall of material. Fur-

thermore, the photo-ionized gas expanding from the high-mass star will influence the accretion disks of stars forming in the vicinity. Since high-mass stars mostly form in clusters, competitive accretion between the protostars plays a role for the growth of the protostars (e.g. Bonnell et al. 2001; Bonnell & Bate 2006). Due to the high energy output of high-mass stars through their stellar winds, H II regions, and supernova explosions, high-mass stars can trigger a second generation of star formation and thus have a huge influence on their surroundings (e.g. Elmegreen & Lada 1977).

Described in the following subsections is an evolutionary sequence for the formation of high-mass stars, based on observational signposts (see Fig. 1.2).

1.2.1 Giant Molecular Clouds and Prestellar Cores

Table 1.1: Properties of molecular clouds, clumps, and cores (Bergin & Tafalla 2007)

Property	Cloud	Clump	Core
Mass ($M_\odot$)	10^3-10^4	50−500	0.5−5
Size (pc)	2−15	0.3−3	0.03−0.2
Mean density (cm^{-3})	50−500	10^3-10^4	10^4-10^5
Velocity extent (km s^{-1})	2−5	0.3−3	0.3−3

The birthplaces of high-mass stars are located in so-called Giant Molecular Clouds (GMCs) which have been detected in large scale CO observations of the Galactic plane (see, e.g. Dame et al. 2001). The sizes and masses of GMCs range between 10−100 pc and $10^{5-6.5}$ $M_\odot$ and have an average density of 10^2 cm^{-3} (e.g. Stutzki & Guesten 1990; Blitz 1993). GMCs are fragmented into "clumps" (following the nomenclature of Williams et al. 2000) which are the formation sites of star clusters. "Cores" are the results of further fragmentation of the clumps in which single high-mass stars (or binaries) form. With decreasing size, the average density of these structures increases. Table 1.1 lists the mass, size, mean density, and velocity extent for clouds, clumps, and cores (Bergin & Tafalla 2007).

The first formation stage of high-mass stars is the collapse of a part of a cold and dense GMC which forms molecular clumps and subsequently molecular cores. These clouds contain cold dust that can be observed in emission at (sub)millimeter wavelengths. A particularly interesting group of objects were observed by Perault et al. (1996), Egan et al. (1998), and Benjamin et al. (2003) who reported dark features in the Infrared Space Observatory (ISO), Midcourse Space Experiment (MSX), and *Spitzer* infrared surveys. They identified these features as clouds with

low temperatures of 10−20 K and very high column densities of $10^{23}-10^{25}$ cm^{-2} which absorb the diffuse mid-infrared emission of the Galactic plane. These clouds were called infrared dark clouds (IRDCs). The low temperatures in the clouds cause molecules to freeze out onto the dust grains.

The *prestellar cores* contract further, releasing gravitational energy and slowly warming up the center of the core. Once a protostar is formed at the center of the core, the so-called *protostellar phase* is reached.

1.2.2 Hot Cores

As for low-mass stars, an accretion disk forms around the protostar from which material falls onto the star. The disk is replenished with material from the surrounding envelope. The excess of angular momentum of the infalling material is thought to be transferred to a polar outflow which is launched perpendicular to the disk. In this phase, methanol, water, and hydroxyl masers start to be observable in the star forming region, close to the central star or in the outflow.

The protostar starts to warm up the surrounding material in the disk and envelope, evaporating the ice mantles off dust grains and facilitating an active gas phase chemistry. This phase is called "hot (molecular) core". It is characterized by high temperatures (> 100 K), high densities (> 10^7 cm^{-3}), and a rich chemistry with rare and complex molecular species (Kurtz et al. 2000). Strong infrared sources are detected in the star forming regions in this phase of evolution. Spectroscopic observations show line-forests of "simple" (CO, H_2CO, CH_3OH, ...) and "complex" (CH_3CCH, CH_3OCH_3, C_2H_5OH, ...) molecules.

1.2.3 H II Regions

When the protostar reaches temperatures which are high enough to ionize the surrounding birth cloud, an H II region emerges. Now the star forming region becomes observable at radio wavelengths. Since only high-mass stars can produce a significant amount of radiation above the Lyman limit, H II regions are a unique signpost of high-mass star formation.

H II regions come in different sizes and densities. The classes that are connected the closest to star formation are hypercompact (HC), ultracompact (UC), and compact H II regions (Kurtz 2005). Due to the overpressure of the hot ionized gas within the H II region compared to the colder molecular material around, H II regions are expected to expand and thus become larger and less dense. Table 1.2 lists the physical properties of these different H II region classes. The different sizes of these classes suggest that compact and UC H II regions are harboring OB clus-

ters while HC H II regions (or even smaller H II regions) are probably excited by a single stellar system (Kurtz 2005).

Table 1.2: Physical properties of the three H II region classes that are linked the closest to star formation (Kurtz 2005).

Class	Size (pc)	Density (cm^{-3})	Emission Measure (pc cm^{-6})	Ionized Mass ($M_\odot$)
Hypercompact	$\lesssim 0.03$	$\gtrsim 10^6$	$\gtrsim 10^{10}$	$\sim 10^{-3}$
Ultracompact	$\lesssim 0.10$	$\gtrsim 10^4$	$\gtrsim 10^7$	$\sim 10^{-2}$
Compact	$\lesssim 0.50$	$\gtrsim 5 \cdot 10^3$	$\gtrsim 10^7$	~ 1

Wood & Churchwell (1989) detected 75 UC H II regions in their targeted Very Large Array survey. They calculated a typical lifetime of $\sim 10^4$ yr for an expanding UC H II region which is not consistent with the high number of detected UC H II regions. They suggest that if the outer envelope around the star is still collapsing, the expansion of the ionized gas could be retarded by the infalling material. When an H II region just emerges, it can be trapped within the accretion flow. Later, the radiation pressure either reverses the accretion flow or the H II region expands since its radius increases beyond the gravitational radius of the accretion flow (Hoare et al. 2007). Hollenbach et al. (1994) and Johnstone et al. (1998) proposed that the surface of the accretion disk is ionized by the Lyman continuum radiation of the star.

In any model explaining the expansion of H II regions, stellar winds have to be taken into account (Hoare et al. 2007). A strong stellar wind not only clears a cavity in the central part of the H II region, it can also slow down the expansion by trapping the ionization front behind a dense shell of swept-up interstellar material (Turner & Matthews 1984). A strong stellar wind can blow the ionized material away from the star but the ionized gas is refueled by the photo-evaporation of the accretion disk, forming a HC H II region around the star.

Figure 1.3 shows a spectrum of the thermal bremsstrahlung of a spherical H II region (Kurtz 2005). The vertical dashed line presents the turnover frequency marking the frequency where the optical depth is unity. Above the turnover frequency, the emission of the ionized gas is optically thin and the flux density drops with frequency as $\nu^{-0.1}$. Below the turnover frequency, the emission is optically thick and the flux density drops more rapidly with ν^2. Since HC H II regions are much smaller and denser than UC H II regions, their emission measure (EM = $\int N_e^2 \, ds$, number of electrons N_e, line-of-sight s) is also much larger. The spectrum of an H II region with a larger emission measure is shifted to higher frequencies and has a higher turnover frequency (dashed line in Fig. 1.3). Thus, at frequencies at which the emission of UC H II regions is already

Figure 1.3: Thermal bremsstrahlung spectrum of a spherical, homogeneous, and isothermal H II region. The vertical dashed line shows the turnover frequency (here 5 GHz). At lower frequencies than the turnover frequency, the emission of the ionized gas is optically thick while at higher frequencies it is optically thin. The dashed line shows the spectrum of an H II region with a higher emission measure, leading to a turnover frequency at much higher frequencies. The image is adopted from Kurtz (2005).

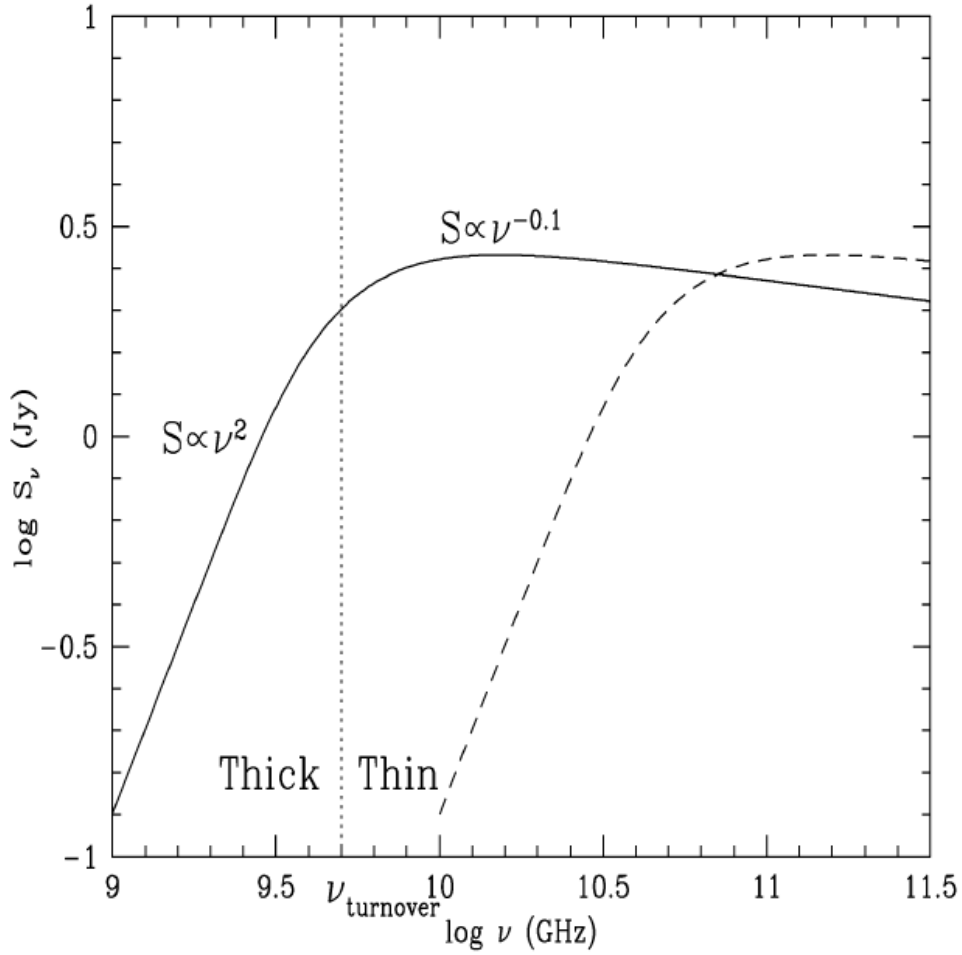

optically thin, the emission of HC H II regions can still be optically thick and it might not be detectable. Another difference between HC and UC H II regions is that radio recombination lines are substantially broader in HC H II regions than towards UC H II regions where the line widths range between 30 and 40 km s^{-1}. There are different explanations for these broad recombination lines: pressure broadening, gas motions from rotation, infall or outflow or a superposition of unresolved sources (Kurtz 2005).

1.3 Radiative Transfer

This section provides a short summary of the theoretical background of the transfer of radiation from the source to the observer and will shortly describe the characteristics of spectral line emission.

Radiative transfer describes the transfer of energy from a source via electromagnetic radiation. Since the radiation passes through a medium on the way to the observer, the radiation is influenced by emission, absorption, and scattering processes. The equation of transfer defines the change of the specific intensity I_ν along the line-of-sight s (Rohlfs & Wilson 2004):

$$\frac{dI_\nu}{ds} = -\kappa_\nu I_\nu + \epsilon_\nu, \tag{1.1}$$

where κ_ν and ϵ_ν denote the opacity and emissivity of the medium. If the medium is not emitting ($\epsilon_\nu = 0$) and the optical depth τ_ν is defined as

$$\tau_\nu = \int_s \kappa_\nu ds, \tag{1.2}$$

then the intensity changes exponentially as

$$I_\nu = I_{\nu,0} \cdot \mathrm{e}^{-\tau_\nu}. \tag{1.3}$$

The optical depth describes the transparency of the medium. If the medium is transparent for radiation or "optically thin", then $\tau_\nu \ll 1$. If the medium is not transparent or "optically thick", then $\tau_\nu \gg 1$ and only the radiation from the surface of the medium is observed.

In local thermodynamic equilibrium (LTE), the medium is described by one temperature T and

$$\frac{\epsilon_\nu}{\kappa_\nu} = B_\nu(T), \tag{1.4}$$

where B_ν(T) is the Planck function of a black body. Then, the equation of transfer 1.1 can be

solved as

$$I_\nu(s) = I_{\nu,0} e^{-\tau_\nu(s)} + B_\nu(T)(1 - e^{-\tau_\nu(s)}). \tag{1.5}$$

Spectral Line Emission

Spectral line emission from an atom or a molecule is detected when the atom/molecule was excited e.g. by a photon or collisions with other atoms/molecules to a higher energy level and then re-emitted a photon spontaneously while descending to a lower energy level. Each atom or molecule has its own particular spectrum. Thus, observing, identifying, and analyzing spectral lines gives information about the chemical composition of the observed object.

The line emission of molecules can be produced in several ways:

- Electronic transitions which occur between electronic levels. These transitions are typically observed at optical and ultraviolet wavelengths.
- Vibrational transitions which arise from periodic motions of the atoms in the molecule. Observations at infrared wavelengths can detect these transitions.
- Rotational transitions occurring from the rotation of the molecule around its center of mass. Pure rotational transitions are observed at far-infrared to radio wavelengths.

Due to different broadening processes, a spectral line extends over a finite frequency range and is not only detected at a single frequency. These processes are

- Natural broadening due to the uncertainty principle which yields a Lorentz profile of the spectral line.
- Thermal broadening due to the thermal motion of the molecules yielding a Gaussian profile of the line. The higher the temperature of the gas, the broader is the line.
- Pressure broadening due to collisions of the molecules in the gas which yields a Lorentz line profile. The strength of the broadening is determined by the temperature and the density of the gas.
- Kinematic effects (e.g. rotation). If the molecules which are emitting the spectral line are receding from us or moving towards us, one observes a frequency shift of the central line frequency due to the Doppler effect. From the size of the Doppler shift, the radial velocity of the material along the line-of-sight can be determined.

Maser Emission

A special kind of molecular emission is known as maser emission where maser stands for "Microwave Amplification by Stimulated Emission of Radiation". Locally, the gas is pumped into a population inversion and the molecules emit amplified radiation due to stimulated emission. If the emission is velocity-coherent along the line-of-sight, high intensities can build up and a maser source can be observed. However, the emission of an astronomical maser is not spatially coherent since the emission is produced by one single pass of the radiation through the masing medium. The population inversion in the masing gas is achieved through excitation by radiation or collisions. Examples of astronomical masers, commonly occurring in star forming regions, are CH_3OH Class I (pumped by collisions) and Class II (pumped by radiation), H_2O, and OH masers.

1.4 Chemical Evolution

In this section, the alterations in chemical composition of the molecular material around the new born star due to changes in temperature and density during the evolution of the star forming regions are shortly described.

During the different stages of star formation, the chemistry of the birth cloud changes dramatically. In the collapse phase, the temperature drops while the density increases and most molecules freeze out onto the dust grains in the regions with the highest density (Langer et al. 2000). The molecules that for example remove $H_3{}^+$ from the gas phase (e.g. CO, H_2O) are frozen onto the grains and the increased abundance of $H_3{}^+$ keeps the abundance of N_2H^+ and HCO^+ high. Thus, the collapsing envelope can be traced by HCO^+ and N_2H^+ where N_2H^+ traces the quiescent gas in the outer envelope (van Dishoeck & Blake 1998). On the dust grains, hydrogenation of CO, N, and C leads to the generation of H_2CO, CH_3OH, NH_3, and CH_4 on the grains (Charnley et al. 1992). With increasing temperature, heavier molecules diffuse over the surface of the grains which permits a more complex surface chemistry.

When the medium around the protostar is heated by the star or shocked by the outflows and stellar winds of the star, the ices are evaporated off the dust grains and released back into the gas phase (Brown et al. 1988). Spectral observations of star forming regions in the hot core phase show the chemical enrichment in organic molecules. Fig. 1.4 shows a sketch of the chemical evolution of a high-mass young stellar object with increasing temperature.

The species, detected in hot cores, can be sorted into three classes (van Dishoeck & Blake 1998; Charnley et al. 1992):

Figure 1.4: Sketch of the chemical evolution of the material around a high-mass young stellar object with increasing temperature. The different temperature steps show how the ice mantles of the dust grains in the envelope change due to the evaporation of the outer layers (based on Tielens et al. 1991; Williams 1993). The image is adopted from van Dishoeck & Blake (1998).

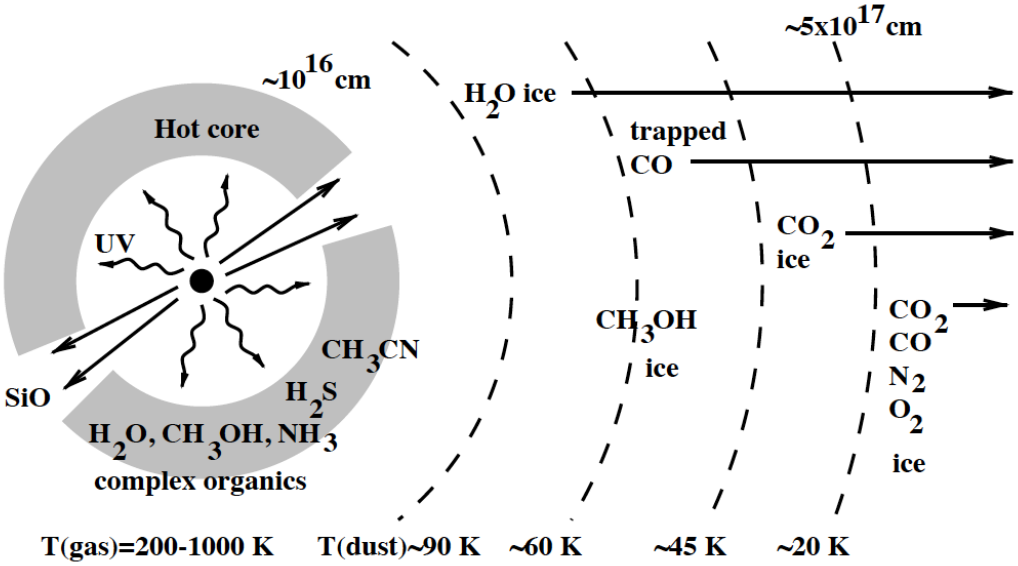

1. Molecules that are produced in the cold clouds before collapse, then frozen onto the dust grains during collapse, and evaporated off the dust grains basically unaltered in the hot core phase (CO, C_2H_2, ...).

2. Molecules made on the surface of dust grains and then released as "primary molecules" into gas phase (CH_3OH, NH_3, H_2CO, ...).

3. Molecules generated by evaporated molecules in the gas phase ("secondary molecules"; $HCOOCH_3$, CH_3OCH_3, CH_3CHO, HCN, HC_3N, CH_3CN, ...).

Thus, models of the chemical evolution of a high-mass star forming region have to combine grain surface chemistry, gas phase chemistry, and interactions between the gas and the grains. Fig. 1.5 shows an example model for the chemical evolution in the hot core phase. At t = 0, primary molecules are released into the gas phase and then secondary molecules are produced. Thus, certain molecules can be used as "chemical clocks", identifying different evolutionary stages.

Shocks from outflows, jets, and stellar winds can also alter the chemistry in the medium around the protostar. SiO is one of the molecules whose abundance is enhanced in shocks and

Figure 1.5: Gas-phase chemical models for the hot core phase (T = 200 K). The molecules H_2CO, CH_3OH, H_2S, and NH_3 are evaporated off the dust grains and released as primary molecules into the gas phase at t = 0. Gas-phase chemistry then produces more complex molecules like CH_3OCH_3 or CH_3CN (based on Charnley et al. 1992; Charnley 1997). The image is adopted from van Dishoeck & Blake (1998).

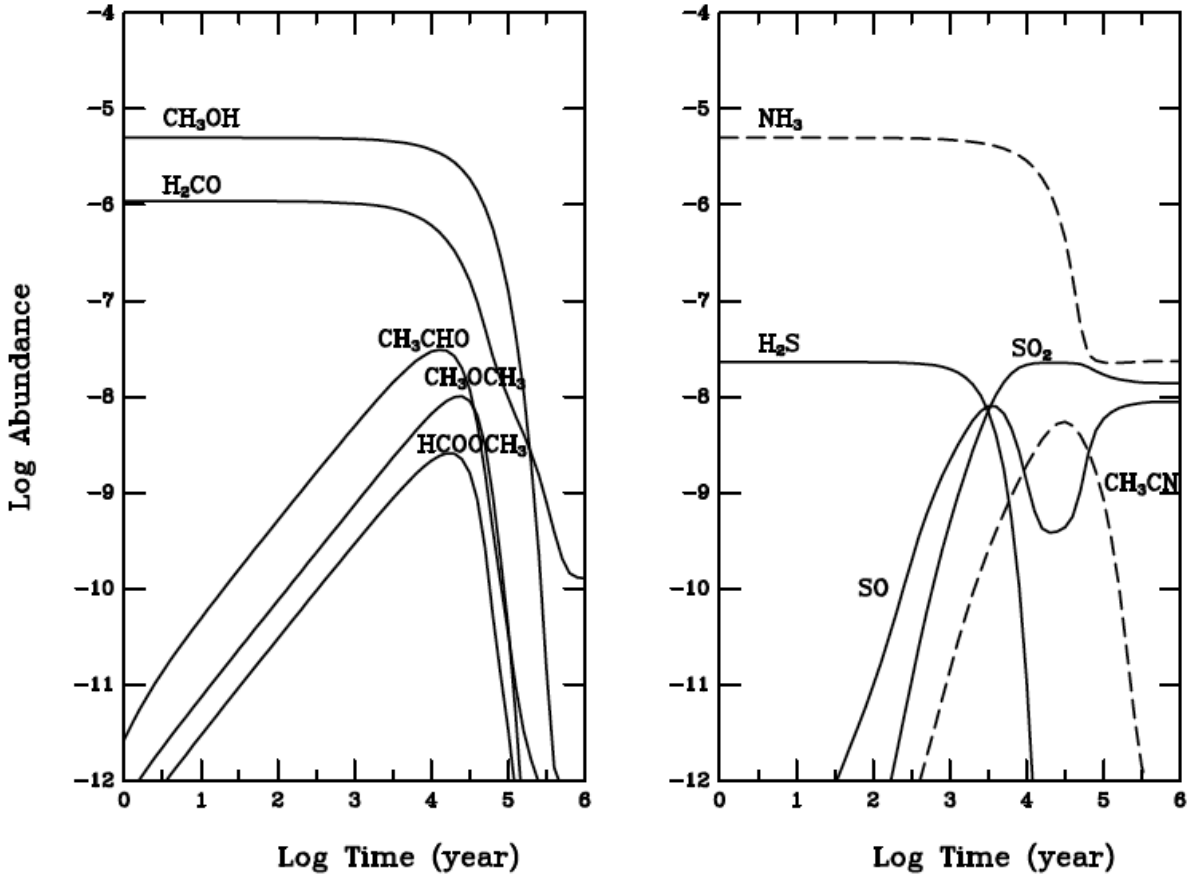

is thus a good tracer for directly shocked material with high velocities (e.g. Martin-Pintado et al. 1992). The molecule CH_3OH, however, is destroyed in high-velocity shocks and can only be detected in low-velocity shocks.

With the onset of the hot core phase, maser sources start to be observed in the star forming region. While water masers and Class I methanol masers are pumped by collisions and thus are often detected in outflows, hydroxyl and Class II methanol masers are excited by radiation and are thus often found close to the new-born star.

1.5 Distance Determination

To derive fundamental physical parameters of the molecular clouds such as their sizes, masses, and the spectral types of embedded stars, we have to know their distances. Accurate distances also allow a meaningful comparison of the physical properties and characteristics of different star forming regions. In the following subsections, the determination of kinematic and trigonometric parallax distances are summarized.

1.5.1 Kinematic Distances

One commonly used method is to determine the kinematic distance of a cloud from radial velocity measurements. Comparing the radial velocity of the cloud with a rotation curve of the Galaxy (e.g. Burton & Gordon 1978; Reid et al. 2009b) yields the Galactocentric radius from which the distance of the cloud can be determined. However, in the first and fourth quadrants there are two possible distances corresponding to a given radius, complicating the distance determination. In addition, local velocity deviations due to shocks, outflows or noncircular motions can lead to large errors of the kinematic distance (Xu et al. 2006). Recent trigonometric parallax measurements have shown that kinematic distance measurements can be wrong by more than a factor of two (e.g. Reid et al. 2009b; Sanna et al. 2009; Sato et al. 2010a).

1.5.2 Trigonometric Parallaxes

A trigonometric parallax results from the apparent motion of an object compared to a distant background due to the movement of the Earth around the Sun (see left panel in Fig. 1.6). Since the parallax method is based only on geometry and does not include further assumptions (except for the well-studied orbit of the Earth around the Sun), it is a reliable method to accurately

Figure 1.6: Left panel: Parallax sketch. Due to the movement of the Earth around the Sun, the front object seems to move in relation to the background sources. Right panel: Right ascension and declination parallax signatures for a source at a distance of 8 kpc.

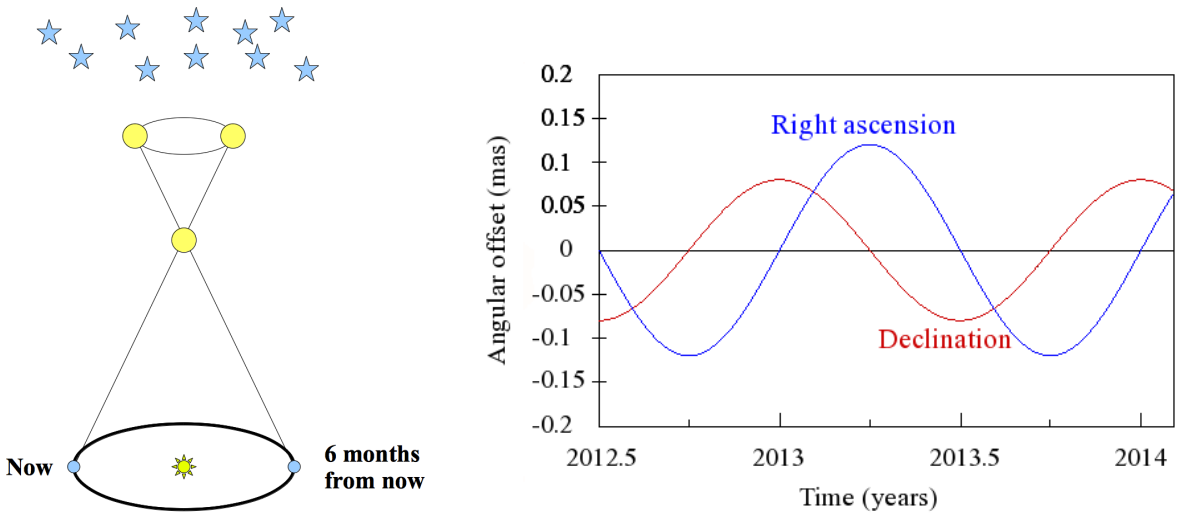

measure distances to star forming regions whose accuracy is limited only by observational uncertainties.

The parallax is determined by observing a strong target source relative to background sources at several epochs over one year. Comparing the apparent motion of the target to the background sources, we get a sinusoidal parallax signature in right ascension and declination (right panel in Fig. 1.6). Since the star forming region is moving, too, in relation to the Sun, trigonometric parallax observations not only yield the distance to the object but also its proper motion. The proper motion adds a linear term to the sinusoidal parallax signature. Combining the distance and proper motion with the coordinates and the radial velocity of the target yields its full six dimensional phase space information.

To determine distances to star forming regions, good targets are maser sources because they are strong radio emitters that are detectable for a fair part of the star formation timescale. We also need strong background sources (usually quasars) that have a small angular distance from the target so that the atmosphere in the background and target observations is similar and can be well-calibrated. Due to the small values of the parallaxes in the milliarcsecond (mas) to microarcsecond (μas) regime (A distance of 1 kpc corresponds to a parallax of 1 mas.), the targets have to be observed with high spatial resolution. Thus, the observations are conducted with

interferometers with long baselines (for more information about interferometry, see Thompson et al. 2001).

The trigonometric parallax observations discussed in Chapter 2 are part of the Bar and Spiral Structure Legacy (BeSSeL) Survey[1] (Brunthaler et al. 2011), a National Radio Astronomy Observatory's[2] Very Long Baseline Array (VLBA) key project. The goal of this survey is the determination of distances and proper motions of hundreds of star forming regions in the Galaxy, yielding the three dimensional motions of the star forming regions. In addition, the distances to star forming regions which are located within the spiral arms of the Galaxy will allow us to trace the spiral structure of the Milky Way.

1.6 Sources

This section describes the two high-mass star forming complexes W33 and DR 21 that were analyzed in this dissertation on the basis of multi-wavelengths observations.

1.6.1 W33

The high-mass star forming complex W33 was first detected as a thermal radio source in the 1.4 GHz survey of Westerhout (1958). Observations of the dust emission in the W33 complex from the Atacama Pathfinder Experiment (APEX) Telescope Large Area Survey of the GALaxy (ATLASGAL, Schuller et al. 2009) at 870 μm show three larger (W33 B, W33 Main, and W33 A) and several smaller dust clouds (e.g. W33 B1, W33 Main1, W33 A1; see Fig. 1.7). A cluster of three infrared sources, residing in W33 Main, was detected by Dyck & Simon (1977) at 3.4−33 μm. Another infrared source was observed in W33 A with deep absorption features at 3 and 10 μm (Dyck & Simon 1977; Capps et al. 1978). Stier et al. (1984) conducted far-infrared observations of W33 at 40−250 μm and detected four sources in the complex (W33 B, W33 B1, W33 Main, and W33 A). Masing transitions of methanol and water have been detected in W33 A, W33 Main, and W33 B (e.g. Genzel & Downes 1977; Jaffe et al. 1981; Menten et al. 1986; Haschick et al. 1990; Green et al. 2010; Immer et al. 2013) and OH masers have been observed in W33 A and W33 B (Wynn-Williams et al. 1974; Caswell 1998). Observations at radio wavelengths show W33 Main as a compact source which is embedded in weaker and extended emission. W33 A

[1] http://bessel.vlbi-astrometry.org/index.shtml

[2] The National Radio Astronomy Observatory (NRAO) is a facility of the National Science Foundation operated under cooperative agreement by Associated Universities, Inc.

Figure 1.7: ATLASGAL 870 μm emission of the W33 complex. The contour levels are at 1, 2, 4, 8, 16, and 32 Jy beam^{-1}. The six clouds in the W33 complex are annotated. In the upper right corner, a 1 pc scale is indicated. The primary beam of the observations is shown in the lower left corner.

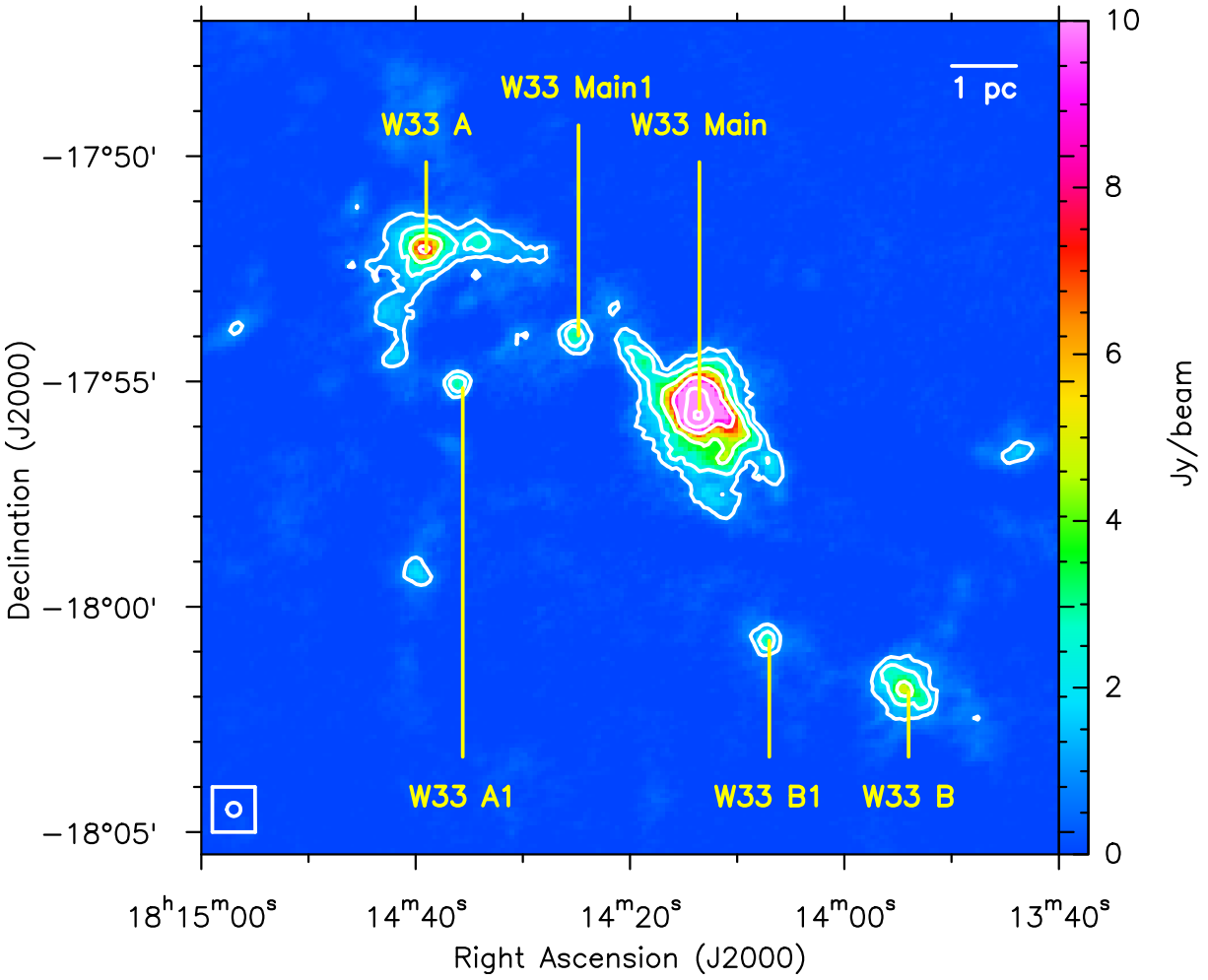

and W33 B are located at the edges of this extended emission (e.g. Wynn-Williams et al. 1981; Stier et al. 1982; Ho et al. 1986; Longmore et al. 2007).

From observations of radio recombination lines, H_2CO absorption, and CO emission, a peculiar velocity field was detected in the W33 complex (e.g. Gardner & Whiteoak 1972; Gardner et al. 1975; Goldsmith & Mao 1983). Towards W33 A and W33 Main, emission/absorption peaks were observed at a radial velocity of ∼36 km s^{-1} while towards W33 B the emission/absorption was maximal at a radial velocity of ∼58 km s^{-1}. However, the CO observations of Goldsmith & Mao (1983) show emission from both velocity components throughout the whole complex. Different explanations for this velocity field have been proposed. Bieging et al. (1978) suggest that W33 is a single connected star forming complex with internal motions of about 20 km s^{-1} at a near-kinematic distance of 3.7 kpc (corresponding to the 36 km s^{-1} velocity component). Goss et al. (1978), however, favor a superposition of two unrelated star forming regions along the line-of-sight. Gardner et al. (1975) interpret the continuum sources with the two different velocity components as the front and back of an expanding sphere at a distance of ∼5 kpc (corresponding to an average velocity of 45 km s^{-1}).

Assuming a near kinematic distance of 3.7 kpc to W33, the angular size of the complex of 15′ can be converted into a physical size of 16 pc. Stier et al. (1984) determined bolometric luminosities of 10^4 $L_\odot$ (W33 B1), 10^5 $L_\odot$ (W33 B and W33 A), and 10^6 $L_\odot$ (W33 Main) at kinematic distances of 3.7 (W33 A, W33 Main, W33 B1) and 4.9 kpc (W33 B). Using ^{13}CO maps and a typical abundance ratio of $n(^{13}CO)/n(H_2) = 4 \cdot 10^{-7}$, Goldsmith & Mao (1983) estimated the total mass of the complex to be $2 \cdot 10^5$ $M_\odot$. Haschick & Ho (1983) detected radio emission towards all three infrared sources in W33 Main. Assuming optically thin emission and an electron temperature of 10^4 K, they conclude that the continuum emission is excited by a cluster of zero age main sequence (ZAMS) stars with spectral types between O6 and B0, based on a kinematic distance of 4 kpc.

W33 A is a well-studied star forming region. The source has a high far-infrared luminosity of 10^5 $L_\odot$ (Faúndez et al. 2004) at the previously assumed kinematic distance of 3.7 kpc. Galván-Madrid et al. (2010) detected parsec-scale filaments of cold molecular gas around two dust cores. The interaction of these filaments might have triggered the star formation activity in the cores. The brightest core drives a strong outflow and the dynamics in this core show evidence for a rotating disk, perpendicular to the outflow. These results are supported by CO observations of Davies et al. (2010) which also suggest the presence of a rotationally-flattened cool molecular envelope. Brγ emission in W33 A seems to trace a fast bipolar wind which has the same orientation as the large-scale outflow (Davies et al. 2010). The colder and more massive sec-

ond core in W33 A seems to be in an earlier evolutionary stage, driving a more modest outflow (Galván-Madrid et al. 2010).

1.6.2 DR 21

DR 21 is the brightest of the thermal radio sources found in the 5 GHz survey of the Cygnus X region by Downes & Rinehart (1966). The star forming region DR 21 is famous for its massive (> 3000 $M_\odot$) and powerful (> 10^{48} erg) outflow (e.g. Garden et al. 1986, 1991; Garden & Carlstrom 1992; Marston et al. 2004). Roy et al. (2011) determined a dust temperature of 36 K, a bolometric luminosity of $8 \cdot 10^4$ $L_\odot$ and a clump mass of ~900 $M_\odot$ for DR 21, assuming a distance of 1.7 kpc. Recent trigonometric parallax observations of 6.7 GHz methanol masers revised the distance to this region to a value of 1.5 kpc (Rygl et al. 2012), which we adopt here. This decreases the luminosity and the mass by a factor of 0.8. For a distance of 1.5 kpc, 0.1 pc corresponds to $13\farcs8$. Zapata et al. (2013) interpret their CO(2−1) observations of the prominent outflow as evidence that a massive explosion, possibly related to the disintegration of a young stellar system, was the trigger of the outflow.

DR 21 contains two cometary H II regions: a compact northern region and an extended southern region, the head of which is resolved into three more compact condensations (e.g. Harris 1973; Dickel et al. 1986; Roelfsema et al. 1989; Cyganowski et al. 2003). The close proximity of two cometary H II regions in DR 21 provides the opportunity to investigate the internal velocity structures of cometary H II regions as well as their motions relative to each other.

1.7 Goals

The aim of this dissertation is to improve our knowledge of the different formation stages of high-mass stars. We conduct observations from submillimeter to radio wavelengths with the Submillimeter Array (SMA) in Hawaii, USA, the Karl G. Jansky Very Large Array (JVLA) in New Mexico, USA, the Very Long Baseline Array (VLBA) in the USA, the APEX telescope in the Atacama Desert in Chile, and the Institut de Radioastronomie Millimétrique (IRAM) 30 m telescope on Pico Veleta in Spain. With these data sets, we investigate the chemistry and kinematics along an evolutionary sequence, from cold quiescent clouds to active compact H II regions. Complimentary observations at infrared wavelengths are obtained from the archives of the MSX, *Spitzer*, and *Herschel* missions. Specific questions that we will tackle are:

- How does the chemistry in star forming regions change with the evolution of the star

forming region? Are there "chemical clocks" that pinpoint certain evolutionary stages?

- Where does the morphology of a cometary H II region originate from?

We conduct case studies of the two high-mass star forming complexes W33 and DR 21. In W33, we compare the chemical composition of six molecular clouds which are in different stages of star formation, from the prestellar phase over hot cores to ultracompact H II regions. Furthermore, we analyze the kinematics within three of the clouds as well as in the whole W33 complex. The compact cometary H II regions in DR 21 are probably more evolved than the ultracompact H II regions in W33 and thus mark a step further along the evolutionary sequence of high-mass star formation. We investigate the velocity fields of the two H II regions in DR 21 and infer possible scenarios for the shaping of the two H II regions.

Chapter 2 Due to a peculiar velocity field in the high-mass star forming complex W33, it is not clear if all W33 clouds belong to the same complex or are located at different distances along the line-of-sight. In Chapter 2, we determine the trigonometric parallax distance to water masers located in three clouds of the W33 complex from observations with the VLBA. We show that all water masers and thus their host clouds are at the same distance, proving that W33 is a physically connected star forming complex. Besides the distances, we present the proper motions of the water masers. From the kinematics of the star forming regions, we infer the internal motions of the W33 complex. The described results are published in Immer et al. (2013).

Chapter 3 The high-mass star forming complex W33 contains star forming regions which are in different phases of star formation, from quiescent molecular clouds to the well-known H II region W33 Main. Since the star forming regions are located at similar distances, a comparative chemical study along an evolutionary sequence is possible. In Chapter 3, we present APEX and SMA observations of six clouds in the W33 complex. Since these two data sets have different spatial resolutions, they trace the chemical composition on different scales in the high-mass star forming regions. We report the detected molecules and compare the chemistry of the envelopes for different star formation stages (prestellar phase, protostellar phase, hot cores, and H II regions). Gas temperatures and column densities of the envelopes are estimated from molecules with several transitions in the observed bands. The dust temperatures and the bolometric luminosities, and consequently the total masses, of the six clouds are obtained from spectral energy distribution fits, covering infrared to submillimeter wavelengths.

Chapter 4 In Chapter 4, we focus on the H II region W33 Main. We present JVLA continuum and line observations in the K band. To study the ongoing star formation in W33 Main, we combine our data with archival data from the Co-Ordinated Radio 'N' Infrared Survey for High-mass star formation (CORNISH) JVLA 5 GHz survey and the *Spitzer* infrared mission. From the radio continuum observations, we are able to determine the spectral type of the dominating star in the UC H II region.

Chapter 5 Although a large fraction of H II regions show a cometary morphology, the origin for the cometary shape is not yet fully understood. However, different models exist that make clear predictions for the velocity fields of cometary H II regions. DR 21 contains two cometary H II regions, DR 21-North and DR 21-South. In Chapter 5, we present H66α radio recombination line observations of DR 21, conducted with the Very Large Array, to study the velocity fields in both H II regions. For the first time, two velocity components in the radio recombination line arising from the same H II region are detected. We compare our results with existing models and draw conclusions about the shaping processes at work in the two H II regions in DR 21. These results have been submitted as a paper to the A&A journal.

Chapter 6 and Chapter 7 In Chapter 6, we give a short résumé of the main conclusions of this dissertation and in Chapter 7, we present an outlook to future developments in observation and analysis.

2 Trigonometric Parallaxes of Water Masers in the High-Mass Star Forming Complex W33

2.1 Motivation

The aim of this project is to obtain the distances and proper motions of the water masers in the W33 complex from trigonometric parallax observations. We address the question of whether the molecular clouds in W33 belong spatially to one connected star forming complex or are at different distances and projected near each other on the sky. Also, solid distances will provide the basis for more accurate values for the luminosity and mass of the complex. The proper motions of the masers yield information about the kinematics of the single star forming regions and of the W33 complex as a whole.

The observations presented in this chapter are part of the BeSSeL survey (Brunthaler et al. 2011), a Very Large Baseline Array (VLBA) Legacy project. The reported results of the parallax and proper motion measurements toward the water masers in the high-mass star forming complex W33 have been published in Immer et al. (2013).

This chapter has the following structure. In Sect. 2.2, the observations and data reduction are described. Section 2.3 presents the parallax and proper motion results. In Sect. 2.4, we discuss the results. In Sect. 2.5, the conclusions of this chapter are presented.

2.2 Observation and Data Reduction

The water masers G012.68−0.18, G012.81−0.19, G012.90−0.24, and G012.90−0.26 in the high-mass star forming complex W33 were observed in the $6_{1,6}-5_{2,3}$ transition of the H_2O molecule (rest frequency 22.23508 GHz), using the VLBA. The general observation setup and data calibra-

tion procedures are described in Reid et al. (2009a). Here, we only describe the details specific to the presented sources.

All water masers were observed at nine epochs (VLBA program BR145I) with a total observing time per epoch of $\sim$ 7 hours. The observing dates (2010 Sep 19, 2010 Oct 22, 2010 Dec 19, 2011 Feb 15, 2011 Mar 26, 2011 May 21, 2011 Jul 30, 2011 Sep 20, 2012 Jan 03) were selected to well sample the Right Ascension parallax signature in time, since the Declination parallax signature is much smaller. However, due to bad weather conditions, the data of the first epoch could not be used for the parallax measurements.

Three different quasars, J1808−1822, J1809−1520, and J1825−1718, from the VLBA calibrator search for the BeSSeL survey (Immer et al. 2011) and the ICRF2 catalog (Fey et al. 2009), were observed for background position references. The background source J1809−1520 could only be detected in the first four epochs, and thus was not used for the parallax determination. Four adjacent frequency bands with 4 MHz bandwidth each were used in right and left circular polarization. The maser signals were centered in the second band at an LSR velocity, V_{LSR}, of 45 km s^{-1} for all masers. The channel spacing of the observations is 0.42 km s^{-1}.

In order to correct for instrumental phase offsets between the frequency bands, observations of the calibrator J1800+3848 from the ICRF2 catalog were used. The strongest maser feature in the water maser G012.68−0.18 at a V_{LSR} of 59.3 km s^{-1} was used for the phase-referencing of the data.

The water masers G012.81−0.19, G012.90−0.24, and G012.90−0.26 were much weaker than G012.68−0.18 and were calibrated using G012.68−0.18 as phase reference. This yields positions relative to G012.68−0.18, from which relative parallaxes can be estimated.

For the data reduction, we used the software Parseltongue [1] (Kettenis et al. 2006), a scripting interface for NRAO's Astronomical Image Processing System (AIPS). After calibrating the data, the maser emission and the continuum sources were imaged with the AIPS task *IMAGR* with a circular clean beam of 2 mas for all epochs. The positions of the masers and the background sources J1808−1822 and J1825−1718 were then determined by fitting Gaussian brightness distributions to the images (see Reid et al. 2009a). Absolute positions of the strongest maser spot in G12.68−0.81 were derived relative to the two background sources. For the remaining water masers, relative positions to G012.68−0.18 were determined. To obtain absolute parallaxes, we added the positions of G012.68−0.18 relative to both background quasars to the position measurements of these water masers.

The positions were modeled with a sinusoidal parallax signature and linear proper motions

[1] http://www.radionet-eu.org/rnwiki/ParselTongue

Table 2.1: Coordinates, line-of-sight velocities, and peak flux densities of the background quasars and the strongest maser spots. Columns 2, 3, and 4 list the coordinates and line-of-sight velocities of the background quasars and the maser spots that were used for parallax fitting. The peak flux densities of the background quasars and the strongest maser spots and the rms of the reference channel images, obtained from epoch 2011 May 21, are listed in Cols. 5 and 6. The last column shows with which cloud the masers in the W33 complex are associated.

Source	R.A. (J2000) (hh mm ss.ssss)	Dec. (J2000) (dd ′ ″.″″)	v_{LSR} (km s^{-1})	F_{Peak} (Jy beam^{-1})	rms (Jy beam^{-1})	Cloud Association
J1808−1822	18 08 55.5150	−18 22 53.383		0.012	0.001	
J1809−1520	18 09 10.2094	−15 20 09.699		0.022	0.001	
J1825−1718	18 25 36.5323	−17 18 49.848		0.096	0.001	
G012.68−0.18	18 13 54.7457	−18 01 46.588	59.3	132.5	0.001	W33 B
G012.81−0.19	18 14 13.8283	−17 55 21.035	34.1/−1.4	1.0/0.2	0.018/0.007	W33 Main
G012.90−0.24	18 14 34.4366	−17 51 51.891	34.9	18.3	0.081	W33 A
G012.90−0.26	18 14 39.5714	−17 52 00.382	37.0	3.0	0.016	W33 A

in each coordinate. Since systematic errors (typically from unmodeled atmospheric delays) are normally much larger than random noise, the formal position errors from the Gaussian fits are mostly too small to account for the total error of the observations which leads to high χ^2 values in the modeling process. The magnitude of the systematic errors can only be inferred from the quality of the parallax fit. Thus, we defined "error-floors" for the Right Ascension and Declination maser positions and added those in quadrature to the Gaussian fit errors. The "error-floor" values were adjusted until the χ^2 value per degree of freedom was close to unity for both coordinates (see Reid et al. 2009a).

In order to determine the internal gas kinematics in each source, we measured the proper motions for all maser spots that were detected in at least three epochs without solving for the parallax parameter.

2.3 Results

Table 2.1 gives the coordinates (Cols. 2, 3), line-of-sight velocities (Col. 4), and peak flux densities (Col. 5) from epoch 2011 May 21 of the background quasars and the maser spots that were used for the parallax fits. Column 6 lists the rms brightnesses of the reference channel images, obtained from epoch 2011 May 21. In the last column, we show the cloud associations of the masers in the W33 complex.

The parallax and proper motion results of all masers are summarized in Table 2.2. Columns 2, 3, and 4 give the line-of-sight velocities of the masing and thermal gas and the parallaxes of the maser sources. In the sixth and seventh columns, the proper motions in eastward and northward

Table 2.2: Parallax and proper motion results. Columns 6 and 7 give the proper motions in eastward and northward directions. The proper motions of the first maser are obtained from fitting a model of expanding outflows to all maser spots. The proper motions of the remaining sources are averages of the proper motions of all maser spots in each source.

Source	$v_{LSR,\,maser}$ (km s^{-1})	$v_{LSR,\,thermal}{}^2$ (km s^{-1})	Parallax π (mas)	Distance d (kpc)	μ_x (mas yr^{-1})	μ_y (mas yr^{-1})
G012.68−0.18 (W33 B)	59.3	∼55	0.416 ± 0.028	$2.40^{+0.17}_{-0.15}$	−1.00 ± 0.30	−2.85 ± 0.29
G012.81−0.19 (W33 Main)	−1.4	∼36	0.343 ± 0.037	$2.92^{+0.35}_{-0.28}$	−0.24 ± 0.17	+0.54 ± 0.12
G012.81−0.19 (W33 Main)	34.1	∼36	0.343 ± 0.037	$2.92^{+0.35}_{-0.28}$	−0.60 ± 0.11	−0.99 ± 0.13
G012.90−0.24 (W33 A)	34.9	∼36	0.408 ± 0.025	$2.45^{+0.16}_{-0.14}$	+0.19 ± 0.08	−2.52 ± 0.32
G012.90−0.26 (W33 A)	37.0	∼37	0.396 ± 0.032	$2.53^{+0.22}_{-0.19}$	−0.36 ± 0.08	−2.22 ± 0.13

directions are listed.

One goal of our observations is to estimate the distance and proper motion of the central object in each source. In G012.68−0.18, we obtained the proper motion of the central object by fitting a model for expanding outflows (Sato et al. 2010b) to the proper motions of all maser spots. In the other sources, the small number of maser spots and their distribution did not allow the fitting of this model to their proper motions. Instead, the presented values are averages of the proper motions of all maser spots in each source.

W33

Figure 2.1 shows the dust emission of the W33 complex from the APEX Telescope Large Area Survey of the GALaxy (ATLASGAL, Schuller et al. 2009) at 870 μm. The three most massive clouds W33 A, W33 Main, and W33 B are indicated. The water masers are marked with black crosses.

Water maser spots were detected in an 0.″15×0.″15 area in W33 B (G012.68−0.18), covering a velocity range of 57−63 km s^{-1}. Figure 2.2 shows that the maser emission in the reference channel (v_{LSR} = 59.3 km s^{-1}, left panel) as well as the emission of the three background quasars J1808−1822 (right upper panel), J1809−1520 (left lower panel), and J1825−1718 (right lower panel) are dominated by one compact component. Since the quasar J1809−1520 was detected only in the first four epochs, we determined the position of the reference maser spot only relative to the background quasars J1808−1822 and J1825−1718 as a function of time (see Fig. 2.3). For three epochs (2010 Oct 22, 2010 Dec 19, 2011 Sep 20), we used a different maser spot at the same velocity as position reference since the original reference maser spot, used in the other epochs, was too weak to serve as a phase reference.

Figure 2.1: 870 μm dust emission of the W33 complex from the ATLASGAL survey with contour levels of 1, 2, 4, 8, 16, and 32 Jy beam^{-1}. The positions of the water masers are indicated with black crosses. The arrows show the internal motion vectors of the two clouds W33 A and W33 B in the reference frame of W33 Main. The length of the arrow in the upper left corner corresponds to a motion vector of 1 mas yr^{-1}. The circle in the lower left corner shows the beam of the ATLASGAL observations.

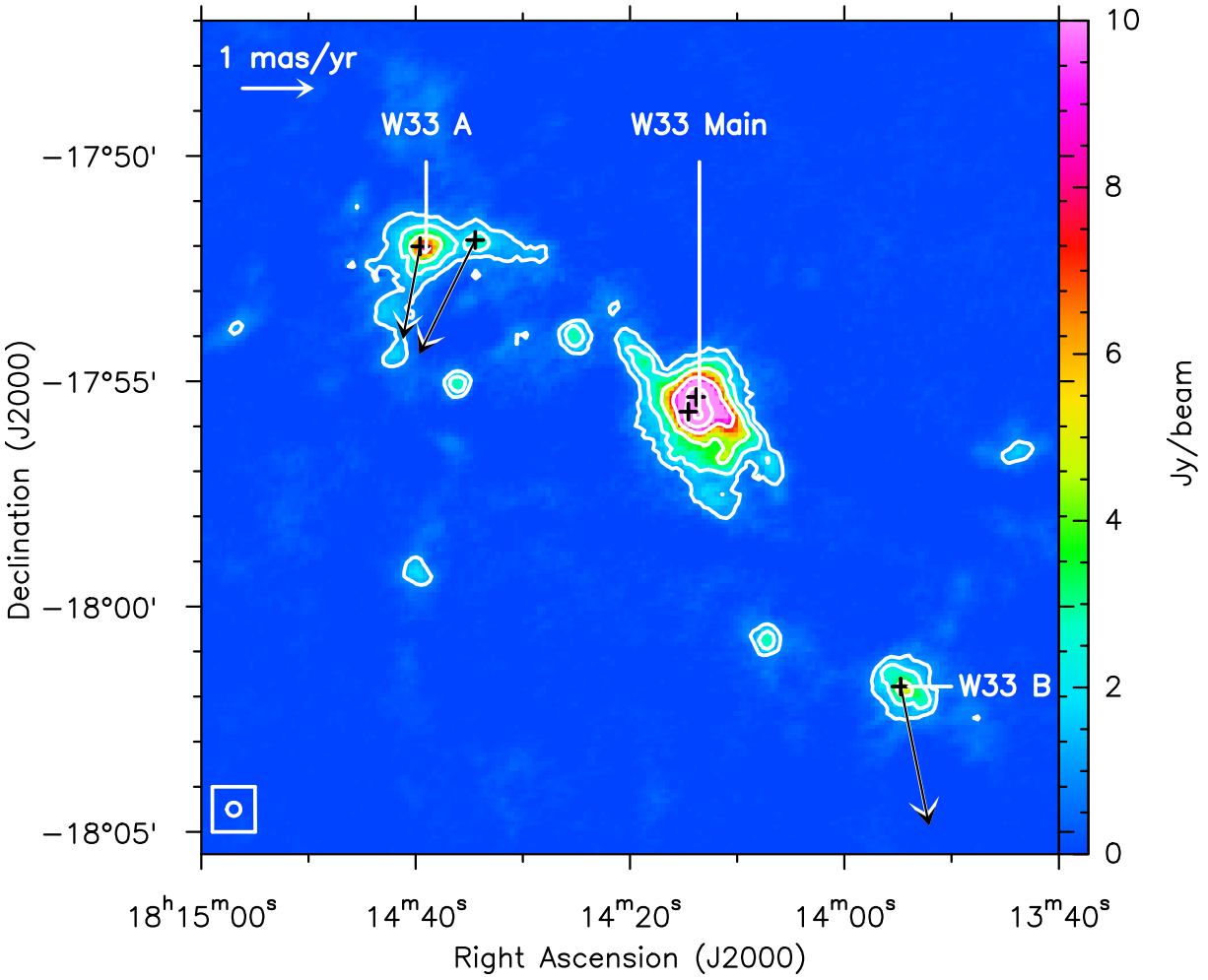

Figure 2.2: Left upper panel: Maser emission of G012.68−0.18 in the reference channel (59.3 km s^{-1}). Right upper, left and right lower panel: Compact emission of the three background quasars J1808−1822, J1809−1520, and J1825−1718, which were phase-referenced to the reference maser channel. The images are obtained from epoch 2011 May 21. The contour levels are 10 to 100 % in steps of 10 % of the maximum in each panel (G012.68−0.18: 132.5 Jy $beam^{-1}$, J1808−1822: 12.3 mJy $beam^{-1}$, J1809−1520: 22.1 mJy $beam^{-1}$, J1825−1718: 96.1 mJy $beam^{-1}$). The restoring beam is shown in the lower left corner.

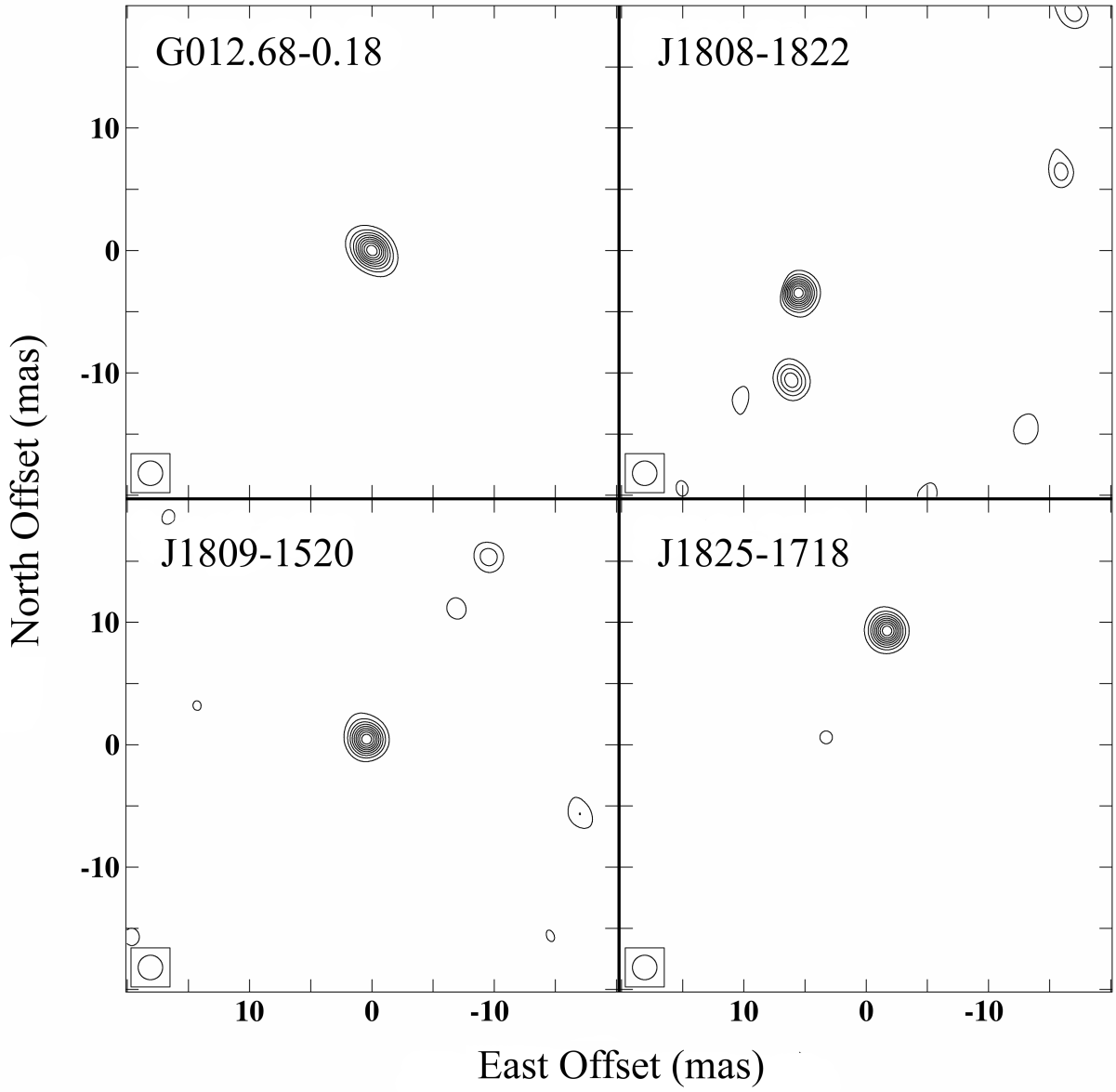

Figure 2.3: Parallax and proper motion fits of G012.68−0.18, yielding a parallax of (0.416 ± 0.028) mas. The positions of the reference maser spot at 59.3 (triangles) km s^{-1} were measured relative to the background quasars J1808−1822 (blue) and J1825−1718 (red). Left Panel: Position on the sky with a label for the first and last epoch. Middle Panel: East (continuous line) and North (dashed line) position offsets with parallax and proper motion fits versus time. Right Panel: Right ascension (continuous line) and Declination (dashed line) parallax fits with the best-fit proper motions removed, showing only the parallax signature.

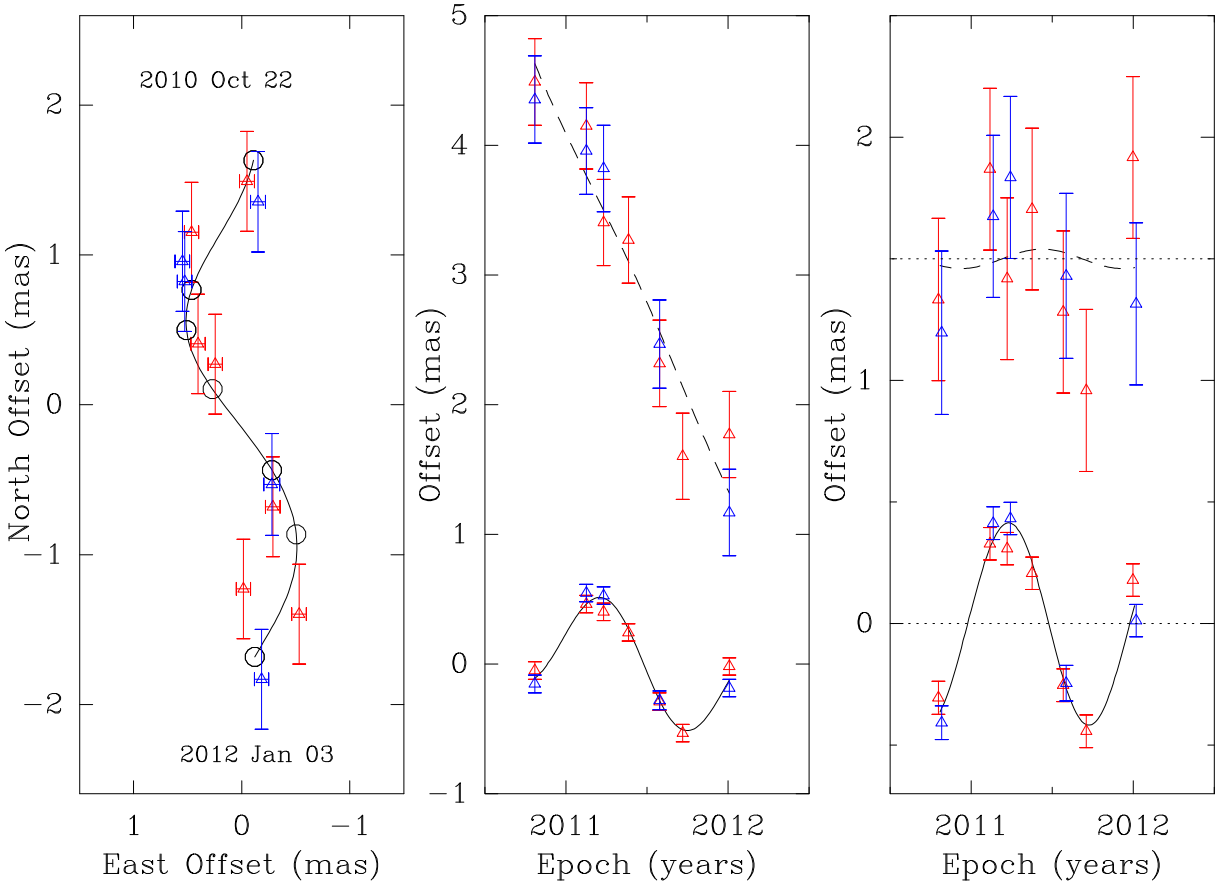

Figure 2.4: Positions of all maser spots in G012.68−0.18 that have been detected in at least three epochs (positions from epoch 2011 May 21). The size of the spots scales logarithmically with the flux density of the spots. The asterisk marks the position of the central star which has an error of ∼0.1″ in both coordinates. The arrows show the proper motions of the maser spots in the reference frame of the central star.

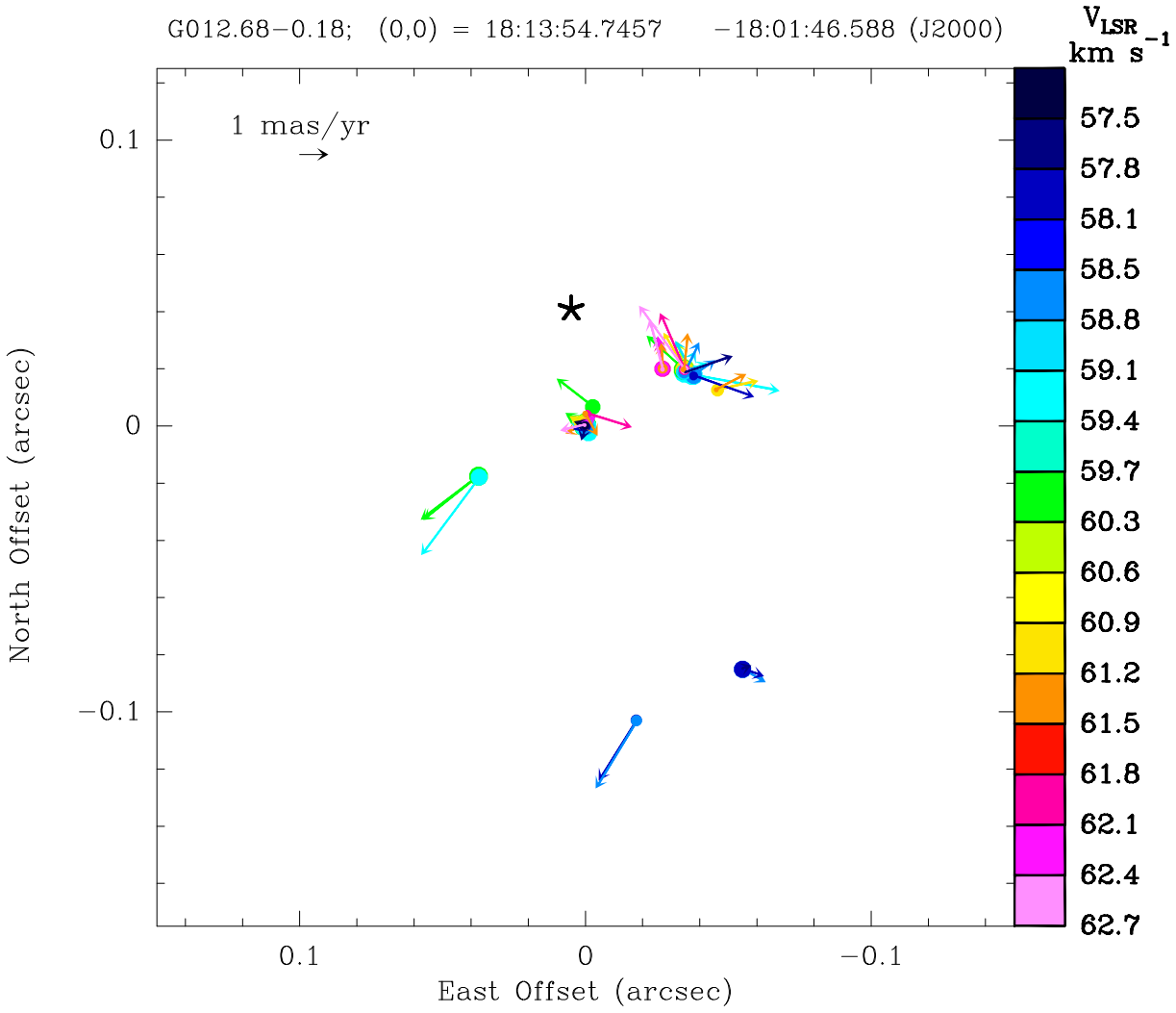

The positions of the reference maser spot in G012.68−0.18 relative to background quasars were fitted with the sinusoidal parallax signature and a linear proper motion. We obtained parallax estimates of $\pi = 0.462 \pm 0.034$ mas and $\pi = 0.387 \pm 0.037$ mas, relative to the background quasars J1808−1822 and J1825−1718, respectively. Since both results are consistent within their joint uncertainty, we combined the two data sets and repeated the fitting, yielding a value of $\pi = 0.416 \pm 0.028$ mas which corresponds to a distance of $2.40^{+0.17}_{-0.15}$ kpc (see Fig. 2.3).

We fitted the proper motions of all maser spots in G012.68−0.18, detected in at least three epochs, with a model for expanding outflows with the position and proper motion of the central driving source as free parameters (for more details about the model see Sato et al. 2010b). The proper motion of the central star is $\mu_x = -1.00 \pm 0.30$ mas yr^{-1} and $\mu_y = -2.85 \pm 0.29$ mas yr^{-1}. Figure 2.4 shows the positions of the maser spots with their proper motions in the reference frame of the central source. Observations with the Submillimeter Array (SMA) at 230 GHz (Immer et al, in prep., see Chapter 3) show that the reference maser spot is located in a dust core, offset by $\sim$0.1″ from the submillimeter continuum peak. The radial velocity of the reference maser spot is similar to the systemic velocity of the thermal gas in this cloud (55 km s^{-1}, Wienen et al. 2012).

The remaining W33 masers were phase-referenced to G12.68-0.18 and the positions of their strongest maser spots were determined relative to this maser, yielding relative parallaxes. To obtain absolute parallax values, the positions of G012.68−0.18 relative to the two background quasars were added to the position measurements of the other water masers.

In G012.81−0.19, we detected two spatially and kinematically distinct maser groups, covering velocity ranges of 33 to 35 km s^{-1} and −5 to 0 km s^{-1}, separated by $\sim$21″. The positions of two maser spots at −1.4 and 34.1 km s^{-1} were determined relative to G012.68−0.18. Combining the two position measurements, we obtained an absolute parallax of $\pi = 0.343 \pm 0.037$ mas (see Fig. 2.5, left panel). The positions of the two maser groups are shown in Fig. 2.6. The images on the right-hand side show both maser groups on a smaller scale with their proper motions. Averaging the proper motions of all maser spots in each group, yields a proper motion value for each velocity group (uncorrected for expansion): $\mu_{x,\,34\ \mathrm{km\,s^{-1}}} = -0.24 \pm 0.17$ mas yr^{-1} and $\mu_{y,\,34\ \mathrm{km\,s^{-1}}} = 0.54 \pm 0.12$ mas yr^{-1} as well as $\mu_{x,\,-1\ \mathrm{km\,s^{-1}}} = -0.60 \pm 0.11$ mas yr^{-1} and $\mu_{y,\,-1\ \mathrm{km\,s^{-1}}} = -0.99 \pm 0.13$ mas yr^{-1}. The maser spots in the velocity group around −1 km s^{-1} are ordered along a ridge with redshifted velocities at the north-east end and blueshifted velocities at the south-west end. The maser spot group at 34 km s^{-1} is located in a dust core, offset by $\sim$7″ from the main continuum emission peak at 230 GHz (Immer et al., in prep., see Chapter 3). The radial velocity of the reference maser spot is similar to the systemic velocity of the thermal gas of 36 km s^{-1}, which was estimated from ammonia observations of the H_2O southern Galactic

Figure 2.5: Right ascension parallax fits of G012.81−0.19 (left), G012.90−0.24 (middle), and G012.90−0.26 (right), yielding absolute parallaxes of 0.343 ± 0.037 mas, 0.408 ± 0.025 mas, and 0.396 ± 0.032 mas, respectively. The positions of the maser spots were measured relative to the water maser G012.68−0.18 and consecutively to the two background quasars J1808−1822 (blue) and J1825−1718 (red). Left panel: Positions of the maser spots at 34.1 (triangles) and −1.4 (squares) km s^{-1}. Middle panel: Positions of the maser spots at 34.5 (triangles), 34.9 (squares), and 35.3 (pentagons) km s^{-1}. Right panel: Positions of the maser spot at 37.0 (triangles) km s^{-1}.

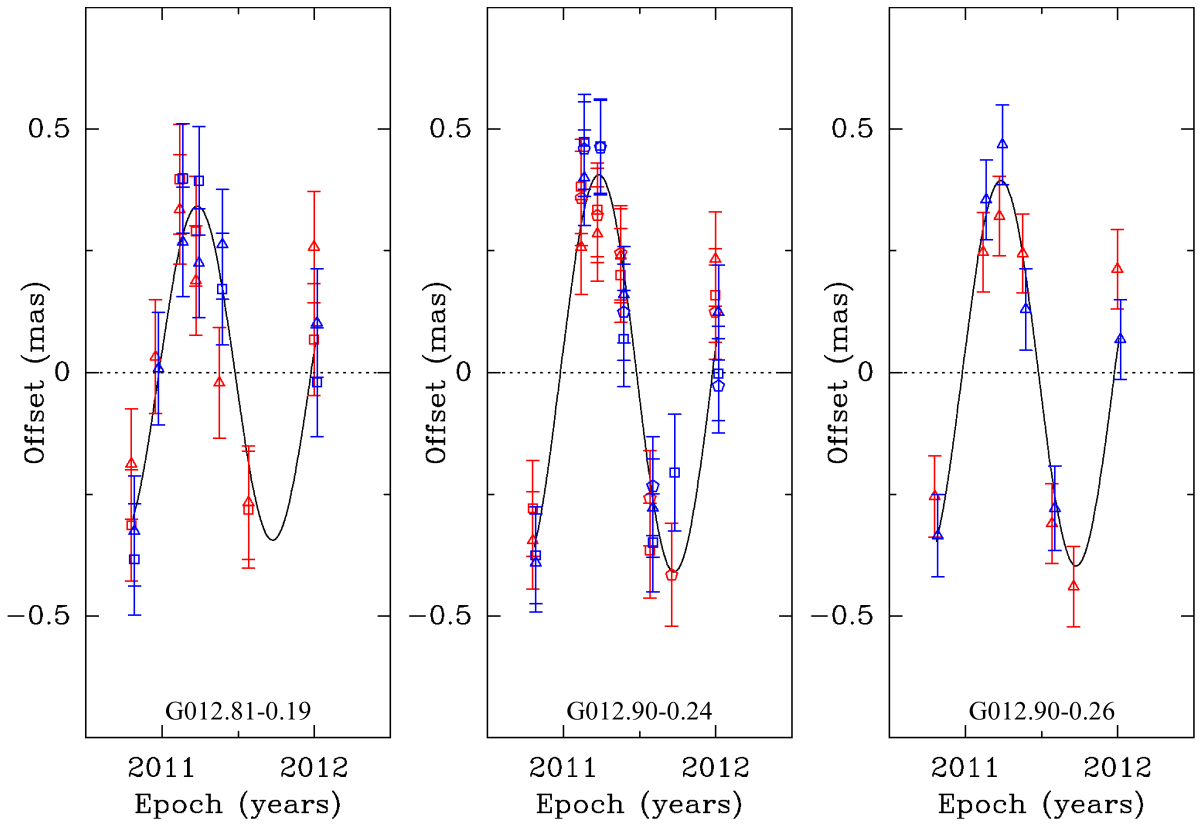

Figure 2.6: Left panel: Positions of all maser spots in G012.81−0.19 that have been detected in at least three epochs (positions from epoch 2011 May 21). Inside panels: Zoom-in on the two maser spot groups at 34 km s^{-1} (lower panel) and −1 km s^{-1} (upper panel). The maser spots in the upper panel are ordered along a ridge. The size of the spots scales logarithmically with the flux density of the spots. The arrows show the absolute proper motions of the maser spots.

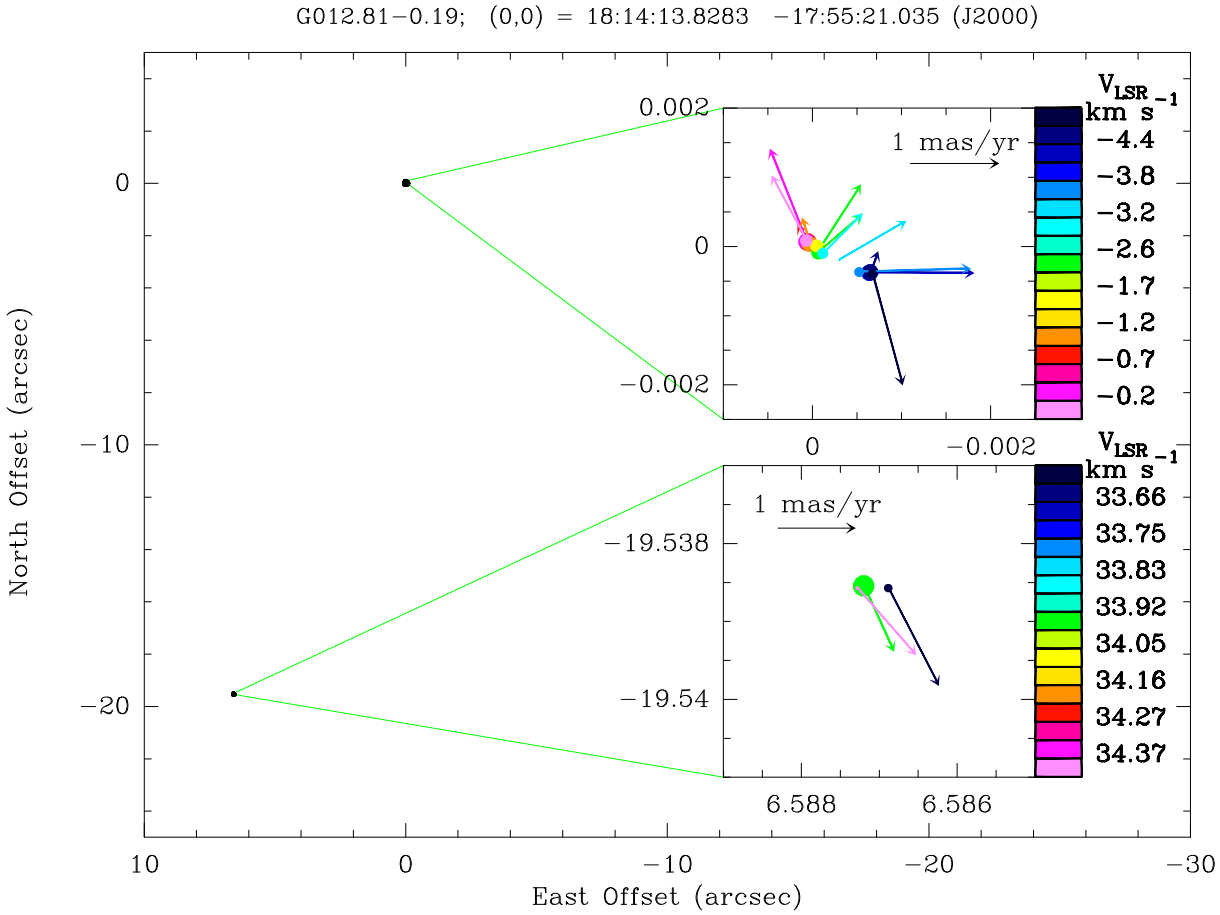

Figure 2.7: Positions of all maser spots in G012.90−0.24 that have been detected in at least three epochs (positions from epoch 2011 May 21). The size of the spots scales logarithmically with the flux density of the spots. The arrows show the absolute proper motions of the maser spots.

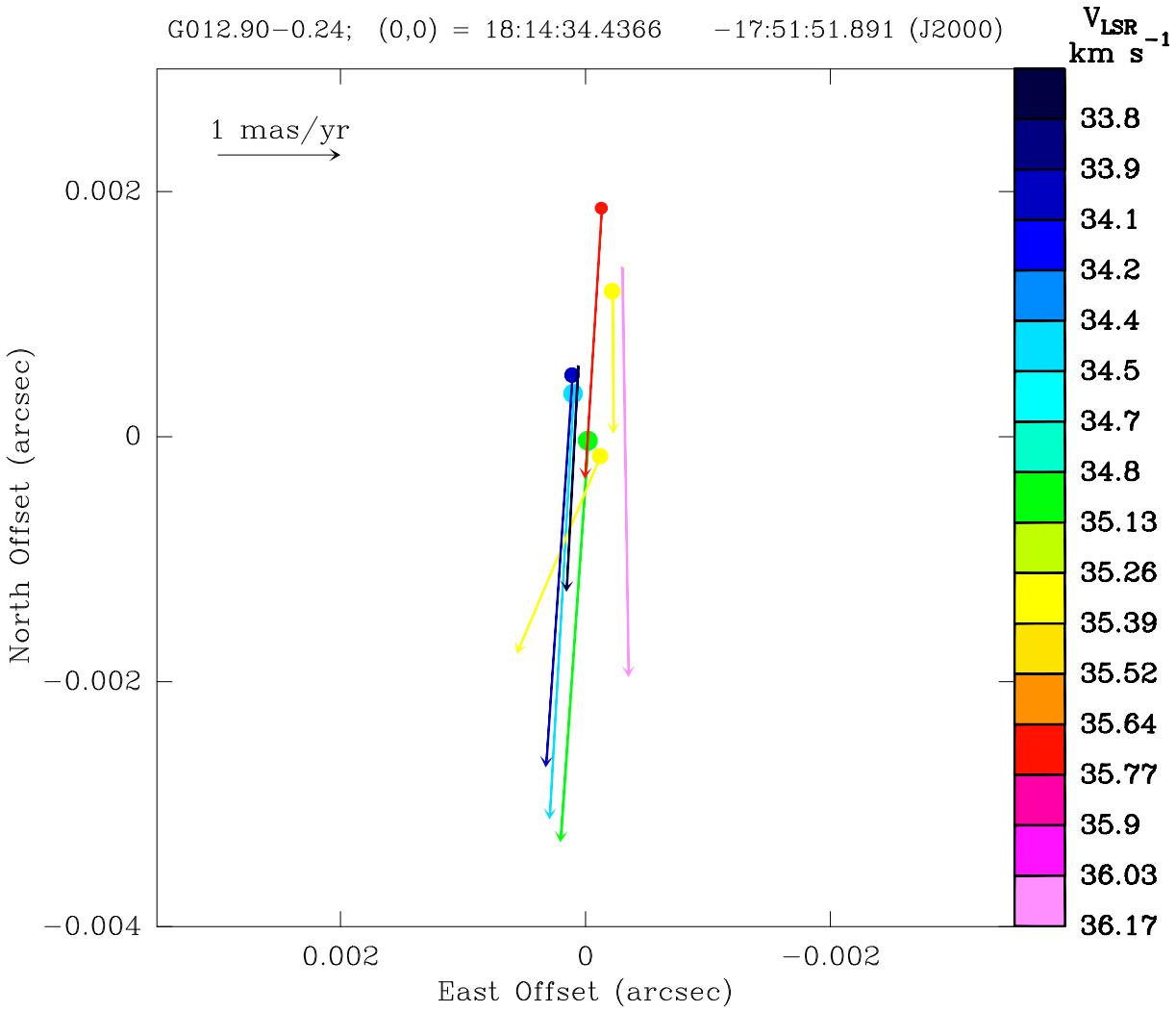

Figure 2.8: Positions of all maser spots in G012.90−0.26 that have been detected in at least three epochs (positions from epoch 2011 May 21). The size of the spots scales logarithmically with the flux density of the spots. The arrows show the absolute proper motions of the maser spots.

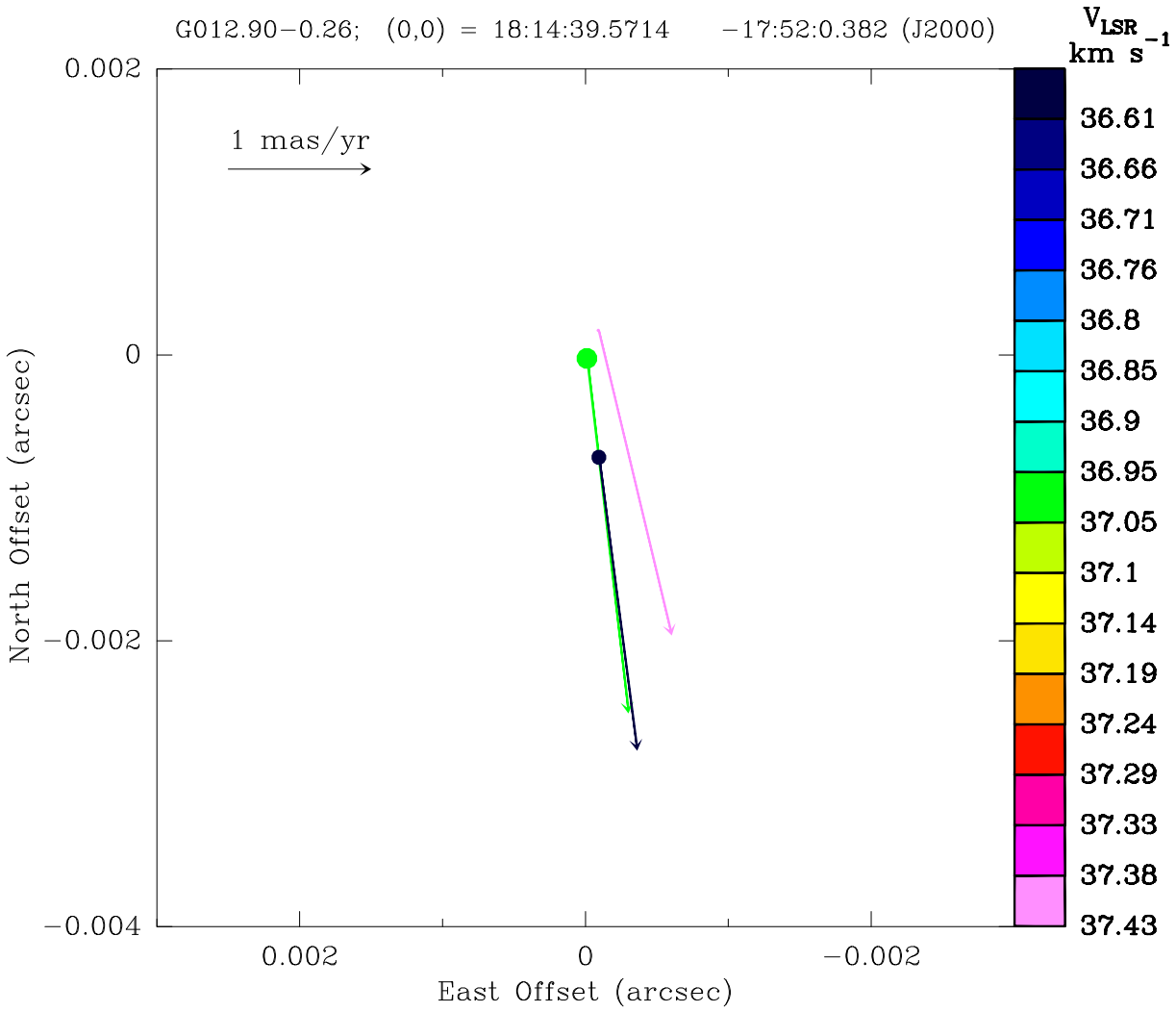

Plane Survey (HOPS, Purcell et al. 2012). The maser spot group at −1 km s^{-1} is associated with emission from a dust core at 345 GHz (Immer et al., in prep., see Chapter 3). However, the radial velocities of these maser spots are very different from the systemic velocity in this source and they might trace the blueshifted shock front of an outflow.

The maser emission from G012.90−0.24 spans a velocity range of 33 to 37 km s^{-1}. For the parallax fitting, we used the positions of three maser spots at velocities of 34.5, 34.9, and 35.3 km s^{-1} and obtained an absolute parallax of $\pi = 0.408 \pm 0.025$ mas (see Fig. 2.5, middle panel). The proper motions of the detected maser spots are very similar (Fig. 2.7). The proper motion of the source (uncorrected for expansion), obtained from averaging all maser spot proper motions, is $\mu_x = 0.19 \pm 0.08$ mas yr^{-1} and $\mu_y = -2.52 \pm 0.32$ mas yr^{-1}. The ATLASGAL map (Fig. 1.7) shows that the reference maser spots are offset by ∼8″ from a submillimeter continuum peak. The radial velocities of the reference maser spots are close to the systemic velocity of G012.90−0.24 (36 km s^{-1}, estimated from the HOPS survey).

Only three maser spots were detected in G012.90−0.26, covering a velocity range of 36 to 38 km s^{-1}. We used the strongest maser spot at 37.0 km s^{-1} for the parallax fitting, yielding an absolute parallax of $\pi = 0.396 \pm 0.032$ mas (see Fig. 2.5, right panel). Averaging the proper motions of the three maser spots, we obtain a proper motion of the source of $\mu_x = -0.36 \pm 0.08$ mas yr^{-1} and $\mu_y = -2.22 \pm 0.13$ mas yr^{-1}. The position of the reference maser spot is consistent with the submillimeter continuum peak MM1-SE, detected by Galván-Madrid et al. (2010) at 230 GHz. This object is associated with a faint radio source at 7 mm (van der Tak & Menten 2005). The radial velocity of the reference maser spot is very close to the systemic velocity of the thermal gas in W33 A (38.5 km s^{-1}, Galván-Madrid et al. 2010). A comparison of the proper motion of G012.90−0.26 with CO observations of the large-scale outflow in W33 A (Galván-Madrid et al. 2010) show that their directions do not agree. Thus, we will assume that the proper motion of this water maser is not strongly influenced by the outflow but probably reflects the motion of the central object.

2.4 Discussion

The absolute parallaxes of G012.81−0.19, G012.90−0.24, and G012.90−0.26 are consistent with a parallax of 0.416 mas within 2σ, i.e. the distances to these masers are in accordance with the distance to G012.68−0.18 (2.40 kpc).

Comparing the coordinates of the W33 complex with a CO latitude-velocity map from the survey of Dame et al. (2001) (Fig. 2.9), we find that the complex is associated with a bright cloud

Figure 2.9: Positions of the W33 water masers in the CO latitude-velocity plot (white dots). The CO emission was integrated over a longitude range from 12.625° to 13.0°. The units of the color bar are degrees Kelvin. The water masers in W33 are associated with a cloud at 34.6 km s^{-1}. The water masers at -1 km s^{-1} (W33 Main) and 58 km s^{-1} (W33 B) seem to be outliers.

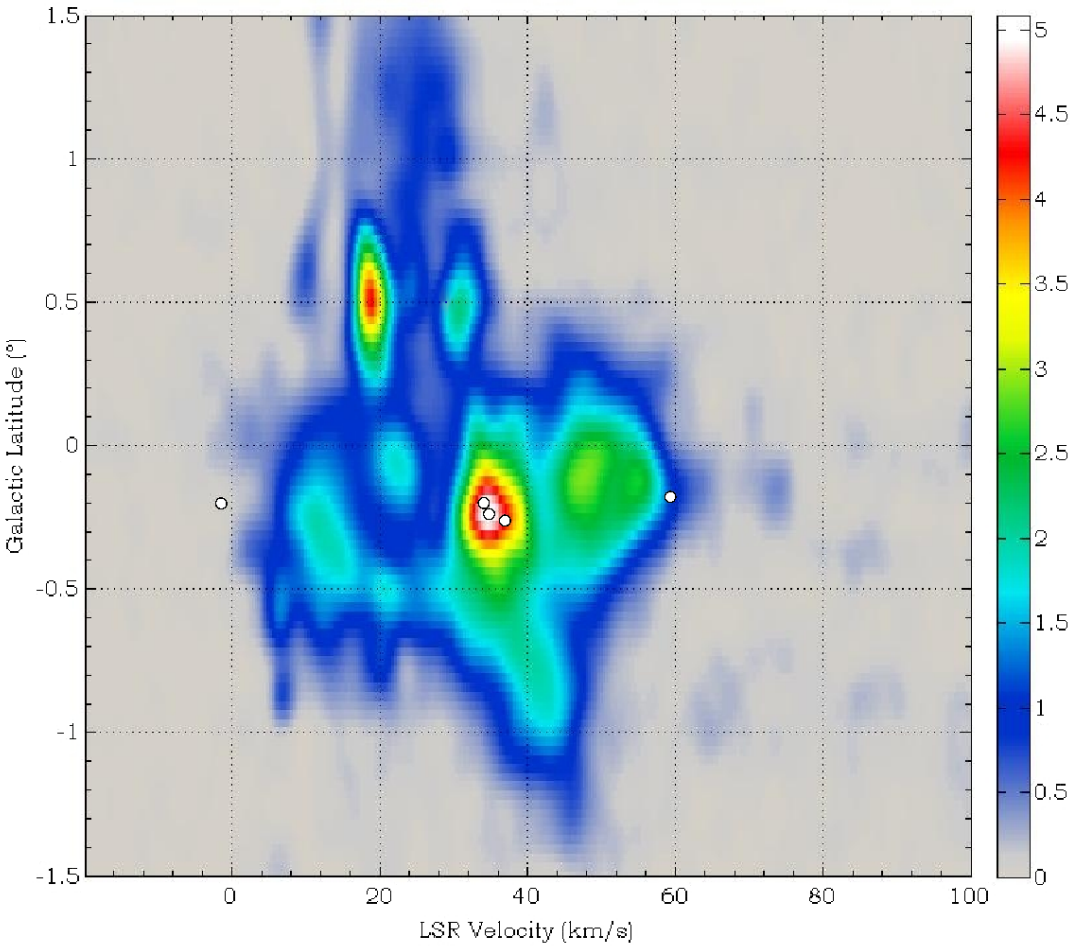

at the same latitude with a mean velocity of 34.6 km s^{-1}, which falls along the longitude-velocity locus of the Scutum spiral arm.

Since all water masers in the W33 complex are at a similar distance, we conclude that the molecular clouds W33 A, W33 Main, and W33 B are connected and belong to the same star forming complex. Our parallax distance to this star forming cluster is a factor of 0.65 (= 2.4 kpc/3.7 kpc) smaller than the kinematic distance. Thus, the luminosity and mass of this complex have been overestimated in the past by a factor of more than two and should be revised to $L \sim 8 \cdot 10^5\ L_\odot$ and $M \sim 8 \cdot 10^4\ M_\odot$.

The spectral types of the stars in the W33 Main cluster were determined from the estimated number of Lyman continuum photons needed to ionize the material in the surrounding H II region. Since the number of photons depends on distance squared, the values have been overestimated by a factor of more than two, changing the spectral types by 1.5 points to later types, i.e., a star previous estimated to be spectral type O6 should have a spectral type O7.5. Thus, the star cluster in W33 Main has spectral types ranging from O7.5 to B1.5.

Our observations show maser detections in the W33 complex in three different velocity ranges:

- 57−63 km s^{-1} in G012.68−0.18,
- 33−38 km s^{-1} in G012.81−0.19, G012.90−0.24, G012.90−0.26,
- −5−0 km s^{-1} in G012.81−0.19.

These findings are confirmed by water and hydroxyl maser observations by Genzel & Downes (1977), Lada et al. (1981), and Argon et al. (2000). Ammonia observations with the Effelsberg 100 meter telescope (Wienen et al. 2012) and from the HOPS survey (Purcell et al. 2012) give line-of-sight velocities of ∼55, ∼36, ∼36, and ∼37 km s^{-1} for G012.68−0.18, G012.81−0.19, G012.90−0.24, and G012.90−0.26, respectively, in accordance with our maser observations. On the other hand, Urquhart et al. (2008) and Chen et al. (2010) detected CO emission peaks at 35, 60, and 52 km s^{-1} in G012.68−0.18, G012.81−0.19, and G012.90−0.26. These results show that both velocity components at ∼36 and ∼58 km s^{-1} are spread over the entire complex but the emission at these velocities peaks in different regions. The ammonia observations of Wienen et al. (2012) show the velocity component at ∼58 km s^{-1} also at positions in the vicinity of W33 (e.g. G11.94−0.26, G12.74−0.10, G12.90−0.03). This indicates that this velocity component is not unique to the inner W33 complex and probably has a different origin than internal motions (e.g. outflows) in the clouds. The velocity component at ∼−1 km s^{-1} in G012.81−0.19 was not detected in previous thermal line observations. The arrangement of the water maser spots in this

velocity group (see Fig. 2.6) might suggest that this velocity component is associated with the shock front of an outflow in the active cloud W33 Main (Immer et al., in prep., see Chapter 3) .

Although water masers are often found at the base of bipolar outflows, the small radial velocity difference between the masing and the thermal gas in G012.81−0.19, G012.90−0.24, and G012.90−0.26 (see Table 2.2), the small radial velocity range of the masing gas and the proximity of the masers to submillimeter dust peaks suggests that the 3D motions of the water masers are similar to the motions of the associated central objects and not drastically altered by strong outflows. The only case where a strong outflow could affect the proper motion of the water maser without changing its radial velocity is if the outflow was aligned with the plane of the sky. However, the probability of outflows being in the plane of the sky in all three sources is small. Thus, we assume that the average proper motion of the water maser spots in each source is similar to the motion of its central object. Under this assumption, we can estimate the cloud motions internal to the W33 complex from the motions of the central objects. In G012.68−0.18, we estimated the motion of the central object by fitting a model of expanding outflows to the proper motions of the maser spots. Since the maser spots in the velocity group around −1 km s^{-1} in G012.81−0.19 have a very different radial velocity than the thermal gas in this cloud, their proper motions probably do not reflect the motion of the central object of the W33 Main cloud. They were thus excluded from the following calculations. We averaged the motions of W33 A (G012.90−0.24, G012.90−0.26), W33 B (G012.68−0.18), and W33 Main (G012.81−0.19, −34 km s^{-1}), yielding an estimate of the average proper motion of the complex: $\mu_x = -0.44 \pm 0.25$ mas yr^{-1} and $\mu_y = -2.14 \pm 0.41$ mas yr^{-1}, corresponding to −5 km s^{-1} and −24 km s^{-1} in the eastward and northward directions, respectively (at the measured distance of 2.40 kpc). To determine the cloud motions of W33 A and W33 B relative to the W33 Main cloud, the motion of W33 Main was subtracted from the motion of each cloud. Figure 1.7 shows the cloud motions of W33 A and W33 B in the reference frame of W33 Main on the 870 μm dust emission map of the W33 complex.

That W33 A and W33 Main have similar radial velocities suggests that most of the motion of W33 A in the reference frame of W33 Main is in the plane of the sky, tangentially to W33 Main (total speed $\approx$ 17 km s^{-1}).

The difference in radial velocity between W33 Main and W33 B is ∼22 km s^{-1}. This large velocity component along the line of sight coincidentially is equal to the velocity component in the plane of the sky of 22 km s^{-1} (relative to W33 Main), yielding a total speed of 31 km s^{-1} for W33 B relative to W33 Main. In Chapter 3, we will compare the gravitational and kinetic energies of the clouds to determine if W33 A and W33 B are gravitationally bound to W33 Main.

2.5 Conclusions

Trigonometric parallax observations of water masers in the high-mass star forming complex W33 (containing G012.68−0.18, G012.81−0.19, G012.90−0.24, G012.90−0.26) yield distances which are all consistent with $2.40^{+0.17}_{-0.15}$ kpc. A combination of our distance with CO observations of the Galactic plane by Dame et al. (2001) allows us to locate the W33 complex in the Scutum spiral arm. We show that W33 is a single star forming complex at about two-thirds the kinematic distance of 3.7 kpc. Thus, the luminosity and mass estimates of this region should be lowered to $L \sim 8 \cdot 10^5$ $L_\odot$ and $M \sim 8 \cdot 10^4$ $M_\odot$. The spectral types in the star cluster in W33 Main should be changed by 1.5 points to later types, yielding spectral types ranging from O7.5 to B1.5.

3 Chemical Evolution in the High-Mass Star Forming Complex W33

3.1 Motivation

Since the W33 complex contains star forming regions at different evolutionary stages which are located at similar distances and probably developed from the same giant molecular cloud, we conducted a chemical study of these star forming regions with the Atacama Pathfinder Experiment (APEX) telescope[1] (Güsten et al. 2006) and the Submillimeter Array (SMA). The goal of this project is to study the chemical composition of the star forming regions along an evolutionary sequence. Since the two data sets have different resolutions, they provide information about the chemical composition of the star forming regions on different scales.

The chapter has the following structure. In Sect. 3.2, we describe the observations and complementary data sets that were analyzed in this chapter. Section 3.3 introduces the W33 complex. Section 3.4 gives dust temperatures and total masses of the studied molecular clouds[2]. In Sect. 3.5, we focus on the kinematics in the W33 complex. In Sects. 3.6 and 3.7, we present the results from the APEX and SMA observations. In Sect. 3.8, we infer column densities and temperatures from the APEX and SMA observations for each cloud. Section 3.9 discusses the chemical diversity in the W33 clouds. In Sect. 3.10, we give a short conclusion of this chapter.

Table 3.1: Pointing center coordinates and rms noise levels of APEX and SMA observations

			APEX	SMA	
Source	R.A. (hh mm ss.ss)	Dec (dd ′ ″.″″)	rms_{Line} (mK)	rms_{Cont} (mJy beam^{-1})	rms_{Line} (mK)
W33 Main1	18 14 25.39	−17 54 00.68	1.83	6	240 (LSB), 330 (USB)
W33 A1	18 14 36.10	−17 55 03.03	1.58	5	250 (LSB), 340 (USB)
W33 B1	18 14 07.07	−18 00 44.72	1.73	5	250 (LSB), 330 (USB)
W33 B	18 13 54.33	−18 01 51.71	0.55	10	240 (LSB), 310 (USB)
W33 A	18 14 39.00	−17 52 05.00	0.5	7	150 (LSB), 110 (USB)
W33 Main	18 14 13.72	−17 55 43.60	0.5	70	260 (LSB), 350 (USB)

3.2 Observation and Data Reduction

3.2.1 Submillimeter Array Data Set

We observed five molecular clouds of the W33 complex (W33 Main1, W33 A1, W33 B1, W33 B, and W33 Main; see contours in Fig. 3.1) at 230 GHz with the SMA. The observations were taken in compact configuration in 2011 May, covering baselines from 16 to 69 kλ (corresponding to detected physical scales of ∼0.04 to ∼0.18 pc). The full width at half maximum (FWHM) of the primary beam is 55″. The five sources were observed with hexagonal seven-pointing mosaics. The two side bands have a bandwidth of 4 GHz each and cover a frequency range of 216.9−220.9 GHz (lower sideband, LSB) and 228.9−232.9 GHz (upper sideband, USB). The observations have a channel spacing of 0.8125 MHz (corresponding to 1.1 km s^{-1}). Table 3.1 lists the coordinates of the mosaic centers (Cols. 2, 3) and the noise levels for the continuum and the line emission per source (Cols. 5, 6). W33 A was observed with a similar setup by Galván-Madrid et al. (2010), but with only 2 GHz of bandwidth per sideband.

The data reduction and analysis was conducted with the software packages MIR[3], Miriad[4], and CASA[5](Jaeger 2008). From observations of Titan, the absolute amplitude was derived. The quasar 3C279 served as bandpass calibrator. The observations were alternated between the target sources and the phase and amplitude calibrators 1733−130 and 1911−201. The continuum data set was constructed from linear baseline fits to line-free channels in the upper and lower sidebands and subtracted from the whole data set to produce a continuum-free line data cube.

[1]The APEX project is a collaborative effort between the Max Planck Institute for Radioastronomy, the Onsala Space Observatory, and the European Southern Observatory.

[2]In the following chapter, the dust condensations on the APEX scales will be called “clouds” and on the SMA scales “cores”.

[3]`https://www.cfa.harvard.edu/~cqi/mircook.html`

[4]`http://www.cfa.harvard.edu/sma/miriad/`

[5]`http://casa.nrao.edu/gettingstarted.shtml`

We imaged the continuum as well as the line emission of all five sources with CASA's interactive cleaning task. We made moment 0 (integrated intensity) and moment 1 (velocity field) maps of all the detected lines in each source.

In 2011 March, W33 Main was observed with the SMA in compact configuration at 345 GHz as part of a filler project. To cover the same area as our 230 GHz observations, W33 Main was observed with 23 pointings in a hexagonal mosaic. The channel width is 3.2 MHz which corresponds to a velocity resolution of ∼3 km s^{-1}. Since the velocity resolution is too coarse compared to the detected line widths at 230 GHz in W33 Main, we only imaged the continuum data of these observations.

3.2.2 Atacama Pathfinder Experiment Telescope Data Set

On-the-fly (OTF) maps of the six molecular clouds W33 Main1, W33 A1, W33 B1, W33 B, W33 A, and W33 Main were observed at 280 GHz with the FLASH receiver at the APEX telescope. The covered area is 1.8′ x 1.8′. The full width at half maximum (FWHM) of the beam is ∼23″. The observations have two sidebands with a bandwidth of 4 GHz each, centered at 280.2 GHz and 292.2 GHz, and a smoothed spectral resolution of 1.6 km s^{-1} (to obtain a higher signal-to-noise ratio). The calibrated data set was analyzed with the software CLASS[6] from the GILDAS[7] (Maret et al. 2011) package. We determined the continuum level from the line-free channels and subtracted it as a linear baseline from the data cube, generating a continuum-free line data set. We generated spectra of each source by averaging the spectra of the OTF maps within an area of 24″ x 24″, covering the area of the primary beam around the (0,0) position. For each source, we produced moment 0 maps of each detected line. Column 4 of Table 3.1 gives the noise level of the line data cubes for each source.

3.2.3 Institut de Radioastronomie Millimétrique 30m Telescope Data Set

To obtain zero-spacing information for the SMA ^{13}CO and C^{18}O observations of W33 Main, the molecular cloud was observed with the HERA instrument at the Institut de Radioastronomie Millimétrique (IRAM) 30m telescope in 2012 February. The observations were centered on the (2−1) transitions of the CO isotopologues ^{13}CO and C^{18}O at 220.398 and 219.56 GHz, respectively. On-the-fly maps were taken in the frequency-switching mode, covering an area of 6′ x 6′. The calibrated data set was further reduced and analyzed with the CLASS software to obtain a

[6] http://iram.fr/IRAMFR/GILDAS/doc/html/class-html/
[7] http://www.iram.fr/IRAMFR/GILDAS/

continuum-free line database. First, baselines of order 7 and 3 were fitted to the line-free channels and subtracted from the data, the spectra were folded and then again a linear baseline was fitted to the line-free channels and subtracted from the data. To combine the IRAM data sets with the SMA data sets, we smoothed the data to a spectral resolution of ∼1.2 km s^{-1} and re-imaged the SMA data of ^{13}CO and C^{18}O with the same spectral resolution. The SMA and IRAM data cubes were combined in the image plane with the CASA task *feather*.

3.2.4 Additional Data Sets

In the framework of the APEX Telescope Large Area Survey of the GALaxy (ATLASGAL, Schuller et al. 2009) , the W33 complex was observed with the APEX telescope at 870 μm. The FWHM beam width of the APEX telescope at this wavelength is 19.2″ and the continuum map has been sampled on 6″ pixels. The rms in regions with no emission is in the range 40−60 mJy beam^{-1} (Schuller et al. 2009).

Continuum observations of W33 at infrared wavelengths were obtained from the *Spitzer* Galactic Legacy Infrared Mid-Plane Survey Extraordinaire (GLIMPSE, Churchwell et al. 2009), the Midcourse Space Experiment (MSX) survey (Price et al. 2001), and the *Herschel* Infrared Galactic Plane Survey (Hi-GAL, Molinari et al. 2010). The *Spitzer*/GLIMPSE observations were conducted at 3.6, 4.5, 5.8, and 8.0 μm with the IRAC instrument and have a resolution of < 2″. To construct spectral energy distributions of the clouds in the W33 complex, we used the MSX observations at 8.3, 12.1, 14.7, and 21.3 μm which have a spatial resolution of 18.3″ and an rms of 1−35 MJy sr^{-1} and the *Herschel*/Hi-GAL observations at 70, 170, 250, 350, and 500 μm with a spatial resolution of 4−40″ and an rms of ∼13−27 mJy beam^{-1}.

To look for supernova remnants in W33, tracing a former generation of high-mass star formation, we used a 330 MHz map, taken with the Very Large Array (VLA) in B, C, and D configuration by Brogan et al. (2006). The observations have a spatial resolution of 42″ and an rms of ∼5 mJy beam^{-1}.

3.3 The W33 Complex

The ATLASGAL observations of the high-mass star forming complex W33 at 870 μm show three large and three smaller molecular clouds (contours in Fig. 3.1). We selected the clouds W33 Main1, W33 A1, W33 B1, W33 B, W33 A, and W33 Main for our chemical study. The coordinates of the dust emission peaks from the ATLASGAL maps in these six clouds are given in Table 3.2.

Figure 3.1: High-mass star forming complex W33 and its surroundings. The background images show infrared and radio continuum emission at 8 μm, 70 μm, and 90 cm. The contours show dust emission at 870 μm from the ATLASGAL survey (levels 1, 2, 4, 8, 16, and 32 Jy beam^{-1}). Black and red crosses mark 6.7 GHz methanol and 22 GHz water masers, respectively. The positions of star clusters are indicated with blue crosses. The pink circles in panel (a) and the pink squares in panel (b) show the sizes of the SMA mosaics and the covered areas of the OTF APEX maps.

(a) Infrared emission at 8 μm

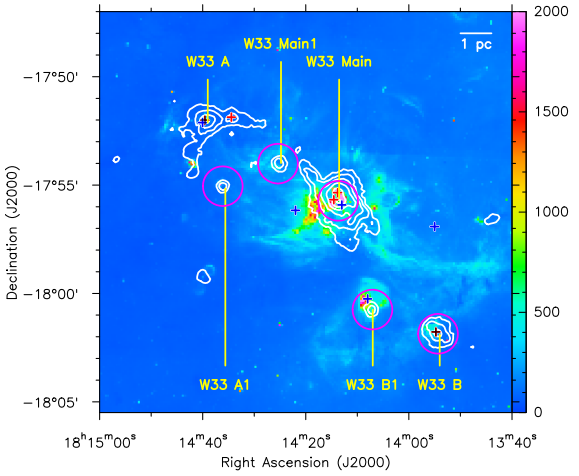

(b) Infrared emission at 70 μm

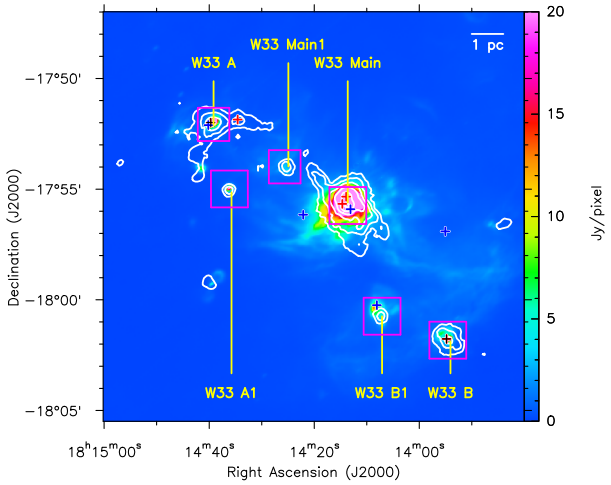

(c) Radio emission at 90 cm

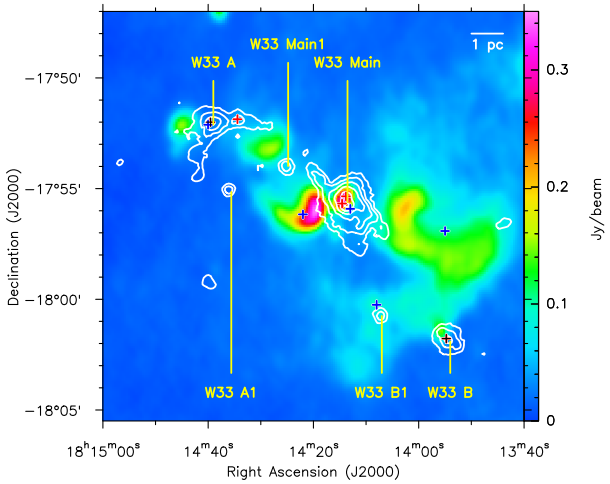

Table 3.2: Sources in the W33 complex.

Source	R.A.	DEC	Object	Reference
W33 Main1	18 14 25.021	−17 53 58.13	Molecular cloud	
W33 A1	18 14 36.087	−17 55 04.95	Molecular cloud	
W33 B1	18 14 07.144	−18 00 45.10	Molecular cloud	
W33 B	18 13 54.368	−18 01 51.92	Molecular cloud	
W33 A	18 14 39.059	−17 52 02.72	Molecular cloud	
W33 Main	18 14 13.531	−17 55 47.47	Molecular cloud	
W33 B-OH	18 13 54.79	−18 01 47.9	OH maser	Caswell (1998)
W33 A-OH	18 14 39.53	−17 52 01.1	OH maser	Caswell (1998)
W33 B-H_2O	18 13 54.7457	−18 01 46.588	H_2O maser	Immer et al. (2013)
W33 A-H_2O-a	18 14 34.4366	−17 51 51.891	H_2O maser	Immer et al. (2013)
W33 A-H_2O-b	18 14 39.5714	−17 52 00.382	H_2O maser	Immer et al. (2013)
W33 Main-H_2O-a	18 14 13.8283	−17 55 21.035	H_2O maser	Immer et al. (2013)
W33 Main-H_2O-b	18 14 14.2315	−17 55 40.573	H_2O maser	Immer et al. (2013)
W33 Main-CH_3OH	18 14 11.09	−17 55 57.4	CH_3OH 25 GHz maser (Class I)	Menten et al. (1986)
W33 B-CH_3OH	18 13 54.75	−18 01 46.6	CH_3OH 6.7 GHz maser (Class II)	Green et al. (2010)
W33 A-CH_3OH	18 14 39.53	−17 52 00.0	CH_3OH 6.7 GHz maser (Class II)	Green et al. (2010)
SNR-1	18 13 19	−17 54	Supernova remnant	Brogan et al. (2006)
SNR-2	18 13 37	−17 49	Supernova remnant	Brogan et al. (2006)
SC-1	18 14 08.0	−18 00 15	Star cluster	Morales, in prep.
SC-2	18 13 55.0	−17 56 55	Star cluster	Morales, in prep.
SC-3	18 13 24.0	−17 53 31	Star cluster	Morales, in prep.
SC-4	18 14 13.0	−17 55 55	Star cluster	Morales, in prep.
SC-5	18 14 22.0	−17 56 10	Star cluster	Morales, in prep.
SC-6	18 14 40.0	−17 52 07	Star cluster	Morales, in prep.

The positions of the methanol, water, and hydroxyl masers that were observed in the W33 complex are listed in Table 3.2. The methanol masers in W33 B and W33 A are radiation pumped (Class II, 6.7 GHz) while the methanol maser in W33 Main is pumped by collisions (Class I, 25 GHz). In W33 B and W33 A, the methanol, water, and hydroxyl masers are separated by less than 8″ and 2″, respectively. No OH and 6.7 GHz CH_3OH masers were detected in W33 Main.

In the center of W33 Main, infrared emission peaks at 3.6−8 μm as well as at 70−500 μm are observed in the *Spitzer*/GLIMPSE and the *Herschel*/Hi-GAL maps (Fig. 3.1a and Fig. 3.1b), respectively. The two water masers are located between these infrared peaks. To the east of W33 Main, two arcs of strong mid-infrared emission can be seen in Fig. 3.1a. In the west, the mid-infrared emission forms a bubble and a ∼5 pc long filament. Both are visible at 70 and 170 μm in the *Herschel*/Hi-GAL maps (Fig. 3.1b) but not at longer wavelengths. Strong mid- and far-infrared emission is also detected at the center of W33 A and at the border of W33 A1 and W33 B1. Weaker and more diffuse emission is observed at the positions of W33 B and W33 Main1.

Star clusters, signs of advanced star formation in the W33 complex, are detected at the border of the W33 B1 cloud, in the centers of W33 Main and W33 A, and east and west of W33 Main (Morales et al., in prep., and references therein; blue crosses in Fig. 3.1). The coordinates of the star clusters are listed in Table 3.2. The vicinity of the star clusters outside of W33 Main to the arc- and filament-shaped infrared emission suggests that this emission is influenced by the high-mass stars in these clusters.

Brogan et al. (2006) observed the W33 complex and its surroundings at 330 MHz with the VLA (Fig. 3.1c) to detect supernova remnants (coordinates in Table 3.2) in the region. Two supernova remnants are found in the north-west of the W33 complex at a distance of about 8 pc from the W33 Main cloud. One strong radio emission peak is detected at the center of W33 Main, located between the infrared peaks. W33 Main is also the only source that shows strong emission at 5 GHz in the Co-Ordinated Radio 'N' Infrared Survey for High-mass star formation (CORNISH) VLA survey (Hoare et al. 2012, see Chapter 4). Outside of W33 Main, strong radio emission at 330 MHz coincides with the arc-shaped infrared emission. Ho et al. (1986) suggested that the extended emission is an ionization front, excited by an earlier generation of high-mass stars, which penetrates the molecular cloud around W33 Main. They conclude that shocks from high-mass stars can compress molecular clouds on short time scales (∼10^4 yr) if these stars are not too luminous. The star cluster SC-5 could be a candidate for this earlier generation of stars. A comparison of the ages of SC-5 and the star cluster in W33 Main (SC-4) could provide information if the star formation in W33 Main was triggered by an earlier generation of stars. Weaker

emission at 330 MHz is detected at the position of the infrared bubble and the filament, forming a bow-shaped structure around the star cluster SC-2. Diffuse emission is observed at the border of the W33 B and W33 B1 clouds. No radio emission at 330 MHz is found in the clouds W33 Main1, W33 A1, and W33 A.

Combining the continuum and maser information, we can sort our sources in different groups (grey colors) which mirrors their evolutionary stages:

Source	Submillimeter	Infrared	Maser	Radio
W33 Main1	✓	weak	–	–
W33 A1	✓	weak	–	–
W33 B1	✓	weak	–	–
W33 B	✓	weak	✓	–
W33 A	✓	✓	✓	–
W33 Main	✓	✓	✓	✓

3.4 Dust Temperatures and Cloud Masses

To determine the dust temperatures of the six W33 clouds, we fit the spectral energy distributions (SEDs) of the clouds with grey-body and black-body models. The SEDs are constructed from infrared maps of the MSX and the *Herschel*/Hi-GAL surveys and the submillimeter ATLASGAL map, covering a wavelength range of 8−870 μm. For all wavelengths, we chose the same circular aperture over which the emission was integrated. The radius of the aperture was selected to correspond to the effective radius of the clouds in the ATLASGAL catalog (Contreras et al. 2013). To estimate the background emission at all wavelengths, we integrated the emission in apertures with a radius of 40″ at 20 positions around the W33 complex. Then, we averaged these values and subtracted the background emission from the total emission of each cloud at each wavelength, following formula 1 of Anderson et al. (2012).

The generated SEDs can be fitted with a “cold” plus a “warm” component. The detection of two temperature components suggests that all six clouds have a heating source inside or nearby. The cold and the warm components were then fitted with a grey-body and a black body model, respectively. From the fits, we determine the bolometric luminosities and the warm and cold temperatures of the clouds. The SED fits are shown in Fig. 3.2. The temperatures and luminosities are listed in Table 3.3 (Cols. 4−6). The cold and warm temperatures range between 26 and 42 K and 142 and 254 K, respectively. The highest values of T_{cold} are estimated for W33 Main and W33 B1. W33 B, W33 B1, and W33 Main1 show the highest T_{warm} values. While the tem-

Figure 3.2: SED fits of the six clouds W33 Main1, W33 A1, W33 B1, W33 B, W33 A, and W33 Main.

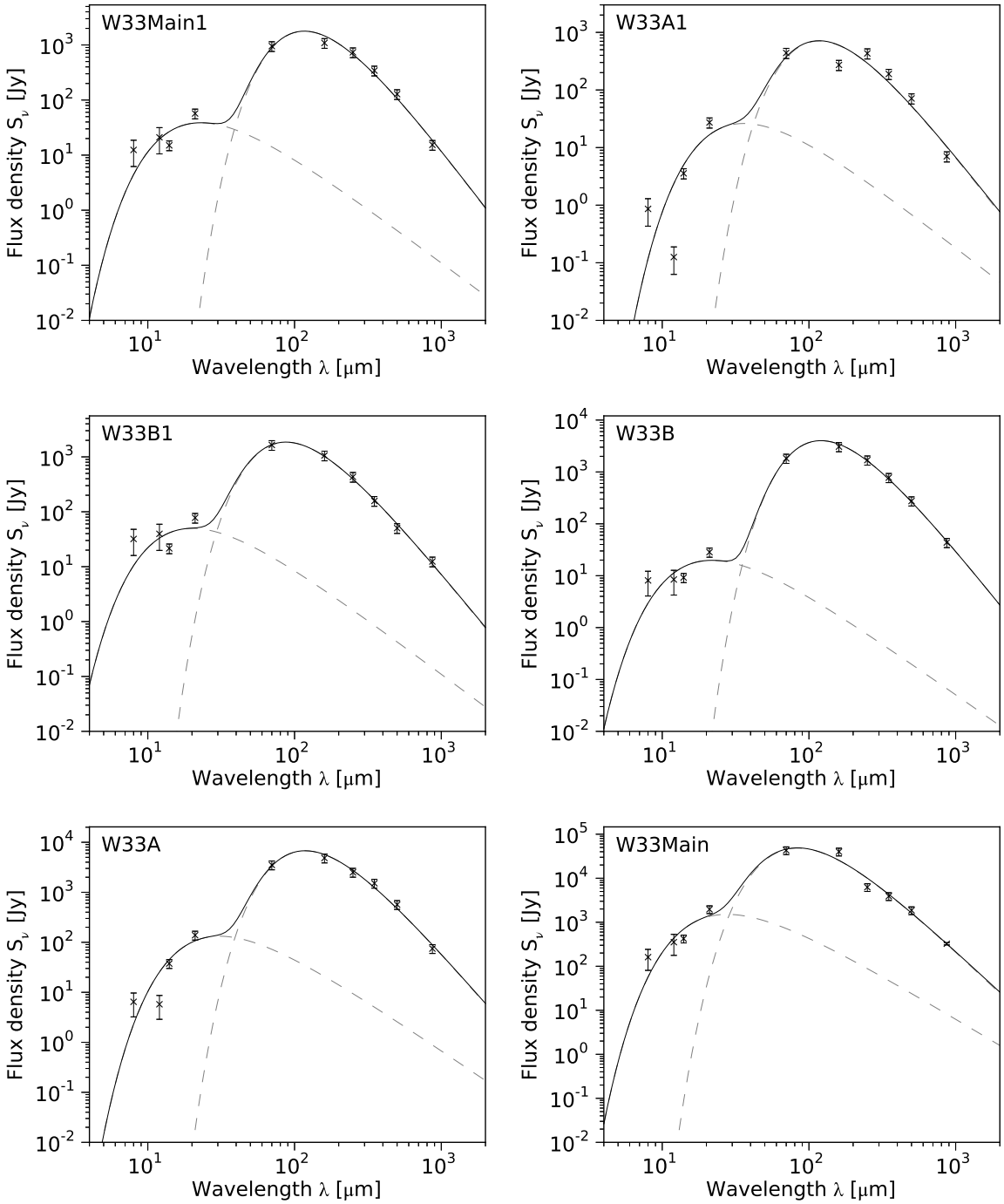

peratures of both components are similar for all sources, the luminosity covers a wide range of values, from 5000 $L_\odot$ in W33 A1 to 445000 $L_\odot$ in W33 Main. The total bolometric luminosity of the W33 complex is $5.5 \cdot 10^5$ $L_\odot$ which is only slightly smaller than the revised value ($8 \cdot 10^5$ $L_\odot$) of Stier et al. (1984). Besides the temperatures and luminosities, the spectral emissivity index β was determined from the SED fitting. This parameter quantifies the frequency-dependence of the emissivity in the Rayleigh-Jeans part of the spectrum (Dent et al. 1998). The spectral emissivity index ranges from 1.2 to 1.6 and no clear trend with the evolutionary stage of the cloud is detected.

Comparing the total masses of the W33 clouds from molecular gas and dust and their virial masses, we can determine if the clouds are gravitationally bound. Under the assumption of no temperature gradient, the total mass of a cloud is given by

$$\frac{M_{\rm tot}}{\rm M_\odot} = \frac{2.0 \cdot 10^{-2}}{J_\nu(T_{\rm cold})} \frac{a}{0.1\ \mu{\rm m}} \frac{\rho}{3\ {\rm g\ cm^{-3}}} \frac{R}{100} \frac{F_\nu}{\rm Jy} \left(\frac{d}{\rm kpc}\right)^2 \left(\frac{\nu}{1.2\ {\rm THz}}\right)^{-3-\beta}$$

(Beuther et al. 2005), where

$$J_\nu(T_{\rm cold}) = \left[\exp\left(\frac{h\nu}{kT_{\rm cold}}\right) - 1\right]^{-1}$$

and a, ρ, R, F_ν, d, ν, and β are the grain size, the grain mass density, the gas-to-dust ratio, the integrated flux density at 345 GHz, the distance, the frequency of the observations (345 GHz), and the spectral emissivity index, respectively. The virial mass is given by

$$\frac{M}{\rm M_\odot} = 190 \cdot \frac{R}{\rm pc} \left(\frac{\Delta v}{\rm km\ s^{-1}}\right)^2$$

(MacLaren et al. 1988), assuming a spherical 1/r density profile, with r being the radius of the source in parsec and Δv the FWHM in km s^{-1}.

The ATLASGAL catalogue lists the integrated flux densities of the clouds at 870 μm as well as the semi major and minor axes. We determined the radius of each source by taking the average of these two axes. For the gas-to-dust ratio, the grain size, and the grain mass density, we assumed typical values of 100, 0.1 μm, and 3 g cm^{-3}, respectively. The distance to the W33 complex is 2.4 kpc (Immer et al. 2013). The FWHM is determined from Gaussian profile fits to the CS spectral lines from our APEX/FLASH observations (see Sect. 3.6). Table 3.3 lists the source names (Col. 1), radii (Col. 2), the integrated flux densities at 870 μm (Col. 3), the dust temperatures of the cold and warm components (Cols. 4, 5), the luminosities of the clouds (Col.

Table 3.3: Dust temperatures, bolometric luminosities, and masses of the six W33 clouds.

Cloud	r (pc)	$F_{870\,\mu m,\,Int.}$ (Jy)	T_{cold} (K)	T_{warm} (K)	L_{bol} (10^3 $L_\odot$)	β	M_{tot} ($M_\odot$)	$FWHM_{CS}$ (km s^{-1})	M_{vir} ($M_\odot$)	$\frac{M_{vir}}{M_{tot}}$
W33 Main1	0.30	26.6	27	223	11	1.6	646	2.6	389	0.7
W33 A1	0.24	13.7	28	142	5	1.4	253	3.1	436	1.6
W33 B1	0.26	21.1	38	254	16	1.4	335	3.9	757	2.7
W33 B	0.38	54.7	26	235	22	1.6	1360	3.5	880	0.7
W33 A	0.44	100.1[a]	28	166	42	1.5	2101[a]	5.5	2508	1.1
W33 Main	0.53	339.2[b]	42	185	445	1.2	4022[b]	7.2	5215	1.2

Notes. [(a)] Whole W33 A cloud: $F_{870\,\mu m,\,Int.}$ = 112 Jy, M_{tot} = 2351 $M_\odot$ [(b)] Whole W33 Main cloud: $F_{870\,\mu m,\,Int.}$ = 357 Jy (∼18 Jy from free-free emission), M_{tot} = 4233 $M_\odot$

6), the spectral emissivity index β (Col. 7), the total masses of the clouds (Col. 8), the FWHM of the CS line (Col. 9), the virial masses (Col. 10), and the ratio of virial to total mass $\frac{M_{vir}}{M_{cloud}}$ (Col. 11).

Since W33 Main contains an H II region, part of the emission at 345 GHz possibly originates from free-free emission. To approximate this fraction, we first obtained an estimate of the radio flux density of W33 Main. Summing the emission of compact components in W33 Main, detected by Haschick & Ho (1983), yields a flux density of 23.9 Jy at 14.7 GHz. Assuming a typical spectral index of $\alpha = -0.1$ between 14.7 and 345 GHz, we estimate a flux density of ∼18 Jy at 345 GHz, originating from free-free emission, which corresponds to 5% of the total flux density at 345 GHz.

The total masses of the clouds range from 253 for W33 A1 to 4022 $M_\odot$ for W33 Main. Overall, the sources follow the trend of increasing luminosity with increasing total mass. Since the integrated flux densities of the whole W33 Main and W33 A clouds are underestimated due to their non-circular shapes, the listed total masses are only a lower limit. Integrating the flux density of the whole W33 Main and W33 A clouds above 5σ (= 0.3 Jy $beam^{-1}$), we estimate the integrated flux densities to be 357 and 112 Jy, respectively, which yields total masses of 4233 and 2351 $M_\odot$. This results in a total mass of the W33 complex of 9200 $M_\odot$ which is a factor of 10 smaller than the revised estimates of Goldsmith & Mao (1983) for the W33 Main cloud alone. The missing mass can partly be explained by the filtering of uniform extended emission above 2.5′ in the ATLASGAL data reduction process (see Schuller et al. 2009). The virial masses are comparable to the total gas+dust masses of the clouds (within a factor of ∼2) in all sources. We conclude that the W33 clouds are gravitationally bound.

Kauffmann & Pillai (2010) recently proposed an empirical limit for high-mass star formation

in molecular clouds, comparing the total mass of the cloud $m(r)$ with its radius r:

$$m(r) > \ 870 \cdot \mathrm{M}_{\odot} \left(\frac{r}{\mathrm{pc}} \right)^{1.33}$$

Inserting the total mass and the radii from Table 3.3 in this formula, we conclude that all W33 clouds fulfill this criterion and thus, in principle, have the potential to form high-mass stars.

3.5 Kinematics in the W33 Complex

From proper motion measurements of water masers in W33 B, W33 A, and W33 Main, Immer et al. (2013) showed that W33 A is moving tangentially to W33 Main in the plane of the sky with a total speed of 17 km s^{-1}. The radial velocities of W33 B and W33 Main differ by 22 km s^{-1}. In the plane of the sky, W33 B moves with a velocity of 22 km s^{-1} relative to W33 Main, yielding a total speed of 31 km s^{-1} of W33 B relative to W33 Main.

To determine if W33 A and W33 B are gravitationally bound to W33 Main, we compare the gravitational and kinetic energies of the clouds. In the following calculations, we used our mass estimate of 4200 $M_{\odot}$ as a lower limit and $8 \cdot 10^4$ $M_{\odot}$ (Goldsmith & Mao 1983, revised) as an upper limit for the total mass of W33 Main. Using the projected distance between W33 Main and W33 A and W33 B, respectively, and the mass of W33 Main, we estimate a lower and an upper limit of the escape speed needed to leave the gravitational field of W33 Main. For a projected distance of 5.5 pc between W33 B and W33 Main and 4.9 pc between W33 A and W33 Main, we calculated a lower limit of 2.6 and 2.7 km s^{-1} and an upper limit of 11.2 and 11.8 km s^{-1} for the escape speed. The total speed of W33 B and W33 A are larger than the limits of the escape speed. We conclude that both clouds are not gravitationally bound to W33 Main and thus, the large clouds in the W33 complex will drift apart with time. However, these results have to be checked carefully with better determined masses of the clouds.

3.6 Results of the APEX Observations

The spectral lines in the APEX spectra were identified, using the Cologne Database for Molecular Spectroscopy catalog (CDMS, Müller et al. 2001), the Jet Propulsion Laboratory spectral line catalog (JPL, Pickett et al. 1998), and the splatalogue catalog (Remijan et al. 2007). In Table 3.5 in the appendix, the rest frequency (Col. 1), the transition (Col. 2), and the upper energy level E_u (Col. 3) of each detected spectral line are listed. In total, we observed 27 transitions of 10

Figure 3.3: APEX spectra, generated over an area of 24″ x 24″ in W33 Main1, W33 A1, and W33 B1. The grey areas mark atmospheric bands in the APEX spectra that were not completely removed by our calibration.

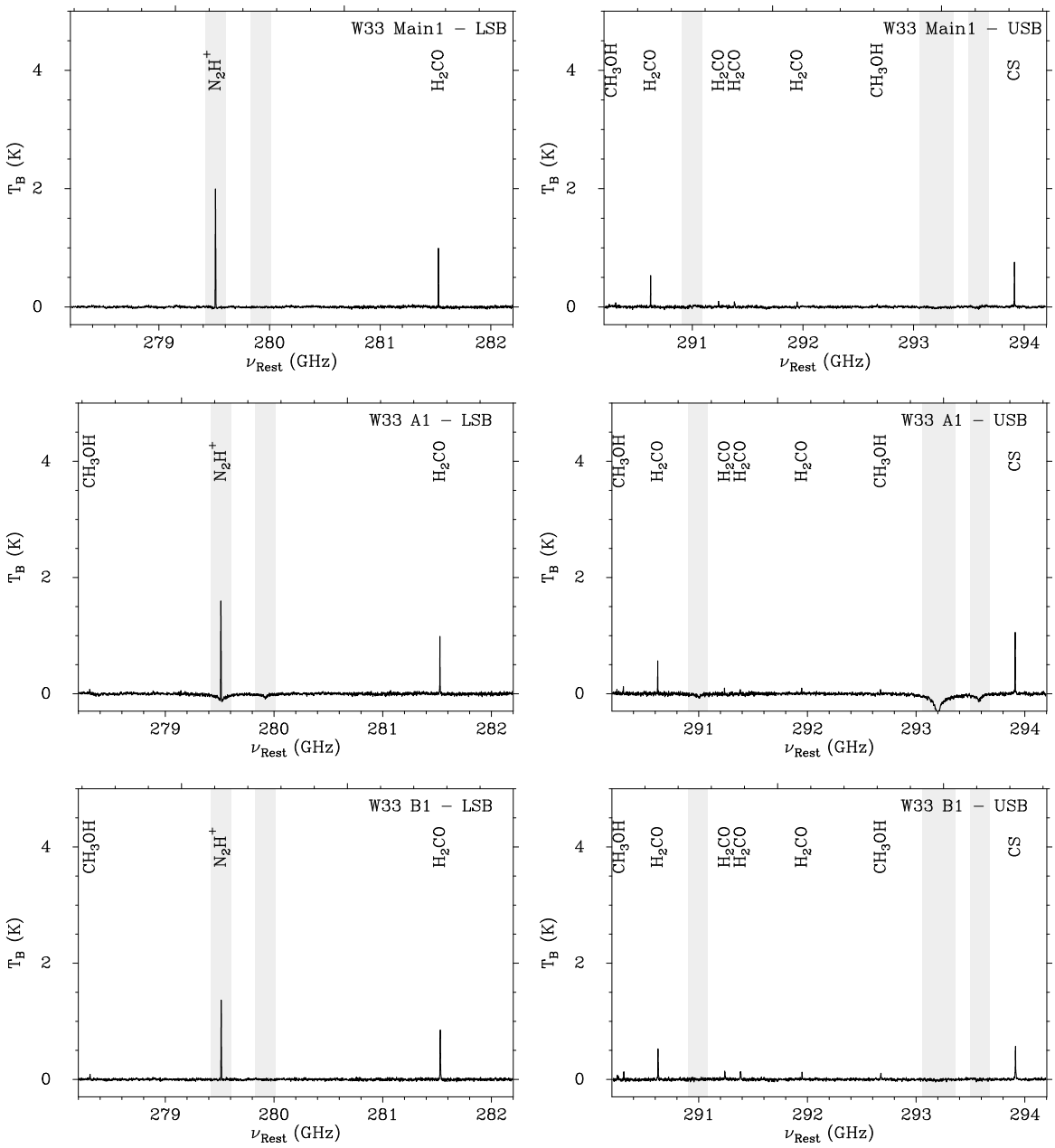

Figure 3.4: APEX spectra, generated over an area of 24″ x 24″ in W33 B, W33 A, and W33 Main. The grey areas mark atmospheric bands in the APEX spectra that were not completely removed by our calibration.

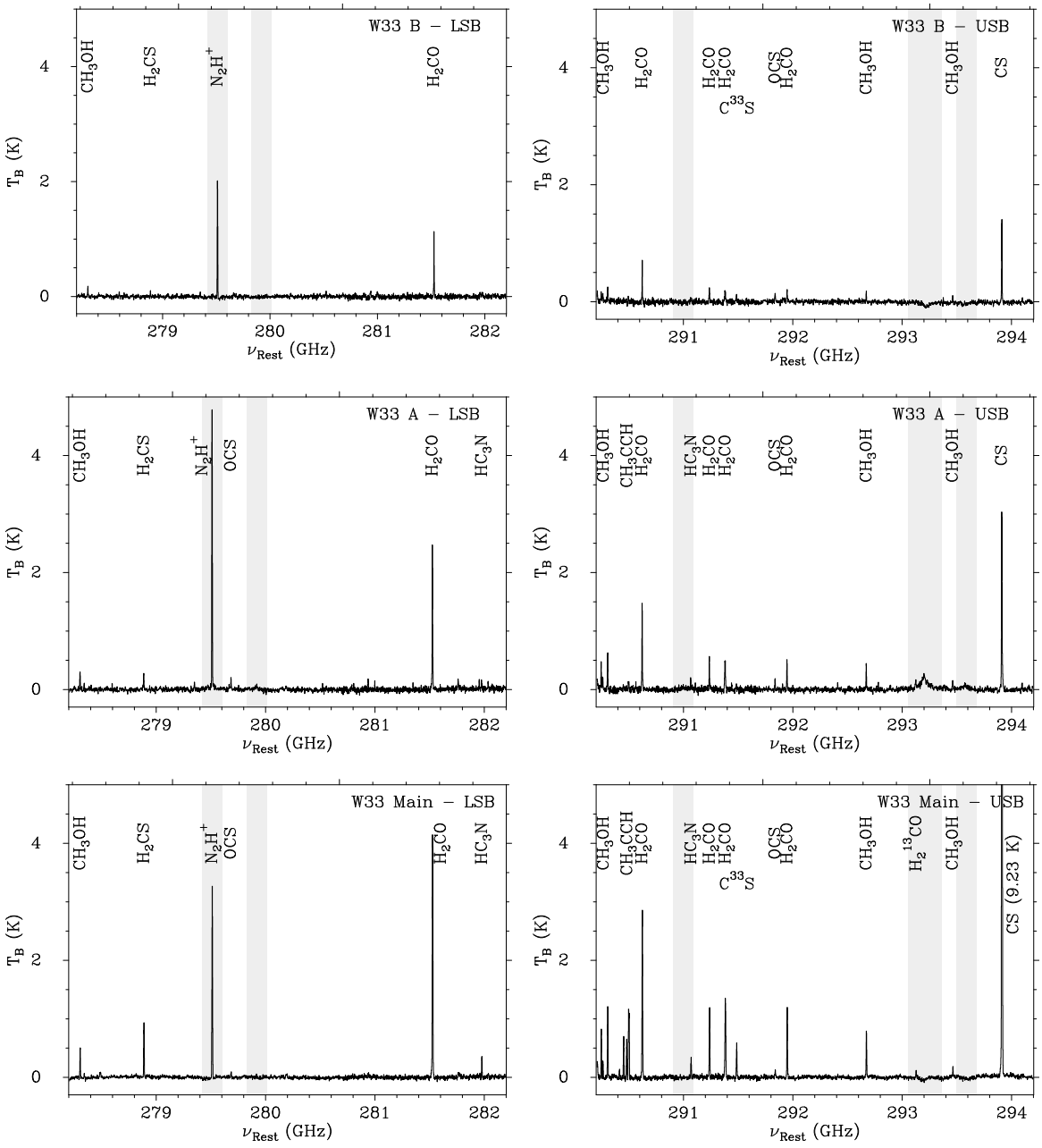

molecules (CH_3OH, H_2CS, N_2H^+, OCS, H_2CO, $H_2{}^{13}CO$, HC_3N, CH_3CCH, $C^{33}S$, and CS) with upper energy levels E_u between 27 and 241 K. The transitions $N_2H^+(3-2)$, $H_2CO(4_{1,4}-3_{1,3})$, $H_2CO(4_{0,4}-3_{0,3})$, $H_2CO(4_{2,3}-3_{2,2})$, $H_2CO(4_{3,2}-3_{3,1})$ and $H_2CO(4_{3,1}-3_{3,0})$ (which are blended), $H_2CO(4_{2,2}-3_{2,1})$, $CH_3OH(6_{-2,5}-5_{-2,4})$ and $CH_3OH(6_{2,4}-5_{2,4})$ (which are blended), $CH_3OH(6_{1,5}-5_{1,4})$, and CS(6−5) are detected in all sources. CS and N_2H^+ trace cold and dense gas in the clouds. The strongest lines in all sources are the two low-temperature transitions of H_2CO at 35 and 46 K, $N_2H^+(3-2)$, and CS(6−5). All detected spectral lines show Gaussian line profiles. We fitted them with single Gaussians to obtain the velocity integrated intensity F_{Int}, the peak intensity F_{Peak}, the central velocity $v_{central}$ and the FWHM of each line in each source. The fitting results are shown in Table 3.5 in the appendix. We made moment 0 maps of each line in each source to study the distribution of the line emission over the entire OTF maps and compare them to the location of the ATLASGAL continuum peaks at 870 μm.

In some of the APEX spectra, absorption features are present (see for example the spectra of W33 A1). These are not "real" features but are caused by badly calibrated atmospheric absorption. We marked the atmospheric bands within our frequency range in the spectra of Figs. 3.3 and 3.4.

W33 Main1 The least number of transitions are detected in W33 Main1. The detected transitions are common to all six sources and are listed in the paragraph before. The upper energy levels E_u of the observed transitions range from 27 to 141 K. The average central velocity is 36.4 km s^{-1} and the average line width is 3.2 km s^{-1}. The detection of high-energy transitions of H_2CO at 82 and 141 K and CH_3OH at 64 and 75 K hints to the existence of a heating source within or near W33 Main1. The moment 0 maps of these lines show only extended emission at the position of the continuum peak while the peak of the line emission is located close to the edge of the maps which point to an external rather than an internal heating source. The moment 0 maps of the two low-temperature transitions of H_2CO at 35 and 46 K and the N_2H^+ and the CS transitions show strong compact emission which peaks within ∼6″ of the continuum peak, indicating that the interior of W33 Main1 is still cold.

W33 A1 and W33 B1 In W33 A1 and W33 B1, we observe the same transitions ($CH_3OH(9_{-1,9}-8_{0,8})$ and $CH_3OH(6_{1,5}-5_{1,4})$, in addition to the spectral lines detected in W33 Main1). The upper energy levels E_u of all detected spectral lines range between 27 and 141 K. The average central velocity is 33.3 km s^{-1} and 36.7 km s^{-1} for W33 B1 and W33 A1, respectively. The spectral lines have an average line width of 5.4 km s^{-1} and 3.9 km s^{-1} in W33 B1 and W33 A1, respectively. In general, the detected spectral lines tend to be stronger and broader

in W33 B1, compared to W33 A1. The peaks of the compact emission of the four strongest lines, as seen in the moment 0 maps, are located within ∼6″ of the continuum peaks in both sources. In W33 B1, the emission of the high-excitation transitions of H_2CO and CH_3OH is also compact and peaks close to the continuum peak. This suggests that a heating source is present in W33 B1. The moment 0 maps of these high-temperature lines in W33 A1 show more extended emission and less isolated peaks which indicates that W33 A1 already contains a heating source but is probably less developed than W33 B1.

W33 B Besides the spectral lines detected in W33 B1 and W33 A1, we observe emission from $H_2CS(8_{1,7}-7_{1,6})$, $CH_3OH(6_{2,4}-5_{2,3})$, $CH_3OH(3_{2,1}-4_{1,4})$, $C^{33}S(6-5)$, and $OCS(24-23)$ in W33 B. The spectral lines have upper energy levels E_u between 27 and 175 K. The average central velocity and line width of W33 B are 55.4 km s^{-1} and 5.3 km s^{-1}, respectively. Although the radial velocity of W33 B differs by ∼20 km s^{-1} from the radial velocities of the other clouds in W33, Immer et al. (2013) (see Chapter 2) have shown that this cloud is located at a similar distance as the other clouds. However, it is still unclear what the reason for this large radial velocity difference is. While the integrated emission of CS and the two low-excitation transitions of H_2CO is compact and peaks close to the continuum peak, the emission of N_2H^+ is extended in south-east direction and peaks ∼12″ east of the continuum peak. The moment 0 map of $H_2CO(4_{2,2}-3_{2,1})$ shows extended emission in north-south direction. The peak of the emission is offset by ∼12″ in north-west direction from the continuum peak. The integrated emission of $C^{33}S(6-5)$ is extended to the west but its maximum is located close to the continuum peak. The emission of the remaining lines is mostly compact and peaks within ∼6″ of the continuum peak. The stronger lines and the detection of transitions at higher excitation energies compared to W33 B1 and W33 A1 suggests that W33 B is even more evolved than W33 B1 and W33 A1.

W33 A In addition to the lines found in W33 B, we also detect emission of $OCS(23-22)$, $HC_3N(31-30)$, $HC_3N(32-31)$, and $CH_3CCH(17_0-16_0)$. However, we do not observe emission of $C^{33}S(6-5)$ or $CH_3OH(3_{2,1}-4_{1,4})$. The upper energy levels of the detected lines are between 27 and 231 K. The average central velocity of all transitions is 37.6 km s^{-1} which is close to the systemic velocity of 38.5 km s^{-1}, determined by Galván-Madrid et al. (2010) from their SMA observations of W33 A. The average line width is 5.4 km s^{-1}. The integrated emission of all lines in W33 A is compact and their maxima are located close to the continuum peak, within ∼6″−12″. W33 A is probably more evolved as W33 B.

W33 Main The spectra of W33 Main are the most line-rich of the six sources. Besides the transitions that we detect in W33 A and W33 B, we observe the higher-excitation transitions of CH_3CCH ($CH_3CCH(17_1-16_1)$, $CH_3CCH(17_2-16_2)$, $CH_3CCH(17_3-16_3)$, $CH_3CCH(17_4-16_4)$), and $H_2{}^{13}CO(4_{1,3}-3_{1,2})$. The transition with the highest upper energy level E_u = 241 K is detected in this source. The average central velocity and line width of W33 Main are 35.6 km s^{-1} and 6.0 km s^{-1}, respectively. Except for the N_2H^+, CS, and OCS transitions, the emission of all spectral lines peaks close to the continuum peak. The N_2H^+ emission is strongest at the north-western edge of the map. Some weaker emission of N_2H^+ is concentrated at the center of the OTF map. The CS emission is spread from the center of the map to the north and peaks about ~24″ from the continuum peak to the north. The emission of $C^{33}S$, CH_3CCH (except $CH_3CCH(17_4-16_4)$), CH_3OH (except $CH_3OH(3_{2,1}-4_{1,4})$ and $CH_3OH(6_{2,4}-5_{2,3})$), H_2CO, and H_2CS is also extended to the north but peaks close to the continuum peak. The OCS emission is extended and the peak close to the center of the map is not very pronounced. The extended emission hints to the existence of another source in the north of the map. Since CS and N_2H^+ trace cold gas, the line peak offsets of the CS and N_2H^+ emission from the continuum peak indicate that the gas towards the center of the W33 Main cloud is not cold anymore. We conclude that W33 Main is probably not in an early stage of star formation anymore.

Following these results, we sort the W33 sources along an evolutionary sequence: W33 Main1, W33 A1, W33 B1, W33 B, W33 A, and W33 Main. The more evolved sources emit transitions with higher excitation energies which indicates that the temperature in these sources increases along this sequence. Furthermore, the detected lines tend to get stronger and broader along this sequence.

3.7 Results of the SMA Observations

3.7.1 230 GHz Continuum Emission

Fig. 3.5 shows the 230 GHz continuum emission of the six W33 sources W33 Main1, W33 A1, W33 B1, W33 B, W33 A, and W33 Main, observed with the SMA. Except for W33 A and W33 Main, the dust cores are single-peaked. W33 B1 is the only source that is nearly circular. The other sources are elongated along one axis. The cores have sizes of about 0.1 pc. The dust emission of W33 Main shows two peaks in the main core which has a size of about 0.25 pc. Surrounding the main core, several smaller cores with weaker emission are observed. The image of W33 A was obtained from a combination of the SMA observations in compact and very

Figure 3.5: 230 GHz continuum maps of W33 Main1, W33 A1, W33 B1, W33 B, W33 A, and W33 Main. The contours start at 3σ and are in steps of 5σ (1σ = 6, 5, 5, 10, 5, and 70 mJy beam^{-1} for W33 Main1, W33 A1 W33 B1, W33 B, W33 A, and W33 Main). The map of W33 A was obtained from Galván-Madrid et al. (2010). The synthesized beams are shown in the lower left corners of the images. In the upper left corners, a 0.1 pc scale is indicated.

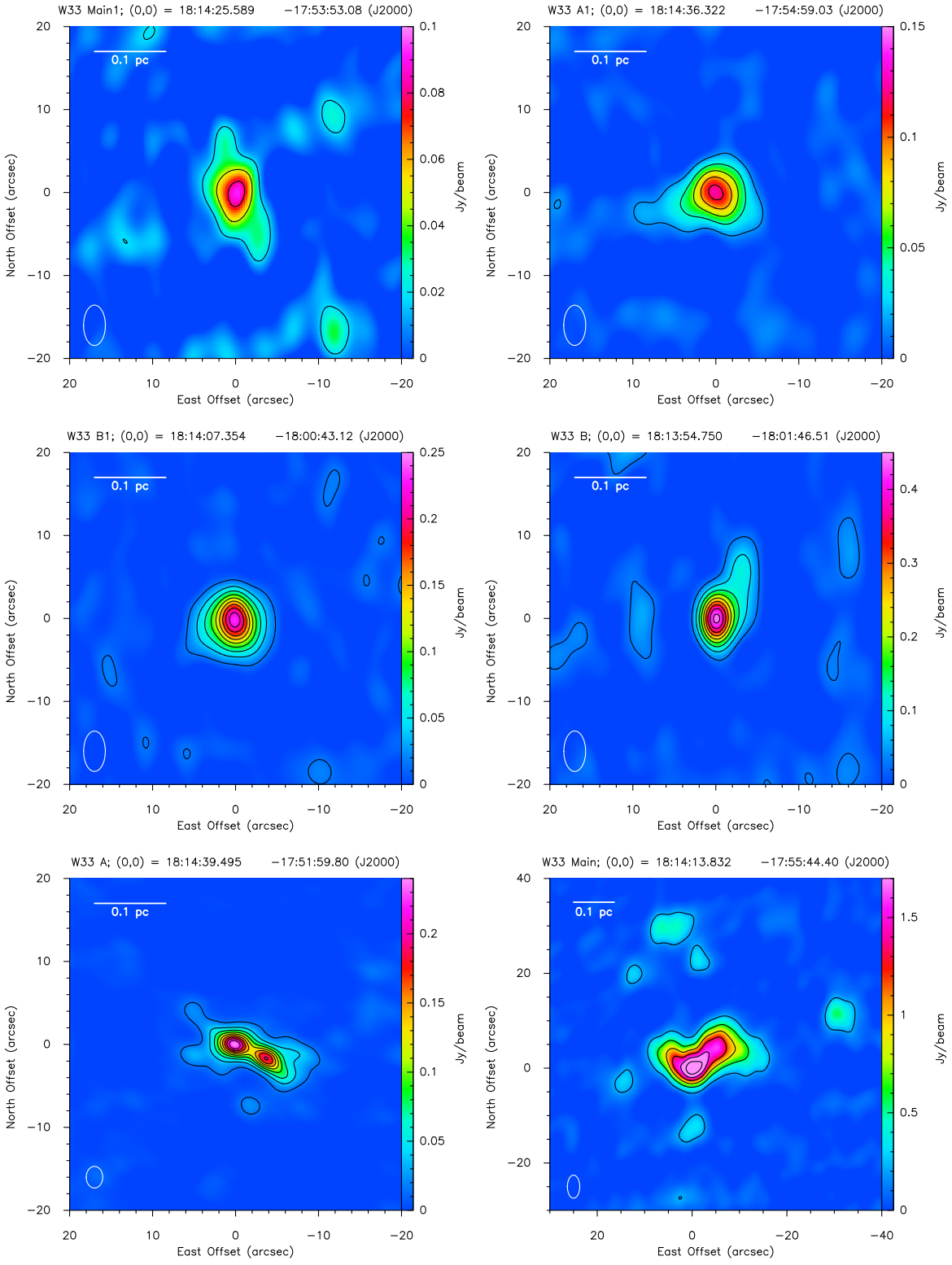

Figure 3.6: 230 (left) and 345 (right) GHz continuum maps of W33 Main. The contours show the 230 GHz emission (same contour levels as in Fig. 3.5, sixth panel). The synthesized beams are indicated by the ellipses in the lower left corners. In the upper left corners, a 0.1 pc scale is indicated.

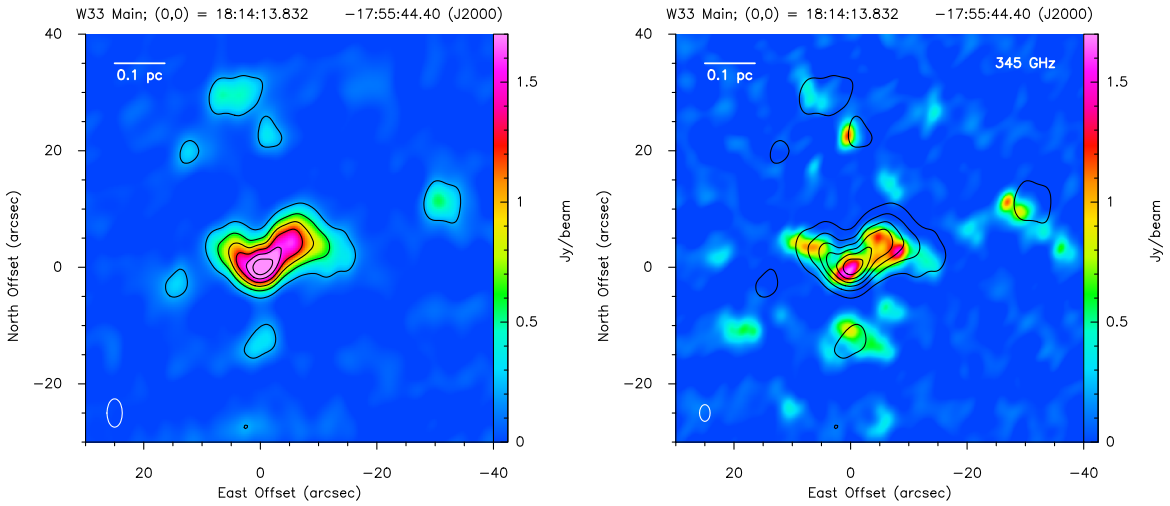

extended configuration of Galván-Madrid et al. (2010). For a better comparison with our SMA observations, the image was cleaned with the MIRIAD *robust* parameter set to 4, which yields a synthesized beam size of 2.6″ x 2.0″. The continuum emission shows two peaks within one core. The core has a size of ~0.15 pc.

The left and right panels of Fig. 3.6 show the continuum emission of W33 Main at 230 and 345 GHz. The contours correspond to the dust emission at 230 GHz with the same levels as in the sixth panel of Fig. 3.5. Several emission peaks are detected in the main core of W33 Main in the 345 GHz map. Outside of the main core, three more cores are detected at both frequencies which we name W33 Main-North, W33 Main-West, and W33 Main-South. In the following text, we will refer to the main core as W33 Main-Central.

3.7.2 230 GHz Line Emission

We generated spectra of all six cores by integrating the emission over one synthesized beam at the 230 GHz continuum peak positions (Figs. 3.7 and 3.8). In W33 Main, we obtained the spectrum at the position of the peak in W33 Main−Central. We again used the CDMS, JPL, and splatalogue catalogues for the spectral line identification. The detected transitions are listed in Table 3.6 in the appendix. In total, we observed 38 transitions of 15 molecules (SO, CO isotopologues ^{12}CO, ^{13}CO, and C^{18}O, the deuterated species DCN, the dense gas tracer ^{13}CS, the dense and hot gas

Figure 3.7: SMA spectra, generated at the continuum peak positions of W33 Main1, W33 A1, and W33 B1.

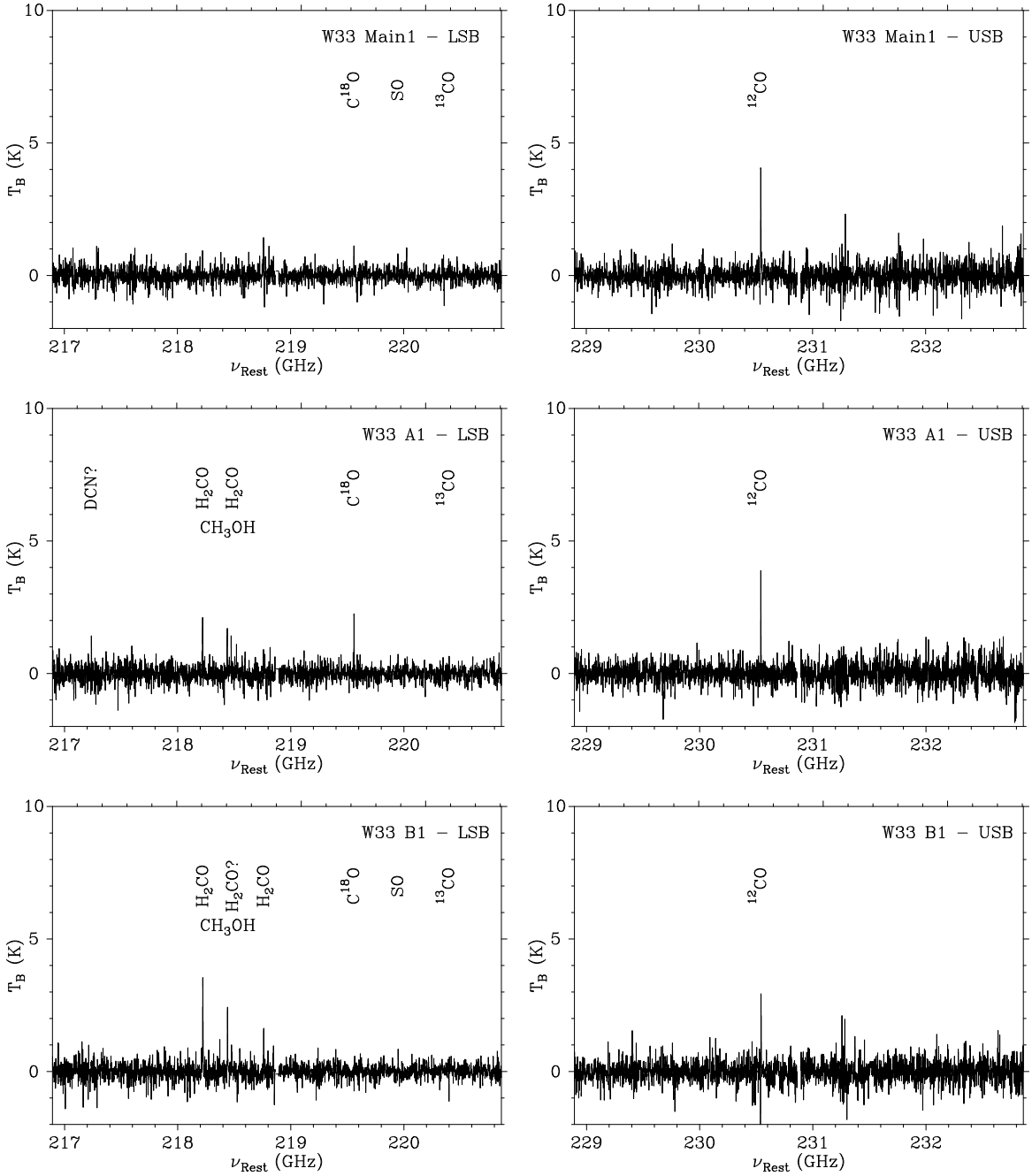

Figure 3.8: SMA spectra, generated at the continuum peak positions of W33 B, W33 A, and W33 Main.

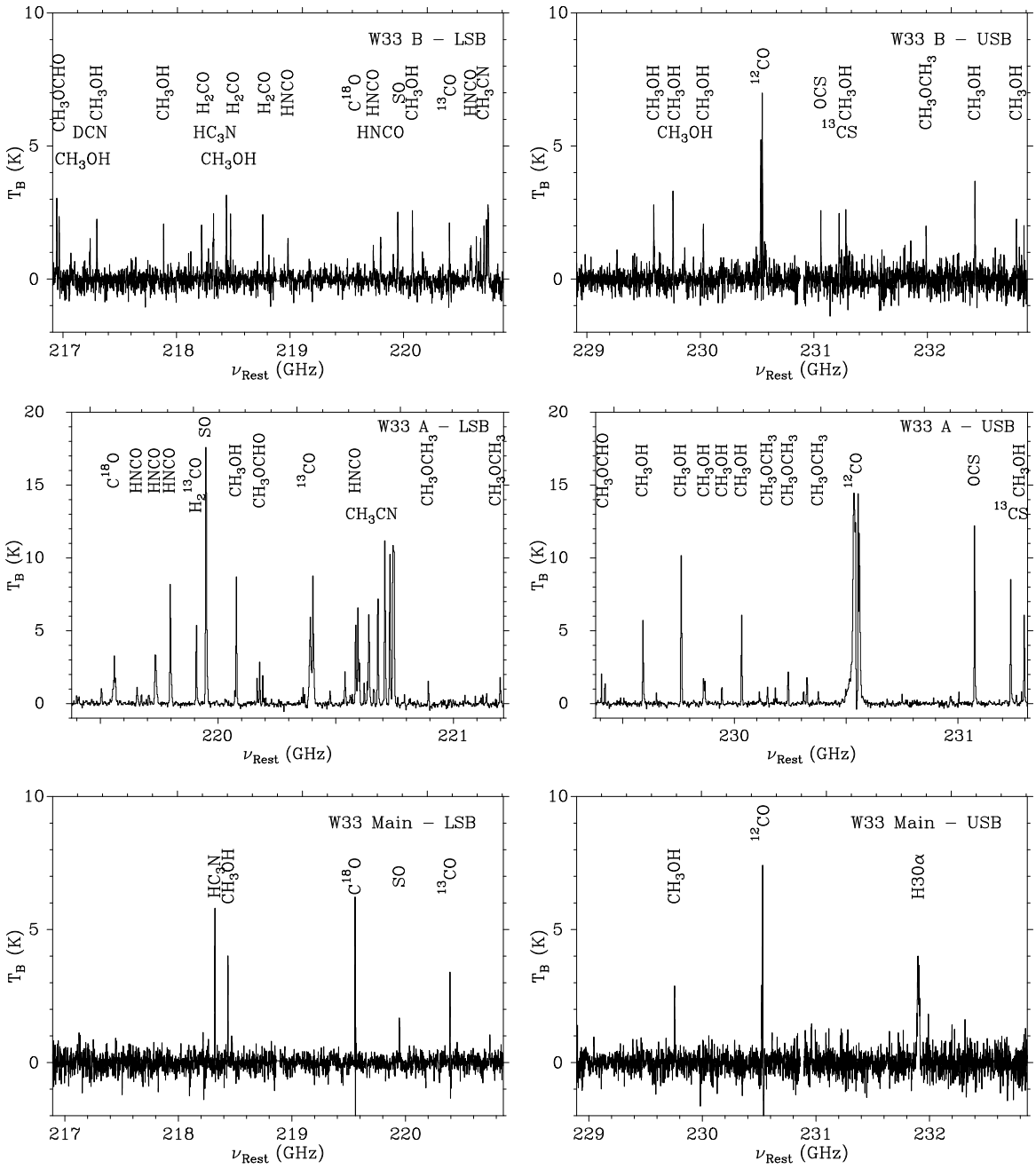

tracers CH_3OH, H_2CO and its isotopologue $H_2{}^{13}CO$, CH_3CN, HNCO, OCS, as well as HC_3N, CH_3OCHO, and CH_3OCH_3). The detected transitions have upper energy levels E_u between 16 and 579 K. Again, the lines with a Gaussian line profile are fitted with single Gaussians to obtain the same line parameters as in Sect. 3.6. Moment 0 and moment 1 maps were generated for all transitions.

As described in Chapter 1, accretion disks and outflows are found during a certain period of the star formation process. Since the spatial resolution of our observations is too coarse to resolve the accretion disk, we are looking for outflow signatures to characterize these evolutionary stages in our sample. Furthermore, velocity gradients, detected in the moment 1 maps of the spectral emission, can give hints to rotation, infall or expansion of material (Figs. 3.9 and 3.10). Since the emission of the CO lines is the most widespread, it is affected the most by the lack of short-spacing information. Thus, the identification and interpretation of outflows and velocity gradients in the moment 0 and 1 maps of the CO lines is complicated.

W33 Main1 W33 Main1 is again the source with the least number of detected spectral lines. Besides the two CO lines ^{12}CO and $C^{18}O$, we only observe emission of $SO(6_5-5_4)$ in the spectrum. ^{13}CO was not detected at the position of the dust continuum peak but extended emission of ^{13}CO was observed in the W33 Main1 mosaic. The upper energy levels E_u of the observed transitions are 16−35 K. The average central velocity and the average line width are 35.9 km s^{-1} and 4.0 km s^{-1}, similar to the results of the APEX observations.

The blueshifted and redshifted $^{12}CO(2-1)$ emission of W33 Main1 shows several peaks at and around the dust continuum peak. The distribution of the emission does not look ordered and might be excited by turbulences in this source.

The moment 0 map of the SO transition shows compact emission whose peak is offset by $\sim 2''$ from the dust continuum peak. The moment 1 map of the SO transition shows a velocity gradient over the central part of the source (Fig. 3.10a).

The lack of spectral lines besides the CO and SO transitions either indicates low temperatures in the dust core or the emission of more complex molecules is not compact enough to be detected with the SMA which both hint to a very early evolutionary age of W33 Main1. We conclude that W33 Main1 is probably still in the prestellar phase before a protostar warms up the surrounding material and strong emission of primary molecules like H_2CO and CH_3OH which evaporate off dust grains is detected.

W33 B1 In the spectrum of W33 B1, we detect the three transitions of H_2CO, $CH_3OH(4_{2,2}-3_{1,2})$, $SO(6_5-5_4)$, and ^{12}CO. Extended emission of ^{13}CO and $C^{18}O$ was observed in the W33 B1 map

Figure 3.9: Velocity gradients in the W33 sources from CH_3OH emission. The contours show the continuum emission at 230 GHz (levels the same as in Fig. 3.5).

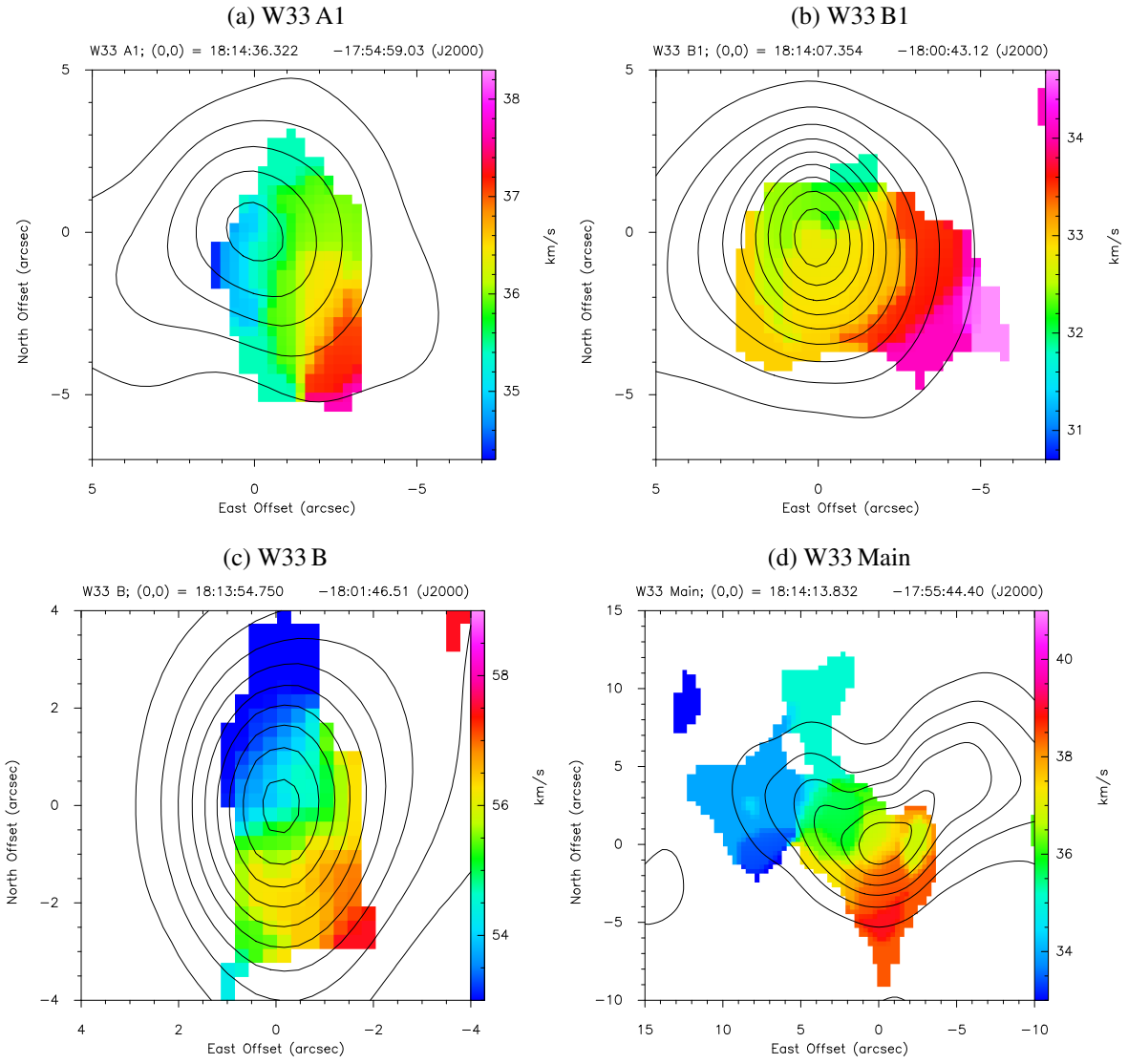

Figure 3.10: Velocity gradients in the W33 sources from SO, H_2CO, and HC_3N emission. The contours show the continuum emission at 230 GHz (levels the same as in Fig. 3.5).

(a) W33 Main1, SO emission

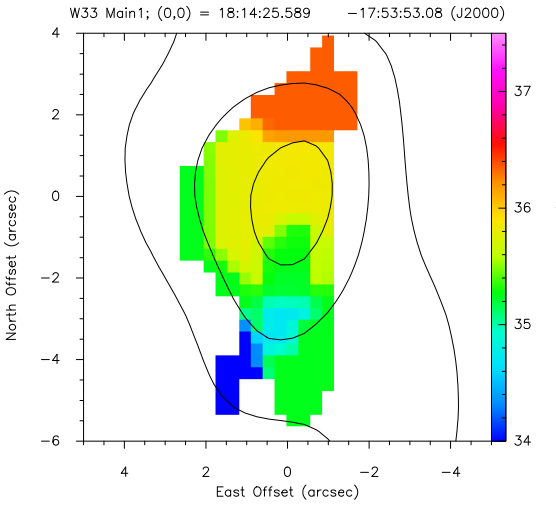

(b) W33 B1, H_2CO emission

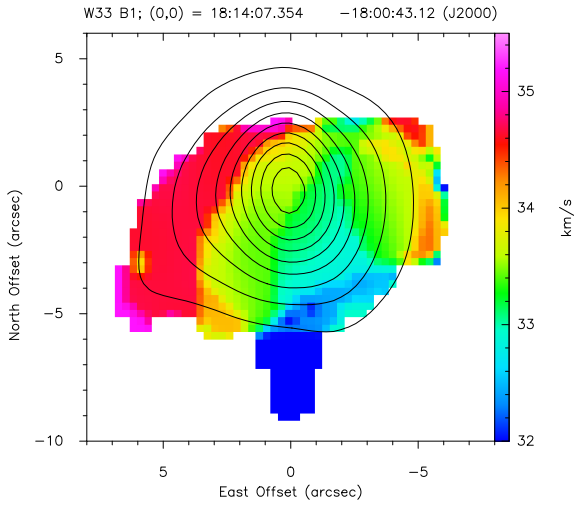

(c) W33 Main, HC_3N emission

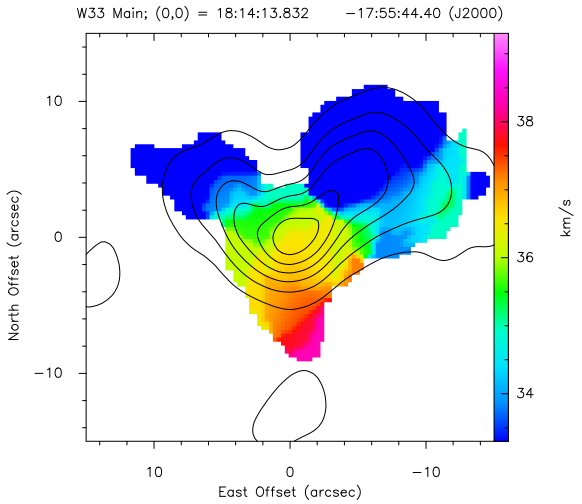

Figure 3.11: Velocity integrated CO emission in W33 A1, W33 B1, W33 B, and W33 Main. The background shows the 230 GHz continuum emission. Blue and red contours correspond to the most blueshifted and redshifted ^{12}CO or C^{18}O emission in the three sources. In W33 A1, the redshifted and blueshifted emission is integrated over velocity ranges of 40–47 km s^{-1} and 25–32 km s^{-1}, respectively (contour levels: 6–28 Jy beam^{-1} km s^{-1} in steps of 3 Jy beam^{-1} km s^{-1}). In W33 B1, the redshifted and blueshifted emission is integrated over velocity ranges of 40–45 km s^{-1} and 24–30 km s^{-1}, respectively (contour levels: 5–35 Jy beam^{-1} km s^{-1} in steps of 5 Jy beam^{-1} km s^{-1}). In W33 B, the redshifted and blueshifted emission is integrated over velocity ranges of 64–69 km s^{-1} and 44–48 km s^{-1}, respectively (contour levels: 10–70 Jy beam^{-1} km s^{-1} in steps of 5 Jy beam^{-1} km s^{-1}). In W33 Main, the redshifted and blueshifted emission is integrated over 39–42 km s^{-1} and 28–32 km s^{-1}, respectively (contour levels: 10–25 Jy beam^{-1} km s^{-1} in steps of 2.5 Jy beam^{-1} km s^{-1}). The synthesized beams are shown in the lower left corners of the images.

(a) ^{12}CO emission in W33 A1

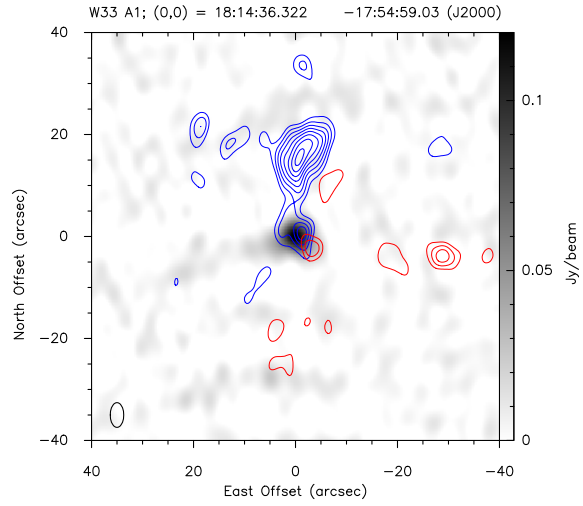

(b) ^{12}CO emission in W33 B1

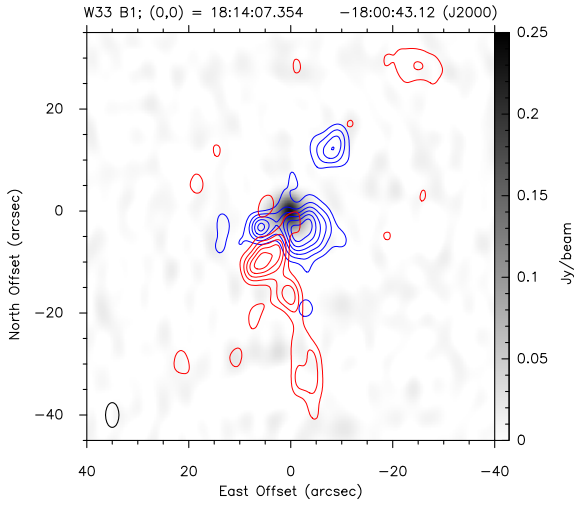

(c) ^{12}CO emission in W33 B

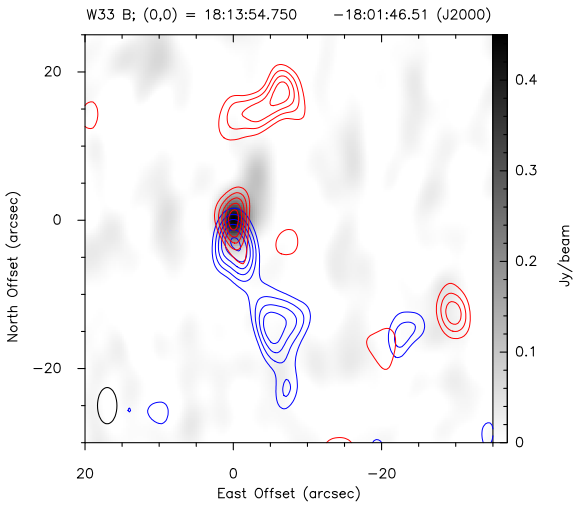

(d) C^{18}O emission in W33 Main

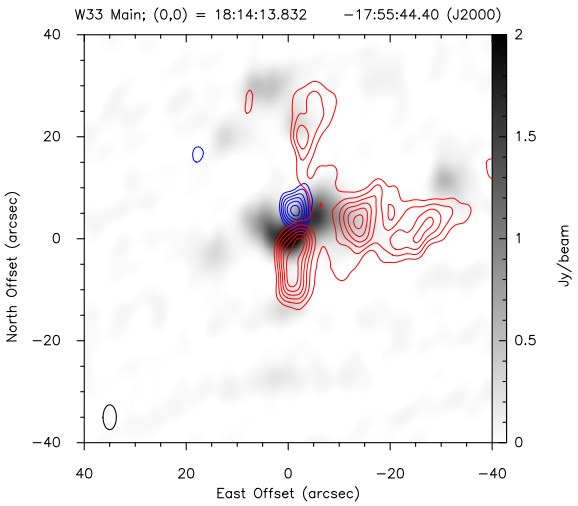

but not at the center of the core. The detected transitions have upper energy levels between 17 and 68 K, indicating that this source is still relatively cold. The average central velocity and the average line width of W33 B1 are 32.7 km s^{-1} and 5.0 km s^{-1}, respectively. The $^{12}CO(2-1)$ emission shows a preferred direction in W33 B1 (north-west to south-east). Most of the emission is detected close to the dust continuum peak (Fig. 3.11b).

The moment 0 maps of CH_3OH and H_2CO show compact emission which peaks close to the dust continuum peak. The emission of SO is also compact but peaks at the edge of the core. The moment 1 maps of $H_2CO(3_{0,3}-2_{0,2})$ and $CH_3OH(4_{2,2}-3_{1,2})$ show opposite velocity gradients across the sources which probably originate from different processes. The velocity gradient of the CH_3OH emission indicates an expansion of the source (Fig. 3.9b) while the velocity gradient of the H_2CO emission is indicative of rotation (Fig. 3.10b).

The higher-energy transitions of H_2CO and CH_3OH hint to the presence of a heating source in W33 B1. However, since we do not see the line-richness of hot cores in this core, we conclude that W33 B1 is a very young protostellar core.

W33 A1 In addition to the lines detected in W33 B1, we observe emission of DCN(3−2) and $C^{18}O$ at the peak of W33 A1. Again, extended emission of ^{13}CO is observed in the map, but not at the position of the continuum peak. The upper energy levels of the detected transitions are between 16 and 68 K. The average central velocity of W33 A1 is 35.5 km s^{-1}. The average line width is 3.7 km s^{-1}.

Two streams of $^{12}CO(2-1)$ emission are detected in W33 A1 that are almost perpendicular to each other (Fig. 3.11a). Blueshifted emission is observed north of the dust continuum peak while redshifted emission is detected west of the continuum peak.

The emission of DCN is compact and peaks close to the dust continuum peak. The moment 0 map of SO shows two peaks at the edges of the dust core with the main peak of the SO emission being offset from the dust continuum peak by $\sim 2''$. In the moment 1 map, a small velocity gradient is visible over both SO emission peaks. The integrated emission of H_2CO and CH_3OH is compact and peaks within $1''$ of the dust continuum peak. The low-energy transitions of H_2CO and CH_3OH both show a velocity gradient over the source (Fig. 3.9a for CH_3OH).

For the same reasons as for W33 B1, we conclude that W33 A1 is a very young protostellar core.

W33 B Besides W33 A, W33 B is the most line-rich source of the six W33 cores. We observed 37 transitions of 13 molecules in the spectrum. Emission of the CO isotopologue $C^{18}O$ is not observed towards the center of the molecular core, but is detected as extended emission in the

map. The ionized gas tracer H30α is not detected in W33 B, indicating that an UC H II region is not yet present. The strongest line in the spectrum is ^{12}CO with a peak brightness temperature of ~6 K. The average central velocity is 55.6 km s^{-1}. The average line width is 6.8 km s^{-1}.

In W33 B, we detect an outflow in almost north-south direction in the ^{12}CO emission. Another stream of ^{12}CO emission at blueshifted velocities points in south-west direction and probably marks another outflow of which we only see the blueshifted side (Fig. 3.11c).

The integrated emission of most of the detected lines is concentrated within the boundaries of the dust emission and only barely resolved. The lines that show more extended emission are ^{13}CS, $CH_3OH(4_{2,2}-3_{1,2})$, $H_2CO(3_{0,3}-2_{0,2})$, $SO(6_5-5_4)$, and the CO lines, which are spread over the whole field of view. Velocity gradients are detected in the moment 1 maps of the H_2CO and CH_3OH transitions as well as the $OCS(19-18)$ and $HC_3N(24-23)$ transitions. Fig. 3.9c shows the velocity gradient in the $CH_3OH(18_{3,16}-17_{4,13})$ transition.

The detection of complex molecules like CH_3CN, HNCO, HC_3N, CH_3OCHO or CH_3OCH_3 indicates that W33 B is in the hot core stage.

W33 A For comparison with our sample of W33 sources, we obtained a spectrum of W33 A from the SMA observations of Galván-Madrid et al. (2010). The data cube of W33 A has a slightly coarser spectral resolution than our observations of 3 km s^{-1}. The data cube was cleaned with the MIRIAD CLEAN parameter *robust* set to 4, resulting in a synthesized beam of 3.9″ x 2.3″ which gives a slightly better spatial resolution than our data sets. However, the data cube has only a bandwidth of 2 GHz per sideband. After flagging bad edge channels, the data cube covers the effective frequency ranges 219.38−221.21 GHz and 229.38−231.31 GHz. We obtained the spectrum of W33 A by integrating the emission over one synthesized beam at the position of the stronger continuum peak (MM1 in Galván-Madrid et al. 2010). The spectra of the two sidebands are shown in Fig. 3.8. In the covered frequency range, we detect the same transitions as in W33 B. In addition, emission of $H_2{}^{13}CO$, high-energy CH_3OH transitions at E_u = 579 K, and emission of more complex molecules (CH_3OCHO, CH_3OCH_3) at higher excitation energies are observed. All transitions have upper energy levels E_u between 16 and 579 K. Unfortunately, the frequency of the radio recombination line (RRL) H30α tracing ionized gas is located outside the frequency range of the W33 A spectra. The variety of detected molecules (including complex molecules) and the high temperature needed for the excitation of the high-energy transitions supports the identification of W33 A as a hot core. Since W33 A shows emission of complex molecules at higher excitation energies, we conclude that W33 A is probably more evolved than W33 B.

W33 Main Compared to W33 B and W33 A, the spectrum of W33 Main shows significantly fewer spectral lines. The dust continuum peak of W33 Main-Central is almost devoid of H_2CO emission. In the spectrum, we detect $H_2CO(3_{0,3}-2_{0,2})$ and $H_2CO(3_{2,2}-2_{2,1})$. However, we observe emission of the 68 K H_2CO transitions $(3_{2,2}-2_{2,1})$ and $(3_{2,1}-2_{2,0})$ in the western part of W33 Main-Central as well as at the peak positions of W33 Main-West and W33 Main-North. Besides two transitions of CH_3OH ($CH_3OH(4_{2,2}-3_{1,2})$, $CH_3OH(8_{-1,8}-7_{0,7})$), we detect SO, the CO isotopologues ^{12}CO, ^{13}CO, and $C^{18}O$, HC_3N, and the RRL H30α in the spectrum. The detected lines have upper energy levels from 16 to 131 K. The two strongest lines are ^{12}CO and $C^{18}O$ with peak brightness temperatures of ∼8 and ∼6.5 K, respectively. The average central velocity and the average line width of W33 Main are 37.1 km s^{-1} and 4.3 km s^{-1}.

Fig. 3.11d shows the outflows in the $C^{18}O$ emission. While there seem to be two redshifted streams of $C^{18}O$ emission, we only see one strong peak of blueshifted emission that is located close to W33 Main-Central. In Fig. 3.12, we show a comparison of the integrated emission of the ^{13}CO and $C^{18}O$ transitions from the SMA data only and from the combination of the SMA and IRAM data. The figure presents the importance of zero-spacing information, especially for widespread line emission and shows the strong filtering of large scale emission.

W33 Main is the only source in our SMA sample that shows emission of the RRL H30α and the shock tracer SiO. The integrated emission of the RRL has the same shape as the dust continuum emission of W33 Main-Central which suggests that part of the dust emission comes from free-free radiation (see Sect. 3.4). The detection of the RRL supports the identification of W33 Main as a more evolved object where ionized emission of H II region(s) is observed. The integrated emission of $CH_3OH(4_{2,2}-3_{1,2})$ and $SO(6_5-5_4)$ also peaks at the center of W33 Main-Central. However, the HC_3N transition peaks in the western part of W33 Main-Central, offset from the main dust peak by ∼0.1 pc. Emission of the SiO(5−4) transition is observed at the western and southern edges of W33 Main-Central.

W33 Main-North is bright in ^{13}CS, $H_2CO(3_{0,3}-2_{0,2})$, $SO(6_5-5_4)$, and SiO(5−4). Weaker emission of $CH_3OH(4_{2,2}-3_{1,2})$ is also observed at this position. The strongest lines in W33 Main-West are $H_2CO(3_{0,3}-2_{0,2})$ and $CH_3OH(4_{2,2}-3_{1,2})$. In addition, weaker emission of ^{13}CS, $SO(6_5-5_4)$, and SiO(5−4) is detected. At the position of W33 Main-South, we only observed diffuse line emission.

In the sources W33 Main1, W33 A1, W33 B1, and W33 Main, we detect $^{12}CO(2-1)$ and $^{13}CO(2-1)$ emission at velocities of ∼60 km s^{-1}. This emission is offset from the dust emis-

Figure 3.12: Velocity integrated emission of ^{13}CO and C^{18}O in W33 Main. The images in the left panels show the data from the SMA observations while the images in the right panels are combinations of the IRAM and SMA data of these two transitions. The contours show the 230 GHz continuum emission in W33 Main (contour levels same as in Fig. 3.5). The ^{13}CO and C^{18}O emission are integrated over velocity ranges of 24−55 km s^{-1} and 28−42 km s^{-1}, respectively.

(a) SMA ^{13}CO emission

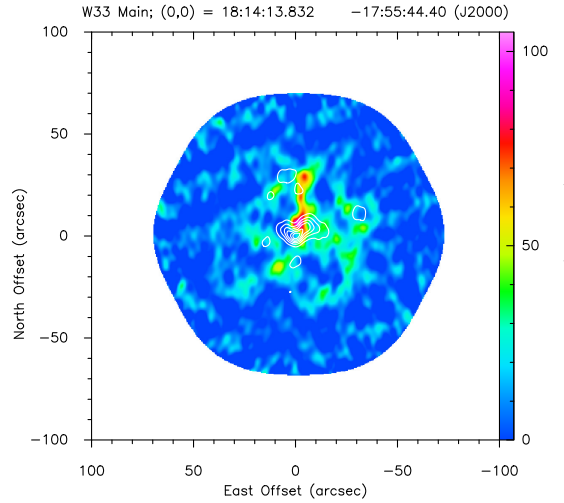

(b) Combined ^{13}CO emission from SMA and IRAM

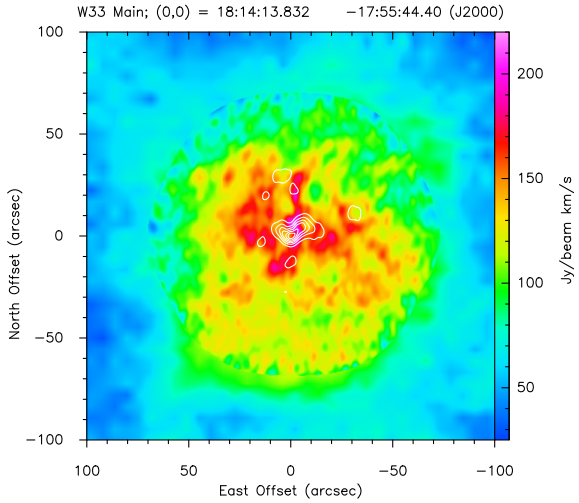

(c) SMA C^{18}O emission

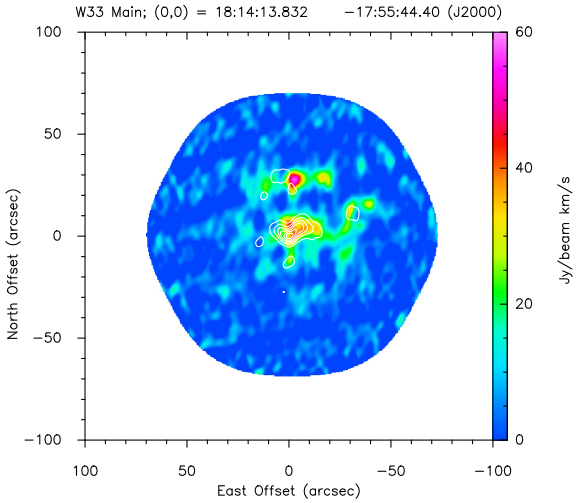

(d) Combined C^{18}O emission from SMA and IRAM

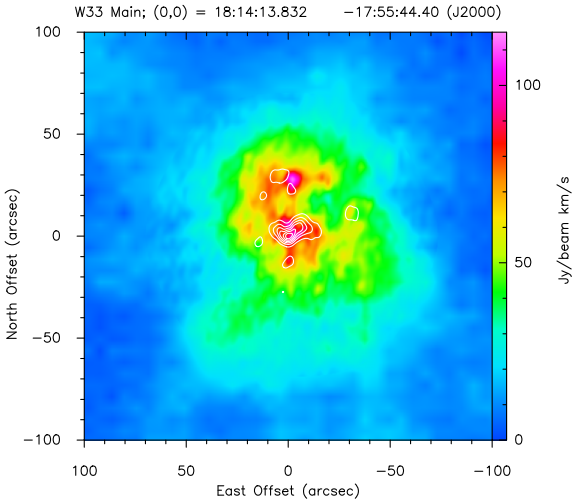

sion peak by several arcseconds in all sources. This shows that the velocity component of W33 B (v_{sys} = 56 km s^{-1}) is not unique in the W33 complex but also observed towards the other sources in the low density gas tracers (see also Goldsmith & Mao 1983; Urquhart et al. 2008; Chen et al. 2010).

3.8 Gas Temperatures and Column Densities

3.8.1 Rotational Temperature Diagrams

From molecules for which multiple transitions can be observed, the rotational temperature and beam-averaged column density of the molecular material can be estimated using the rotational temperature diagram (RTD) method. Under the assumption of optically thin emission and local thermodynamic equilibrium (LTE), the observed line intensities are proportional to the level populations and the level populations are determined by a single temperature T_{rot}. The level populations are given by

$$N_u = \frac{8\pi^3 k\nu^2}{hc^3 A_{ul}} \int T_b dv, \tag{3.1}$$

where A_{ul} is the Einstein coefficient of the transition (see the detailed description of this method in Goldsmith & Langer 1999).

In LTE,

$$\ln \frac{N_u}{g_u} = \ln \frac{N_{tot}}{Q(T_{rot})} - \frac{E_u}{k} \frac{1}{T_{rot}} \tag{3.2}$$

where g_u is the statistical weight of the upper level, $Q(T_{rot})$ the partition function, and N_{tot} the total number density.

APEX Observations Since we observe the H_2CO transitions in the APEX spectra of all six W33 sources and they span a broad range of upper energy levels, from 35 to 141 K, we first calculated the level populations for these transitions from the observed integrated intensities, using equation 3.1 and assuming that the beam filling factor for the APEX data is unity. Then, we plotted the results in RTDs. Following equation 3.2, a straight line least-square fit to the data yields the rotational temperature and total column density of the molecule, which can be calculated from the slope and the y-intercept of the fitted line. We also tried to fit the CH_3OH transitions in RTDs but except for W33 Main the level populations in W33 B, W33 B1, W33 A1, and W33 A

Figure 3.13: Rotational temperature diagrams (RTDs) of the six W33 sources from the APEX observations.

(a) RTD of H_2CO in W33 Main1

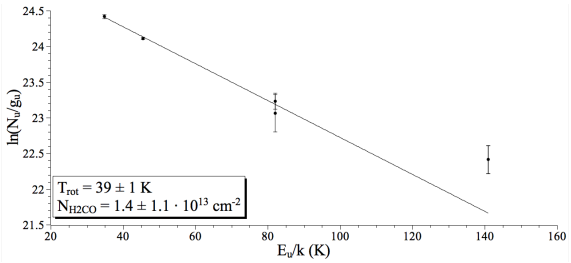

(b) RTD of H_2CO in W33 A1

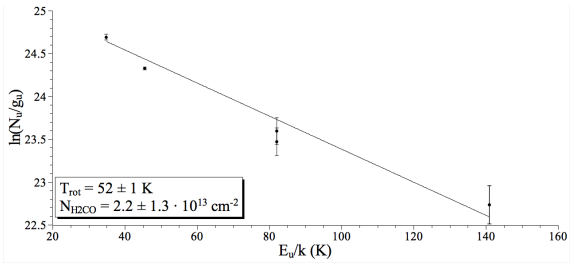

(c) RTD of H_2CO in W33 B1

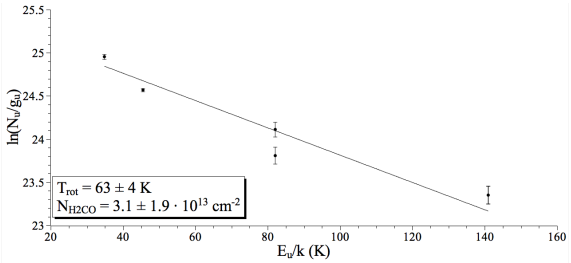

(d) RTD of H_2CO in W33 B

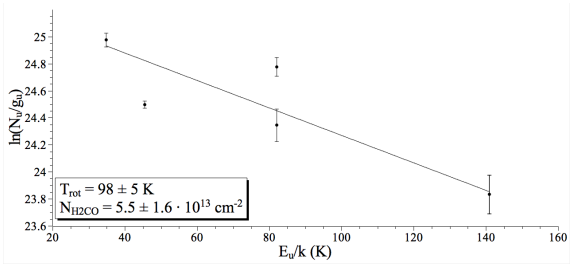

(e) RTD of H_2CO in W33 A

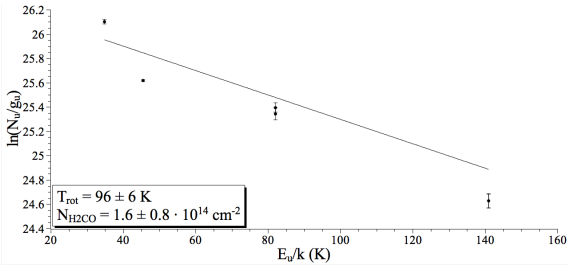

(f) RTD of H_2CO in W33 Main

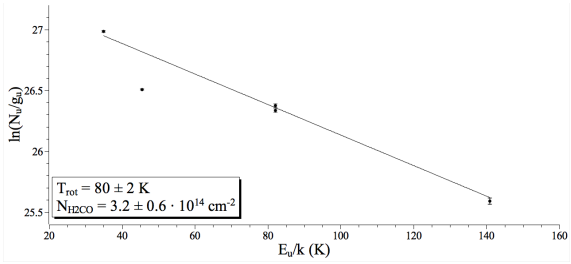

(g) RTD of CH_3OH in W33 Main

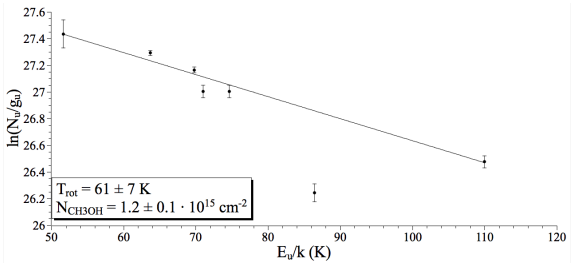

(h) RTD of CH_3CCH in W33 Main

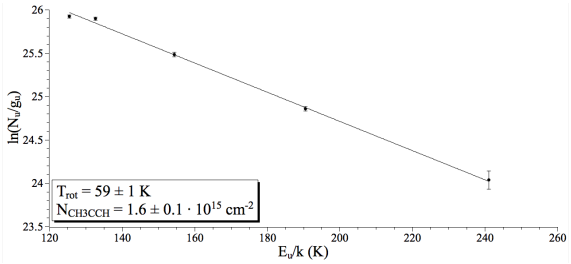

Table 3.4: Gas temperatures T and column densities N_{tot} from RTDs and Weeds modeling of the APEX (upper part) and SMA (lower part) spectra.

		RTD		Weeds	
Source	Molecule	T (K)	N_{tot} (10^{13} cm^{-2})	T (K)	N_{tot} (10^{13} cm^{-2})
W33 Main1	H_2CO	39	1.4	40	3
W33 A1	H_2CO	52	2.2	25	1.8
W33 A1	H_2CO			55	2.5
W33 B1	H_2CO	63	3.1	30	1.8
W33 B1	H_2CO			80	3.5
W33 B	H_2CO	98	5.5	30	1.8
W33 B	H_2CO			100	5.7
W33 A	H_2CO	96	16.1	40	7
W33 A	H_2CO			100	15
W33 Main	H_2CO	80	31.8	50	18.0
W33 Main	H_2CO			100	40.0
W33 Main	CH_3OH	61	116	40	130
W33 Main	CH_3CCH	59	159.6	59	300
W33 B	HNCO	351	161.3	280	250
W33 B	CH_3CN	335	83.1	350	300
W33 B	CH_3OH	219	4194.3	350	300

Figure 3.14: CH_3CN ladder spectrum (continuous line) and Gaussian fits (dashed line) from the SMA observations of W33 B.

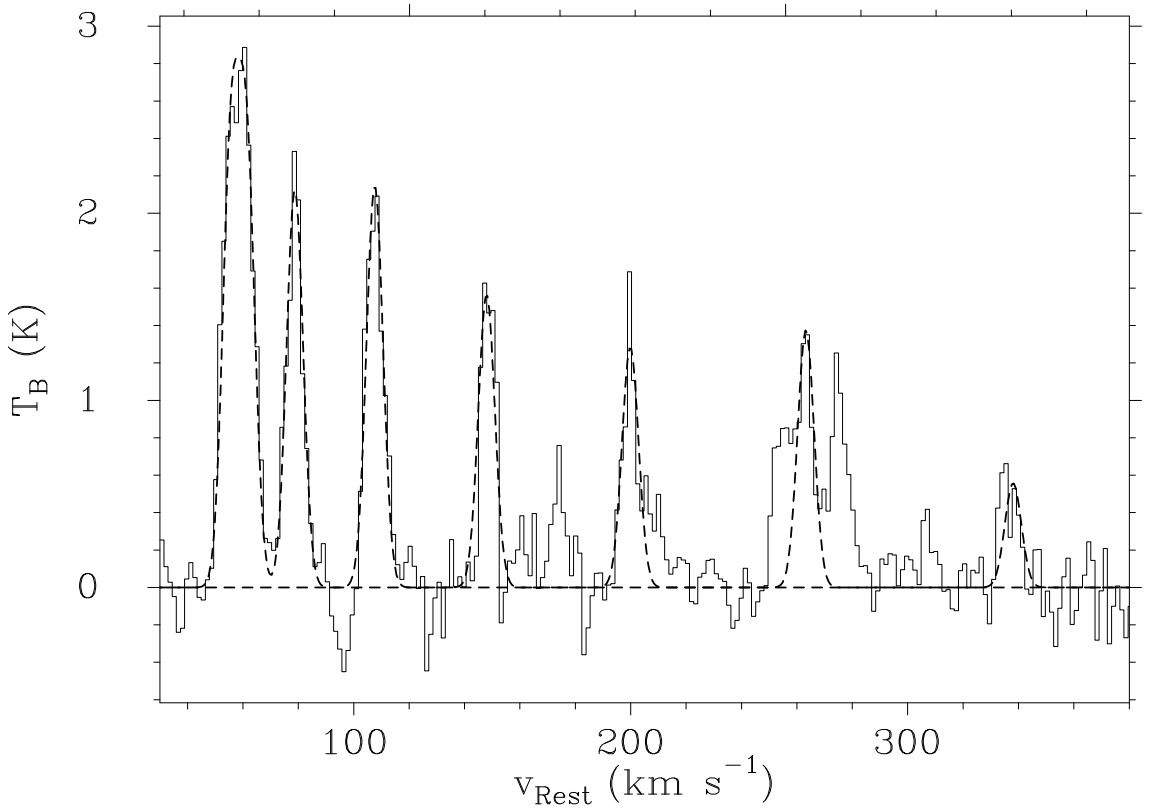

did not fall along a line in the RTDs. This indicates that either the assumption of optically thin gas does not apply for CH_3OH or that the CH_3OH emission has a temperature substructure in these sources. In the CH_3OH-RTD of W33 Main, the transition at 86 K was ignored in the fitting due to the strong difference of the level population compared to the other CH_3OH transitions. We also generated a RTD for the CH_3CCH transitions detected in W33 Main and fitted the level populations. The RTDs are shown in Fig. 3.13 and the temperatures (Col. 3) and total column densities (Col. 4) are listed in Table 3.4. Comparing the H_2CO-RTDs of the six W33 sources, we notice that temperature and column density increase from W33 Main1 to W33 Main along the evolutionary sequence that we established in Sects. 3.6 and 3.7. The temperatures and column densities, determined from the CH_3OH- and CH_3CCH-RTDs, are similar. Compared to the H_2CO-RTD, the temperatures are slightly lower and the column densities are a factor of 4−5 higher.

Figure 3.15: Rotational temperature diagrams of CH_3CN, CH_3OH, and HNCO from the SMA observations of W33 B.

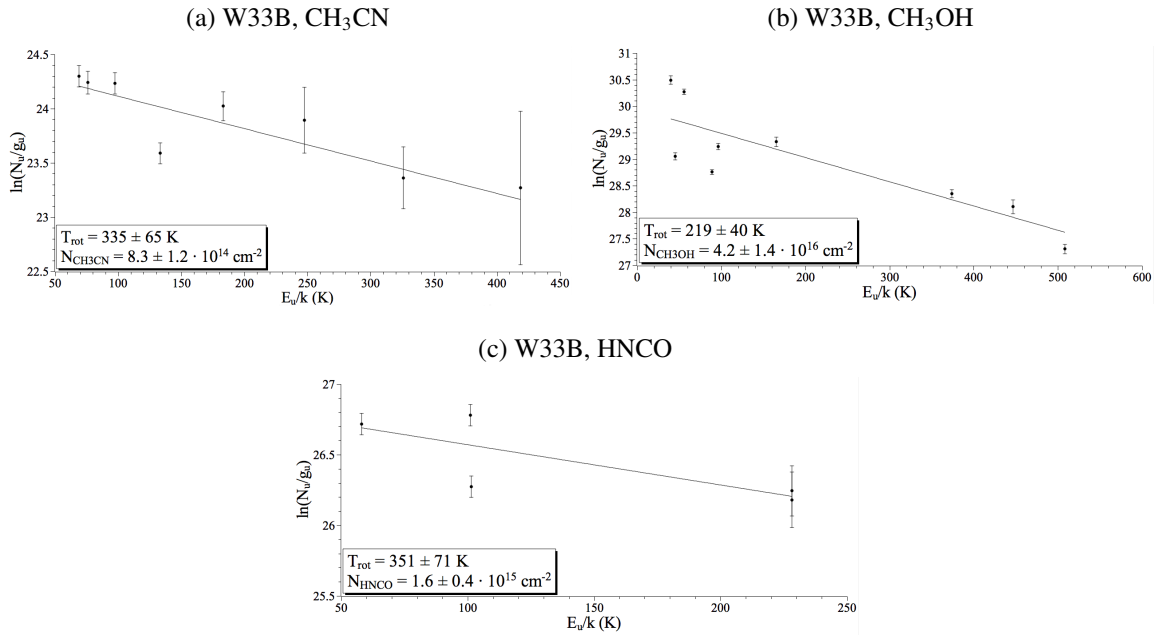

SMA Observations In the SMA spectra, we only observe molecules with multiple transitions in W33 B. Although the other sources show three transitions of H_2CO, two of these transitions are at the same upper energy level. Thus, H_2CO cannot be used for the RTD method. In W33 B, we detect multiple transitions from CH_3OH, HNCO, and CH_3CN.

Fig. 3.14 shows the spectrum of the K = 0...7 $CH_3CN(12_K-11_K)$ ladder in W33 B. The K = 0 and K = 1 transitions are blended together and K = 6 and 7 are blended with emission from other lines. Since the K-transitions are so close in frequency, they can be fitted simultaneously. We assume that the K-components have the same line width. To estimate the line width, we first fitted the K-components 2, 3, 4, and 5 with Gaussian line profiles, yielding a line width of 7.0 ± 0.5 km s^{-1}. We then fitted all lines with Gaussian line profiles with fixed frequency spacings and a line width of 7 km s^{-1} (see Fig. 3.14). The integrated intensities of the CH_3CN transitions are used to calculate the level populations of the different transitions which are then plotted in a RTD (Fig. 3.15). The least-square fit to the level populations yields a rotational temperature of 335 ± 65 K and a CH_3CN column density of $8.3 \pm 1.2 \cdot 10^{14}$ cm^{-2}.

The RTDs of CH_3OH and HNCO are also shown in Fig. 3.15. The rotational temperature and column density of HNCO are similar to the values of CH_3CN. The RTD of CH_3OH yields a rotational temperature that is much lower and a column density that is a factor 25 larger than for

HNCO. However, the CH_3OH-RTD shows that a line is not a good fit to the level populations, especially for transitions at lower excitation energies, indicating that either the emission is not optically thin or the CH_3OH gas has a temperature substructure. Comparing the RTD results for the APEX and SMA observations of W33 B, it is clear that the SMA observations trace a hotter and denser region in the source than the APEX data.

Galván-Madrid et al. (2010) produced a RTD of CH_3CN for W33 A, yielding a rotational temperature of 410 K and a column density of $3.4 \cdot 10^{16}$ cm^{-2}. Although the rotational temperatures of W33 B and W33 A are comparable within the errors, the column density of CH_3CN in W33 A is a factor of 40 larger than the column density of CH_3CN in W33 B.

3.8.2 Weeds Modeling

Weeds is an extension of the CLASS software which belongs to the GILDAS package. It is mostly written in Python. Weeds allows to search for spectral lines in a given frequency range from different spectral line catalogues (CDMS, JPL, splatalogue, ...). If several transitions of a given species are detected, Weeds permits the computation of a synthetic spectrum to inspect if the relative intensities of the transitions are in agreement with a single excitation temperature. The synthesized spectrum is constructed under the assumption of LTE conditions in the gas. The advantage of Weeds compared to the rotational temperature diagram method is that the modeling directly includes opacity effects and that the synthetic spectrum can directly be compared to the observed spectrum. To compute a synthetic spectrum, the user has to provide a text file including the name of the modeled species, the column density, the kinetic temperature, source size, and line width. In the optically thin case, the column density and the source size are degenerate. In the following two paragraphs, the synthetic spectra were produced assuming that the source size equals the APEX and SMA beams at 280 and 230 GHz, respectively.

APEX Observations As initial parameters for the construction of the synthetic spectrum for the H_2CO transitions, we used the temperatures and column densities, determined from the RTD fitting. The line width was determined from the average of the FWHMs of the detected transitions. The synthetic spectra, computed from the RTD results, did not yield a good fit of the observed spectra for any of the sources but underestimated the emission of all transitions. Thus, we changed the temperature and column density until we reached a good fit to the strongest transitions by eye. Since the column densities from the RTD fitting have larger uncertainties than the determined temperatures, we tried to keep the input temperature for the synthetic spectrum close to the RTD temperature. Due to uncertainties in the source size and possible temperature

Figure 3.16: Observed (black) and synthetic (red) spectra of CH_3CCH in W33 Main.

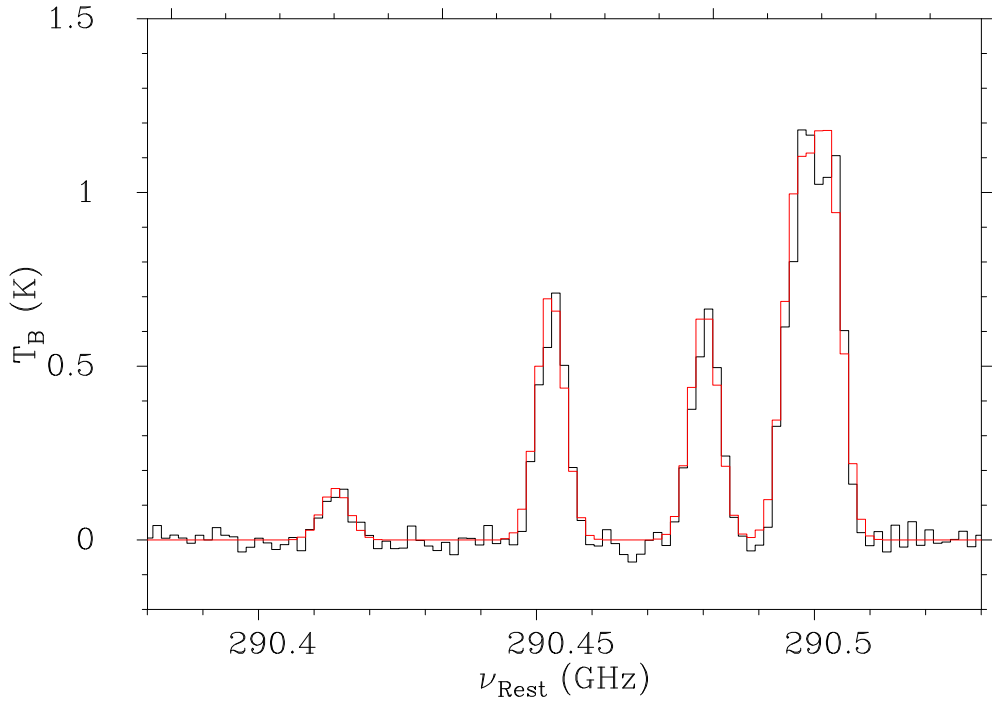

substructures, the synthetic spectra only give an estimate of the temperature and column density of the material but do not yield a perfect fit of the observed spectra. The results of the Weeds modeling are listed in Table 3.4 (Cols. 5, 6).

A good fit of the 46 K spectral line in W33 Main1 is achieved with a temperature of 40 K and a column density of $3 \cdot 10^{13}$ cm^{-2}. The synthetic spectrum slightly underestimates the 35 and 141 K transitions and slightly overestimates the two 82 K transitions.

In W33 A1, the synthetic spectrum, based on a kinetic temperature of 40 K and a column density of $3.8 \cdot 10^{13}$ cm^{-2}, gives a good fit to the 46 K transition. As in W33 Main1, the emission of the 35 K and the 141 K lines is a bit underestimated and the emission of the 82 K lines a bit overestimated. A slightly better fit for all transitions is achieved if we fit two components with 25 K and $1.8 \cdot 10^{13}$ cm^{-2} and 55 K and $2.5 \cdot 10^{13}$ cm^{-2}.

The synthetic spectrum, computed from the RTD results of W33 B1, is a good fit to the transitions with E_u above 45 K but underestimated the emission of the 35 K line. We conclude that a low-temperature component is missing in the construction of the synthesized spectrum. Thus, a new synthetic spectrum was produced, based on two components with 30 K and $1.8 \cdot 10^{13}$ cm^{-2} and 80 K and $3.5 \cdot 10^{13}$ cm^{-2} which again yields a good fit for the high-energy transitions. The emission of the 35 K line is still a bit underestimated but the emission of the 46 K line is now

slightly overestimated. Further changing temperature and column density of both components will either yield a better fit for the 46 K line and a worse fit for the 35 K line or vice versa.

In W33 B, the synthetic spectrum, constructed from the RTD results, is only a good fit for the 141 K transition. We produce another synthetic spectrum with two components of 30 K and $1.8 \cdot 10^{13}$ cm^{-2} and 100 K and $5.7 \cdot 10^{13}$ cm^{-2}. This spectrum reproduces the transitions of the upper sideband well but overestimates the emission of the 46 K line.

Again, the synthetic spectrum, based on the RTD results of W33 A, is only a good fit for the 141 K transition. The synthetic spectrum, constructed from two components of 40 K and $7 \cdot 10^{13}$ cm^{-2} and 100 K and $1.5 \cdot 10^{14}$ cm^{-2}, yields a good fit for the high-energy and the 35 K transitions but overestimates the emission of the 46 K line by about 25%.

The RTD results of W33 Main yield a synthetic spectrum that is a bad fit for all observed transitions. Two components with 50 K and $1.8 \cdot 10^{14}$ cm^{-2} and 100 K and $4 \cdot 10^{14}$ cm^{-2} give a synthetic spectrum which fits all transitions except the 46 K very well. However, the emission of the 46 K line is overestimated by about 50%. In W33 Main, we also produced synthetic spectra for CH_3OH and CH_3CCH. The RTD results of CH_3CCH give a synthetic spectrum that underestimates the emission of all detected transitions. A better fit is achieved using a kinetic temperature of 59 K and a column density of $3 \cdot 10^{15}$ cm^{-2} for the construction of the synthetic spectrum. The observed and the synthetic spectrum of CH_3CCH are shown in Fig. 3.16. For CH_3OH, we find a fairly good fit of the transitions for one component with 40 K and $1.3 \cdot 10^{15}$ cm^{-2}. However, the synthetic spectrum underestimates the emission of $CH_3OH(9_{-1,9}-8_{0,8})$.

The results show that for all sources except W33 Main1 we need a cold and a warm component to fit the H_2CO spectral lines well. In all five sources, the warm component has a higher column density as the cold component which indicates that it is excited closer to the center of the core. Since we estimate high temperatures for the warm component in W33 B1, W33 B, W33 A, and W33 Main, we expect the existence of a heating source in these sources.

The temperatures and column densities of both components increase from W33 Main1 to W33 Main (see Table 3.4), supporting the sorting of the sources along an evolutionary sequence.

SMA Observations We tried to compute synthetic spectra from one component for the H_2CO transitions in W33 A1, W33 B1, and W33 B but it was not possible to well-fit all three transitions. The synthetic spectra show that the peak line ratio between $H_2CO(3_{2,1}-2_{2,0})$ and $H_2CO(3_{2,2}-2_{2,1})$ should be close to 1 and the peak of the $H_2CO(3_{0,3}-2_{0,2})$ line is larger than the peaks of the other two transitions. The peak line ratios in W33 A1 and W33 B1 are 0.6 and 2.0. In W33 B, the line ratio is close to 1 but the peak of $H_2CO(3_{0,3}-2_{0,2})$ is smaller than the peaks of the other two

transitions. This indicates that in all three sources the assumption of a single temperature relating the level populations is not justified for H_2CO.

We constructed a synthetic spectrum for HNCO in W33 B for one component with the RTD results. The synthetic spectrum underestimates the emission of all transitions. A good fit of the observed spectrum is achieved with 280 K and $2.5 \cdot 10^{15}$ cm^{-2}. However, the emission of the transition at 220.58 GHz is slightly overestimated while the emission of the transition at 218.98 GHz is slightly underestimated. Through comparison with the synthetic spectrum, we found two additional transitions of HNCO at 219.66 GHz (HNCO($10_{3,8}$−93,7), HNCO($10_{3,7}$−93,6)) which are blended and a 2σ detection in our data. The synthetic spectrum of the CH_3CN emission in W33 B which was compiled from the RTD results is only a good fit for the $CH_3CN(12_3-11_3)$ transition. A better fitting synthetic spectrum is constructed from a kinetic temperature of 280 K and a column density of $1.3 \cdot 10^{15}$ cm^{-2}. However, the emission of the $CH_3CN(12_3-11_3)$ transition is now overestimated. The comparison of synthetic and observed spectrum yield the identification of another transition of the CH_3CN ladder ($CH_3CN(12_7-11_7)$) which is a 2σ detection in our data. The RTD results of CH_3OH in W33 B yield a synthetic spectrum which underestimates the emission of all CH_3OH transitions. The synthetic spectrum shows that at least two components are necessary to fit the observed spectrum. However, we do not find two combinations of temperatures and column densities that fit all transitions well. Since the opacities of the synthesized spectra are consistent with optically thin emission, the bad fits indicate that the CH_3OH gas has a more complex temperature substructure.

3.9 Chemical Diversity in the W33 Complex

Studying the chemistry of high-mass star forming regions in one star forming complex like W33 has several advantages. Since all star forming regions belong to the same complex and probably evolved from the same giant molecular cloud, the primary material of the birth clouds is the same or at least similar (w.r.t. metallicity, for example). Furthermore, the star forming regions are at very similar distances. Thus, the observations of each telescope cover the same spatial scales which makes the observations per telescope directly comparable for the different star forming regions. In addition, missing short spacings in the SMA observations have a similar effect on the data of all star forming regions, assuming the line emission is similarly extended in all the sources.

Due to the different resolutions and the filtering of the interferometer data, the APEX and SMA data sets are sensitive to different physical scales (APEX: > 0.2 pc, SMA: 0.05−0.2 pc).

The APEX observations are sensitive to all the emission from the cloud. However, if the emitting gas is confined to a small region and thus the emission is very compact, the large APEX beam dilutes the emission and depending on the strength of the signal compared to the noise level of the observations the emission might be undetected. The SMA observations on the contrary are only sensitive to compact emission while the more extended emission is resolved out. Thus, with these two data sets we are able to trace the chemical composition on different scales in the star forming regions.

In W33, the molecular clouds cover a range of bolometric luminosities from $5-445 \cdot 10^3$ $L_\odot$ and they seem to be in different evolutionary stages of star formation. Thus, we can compare the observations for different luminosities and along an evolutionary sequence. We will first discuss each of the W33 sources and then draw conclusions about the change of chemistry along the detected evolutionary sequence.

3.9.1 Single Sources

W33 Main1

W33 Main1 seems to be in a very early stage of star formation. On larger scales (> 0.2 pc), traced by the APEX data, transitions from H_2CO and CH_3OH up to an upper energy level of 141 K are detected. However, these molecules are not detected on smaller scales, traced by the SMA data. Either the medium is too cold and the molecules are not released yet into the gas phase or the emission is too diffuse to be detected with the SMA interferometer. This suggests that if a heating source is present in W33 Main1, it does not strongly influence the chemistry yet. The lack of molecules other than CO (and its isotopologues) and SO, which traces shocked gas, suggests that W33 Main1 is in the collapse phase before or during the formation of a protostar.

W33 A1

W33 A1 is the source with the lowest cloud mass and luminosity of our sample. The chemistry on larger scales looks similar to W33 Main1 except that two more CH_3OH transitions are observed. On smaller scales, we observe low-energy transitions of H_2CO and CH_3OH, indicating the presence of a heating source which evaporates these ices off the dust grains. The necessity of a second warmer component in the LTE modeling supports the existence of a heating source in W33 A1. We also observe emission of the DCN molecule which is a tracer of cold and dense gas. Although W33 A1 is a factor of two less luminous than W33 Main1, it is probably more evolved. We conclude that W33 A1 is in the protostellar phase but before the excitation of a hot

core.

W33 B1

The APEX and SMA spectra of W33 B1 look very similar to the spectra of W33 A1 but the H_2CO gas in W33 B1 seems to have a slightly higher temperature and column density than in W33 A1. The dust temperature of W33 B1, determined from the SED fits, is ∼10 K higher than the dust temperatures of the other sources (except W33 Main). This might be explained by the proximity of the star cluster SC-1 whose infrared emission seems to penetrate the W33 B1 cloud. Although the luminosity of W33 B1 is a factor of three larger than the luminosity of W33 A1, there are no obvious differences in the SMA or APEX observations between these two sources, except that the detected lines tend to be stronger and broader in W33 B1. We deduce that W33 B1 is also in the protostellar phase before the excitation of a hot core.

W33 B

Observations of water, methanol, and hydroxyl masers in W33 B indicate that high-mass stars are forming in this cloud. However, the APEX spectra of W33 B are comparable to the spectra of W33 B1 or W33 A1, except that we additionally observe transitions of OCS, H_2CS, and $C^{33}S$. The compactness of the OCS emission and the high energy needed to excite the detected transition suggest that the emission is excited closer to the forming star at temperatures that are higher than the temperatures traced by H_2CO and CH_3OH. The LTE modeling of the APEX data of W33 B shows that column density and temperature of the envelope are higher than for the previous sources with the temperature of the warm component reaching ∼100 K.

On smaller scales, W33 B shows a forest of lines. Especially nitrogen-bearing molecules like HNCO, CH_3CN or HC_3N are detected in the SMA spectra, indicating that W33 B is already in the hot core phase. However, from more complex molecules only one transition of CH_3OCHO and one of CH_3OCH_3 are observed. Other complex molecules like e.g. CH_3CH_2CN, CH_2CHCN, C_2H_5OH or $HCOOCH_3$ as seen in "typical" hot cores like Orion-KL or G29.96 (e.g. Beuther et al. 2009) are not detected in W33 B.

The temperatures and column densities of W33 B on smaller scales, inferred from LTE modeling of the SMA data, are much higher than on larger scales, indicating temperature and column density gradients in W33 B.

W33 A

As in W33 B, methanol, water, and hydroxyl masers are detected in W33 A indicating that high-mass star formation is taking place in this cloud. The high-energy transitions of HC_3N and CH_3CCH in the APEX data of W33 A reveal that more complex molecules are detected on larger scales. The LTE modeling shows that the temperatures of the two components are comparable to the temperatures in W33 B but the column densities are a factor of three higher. In the SMA spectra, many transitions of a large number of "simple" and complex molecules are detected, evidence for W33 A being in the hot core phase. Compared to W33 B, several transitions of complex molecules like CH_3OCHO and CH_3OCH_3 are observed. However, also the spectra of W33 A lack emission of complex molecules that are observed in "typical" hot cores. Although W33 A and W33 B have very similar masses, W33 A is twice as luminous as W33 B. W33 A is probably more evolved than W33 B. Radio continuum observations of W33 A by Rengarajan & Ho (1996) and van der Tak & Menten (2005) with the VLA suggest that the detected emission either comes from an ionized wind or a hypercompact H II region in W33 A. This is evidence for W33 A being more evolved than W33 B, maybe in transition from the "pure" hot core phase to the more evolved H II region phase.

W33 Main

W33 Main is the only source in the W33 complex that shows strong radio emission (see Chapter 4), indicating that this source is in the H II region phase. Water and Class I methanol masers are observed in W33 Main. The mass and luminosity of W33 Main are a factor of three and ten higher than for W33 A, respectively. The APEX spectra of W33 Main are similar to the spectra of W33 A, except that we detect higher-energy transitions of CH_3CCH as well as emission of $C^{33}S$ and $H_2{}^{13}CO$. In addition, the column density of the H_2CO gas is highest in W33 Main. However, at smaller scales, we do not detect emission of complex molecules like in the hot core sources anymore. The SMA spectra of W33 Main are similar to the spectra of W33 A1 and W33 B1 plus emission of HC_3N and the radio recombination line H30α which traces ionized gas. HC_3N is the only complex molecule that is detected in W33 Main and it peaks at the edge of W33 Main-Central. Other complex molecules (like CH_3CN, CH_3OCHO or CH_3OCH_3) are either destroyed close to the heating source or their emission is extended without compact peaks and thus resolved out by the interferometer observations. We conclude that W33 Main is already in the H II region phase.

3.9.2 Chemical Complexity – Evolutionary Sequence

From our SMA and APEX observations, we infer an evolutionary sequence of star formation in W33. We sort the sources in four different groups:

- Prestellar Phase (W33 Main1): Cold interior, probably still contracting, no strong heating source yet

- Protostellar Phase (W33 A1, W33 B1): Heating source starts to warm up the surrounding material, release of primary molecules from dust grains into gas phase

- Hot Cores (W33 B, W33 A): Heating source strongly influences the chemistry of the surrounding material, release of primary molecules from dust grains and synthesis of complex secondary molecules in gas phase

- H II regions (W33 Main): Heating source ionizes the surrounding material, strong radio emission detectable, complex molecules probably photo-dissociated

Our observations show that the chemistry changes dramatically along this evolutionary sequence, especially on smaller spatial scales. The detected transitions tend to get stronger and broader along this sequence in both the SMA and APEX data sets.

Our SMA observations suggest that in early phases of star formation emission of CO and its isotopologues dominates. Once a heating source is present, H_2CO and CH_3OH are evaporated off dust grains. When the temperature in the core rises, also more complex molecules are evaporated off the dust grains or synthesized in the gas phase. Once an H II region emerges, the more complex molecules seem to be destroyed by the ionization or their emission is too diffuse to be detected by the interferometer. On larger scales, traced by the APEX observations, the chemical diversity and complexity increases with the evolution of the star forming region and complex molecules are still detected in the H II region phase.

We show the importance of combining spectral information on different scales. While the APEX data show emission of more complex molecules for more evolved star forming regions, the SMA spectra show an increase in chemical complexity up to the hot core stage but then a decrease in detected molecules in the H II region phase. Thus, the sources W33 B and W33 Main would probably have been classified differently if only one of the data sets would have been considered.

3.10 Conclusions

Infrared, submillimeter, and radio continuum and maser observations of the high-mass star forming complex W33 show that it contains star forming regions at different stages of formation, from clouds in the prestellar phase to developed H II regions. The star forming regions are located at the same distance of 2.4 kpc and probably consisted of the same birth material making a comparative chemical study along the evolutionary sequence feasible. We conducted SMA and APEX observations of six molecular clouds in the W33 complex at 230 and 280 GHz, respectively. In the APEX and SMA data, 27 transitions of 10 different molecules and 38 transitions of 14 different molecules, respectively, were detected, from simple molecules like CO with widespread emission to complex molecules like CH_3CCH, CH_3OCHO or CH_3OCH_3 with compact emission. The two data sets probe different physical scales. While the APEX data are sensitive to emission on scales of > 0.2 pc, the SMA data trace compact emission on smaller scales ($\sim 0.05-0.2$ pc), allowing us to compare the chemical compositions with different resolutions.

We constructed SEDs for the six clouds W33 Main1, W33 A1, W33 B1, W33 B, W33 A, and W33 Main, determined dust temperatures, bolometric luminosities, and spectral emissivity indices, and inferred the total masses of the clouds.

A study of the kinematics of the W33 complex show that W33 A and W33 B are not gravitationally bound to W33 Main and thus, the larger clouds in the W33 complex will probably drift apart with time.

In the prestellar phase (W33 Main1), the APEX observations show traces of H_2CO and CH_3OH ice while in the SMA data only low-excitation transitions of CO and its isotopologues and SO are detected. Either the emission of the more complex molecules is too diffuse to be detected or these molecules are not released yet from the dust grains on smaller scales and thus the temperature is lower. Once a protostar is formed, it releases H_2CO and CH_3OH from the dust grains, detected on small scales in all sources except W33 Main1. However, the APEX spectra of the sources in the protostellar phase (W33 A1, W33 B1) did not change significantly compared to the prestellar phase. In the hot core phase (W33 A, W33 B), the diversity and complexity of the chemical composition in the SMA spectra changes strongly. The chemistry on larger scales in the APEX spectra of W33 B and W33 A is more evolved than in the protostellar phase but does not show the chemical complexity observed on smaller scales in the SMA data. W33 Main is in the H II region phase. We detected the radio recombination line H30α in W33 Main which traces ionized gas. The SMA spectra of W33 Main are similar to the spectra of the sources in the protostellar phase, except for the detection of the radio recombination line and a transition of HC_3N. This indicates that the complex molecules that are observed in the hot core phase are

either destroyed through photo-dissociation by the H II region or their emission is too diffuse to be detected by the SMA. The APEX data of W33 Main show transitions of complex molecules which indicates that the destruction of complex molecules has not reached the larger scales yet.

3.A Appendix

Table 3.5: Transitions, detected in W33 with the APEX telescope.

			W33 Main1				W33 A1				W33 B1			
ν_0 (GHz)	Transition	E_u (K)	F_{Int} (K km s^{-1})	F_{Peak} (K)	$v_{central}$ (km s^{-1})	FWHM (km s^{-1})	F_{Int} (K km s^{-1})	F_{Peak} (K)	$v_{central}$ (km s^{-1})	FWHM (km s^{-1})	F_{Int} (K km s^{-1})	F_{Peak} (K)	$v_{central}$ (km s^{-1})	FWHM (km s^{-1})
278.3045	$CH_3OH(9_{-1,9}-8_{0,8})$	109.97					0.28	0.10	36.48	2.79	0.59	0.10	33.21	5.65
278.8864	$H_2CS(8_{1,7}-7_{1,6})$	73.41												
279.5117	$N_2H^+(3-2)$	26.83	11.13	2.16	36.61	4.85	9.43	1.83	36.74	4.85	7.38	1.47	33.57	4.71
279.6853	OCS(23−22)	161.09												
281.5269	$H_2CO(4_{1,4}-3_{1,3})$	45.57	3.05	1.00	36.53	2.87	3.78	0.98	36.68	3.62	4.82	0.79	33.69	5.73
281.9768	$HC_3N(31-30)$	215.55												
290.2487	$CH_3OH(6_{1,5}-5_{1,4})$	69.80					0.28	0.07	37.08	3.78	0.56	0.07	32.65	8.10
290.2641	$CH_3OH(6_{2,4}-5_{2,3})$	86.46												
290.3073	$CH_3OH(6_{-2,5}-5_{-2,4})$[a]	74.66	0.19	0.08	35.96	2.39	0.48	0.12	36.75	3.78	0.88	0.15	32.74	5.58
290.3076	$CH_3OH(6_{2,4}-5_{2,3})$[a]	71.00												
290.4135	$CH_3CCH(17_4-16_4)$	241.05												
290.4523	$CH_3CCH(17_3-16_3)$	190.50												
290.4799	$CH_3CCH(17_2-16_2)$	154.39												
290.4965	$CH_3CCH(17_1-16_1)$	132.71												
290.5021	$CH_3CCH(17_0-16_0)$	125.49												
290.6234	$H_2CO(4_{0,4}-3_{0,3})$	34.90	1.52	0.53	36.54	2.67	2.00	0.55	36.58	3.40	2.60	0.49	33.63	5.00
291.0684	$HC_3N(32-31)$	230.52												
291.2378	$H_2CO(4_{2,3}-3_{2,2})$	82.07	0.35	0.10	36.46	3.25	0.44	0.13	36.33	3.26	0.84	0.14	33.18	5.78
291.3805	$H_2CO(4_{3,2}-3_{3,1})$[a]	140.94	0.54	0.07	36.14	7.72	0.74	0.08	36.49	8.43	1.38	0.14	32.92	9.36
291.3843	$H_2CO(4_{3,1}-3_{3,0})$[a]	140.94												
291.4859	$C^{33}S(6-5)$	38.66												
291.8397	OCS(24−23)	175.10												
291.9481	$H_2CO(4_{2,2}-3_{2,1})$	82.12	0.30	0.09	36.34	2.93	0.50	0.09	36.88	5.48	0.62	0.14	33.34	4.32
292.6729	$CH_3OH(6_{1,5}-5_{1,4})$	63.71	0.16	0.06	36.13	2.46	0.42	0.09	36.77	4.51	0.80	0.12	32.92	6.17
293.1265	$H_2{}^{13}CO(4_{1,3}-3_{1,2})$	47.01												
293.4640	$CH_3OH(3_{2,1}-4_{1,4})$	51.64												
293.9122	CS(6−5)	49.37	2.82	0.89	36.56	2.97	4.39	1.22	36.96	3.38	2.86	0.62	34.16	4.34

Table 3.5: Continued.

			W33 B				W33 A				W33 Main			
ν_0 (GHz)	Transition	E_u (K)	F_{Int} (K km s^{-1})	F_{Peak} (K)	$v_{central}$ (km s^{-1})	FWHM (km s^{-1})	F_{Int} (K km s^{-1})	F_{Peak} (K)	$v_{central}$ (km s^{-1})	FWHM (km s^{-1})	F_{Int} (K km s^{-1})	F_{Peak} (K)	$v_{central}$ (km s^{-1})	FWHM (km s^{-1})
278.3045	$CH_3OH(9_{-1,9}-8_{0,8})$	109.97	0.98	0.19	54.73	4.88	2.24	0.34	37.52	6.12	3.05	0.56	36.07	5.12
278.8864	$H_2CS(8_{1,7}-7_{1,6})$	73.41	0.49	0.13	54.12	3.69	1.62	0.28	36.63	5.40	5.90	0.99	34.59	5.58
279.5117	$N_2H^+(3-2)$	26.83	12.26	2.24	55.39	5.16	31.07	5.11	37.28	5.71	22.91	3.35	35.40	6.43
279.6853	OCS(23−22)	161.09					1.05	0.21	37.81	4.69	0.81	0.11	36.45	7.20
281.5269	$H_2CO(4_{1,4}-3_{1,3})$	45.57	4.49	1.04	55.44	4.07	13.74	2.35	37.56	5.50	33.50	4.11	35.87	7.66
281.9768	$HC_3N(31-30)$	215.55					0.62	0.14	38.23	4.04	2.21	0.37	35.27	5.59
290.2487	$CH_3OH(6_{1,5}-5_{1,4})$	69.80	0.97	0.13	55.39	6.88	2.54	0.41	37.51	5.77	5.27	0.86	35.97	5.78
290.2641	$CH_3OH(6_{2,4}-5_{2,3})$	86.46	0.87	0.12	55.39	6.72	1.50	0.18	37.51	7.68	1.75	0.30	36.32	5.54
290.3073	$CH_3OH(6_{-2,5}-5_{-2,4})$[a]	74.66	1.08	0.24	55.38	4.22	3.51	0.63	37.19	5.25	7.96	1.27	36.08	5.90
290.3076	$CH_3OH(6_{2,4}-5_{2,3})$[a]	71.00												
290.4135	$CH_3CCH(17_4-16_4)$	241.05									0.94	0.15	35.24	5.98
290.4523	$CH_3CCH(17_3-16_3)$	190.50									4.40	0.69	35.24	5.98
290.4799	$CH_3CCH(17_2-16_2)$	154.39									4.18	0.66	35.24	5.98
290.4965	$CH_3CCH(17_1-16_1)$	132.71									6.40	1.00	35.24	5.98
290.5021	$CH_3CCH(17_0-16_0)$	125.49					1.07	0.13	37.02	7.68	6.58	1.03	35.24	5.98
290.6234	$H_2CO(4_{0,4}-3_{0,3})$	34.90	2.66	0.69	55.20	3.65	8.19	1.48	37.50	5.19	19.83	2.83	35.56	6.57
291.0684	$HC_3N(32-31)$	230.52					0.90	0.18	38.65	4.64	2.00	0.32	35.06	5.97
291.2378	$H_2CO(4_{2,3}-3_{2,2})$	82.07	1.64	0.20	55.69	7.63	3.04	0.56	37.52	5.08	8.10	1.22	35.39	6.25
291.3805	$H_2CO(4_{3,2}-3_{3,1})$[a]	140.94	2.23	0.17	55.86	12.48	4.93	0.52	37.76	8.99	12.93	1.39	34.97	8.75
291.3843	$H_2CO(4_{3,1}-3_{3,0})$[a]	140.94												
291.4859	$C^{33}S(6-5)$	38.66	0.49	0.13	55.67	3.51					3.91	0.57	35.65	6.46
291.8397	OCS(24−23)	175.10	1.06	0.14	55.97	7.30	1.41	0.18	38.58	5.49	0.90	0.12	36.41	7.23
291.9481	$H_2CO(4_{2,2}-3_{2,1})$	82.12	1.07	0.17	54.98	5.84	2.89	0.54	37.82	5.05	7.80	1.23	35.40	5.97
292.6729	$CH_3OH(6_{1,5}-5_{1,4})$	63.71	1.08	0.22	55.66	4.59	2.76	0.55	37.68	4.70	5.90	0.96	36.11	5.77
293.1265	$H_2{}^{13}CO(4_{1,3}-3_{1,2})$	47.01									1.00	0.14	34.95	6.58
293.4640	$CH_3OH(3_{2,1}-4_{1,4})$	51.64	0.79	0.14	56.62	5.34					0.98	0.20	36.32	4.64
293.9122	CS(6−5)	49.37	6.86	1.71	55.58	3.76	19.52	3.22	37.58	5.70	81.86	9.23	36.39	8.33

Notes. [(a)] Blended transitions.

Table 3.6: Transitions, detected in W33 with the SMA.

			W33 Main1				W33 A1				W33 B1			
ν_0 (GHz)	Transition	E_u (K)	F_{Int} (K km s^{-1})	F_{Peak} (K)	$v_{central}$ (km s^{-1})	FWHM (km s^{-1})	F_{Int} (K km s^{-1})	F_{Peak} (K)	$v_{central}$ (km s^{-1})	FWHM (km s^{-1})	F_{Int} (K km s^{-1})	F_{Peak} (K)	$v_{central}$ (km s^{-1})	FWHM (km s^{-1})
216.9456	$CH_3OH(5_{1,4}-4_{2,2})$	55.87												
216.9659	$CH_3OCHO(20_{1,20}-19_{1,19})A$	111.48												
217.1050	SiO(5−4)	31.26												
217.2386	DCN(3−2)	20.85					5.75	1.29	34.14	4.19				
217.2992	$CH_3OH(6_{1,5}-7_{2,6})$	373.93												
217.8864	$CH_3OH(20_{1,19}-20_{0,20})$	508.38												
218.2222	$H_2CO(3_{0,3}-2_{0,2})$	20.96					8.33	2.22	35.43	3.52	21.98	3.33	32.94	6.20
218.3248	$HC_3N(24-23)$	130.98												
218.4401	$CH_3OH(4_{2,2}-3_{1,2})$	45.46					7.74	1.64	36.33	4.43	13.63	2.51	32.72	5.10
218.4756	$H_2CO(3_{2,2}-2_{2,1})$	68.09					4.61	1.50	36.71	2.89	5.37	0.81	31.69	6.20
218.7601	$H_2CO(3_{2,1}-2_{2,0})$	68.11					3.44	0.96	35.43	3.38	8.73	1.64	32.78	5.02
218.9810	$HNCO(10_{1,10}-9_{1,9})$	101.08												
219.5604	$C^{18}O(2-1)$	15.81	3.41	1.38	36.13	2.32	10.08	2.51	34.87	3.77		*		
219.6568	$HNCO(10_{3,8}-9_{3,7})$[a]	432.96												
219.6568	$HNCO(10_{3,7}-9_{3,6})$[a]	432.96												
219.7339	$HNCO(10_{2,9}-9_{2,8})$[a,b]	228.28												
219.7372	$HNCO(10_{2,8}-9_{2,7})$[a,b]	228.29												
219.7982	$HNCO(10_{0,10}-9_{0,9})$	58.02												
219.9085	$H_2{}^{13}CO(3_{1,2}-2_{1,1})$	15.56												
219.9494	$SO(6_5-5_4)$	34.98	4.17	0.82	35.75	4.80					3.37	0.9	33.35	3.53
220.0785	$CH_3OH(8_{0,8}-7_{1,6})$	96.61												
220.1669	$CH_3OCHO(17_{4,13}-16_{4,12})E$	103.15												
220.1903	$CH_3OCHO(17_{4,13}-16_{4,12})E$	103.15												
220.3989	$^{13}CO(2-1)$	15.89		*				*				*		
220.5392	$CH_3CN(12_7-11_7)$	418.63												
220.5848	$HNCO(10_{1,9}-9_{1,8})$	101.50												
220.5944	$CH_3CN(12_6-11_6)$	325.90												
220.6410	$CH_3CN(12_5-11_5)$	247.40												
220.6792	$CH_3CN(12_4-11_4)$	183.15												
220.7090	$CH_3CN(12_3-11_3)$	133.16												
220.7302	$CH_3CN(12_2-11_2)$	97.44												
220.7430	$CH_3CN(12_1-11_1)$	76.01												
220.7472	$CH_3CN(12_0-11_0)$	68.87												
220.8934	$CH_3OCH_3(23_{4,20}-23_{3,21})$[c]	274.44												

Table 3.6: Continued.

			W33 Main1				W33 A1				W33 B1			
ν_0 (GHz)	Transition	E_u (K)	F_{Int} (K km s^{-1})	F_{Peak} (K)	$v_{central}$ (km s^{-1})	FWHM (km s^{-1})	F_{Int} (K km s^{-1})	F_{Peak} (K)	$v_{central}$ (km s^{-1})	FWHM (km s^{-1})	F_{Int} (K km s^{-1})	F_{Peak} (K)	$v_{central}$ (km s^{-1})	FWHM (km s^{-1})
221.1984	$CH_3OCH_3(27_{5,22}-27_{4,23})$[c]	257.14												
229.4050	$CH_3OCHO(18_{3,15}-17_{3,14})$	110.74												
229.4203	$CH_3OCHO(18_{3,15}-17_{3,14})$	110.74												
229.5891	$CH_3OH(15_{4,11}-16_{3,13})$	374.44												
229.7588	$CH_3OH(8_{-1,8}-7_{0,7})$	89.10												
229.8641	$CH_3OH(19_{5,15}-20_{4,16})$	578.60												
229.9392	$CH_3OH(19_{5,14}-20_{4,17})$	578.60												
230.0270	$CH_3OH(3_{-2,2}-4_{-1,4})$	39.83												
230.1414	$CH_3OCH_3(25_{4,22}-25_{3,22})$	319.21												
230.2338	$CH_3OCH_3(17_{2,15}-16_{3,14})$	147.65												
230.3682	$CH_3OCH_3(28_{5,23}-27_{6,22})$	406.35												
230.5380	$^{12}CO(2-1)$	16.60	21.51	4.08	30.01	4.95	14.19	3.56	29.44	3.74	12.76	3.16	26.40	3.79
231.0610	OCS(19−18)	110.90												
231.2210	$^{13}CS(5-4)$	33.29												
231.2811	$CH_3OH(10_{2,9}-9_{3,6})$	165.35												
231.9009	H30α													
231.9879	$CH_3OCH_3(13_{0,13}-12_{1,12})$	80.92												
232.4186	$CH_3OH(10_{2,8}-9_{3,7})$	165.40												
232.7836	$CH_3OH(18_{3,16}-17_{4,13})$	446.53												

Table 3.6: Continued.

			W33 B				W33 A	W33 Main			
ν_0 (GHz)	Transition	E_u (K)	F_{Int} (K km s^{-1})	F_{Peak} (K)	$v_{central}$ (km s^{-1})	FWHM (km s^{-1})		F_{Int} (K km s^{-1})	F_{Peak} (K)	$v_{central}$ (km s^{-1})	FWHM (km s^{-1})
216.9456	$CH_3OH(5_{1,4}-4_{2,2})$	55.87	20.52	2.78	55.91	6.95					
216.9659	$CH_3OCHO(20_{1,20}-19_{1,19})A$	111.48	19.95	2.72	55.07	6.89					
217.1050	SiO(5−4)	31.26							*		
217.2386	DCN(3−2)	20.85	10.68	1.34	55.78	7.47					
217.2992	$CH_3OH(6_{1,5}-7_{2,6})$	373.93	12.48	2.49	56.45	4.71					
217.8864	$CH_3OH(20_{1,19}-20_{0,20})$	508.38	10.91	2.19	55.71	4.69					
218.2222	$H_2CO(3_{0,3}-2_{0,2})$	20.96	17.55	1.92	56.67	8.61		4.63	1.12	39.59	3.89
218.3248	HC_3N(24−23)	130.98	22.17	2.02	55.40	10.32		21.89	5.96	37.40	3.45
218.4401	$CH_3OH(4_{2,2}-3_{1,2})$	45.46	18.77	2.92	55.80	6.04		19.15	4.21	37.78	4.27
218.4756	$H_2CO(3_{2,2}-2_{2,1})$	68.09	12.37	2.16	55.12	5.37		4.14	0.81	36.00	4.79
218.7601	$H_2CO(3_{2,1}-2_{2,0})$	68.11	14.34	2.57	56.26	5.23					
218.9810	$HNCO(10_{1,10}-9_{1,9})$	101.08	13.56	1.60	54.58	7.94					
219.5604	$C^{18}O$(2−1)	15.81		*			✓	22.99	6.46	38.57	3.34
219.6568	$HNCO(10_{3,8}-9_{3,7})$[a]	432.96	5.54	0.58[d]	54.68	8.94					
219.6568	$HNCO(10_{3,7}-9_{3,6})$[a]	432.96									
219.7339	$HNCO(10_{2,9}-9_{2,8})$[a,b]	228.28	5.30	1.29	56.32	3.85	✓				
219.7372	$HNCO(10_{2,8}-9_{2,7})$[a,b]	228.29	2.19	0.53	56.32	3.85	✓				
219.7982	$HNCO(10_{0,10}-9_{0,9})$	58.02	13.99	1.56	55.82	8.44	✓				
219.9085	$H_2{}^{13}CO(3_{1,2}-2_{1,1})$	15.56					✓				
219.9494	$SO(6_5-5_4)$	34.98	21.40	2.34	55.15	8.60	✓	14.61	1.45	36.18	9.48
220.0785	$CH_3OH(8_{0,8}-7_{1,6})$	96.61	22.74	2.34	55.22	9.13	✓				
220.1669	$CH_3OCHO(17_{4,13}-16_{4,12})E$	103.15					✓				
220.1903	$CH_3OCHO(17_{4,13}-16_{4,12})E$	103.15					✓				
220.3989	^{13}CO(2−1)	15.89	10.18	1.98	48.46	4.82	✓	12.74	3.20	41.69	3.74
220.5392	$CH_3CN(12_7-11_7)$	418.63	4.18	0.56[d]	55.65[b]	7.04[b]	✓				
220.5848	$HNCO(10_{1,9}-9_{1,8})$	101.5	5.42	0.94	54.63	5.44	✓				
220.5944	$CH_3CN(12_6-11_6)$	325.9	10.31	1.38	55.65[b]	7.04[b]	✓				
220.6410	$CH_3CN(12_5-11_5)$	247.4	9.63	1.28	55.65[b]	7.04[b]	✓				
220.6792	$CH_3CN(12_4-11_4)$	183.15	11.74	1.57	55.65[b]	7.04[b]	✓				
220.7090	$CH_3CN(12_3-11_3)$	133.16	16.11	2.15	55.65[b]	7.04[b]	✓				
220.7302	$CH_3CN(12_2-11_2)$	97.44	15.95	2.13	55.65[b]	7.04[b]	✓				
220.7430	$CH_3CN(12_1-11_1)$	76.01	16.72	2.23	55.65[b]	7.04[b]	✓				
220.7472	$CH_3CN(12_0-11_0)$	68.87	17.12	2.28	55.65[b]	7.04[b]	✓				
220.8934	$CH_3OCH_3(23_{4,20}-23_{3,21})$[c]	274.44					✓				

Table 3.6: Continued.

			W33 B				W33 A	W33 Main			
ν_0 (GHz)	Transition	E_u (K)	F_{Int} (K km s^{-1})	F_{Peak} (K)	$v_{central}$ (km s^{-1})	FWHM (km s^{-1})		F_{Int} (K km s^{-1})	F_{Peak} (K)	$v_{central}$ (km s^{-1})	FWHM (km s^{-1})
221.1984	$CH_3OCH_3(27_{5,22}-27_{4,23})$[c]	257.14					✓				
229.4050	$CH_3OCHO(18_{3,15}-17_{3,14})$	110.74					✓				
229.4203	$CH_3OCHO(18_{3,15}-17_{3,14})$	110.74					✓				
229.5891	$CH_3OH(15_{4,11}-16_{3,13})$	374.44	21.97	2.40	54.87	8.61	✓				
229.7588	$CH_3OH(8_{-1,8}-7_{0,7})$	89.10	21.57	3.06	55.8	6.62	✓	15.01	2.95	37.67	4.78
229.8641	$CH_3OH(19_{5,15}-20_{4,16})$	578.60					✓				
229.9392	$CH_3OH(19_{5,14}-20_{4,17})$	578.60					✓				
230.0270	$CH_3OH(3_{-2,2}-4_{-1,4})$	39.83	17.40	2.19	57.01	7.46	✓				
230.1414	$CH_3OCH_3(25_{4,22}-25_{3,22})$	319.21					✓				
230.2338	$CH_3OCH_3(17_{2,15}-16_{3,14})$	147.65					✓				
230.3682	$CH_3OCH_3(28_{5,23}-27_{6,22})$	406.35					✓				
230.5380	$^{12}CO(2-1)$	16.60	45.09	6.21	46.31	6.82	✓	18.62	7.95	42.98	2.20
231.0610	OCS(19−18)	110.90	14.26	2.33	55.82	5.76	✓				
231.2210	$^{13}CS(5-4)$	33.29	13.55	1.78	54.81	7.16	✓			*	
231.2811	$CH_3OH(10_{2,9}-9_{3,6})$	165.35	16.79	1.70	54.67	9.30	✓				
231.9009	H30α							83.80	3.19	32.91	24.65
231.9879	$CH_3OCH_3(13_{0,13}-12_{1,12})$	80.92	12.04	1.93	54.72	5.87					
232.4186	$CH_3OH(10_{2,8}-9_{3,7})$	165.40	20.10	3.12	55.86	6.05					
232.7836	$CH_3OH(18_{3,16}-17_{4,13})$	446.53	12.13	2.32	56.07	4.92					

Notes. [(*)] Emission detected in map but not in the spectrum at the center of the core. [(a)] Blended transitions. [(b)] Spectral lines fitted with same central velocity and FWHM. [(c)] Only in frequency range of W33 A. [(d)] Weak transition ($< 3\sigma$), detected with Weeds (see Sect. 3.8).

4 The Ultracompact H II Region in W33 Main

4.1 Motivation

W33 is a well-known Galactic source of radio emission. First radio continuum observations of the W33 complex date back to 1958 (Westerhout 1958). These low resolution observations at 1390 MHz show a large H II region with strong emission at W33 Main but extended emission spreading out to W33 B and W33 A. To detect more compact emission from smaller compact or ultracompact (UC) H II regions, observations with higher spatial resolution and sensitivity had to be conducted. Observations from the Coordinated Radio 'N' Infrared Survey for High-Mass Star Formation (CORNISH, Hoare et al. 2012) at 5 GHz with a resolution of 1″ show extended continuum emission with multiple peaks in the W33 Main cloud. The strongest emission, from a compact H II region, is detected towards the dust core of W33 Main-Central (Fig. 4.1, see Chapter 3). Since the emission of an UC H II region becomes optically thin at higher frequencies than the emission of a compact H II region and that of a hypercompact H II region at even higher frequencies (e.g. Kurtz 2005, see Chapter 1), radio continuum observations have to be conducted at high frequencies to detect emission of UC or HC H II regions. This chapter describes a search for HC and UC H II regions in W33 Main which pinpoint the locations of very recently formed high-mass stars. We conducted K band radio continuum observations of W33 Main with the Karl G. Jansky Very Large Array (JVLA). In addition, H_2O, CH_3OH, and NH_3 lines were observed.

This chapter is structured as follows. In Sect. 4.2, the observations and the data reduction are described. The results of the continuum and line observations are presented in Sect. 4.3. In Sect. 4.4, we determine the physical properties of the radio emission and discuss the obtained results. Section 4.5 draws a multi-wavelength picture of W33 Main from infrared to radio wavelengths. Section 4.6 summarizes the results.

Figure 4.1: 5 GHz radio continuum emission of W33 Main from the CORNISH survey. The contours show the 230 GHz dust emission with contour levels starting at 3σ in steps of 5σ (1σ = 70 mJy beam^{-1}). A scale of 0.1 pc is indicated in the upper left corner.

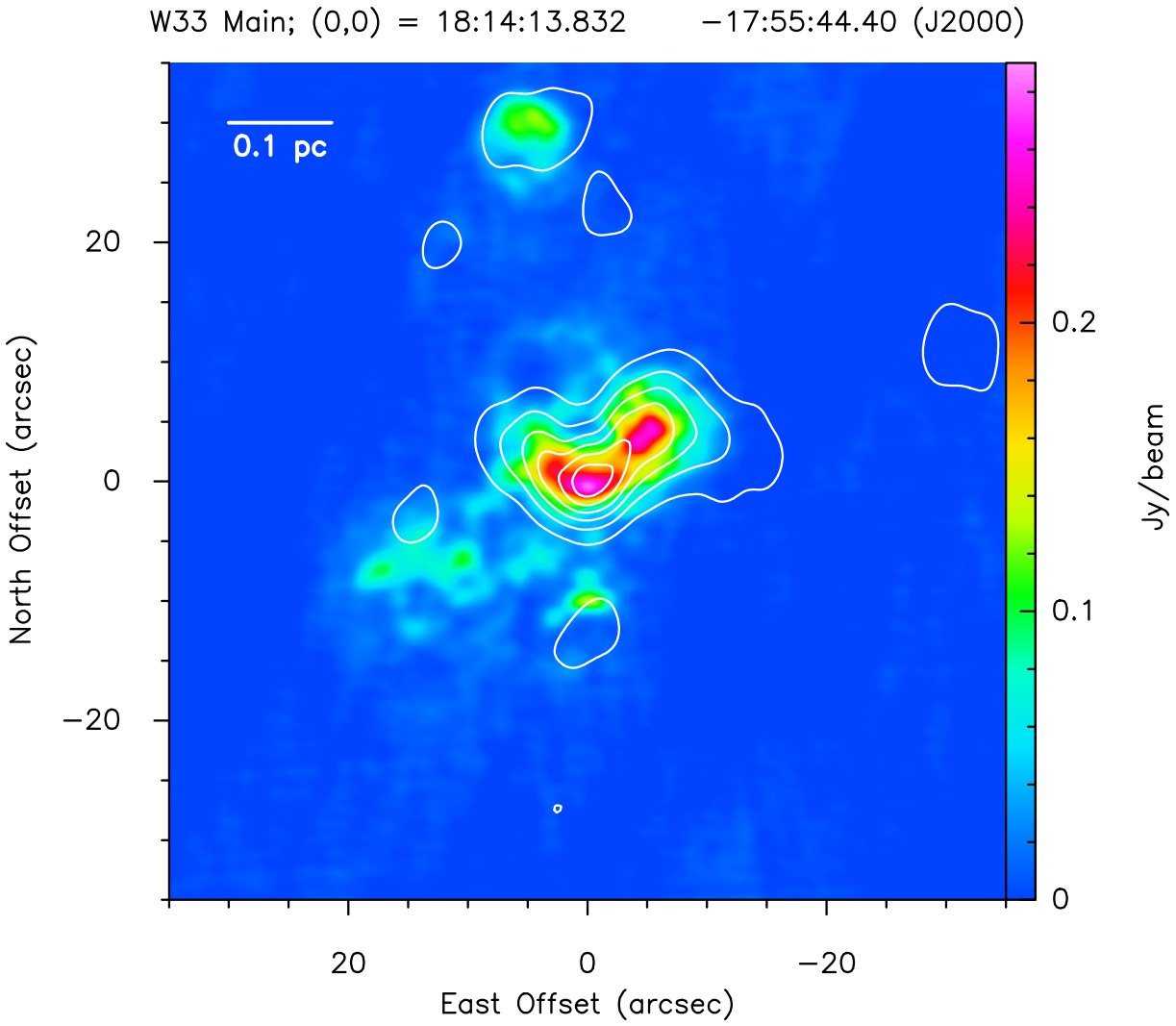

Table 4.1: Coordinates and observing times for W33 Main and calibrators.

Source	RA (hh mm ss.sss)	Dec (dd ′ ″.′″)	t_{Cont} (min)	t_{H_2O} (min)	t_{CH_3OH} (min)	t_{NH_3} (min)	Remarks
J1310+3220	13 10 28.664	+32 20 43.78	11	1	1	1	
3C286	13 31 08.288	+30 30 32.96	3	3	3	3	Flux-Calibrator, Bandpass-Calibrator
J1825−1718	18 25 36.536	−17 18 49.95	35	6	6	14	Phase-Calibrator
W33 Main	18 14 13.720	−17 55 43.60	41	12	12	36	Target

Table 4.2: Observing setups.

Setup	ν_{rest} (GHz)	spw	BW/spw (MHz)	channel/spw	Δv (km s^{-1})	rms (mJy beam^{-1})
Continuum	19−20 & 24−25	16	128	64	–	0.7 (19.5 GHz), 1.2 (24.5 GHz)
H_2O	22.24	1	16	1024	0.21	7
CH_3OH	24.93	1	16	1024	0.19	8
NH_3	23.40−25.00	8	16	256	0.79	3

4.2 Observation and Data Reduction

In July and August 2011, we observed continuum and line emission from the molecular cloud W33 Main in the K band with the JVLA in the most extended (A) configuration. The full width at half maximum of the primary beam at 22 GHz is 2′. Radio continuum and spectral line emission from the H_2O, CH_3OH, and NH_3 molecules was recorded with three different observation setups. The calibrators J130+3220, 3C286, and J1825−1718 were observed for flux, bandpass, and phase calibration. The positions (Cols. 2, 3) of the observed sources (target and calibrators) and the observing times per setup (Cols. 4, 5, 6, 7) are listed in Table 4.1.

The continuum setup consists of 16 spectral windows (spw) with 64 channels each, covering a frequency range of 19−20 and 24−25 GHz. The bandwidth of each spectral window is 128 MHz. The observations are conducted in full polarization mode.

The H_2O $J_{K_a,K_c} = 6_{1,6}-5_{2,3}$ transition (rest frequency 22.23508 GHz) and the CH_3OH $2_{2,0}-2_{2,1}$, $3_{2,1}-3_{1,2}$, and $4_{2,2}-4_{1,3}$ lines (rest frequencies 24.93438, 24.92871, and 24.93347 GHz) are each observed in one spectral window (spw 0: H_2O, spw 1: CH_3OH) with 1024 channels, respectively. The NH_3 emission is recorded in eight spectral windows (spw 2−9) with 256 channels, covering a frequency range of 23.4 to 25.0 GHz. The $J, K = (1,1)$, $(2,2)$, $(3,3)$, $(4,4)$, $(5,5)$, and $(6,6)$ inversion transitions (rest frequencies 23.69447, 23.7226, 23.87008, 24.13935, 24.53292, and 25.05596 GHz) are located within the spectral windows 3, 4, 5, 6, 8, and 9. The bandwidth of

each of the 10 spectral windows is 16 MHz. The observations are conducted in dual polarization mode. The four different observing setups are summarized in Table 4.2. The first two columns list the different setups and the rest frequencies. Cols. 3, 4, and 5 show the number of spws, the bandwidth (BW) per spw, and the number of channels per spw. In the last two columns, the spectral resolution and the rms of the data cubes are listed.

The data reduction of both the continuum and the line data sets has been carried out with the JVLA pipeline (version 1.2.0, March 27 2013), which runs a set of python scripts within the CASA software. The pipeline[1] performs basic "flagging" (i.e., compromised data recognition and removal) and calibration steps. For the continuum data set, we applied Hanning smoothing at the beginning of the pipeline. For the line data set, we first separated the data for each spectral line (spw 0, spw 1, spw 2−9) with the CASA task *split* and then run the pipeline on each line data set.

The continuum data set was imaged with the CASA task *clean* with the number of Taylor terms (*nterms*) for the modeling of the frequency dependence of the sky emission set to 2. One of the images produced by the cleaning task is a spectral index map. To improve the signal-to-noise ratio, we selfcalibrated the continuum image. The synthesized beam of the selfcalibrated image is 0.64″ x 0.19″.

Due to the high level of the continuum emission, the H_2O, CH_3OH, and NH_3 lines were hidden in the broad continuum in the spectra of the line data cubes. Thus, we first made dirty maps of the three lines to determine the channels with line emission. No NH_3 emission was detected in the dirty images. The line-free channels of the H_2O and CH_3OH data cubes were fitted with a flat baseline to determine the continuum contribution which was then subtracted from the data cube to construct continuum-free line databases.

For NH_3, we defined the line channels within ±20 km s^{-1} of the rest velocity 36 km s^{-1} for the different transitions. The "line-free" channels were then again fitted with a flat baseline and the so-determined continuum was subtracted from the line database.

The continuum-free line databases were imaged with the CASA task *clean*. The position of the maser spots of H_2O and CH_3OH were then determined with the interactive 2D fitting tool of the CASA viewer.

[1]for more information about the pipeline see `https://science.nrao.edu/facilities/vla/data-processing/pipeline`

4.3 Results

4.3.1 Continuum

The K band radio continuum emission at a central frequency of 22 GHz is plotted in the left panel of Fig. 4.2. The overlayed contours show the dust emission at 230 GHz from the SMA observations (see Chapter 3). Strong radio emission is observed at the center of W33 Main-Central. No radio emission is detected towards the other dust cores. The right panel in Fig. 4.2 focuses on the radio continuum emission in W33 Main-Central. The emission is extended and shaped like an arc, similar to cometary H II regions. The size of the arc is ~0.06 pc which classifies the H II region in W33 Main as an UC H II region. The continuum emission has a peak intensity of 0.11 Jy beam^{-1} and an integrated intensity of 1.74 Jy and covers an area of ~5.8 arcsec^2.

Figure 4.2: Left panel: K band radio continuum emission of W33 Main. The contours show the 230 GHz dust continuum emission of W33 Main (see Chapter 3, contour levels the same as in Fig. 4.1). The strongest radio emission is seen at the center of the dust core W33 Main-Central. No radio emission is detected towards the other dust cores. Right panel: Zoom on the strongest emission in W33 Main-Central. The diameter of the H II region is about 0.06 pc, similar to typical extensions of UC H II regions. The bar in the upper part of the image presents a scale of 0.1 pc. The synthesized beam is shown in the lower left corner.

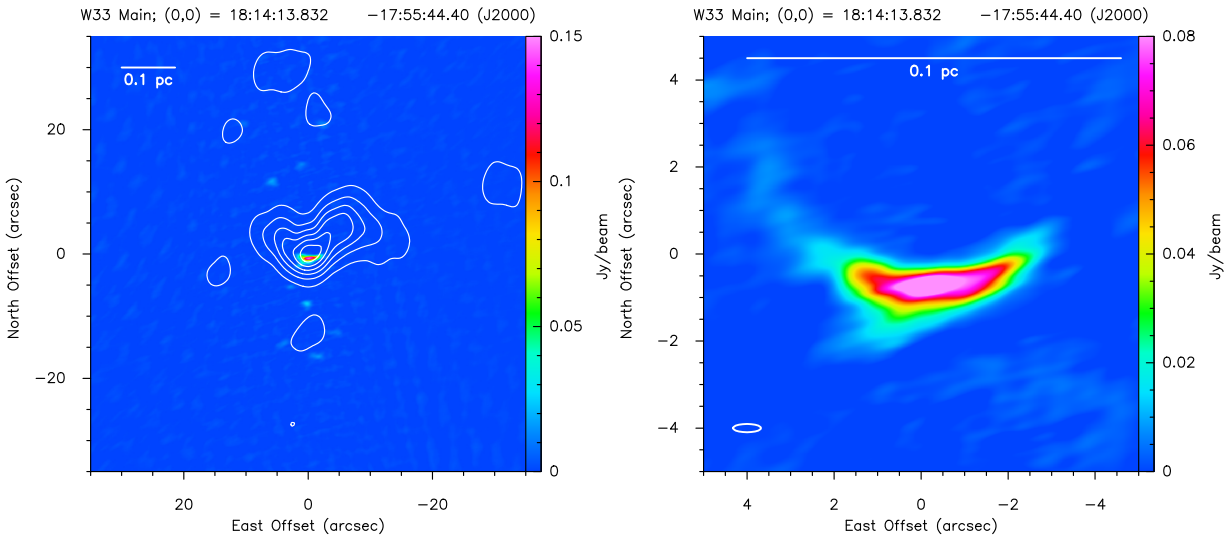

Since we have radio continuum observations in two different frequency ranges, we can determine the spectral index between 19−20 and 24−25 GHz which is plotted in Fig. 4.3. At the

peak of the radio continuum emission, the spectral index is close to 0, indicating optically thin emission. Closer to the edges of the H II region, the spectral index ranges between −2 and 2.

4.3.2 Masers

H_2O The spectrum of the H_2O emission covers a velocity range of −5−36 km s^{-1} (Fig. 4.4). H_2O maser spots are plotted in Fig. 4.5, overlayed on the C^{18}O emission of W33 Main (see Chapter 3). H_2O maser emission at velocities of ∼33 km s^{-1} are spread over an area of 40″ x 90″, along the north-south oriented outflow in W33 Main. Two maser spot groups at velocities around 20 km s^{-1} are located within the 230 GHz dust emission of W33 Main-Central and one group in W33 Main-North. Another group of maser spots is detected at velocities of ∼−2 km s^{-1} in W33 Main-North as well as west of W33 Main-Central. The maser spots at 34 km s^{-1}, located at the north-eastern edge of W33 Main-Central, and at −2 km s^{-1} in W33 Main-North were previously detected by Immer et al. (2013) with the Very Long Baseline Array (see Chapter 2).

CH_3OH The CH_3OH maser emission at 25 GHz is pumped by collisions (Class I methanol maser, Menten 1991). We observe maser emission from the $4_{2,2}$−$4_{1,3}$ transition at 33 km s^{-1}. The maser line has a FWHM of ∼0.8 km s^{-1} and a peak flux of 1.2 Jy. CH_3OH emission from the $2_{2,0}$−$2_{2,1}$ and $3_{2,1}$−$3_{1,2}$ transitions was not detected. The position of the maser is $\alpha = 18^h14^m10^s.9$ and $\delta = -17°55'58.91''$, in remarkable agreement (within 3″) with the Effelsberg observations of Menten et al. (1986). Fig. 4.6 shows a map of the single CH_3OH maser spots in relation to the 230 GHz dust emission of W33 Main. Comparing the position of the methanol maser with the dust emission or the C^{18}O in W33 Main, we conclude that the methanol maser is located offset from the dust cores or the north-south oriented outflow. No water maser emission was detected at the position of the methanol maser. The closest water maser spot is located 15″ north of the methanol maser. Since this methanol maser is offset from emission at other wavelengths, it is not clear what powers this maser.

NH_3 No NH_3 emission was detected in the clean images from any of the transitions. The NH_3 emission is either destroyed by photo-dissociation in the vicinity of the H II region or the emission is not compact enough and thus resolved out in our the observations. Since Wilson et al. (1982) and Keto & Ho (1989) detected emission of the $(J, K) = (3, 3)$ and (1, 1) inversion lines towards W33 Main with the Effelsberg 100 m telescope and the Very Large Array in D configuration, respectively, it is more likely that missing short spacings in our observations prevent the detection of the widespread ammonia emission.

Figure 4.3: Spectral index of the K band radio continuum emission.

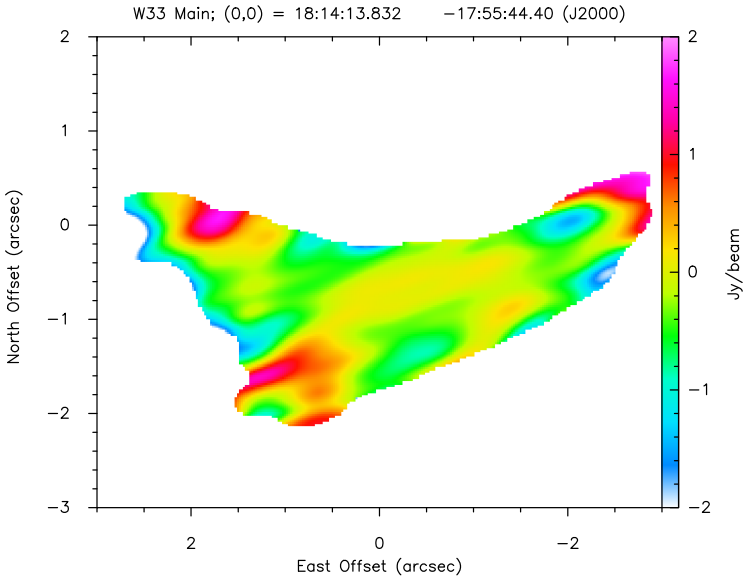

Figure 4.4: Continuum-subtracted spectrum of the H_2O emission (obtained with the CASA task *plotms*). Maser lines are detected at velocities of ∼34, 20−30, and ∼−5 km s^{-1}.

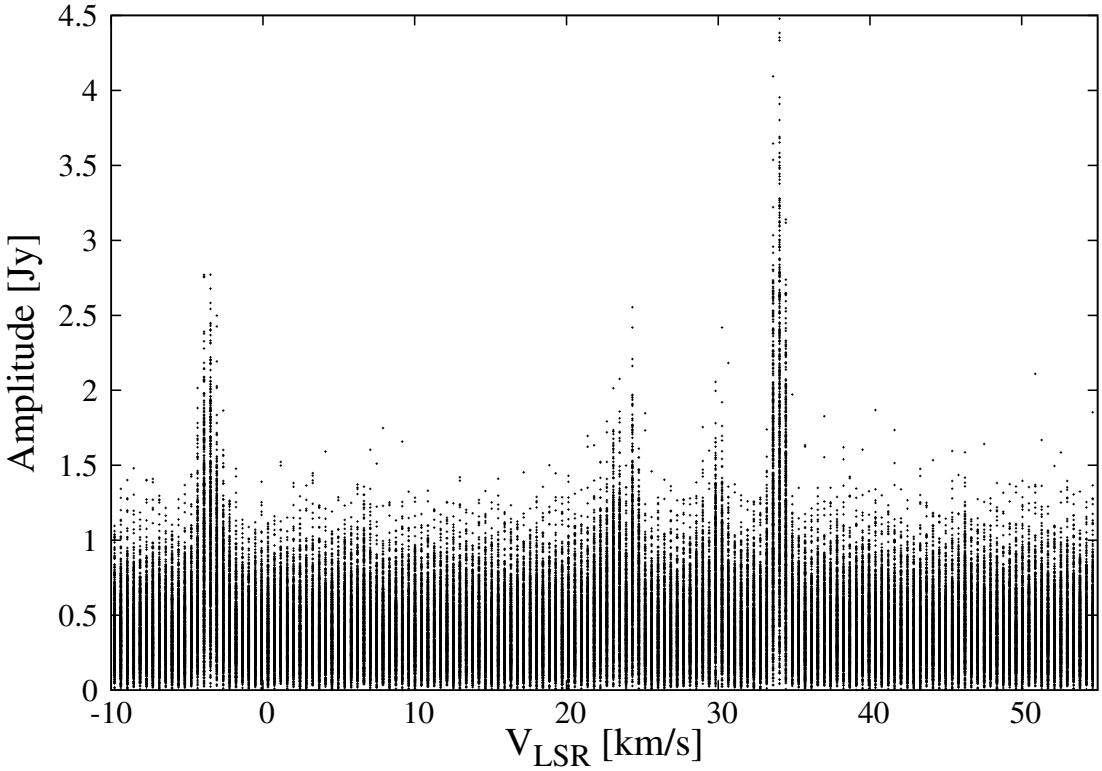

Figure 4.5: Map of the H_2O maser spots. The background shows the $C^{18}O$ emission of W33 Main from a combination of SMA and IRAM observations. The contours present the 230 GHz dust emission of W33 Main (same contour levels as in Fig. 4.1).

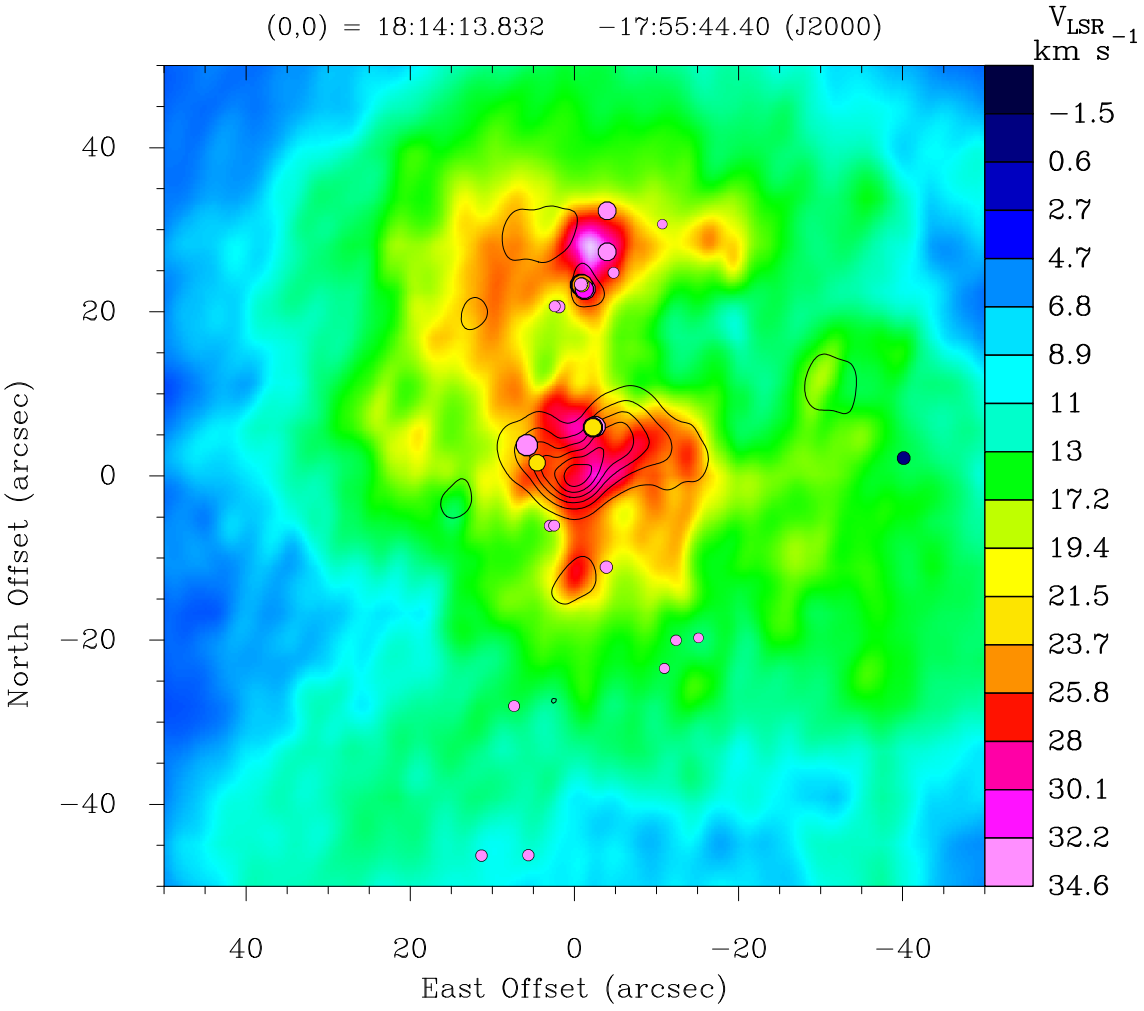

Figure 4.6: Map of the CH_3OH maser spots. The background shows the $C^{18}O$ emission of W33 Main from a combination of SMA and IRAM observations. The contours present the 230 GHz dust emission of W33 Main (same contour levels as in Fig. 4.1).

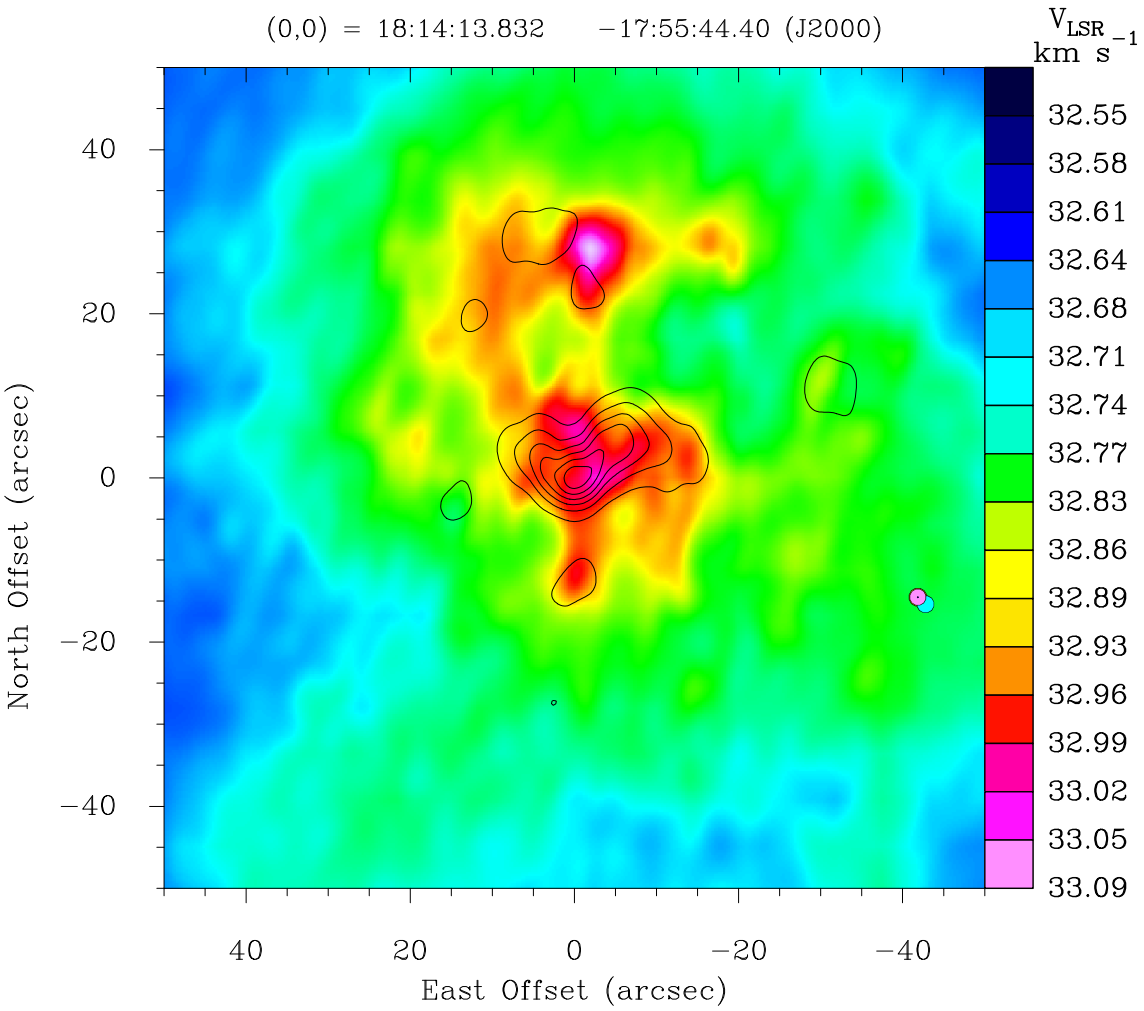

4.4 Discussion

Figure 4.7: K band radio continuum emission of W33 Main. The contours show the 5 GHz radio emission from the CORNISH survey (levels starting at 3σ in steps of 5σ to 0.1 Jy beam^{-1}, then in steps of 10σ, 1σ = 3.7 mJy beam^{-1}).

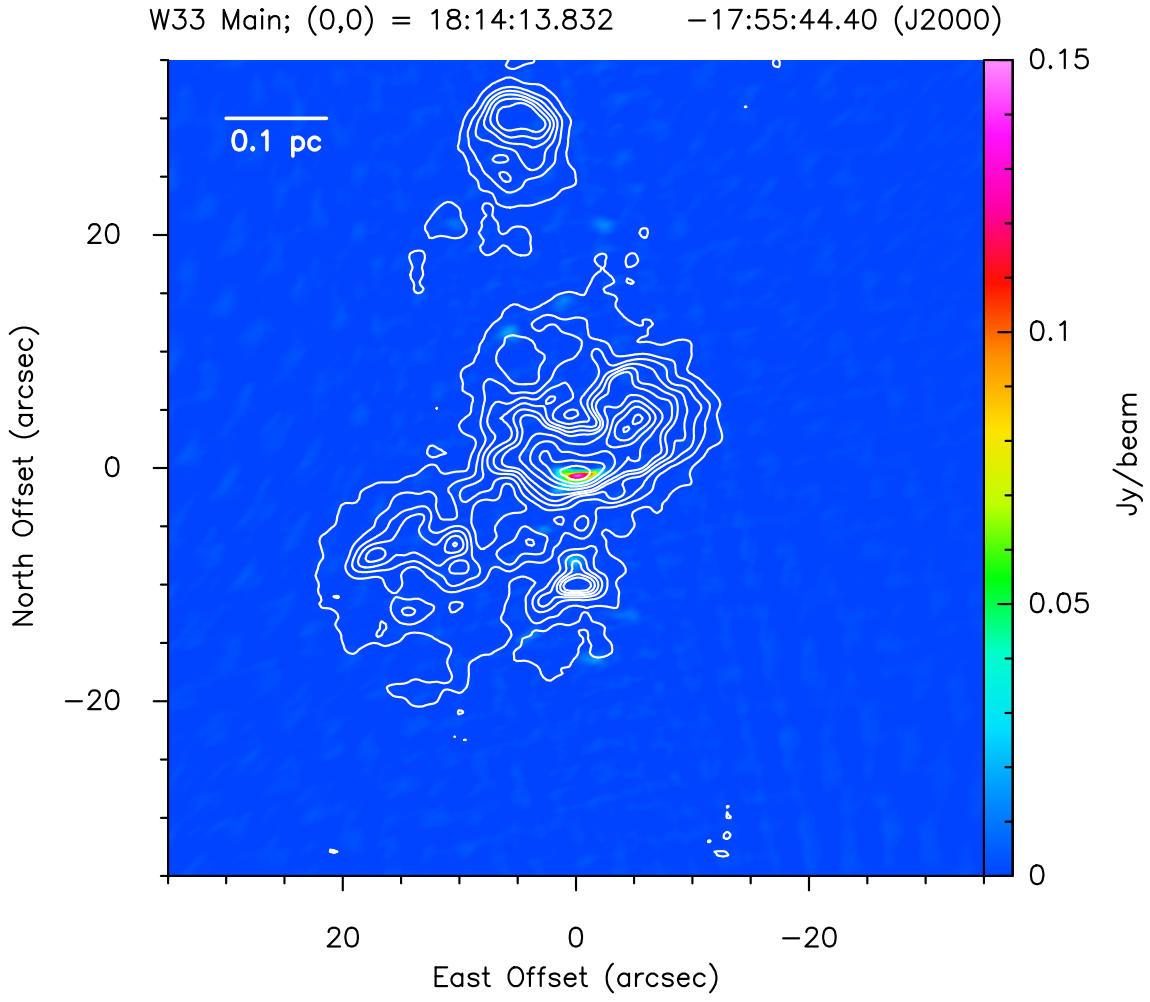

The detection of strong radio emission in the W33 Main star forming region indicates that the central star has already evolved to a state in which its energy is high enough to cause the ionization of the surrounding material. However, the H II region in W33 Main is still very compact with a size of less than 0.06 pc in diameter. This H II region is probably powered by only one or a few stars. Assuming that the H II region is excited by a single star already on the zero-age main sequence (ZAMS), we can determine its spectral type by first estimating the emission measure and the electron density of the H II region. For an optically thin, spherically symmetric H II

region, the emission measure EM is given by

$$EM = 5.638 \cdot 10^4 \left(\frac{S}{\mathrm{Jy}}\right)\left(\frac{T}{10^4\ \mathrm{K}}\right) b(\nu, T) \left(\frac{\Theta_R}{'}\right)^{-2} \mathrm{cm}^{-6}\ \mathrm{pc} \tag{4.1}$$

(Panagia & Walmsley 1978), where S is the flux density, T the electron temperature, ν the frequency of the radio observations, Θ_R the angular radius of the H II region in arcminutes, and

$$b(\nu, T) = 1 + 0.3195 \cdot \log\left(\frac{T}{10^4\ \mathrm{K}}\right) - 0.213 \cdot \log\left(\frac{\nu}{1\ \mathrm{GHz}}\right).$$

Although the H II region in W33 Main-Central is not spherically symmetric, we will translate the area of the emission to an effective angular radius to obtain an estimate of the emission measure. The area of the emission at the central frequency of 22 GHz is 5.8 arcsec^2, yielding an effective radius of 1.36″. Using a typical value for the electron temperature of 10^4 K and the flux density of the H II region of 1.74 Jy (at 22 GHz), we obtain an emission measure of $1.36 \cdot 10^8$ cm^{-6} pc. Panagia & Walmsley (1978) give a formula for the electron density

$$n_e = 3.113 \cdot 10^2 \left(\frac{S}{\mathrm{Jy}}\right)^{0.5} \left(\frac{T}{10^4\ \mathrm{K}}\right)^{0.25} \left(\frac{D}{\mathrm{kpc}}\right)^{-0.5} b(\nu, T)^{-0.5} \left(\frac{\Theta_R}{'}\right)^{-1.5} \mathrm{cm}^{-3}. \tag{4.2}$$

The distance D to W33 Main is 2.4 kpc (Immer et al. 2013). We estimate an electron density of $9.2 \cdot 10^4$ cm^{-3}. The number of Lyman photons N_Lyman which are needed to evoke the emission measure of the H II region and from which the spectral type of the star can be determined is given by

$$\left(\frac{N_\mathrm{Lyman}}{5 \cdot 10^{49}\ \mathrm{photon\ s^{-1}}}\right) = \left[\left(\frac{EM}{1.6 \cdot 10^6\ \mathrm{cm^{-6}\ pc}}\right)\left(\frac{n_e}{10^3\ \mathrm{cm^{-3}}}\right)^{-\frac{4}{3}}\right]^3 \tag{4.3}$$

(Tielens 2005). From the emission measure and the electron density, we estimate the number of Lyman continuum photons to $4.3 \cdot 10^{47}$ photons s^{-1}. Following Panagia (1973), we determine the spectral type of the dominating star in W33 Main-Central to be B0−O9.5. Combining the electron density and the number of Lyman photons, we estimate the mass of the ionized gas $\mathrm{M_{H\,II}}$ with

$$M_\mathrm{H\,II} \approx 80 \cdot \left(\frac{n_e}{10^3\ \mathrm{cm^{-3}}}\right)^{-1} \left(\frac{N_\mathrm{Lyman}}{5 \cdot 10^{49}\ \mathrm{photons\ s^{-1}}}\right) M_\odot \tag{4.4}$$

(Tielens 2005) to 0.008 $\mathrm{M_\odot}$. The values for electron density, emission measure, and ionized mass are consistent with typical values of UC H II regions (Bergin & Tafalla 2007, see Chapter 1).

Fig. 4.7 shows an overlay of the 5 GHz emission of the CORNISH survey in contours on the 22 GHz radio continuum emission (background). While the 5 GHz emission coincides with the 22 GHz emission at the center of W33 Main, the 5 GHz emission shows several more peaks in the W33 Main cloud, especially to the north and the south-east of W33 Main-Central. Apparently, our continuum observations only pick up the strongest and most compact radio emission in the region. Since the above determined parameters depend on the measured radio flux density, missing flux due to missing short spacings will lead to a lower limit of these parameters. Thus, our observations have to be combined with single-dish observations or interferometer observations with shorter baselines to recover the more diffuse radio emission and to better constrain the physical parameters of the UC H II region as well as the spectral type of the ionizing star.

4.5 A Multi-Wavelength View of W33 Main

Three strong infrared sources (W33M-IR1, W33M-IR2, W33M-IR3) are detected at the center of the W33 Main dust cloud with distances of 26″, 40″, and 28″ to each other (Fig. 4.8). The submillimeter emission of W33 Main-Central, detected with the SMA at 230 GHz, is located between W33M-IR2 and W33M-IR1. Although no infrared emission is detected at the center of the core, the western side of W33 Main-Central coincides with the strong emission of W33M-IR1. The dust emission of W33 Main-North is located close to W33M-IR3. However, no compact dust emission is observed towards W33M-IR2. Extended radio emission at 5 GHz from the CORNISH survey is detected between W33M-IR1 and W33M-IR2 (Fig. 4.9). The emission peaks at the 230 GHz dust continuum peak (Fig. 4.1). Another radio peak is observed towards W33 Main-South. At W33M-IR3, compact radio emission is detected.

4.6 Conclusions

We presented 19−25 GHz JVLA observations of the W33 Main cloud in continuum and H_2O, CH_3OH, and NH_3 lines. Strong continuum emission is only detected towards the center of the W33 Main-Central dust core. Assuming that the emission is excited by a single ZAMS star, we estimated its spectral type to B0−O9.5. The determined emission measure, electron density, and mass of the ionized gas for the H II region in W33 Main are consistent with typical values of UC H II regions.

Water masers are detected in three different velocity groups: ∼−2, ∼20, and ∼33 km s^{-1}. The maser spots at ∼33 km s^{-1} are located along a north-south ridge, with many maser spots

Figure 4.8: 8 μm continuum emission of W33 Main from the *Spitzer*/GLIMPSE survey. Three strong sources are clearly visible (W33M-IR1, W33M-IR2, W33M-IR3). Overlayed in contours is the 230 GHz dust continuum emission, observed with the SMA (contour levels the same as in Fig. 4.1). A scale of 0.1 pc is indicated in the upper left corner. The plus signs show the positions of the two water maser spot groups at 36 km s^{-1} and −2 km s^{-1} from Immer et al. (2013) and our water maser observations. The asterisk marks the position of the Class I methanol maser at 25 GHz.

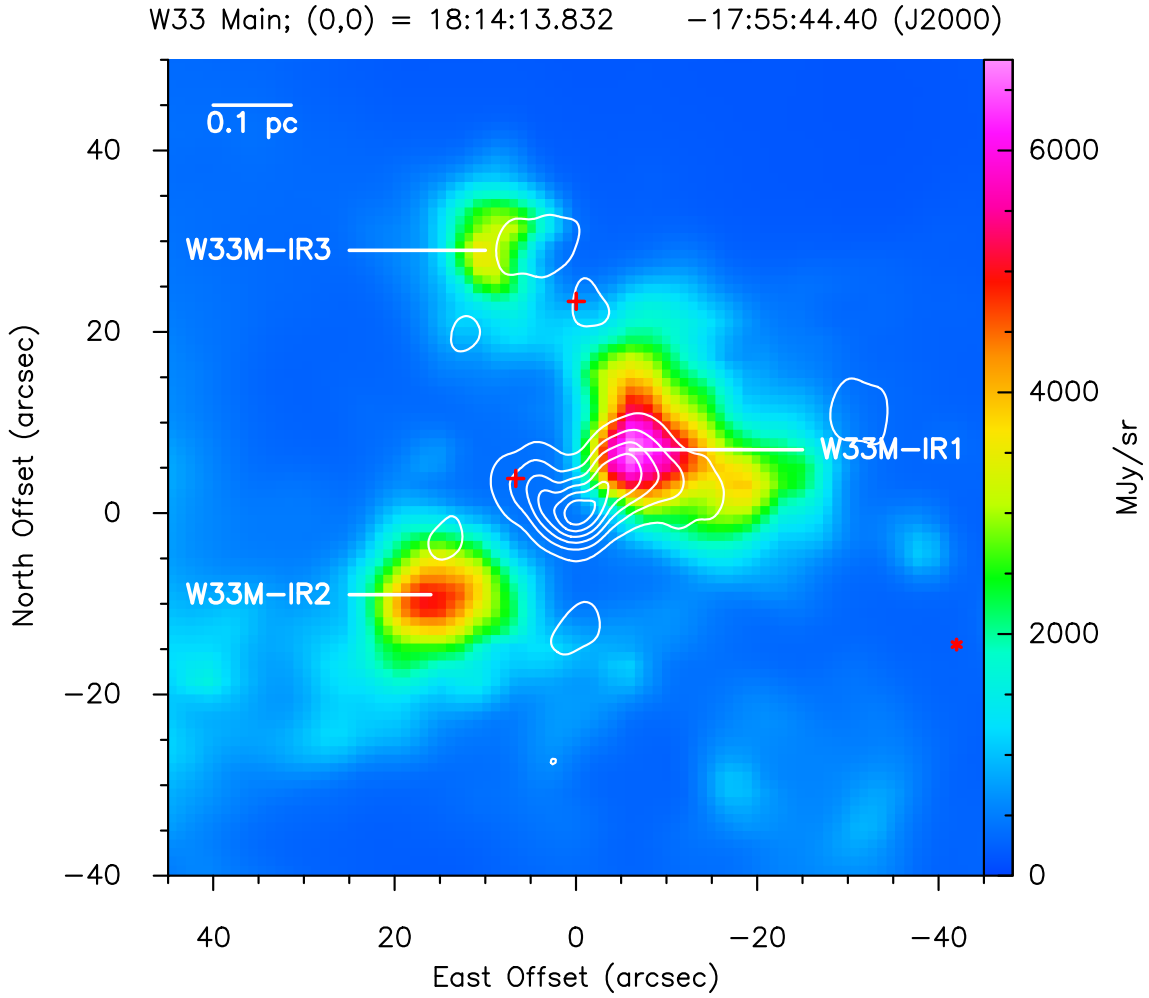

Figure 4.9: 8 μm continuum emission of W33 Main from the *Spitzer*/GLIMPSE survey. The contours show the 5 GHz radio emission from the CORNISH survey (contour levels the same as in Fig. 4.7). A scale of 0.1 pc is indicated in the upper left corner. The plus signs show the positions of the two water maser spot groups at 36 km s^{-1} and −2 km s^{-1} from Immer et al. (2013) and our water maser observations. The asterisk marks the position of the Class I methanol maser at 25 GHz.

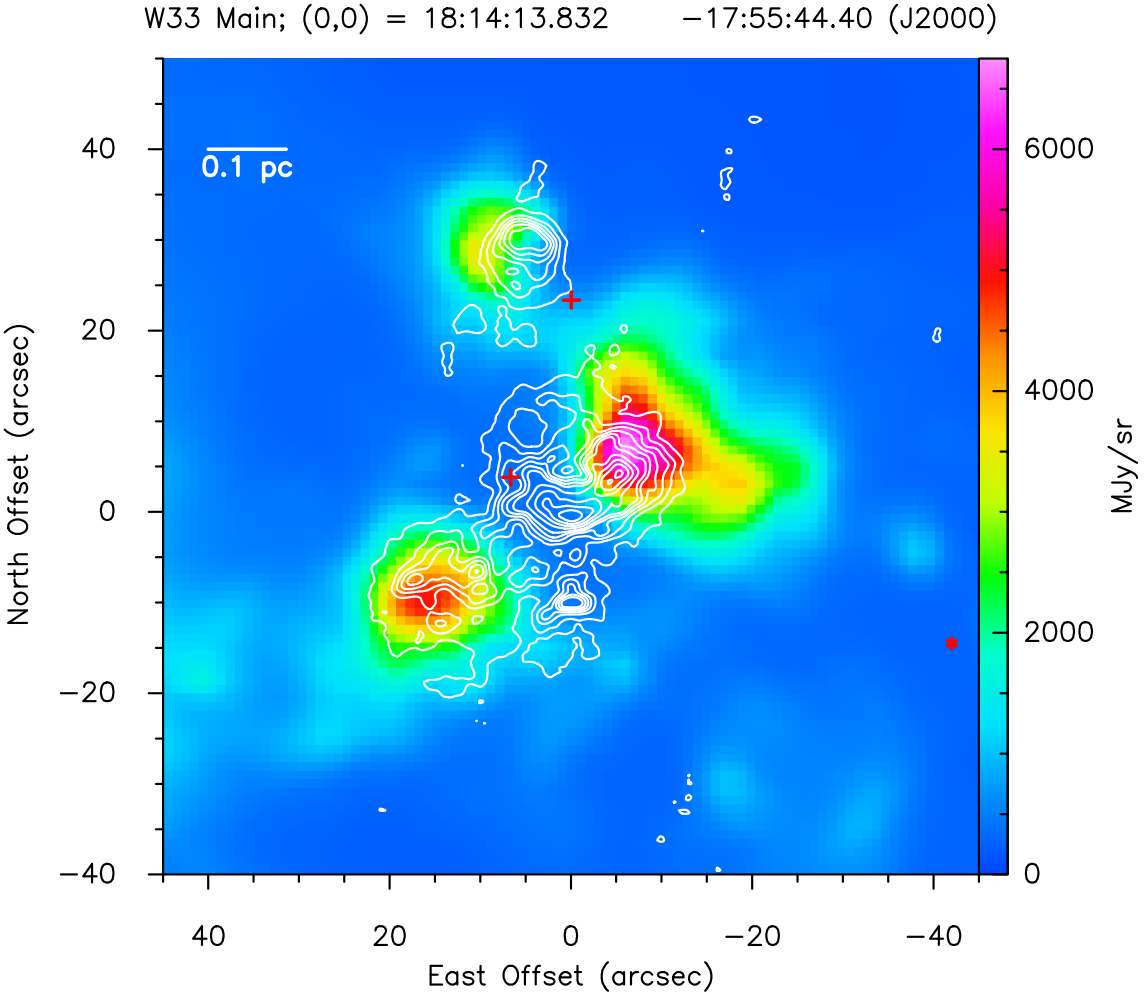

being detected in W33 Main-North. Two water maser spot groups at 20 km s^{-1} are observed in W33 Main-Central and one group in W33 Main-North. The masers at negative velocities are located in W33 Main-North and west of W33 Main-Central. The class I methanol maser at 25 GHz is detected south-west of W33 Main-Central. No NH_3 emission is observed towards W33 Main.

Radio continuum observations at 5 GHz with 10 times lower resolution show extended emission towards all three infrared sources that have been detected in W33 Main. Our radio continuum observations are only sensitive to the strongest and most compact emission which coincides with the peaks of the 5 GHz radio emission and the 230 GHz dust emission between the infrared sources W33M−IR1 and W33M−IR2.

5 The Cometary H II Regions of DR 21

5.1 Motivation

Wood & Churchwell (1989) sorted their UC H II regions into five different groups depending on their morphology: spherical or unresolved (43%), cometary (20%), irregular or multiple peaked (17%), core-halo (16%), and shell (4%). Walsh et al. (1998), who imaged a sample of ~180 *IRAS*-selected southern UC H II regions, classified most of their resolved sources as either cometary (43%) or irregular (40%). The highly-organized shape of cometary H II regions makes them favored targets for studying the morphology and kinematics of H II regions.

There are several models that propose how an H II region may develop a cometary shape. These models make different predictions for the velocity structure of the ionized gas (see Sect. 5.4). In the "blister" or "champagne flow" models (e.g. Israel 1978; Bodenheimer et al. 1979; Yorke et al. 1983), the ionized gas breaks into the diffuse intercloud medium at the edge of a molecular cloud or flows down a density gradient in the birth cloud of the star. The velocities of the ionized gas at the head of the cometary H II region are close to the systemic velocity of the neutral material. Down the tail, the velocities of the ionized gas increase due to the pressure difference along the density gradient. In the bow shock model, the new born star moves supersonically through the surrounding medium (e.g. Reid & Ho 1985; Mac Low et al. 1991; van Buren & Mac Low 1992). Here, the velocities of the ionized gas at the head are close to the velocity of the star. Down the tail, the ionized gas velocities converge to the systemic velocity. These opposed kinematic signatures allow to easily distinguish between the two models. In more recent works, the influence of a strong stellar wind is incorporated into the models (e.g. Gaume et al. 1994; Zhu et al. 2005; Arthur & Hoare 2006; Zhu et al. 2008). The stellar wind modifies the structure of the H II region by trapping it in a swept-up shell and forcing ionized flows in that

Figure 5.1: Upper left panel: 22 GHz continuum image of the two cometary H II regions in DR 21. The contour levels are 0.01, 0.02, 0.05, 0.1, 0.2, 0.5, and 1 Jy beam^{-1}, chosen to match the contour levels of Fig. 2 in Paper I as closely as possible. (The lowest contour level in Fig. 2 of Paper I is 0.02 Jy beam^{-1}.) Upper right and lower panel: Same as upper left panel. The boxes show the areas over which the emission was summed to generate the "long slit" and the "box" spectra in Figs. 5.4 and 5.10. The numbers in the boxes correspond to the position numbers in Tables 5.1 and 5.2, respectively. The 3.4″ (FWHM) synthesized beam is shown in the lower left corners. A scale of 0.1 pc is indicated by the horizontal line in the upper left corners.

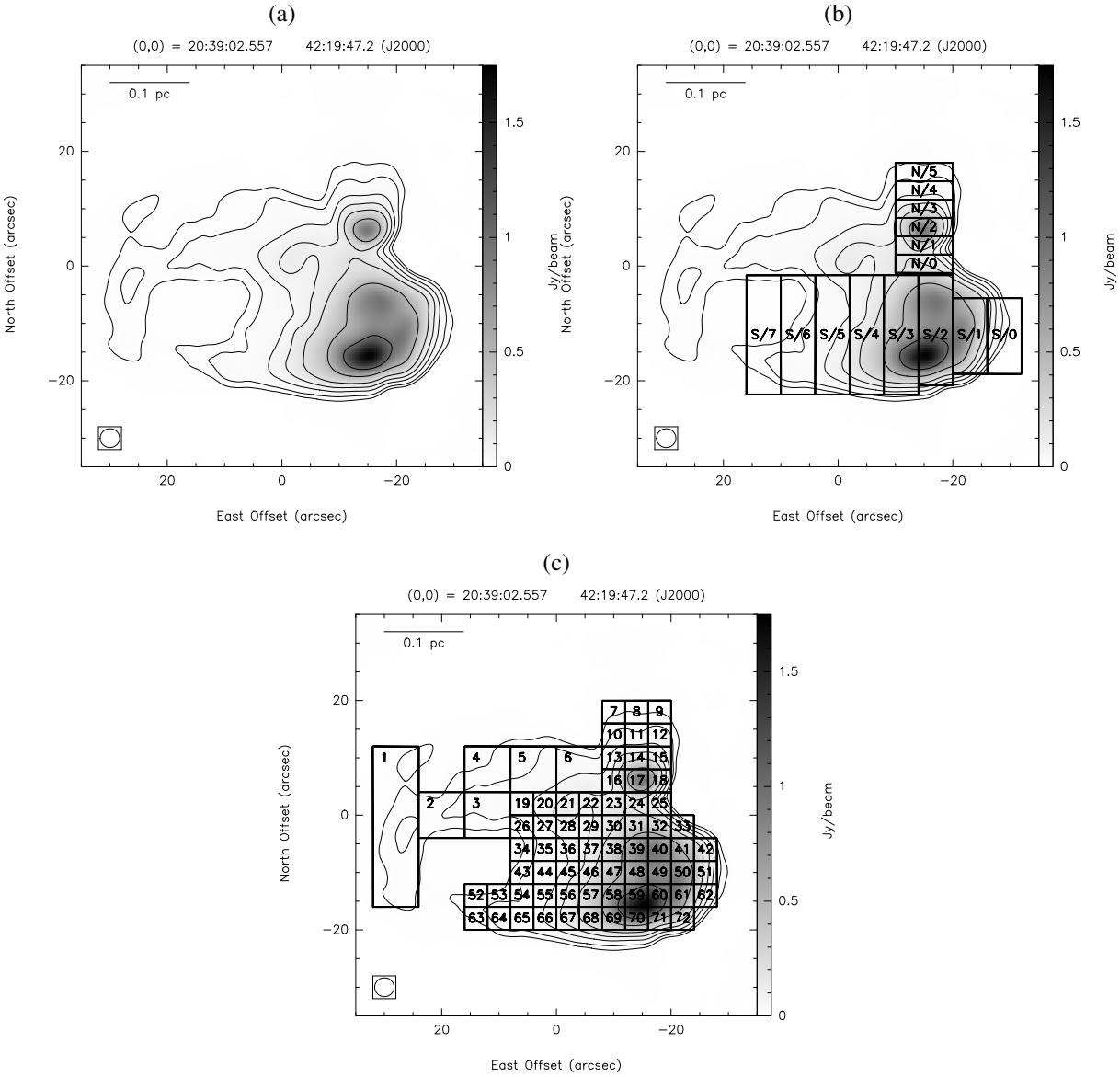

shell. Zhu et al. (2008) predict two velocity components along the line-of-sight in the presence of a stellar wind. The two components emanate from the near and far sides of the swept-up shell.

Cyganowski et al. (2003) (hereafter Paper I) observed the two cometary H II regions in DR 21 in NH_3 and the H53α and H66α radio recombination lines with the Very Large Array (VLA) to investigate whether the gas kinematics were consistent with bow shock or champagne flow models. They found supersonic velocity differences between the two cometary "heads", and between each "head" and the molecular gas, consistent with simple bow shock models. However, indications of increased ionized gas velocities (relative to systemic) towards the tail of the southern DR 21 H II region led the authors of Paper I to suggest a "hybrid" model, in which the ionized gas kinematics are bow-shock-like in the cometary head, and champagne-flow-like in the cometary tail (their Fig. 4). More sensitive hydrogen recombination line data were, however, required to probe the velocity field of the ionized gas further down the cometary tail and test the hybrid model. In this chapter, we present deep H66α observations of the cometary H II regions in DR 21, obtained with the VLA. These new data are ∼3 times more sensitive than the observations of Paper I, allowing us to detect emission further down the tail of the southern H II region.

This chapter is structured as follows: In Sect. 5.2, we describe the observations and we present the results in Sect. 5.3. In Sect. 5.4, we compare the results with existing models for cometary H II regions. Complementary observations at infrared and submillimeter wavelengths are presented in Sect. 5.5. Section 5.6 gives the conclusions of this chapter. The results presented in this chapter have been submitted as a paper to the A&A journal.

5.2 Observation and Data Reduction

On July 21 2004, DR 21 was observed in the hydrogen recombination line H66α (rest frequency 22364.17 MHz) using the Very Large Array (VLA)[1] in D configuration. At this frequency, the VLA had a primary beam size of ∼2′. The pointing center of the observations was $\alpha = 20^h39^m02^s.0$ and $\delta = +42°19'42.00''$ (J2000). The total observing time was 9 hr with an on-source integration time of approximately 6.3 hr. The primary flux calibrator was J1331+305; J2015+371 was observed as the phase calibrator and used for bandpass calibration. The derived flux density of J2015+371 was 2.92 Jy. The bandwidth of the observations was 12.5 MHz, divided into 32 channels, resulting in a spectral resolution of 390.625 kHz/channel (5.2 km s^{-1}/channel). The band center was set to an LSR velocity of −2.0 km s^{-1}. The full width at

[1]The National Radio Astronomy Observatory (NRAO) operates the VLA and is a facility of the National Science Foundation operated under agreement by the Associated Universities, Inc.

Figure 5.2: Individual channel maps of the H66α line emission, showing every channel between 40 and -39 km s^{-1}. The velocity of each channel is given in the upper left corner of each plot. The contour levels are at 3σ, 5σ, 10σ, 20σ, 50σ, 100σ, 200σ, and 500σ ($1\sigma = 0.7$ mJy beam^{-1}). The image shows the inner $(1')^2$ of the primary beam. The 3.4″ synthesized beam is indicated by the ellipse in the lower left corner of each channel map. A scale of 0.1 pc is shown in the lower right channel map. The (0,0) position is at $\alpha = 20^h39^m02^s.557$ and $\delta = +42°19'47.20''$ (J2000).

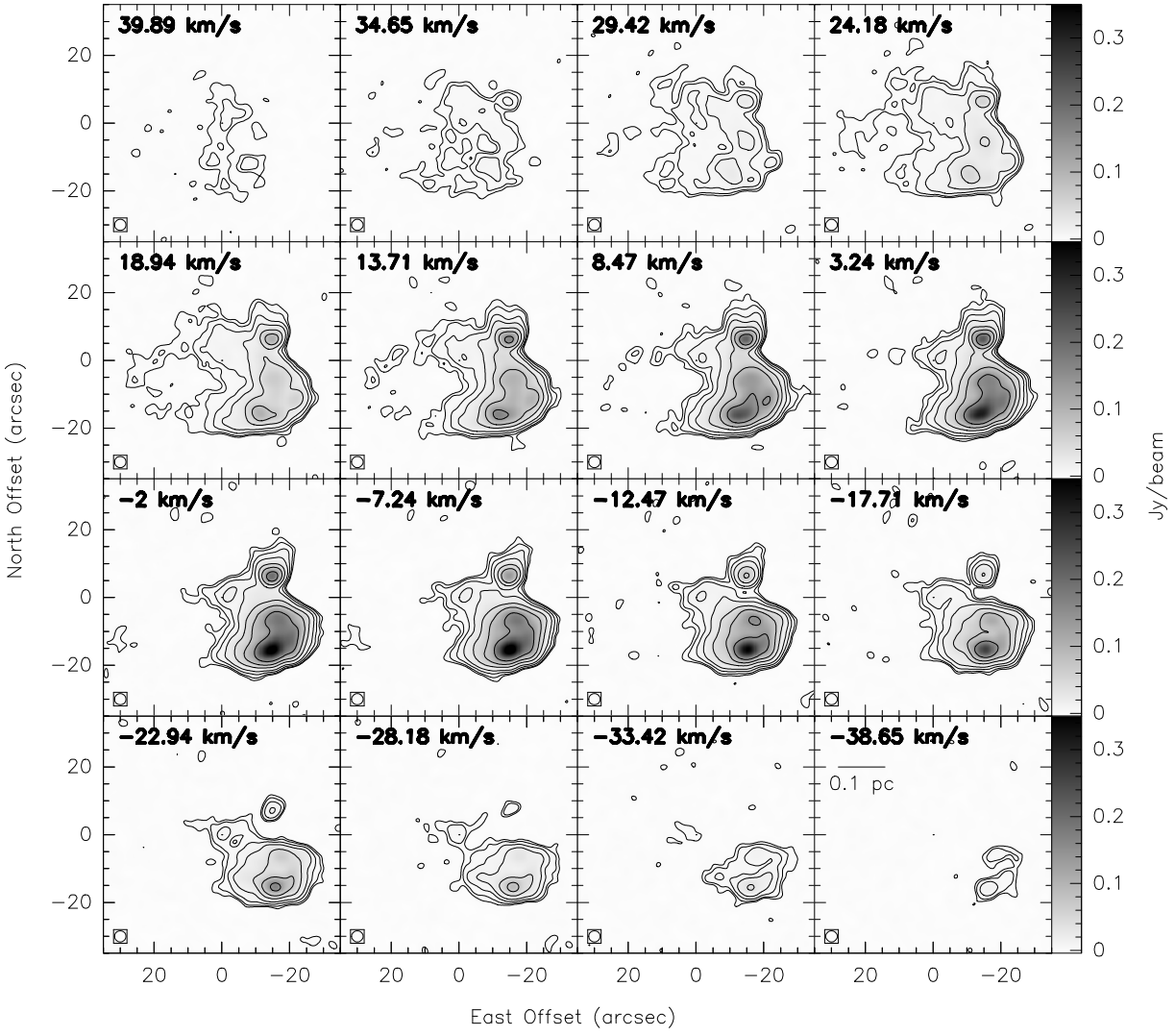

half maximum (FWHM) size of the synthesized beam was 3.4″ x 3.3″. Since our observations are only sensitive on angular scales of less than 60″, smoothly distributed emission at scales larger than ∼0.4 pc was resolved out.

The data reduction was conducted with the NRAO Astronomical Image Processing System (AIPS). After calibration and flagging bad data, we inspected the line data set for spectral channels with no or almost no line emission. Since the radio recombination line is very broad, only a small number of line-free channels were available for spectral baseline determination on the low- and high-frequency ends of the spectrum. The continuum in the line-free channels was fitted with a flat baseline which was then subtracted from the entire spectrum, yielding a continuum-free line database. Beside the continuum-free line database, a line-free continuum database was constructed from the baseline fit.

The continuum data were self-calibrated, and the solutions transferred to the line data. A *uv* taper was applied to baselines longer than 50 kλ to improve the signal-to-noise ratio and the data were weighted with an AIPS *robust* parameter of 0. The rms of the resulting continuum image is 1 mJy beam^{-1}, and of the line image cube 0.7 mJy beam^{-1} per channel. The higher continuum rms is due to the continuum image being dynamic-range limited, as opposed to thermal-noise limited. The continuum image does not reach the thermal noise level because of dynamic range limitations and the effects of poorly-represented large scale structure. The continuum peak is 1722 mJy beam^{-1}, corresponding to a dynamic range of > 1700 (compared to a peak of 395 mJy beam^{-1} and dynamic range of ∼560 for the H66α line image cube).

5.3 Velocity Structure of the DR 21 Cometary H II Regions

Our goal was to obtain more sensitive observations than those presented in Paper I, and in particular to probe the velocity structure of the ionized gas further down the cometary tails of both H II regions to distinguish between the different classes of models for cometary H II regions. As in Paper I, we resolve the two cometary H II regions in our continuum image (Fig. 5.1a), which we will refer to as "northern" (N) and "southern" (S). A comparison of our continuum image with that in Paper I (their Fig. 2) illustrates the increase in sensitivity. We detect continuum emission further down the tail of the southern H II region by about 0.14 pc which increases the east-west extent of the H II region by ∼50%. More emission was also recovered from the northern H II region where the north-south extent increased by about 0.04 pc (∼33%).

To study the general kinematics of the DR 21 H II regions, we made individual channel maps of the continuum-free emission of the H66α line (see Fig. 5.2), showing emission between

Table 5.1: Fitting results for the "long slit" spectra. The values obtained in Paper I are shown in the last three columns for comparison.

	Gauss 1			Gauss 2			Paper I		
Position	Amplitude (mJy)	Velocity (km s^{-1})	FWHM (km s^{-1})	Amplitude (mJy)	Velocity (km s^{-1})	FWHM (km s^{-1})	Amplitude (mJy)	Velocity (km s^{-1})	FWHM (km s^{-1})
S/0	23.8	4.8	19.2	22.3	−16.5	32.5			
S/1	612.6	−3.3	32.3				398	−2.6	30.9
S/2	1611.1	−2.9	31.6				1132	−2.5	30.9
S/3	1110.9	−0.5	32.2				770	−0.8	31.3
S/4	282.0	0.4	38.7				168	0.2	35.4
S/5	59.3	21.6	34.2	37.2	−10.1	28.2			
S/6	23.7	27.1	30.4						
S/7	14.3	26.3	22.3						
N/0	106.9	8.9	27.8						
N/1	145.4	6.5	26.9				145	5.9	23.9
N/2	280.1	4.9	27.6				186	5.1	26.7
N/3	92.6	4.2	30.4				38	4.1	29.3
N/4	24.1	5.5	32.7				9	−0.5	29.3
N/5	7.0	19.5	24.3	7.7	0.4	18.5			

± 40 km s^{-1}. The RRL emission from the northern H II region generally covers a smaller velocity range than that from the southern H II region. Emission from the northern H II region peaks at ∼3 km s^{-1}, while the emission of the southern H II region peaks at ∼−7 km s^{-1}. At high positive velocities the north-east part of the southern H II region is more prominent whereas its south-west part is more prominent at high negative velocities. As described in Paper I, the molecular gas in DR 21 − traced by NH_3 − shows only a small velocity dispersion with an average systemic velocity of ≈−1.5 km s^{-1}.

Since we detected more emission along the tail of both H II regions, we first extended the "long slit" analysis of Paper I to positions further down the tails of the two H II regions. We generated spectra by summing the emission over eight slits in the southern H II region and six slits in the northern H II region (for the positions of the slits, see Fig. 5.1b). For a better comparison with the results of Paper I, we chose similar sizes and positions for the slits S/1 to S/4 and N/1 to N/4 as in Paper I. Then, we added the slits S/0 (with the same size as S/1, 6″ x 13.2″) at the head of the southern H II region and S/5−S/8 (with the same size as S/4, 6″ x 20.8″) along the tail of the southern H II region. Similarly, we added slits N/0 (with the same size as N/1, 10″ x 3.2″) at the head of the northern H II region, and N/5 (with the same size as N/4, 10″ x 3.2″) at the end of the tail of the northern H II region. Each spectrum was fitted with a Gaussian line profile, yielding the amplitude, the central velocity, and the FWHM of the line. The spectra and the fitting results are shown in Fig. 5.3 and Table 5.1, respectively.

Our velocity results for the spectra at positions S/1−S/4 and N/1−N/3 are consistent with the

Figure 5.3: H66α spectra of the "long slits" (see Fig. 5.1b). The vertical line marks the systemic velocity of the molecular gas in DR 21, measured from NH_3 (-1.5 km s^{-1}). Positions S/0, S/5, and N/5 clearly show two velocity components.

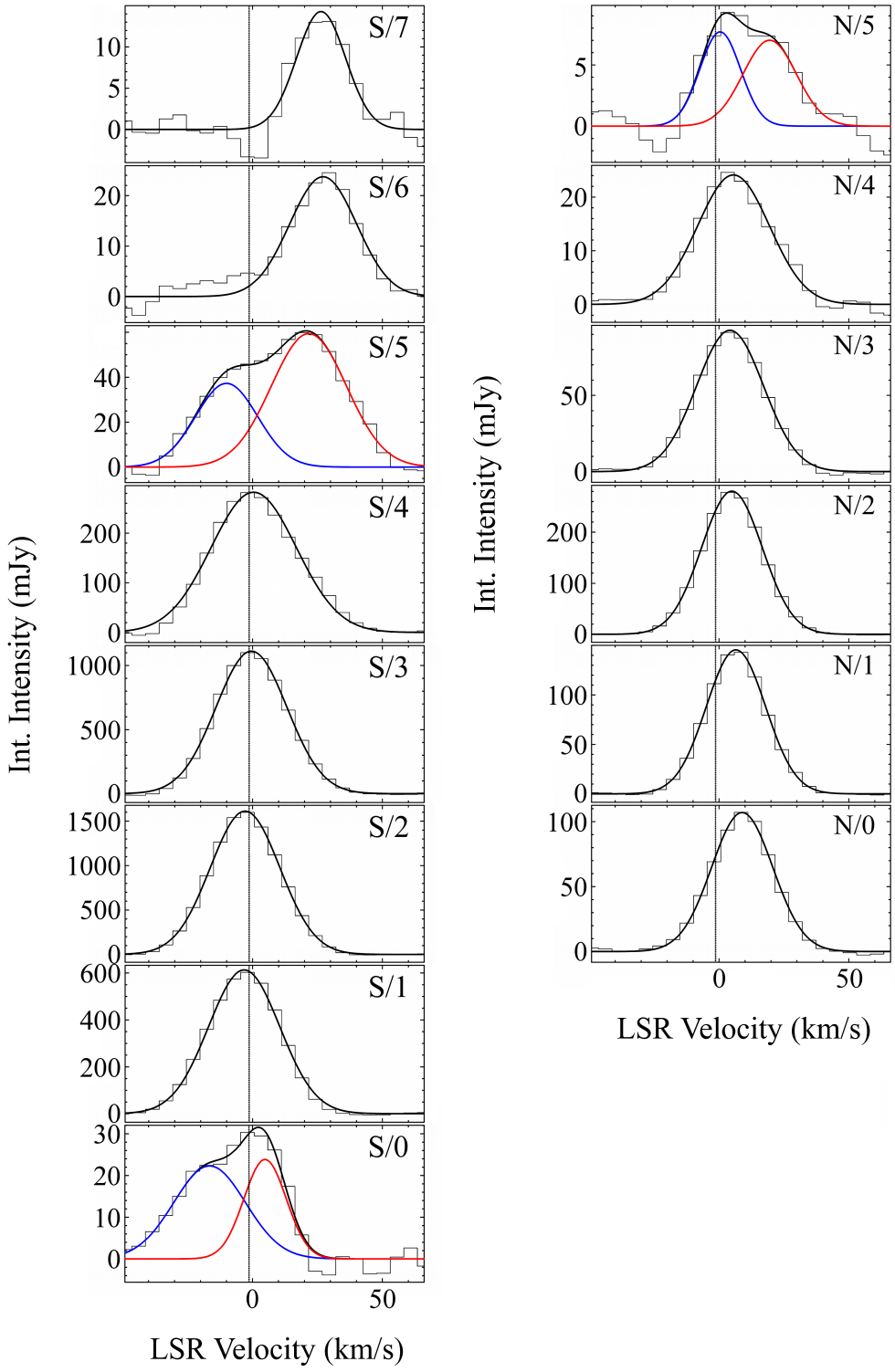

Figure 5.4: Example H66α spectrum (position 36). The red and the blue lines show the red- and blueshifted Gaussian fits, respectively. The dashed black line presents the sum of the two Gaussian fits. The vertical black line marks the systemic molecular gas velocity of -1.5 km s^{-1}.

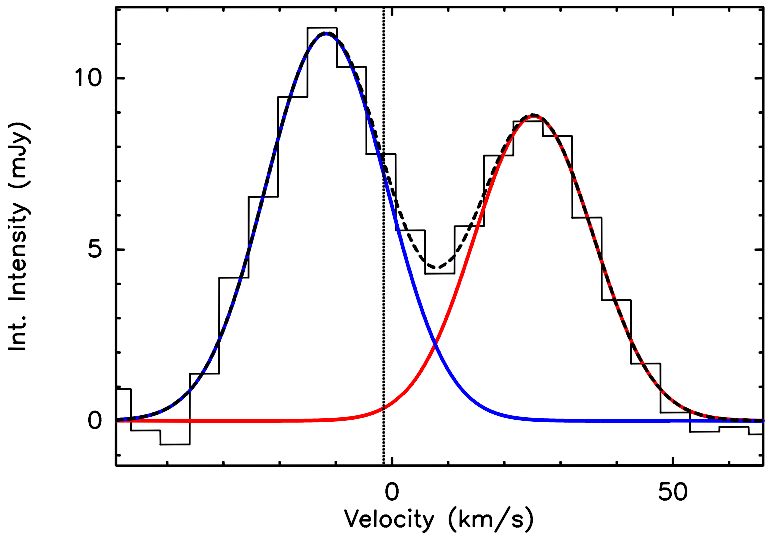

findings of Paper I. However, in the northern H II region, the fit of the spectrum at position N4 yields a central velocity of 5.5 ± 0.4 km s^{-1}, compared to -0.5 ± 1.6 km s^{-1} in Paper I. In the northern H II region, the central velocity at the head is ∼9 km s^{-1} (position N/0). Due to the proximity of the southern H II region, the spectrum at N/0 might be confused by a contribution from the southern H II region. Moving along the tail, the Gaussian shifts blueward until position N/3, then shifts redward at position N/4, where the broader wing at higher positive velocities indicates the presence of a second velocity component. In the spectrum at position N/5, two velocity components can clearly be distinguished. Apparently, positions N/3 and N/4 are marking a turn-over point in this kinematic structure. Thus, a small shift in the position of the slit over which the emission is integrated might cause a big shift in the central velocity of the integrated intensity, explaining the difference in velocity between our results and Paper I for position N/4. The redward shift in velocity in positions N/4 and N/5 as well as the two velocity components have not been seen in Paper I.

In the southern H II region, the spectrum at the head (S/0) also shows two velocity components, one blueshifted at -17 km s^{-1} and one redshifted at 5 km s^{-1}. In spectra S/1−S/4, we detect single Gaussians whose central velocities increase (shift redward) along the tail. Here, the velocity components might be too close in velocity to be resolved. The spectrum at S/4 shows a broader wing at positive velocities, indicating an increasing velocity difference between the central velocities of the two components, supported by the spectrum at S/5 in which the two

components can be distinguished again. In the spectra at positions S/6 and S/7 we only detect the redshifted velocity component, at large positive velocities (~27 km s^{-1}). The turn-over point from decreasing to increasing velocities is located between S/0 and S/1. The increase in velocity along the tail was already tentatively seen in Paper I but now clearly confirmed. Again, the two velocity components were not detected in Paper I. To our knowledge, these are the first observations of cometary H II regions in which two velocity components, belonging to the same region, have been detected in RRLs.

Due to the higher signal-to-noise ratio of our data (compared to Paper I), we decided to investigate the velocity structure in DR 21, particularly the distribution of the two velocity components, over "symmetric" boxes parallel and perpendicular to the major axes of both cometary H II regions. We generated 66 spectra by summing the emission over 4″ x 4″ boxes, chosen to approximately correspond to the area of the synthesized beam. Further along the tail of the southern H II region the emission is weaker; thus, we chose larger boxes (five boxes of 8″ x 8″ and one box of 28″ x 48″) to increase the signal-to-noise ratio. The positions and sizes of the boxes are shown in Fig. 5.1c. Analyzed on these spatial scales, many of the H66α spectra along the tail of the southern H II region (positions 3, 4, 5, 19, 20, 27, 28, 35, 36, 44, 45, 55, 63, and 64) clearly show two velocity components. An example (for position 36) is shown in Fig. 5.4; spectra for all positions are included in the appendix (Fig. 5.10). At the cometary heads, the spectra appear as single Gaussians (Fig. 5.10); however, a single broad Gaussian can approximate a blend of two narrower Gaussians. The observed linewidths are consistent with two velocity components being present throughout the northern and southern H II regions. Where two clearly separated velocity components are observed, their line widths are generally close to the thermal line width (FWHM ~ 20 km s^{-1}). In contrast, where the observed RRL could be interpreted as a single line, the line widths are broader, consistent with the presence of two, blended velocity components (Fig. 5.10). We thus fitted all spectra with two Gaussian line profiles to study the distribution of both velocity components over the entire H II regions. However, in ten spectra at the end of the tail of the southern H II region (positions 1, 2, 26, 34, 43, 52, 53, 54, 65, and 67), the second velocity component is too weak to be a 3σ detection. Therefore, we fitted these spectra with only one Gaussian. The fitting results are summarized in Table 5.2, and the Gaussian fits are overlaid on the spectra in Figs. 5.4 and 5.10.

The left and the right upper panels in Fig. 5.5 show the central velocities of the "blueshifted"[2] and the "redshifted"[2] Gaussians, respectively. The positions of the dots correspond to the centers of the 72 boxes; the dot size scales logarithmically with the amplitude of the Gaussian. The ve-

[2]Here and in the following text, the blueshifted/redshifted designation specifies the relationship of the two Gaussian peak velocities in each spectrum and not their relationship to the systemic molecular gas velocity.

locity of the ionized material spans a range of ∼39 km s^{-1} (−2.4 to 36.6 km s^{-1}) in the redshifted Gaussian and ∼36 km s^{-1} (−28.1 to 7.5 km s^{-1}) in the blueshifted Gaussian. In the lower left panel of Fig. 5.5, the velocity difference of the two Gaussian components ($v_{red}-v_{blue}$) is plotted, showing that the two velocity components are more separated further down the tails of both H II regions. The lower right panel shows the difference of the absolute velocities of the two fitted Gaussians ($|v_{red}-v_{sys}|-|v_{blue}-v_{sys}|$), from which we will draw conclusions about the orientation of the southern H II region in Sect. 5.4.

In the southern H II region, emission at velocities close to the systemic velocity is detected in the vicinity of the continuum emission peak for the redshifted Gaussian (e.g. positions 49, 60, 71). Single-peaked Gaussian line profiles at the head indicate that the velocity difference between the two components is small (see Fig. 5.10). Down the tail of the southern H II region, the velocity difference increases, with the velocities of the redshifted and the blueshifted Gaussians reaching +37 km s^{-1} and −28 km s^{-1}, respectively (Fig. 5.5c). The maximum velocities at the head are 7 (Pos. 51) and −18 km s^{-1} (Pos. 42) for the redshifted and blueshifted Gaussians, respectively. The turn-over point is roughly located between positions 60/49/40 and 59/48/39.

In the northern H II region, velocity components close to the systemic velocity are also detected around the continuum emission peak, near the head of the cometary H II region. Here again, the spectra show single broad Gaussians, approximating a blend of two narrower Gaussians close in velocity. Down the tail, the velocities of both components first decrease until the turn-over point is reached between positions 13/14/15 and 10/11/12 and the velocities increase again. This increase is more prominently seen in the redshifted than the blueshifted Gaussian where the velocity reaches ∼25 km s^{-1} (position 8). Across the flow, a velocity gradient of about 9 km s^{-1} in each Gaussian is detected (e.g. positions 10−12) that was not seen in Paper I before. The velocity field (moment 1 map) of the northern H II region is presented in Fig. 5.6. It shows that the north-eastern part of the northern H II region is dominated by emission at large positive velocities, while emission at negative velocities peaks toward the north-western part.

5.4 Comparison with Cometary H II Region Models

Since the publication of Paper I, the state of the art in compact H II region modeling has advanced considerably. Of particular relevance, Arthur & Hoare (2006) present a suite of radiation-hydrodynamic simulations of cometary H II regions. They determine line intensity, mean velocity, and velocity dispersion at different positions in the H II region for four groups of models:

i) Pure bow shock: stellar motion + stellar wind, no density gradient

Figure 5.5: 22 GHz continuum map of DR 21 (contours; same as Fig. 5.1). The dots represent the Gaussian fitting results with their positions corresponding to the centers of the boxes. In the top panels, the dot size scales logarithmically with the amplitude of the Gaussians. The systemic velocity of the molecular material is ≈ -1.5 km s^{-1} (green in the upper panels). In the lower left panel, the velocity difference between the two Gaussian components is plotted. The figure shows that the velocity difference between the two components increases from the head down the tail in both H II regions. In the lower right panel, the difference of the absolute velocities of the Gaussian components is plotted to show that the velocity difference does not increase symmetrically to the systemic velocity. The synthesized beam is shown in the lower left corners of all figures. In the upper left corners, a scale of 0.1 pc is indicated.

(a) Redshifted Gaussian

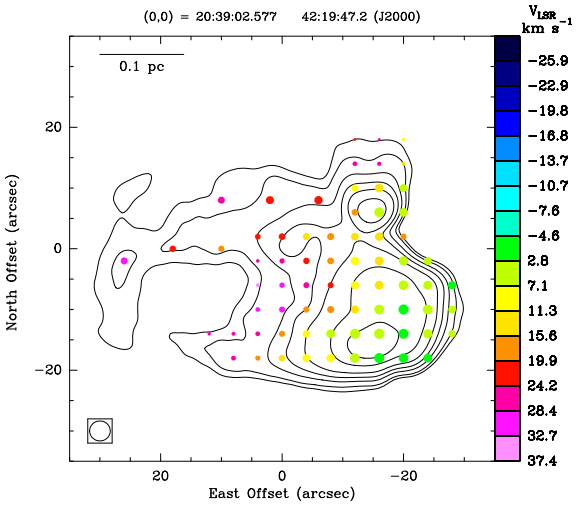

(b) Blueshifted Gaussian

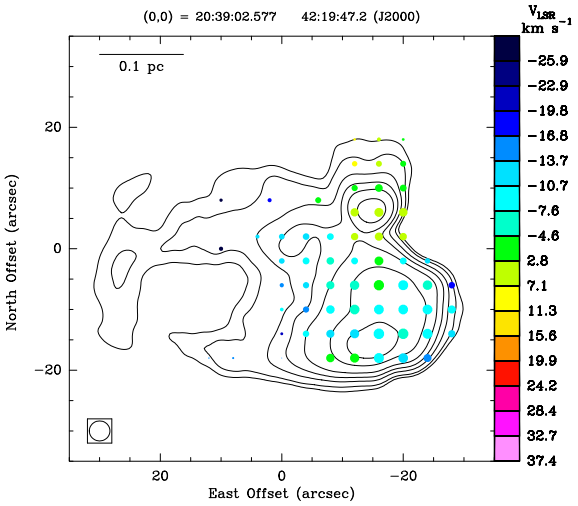

(c) Velocity difference of the two fitted Gaussians ($v_{red}-v_{blue}$)

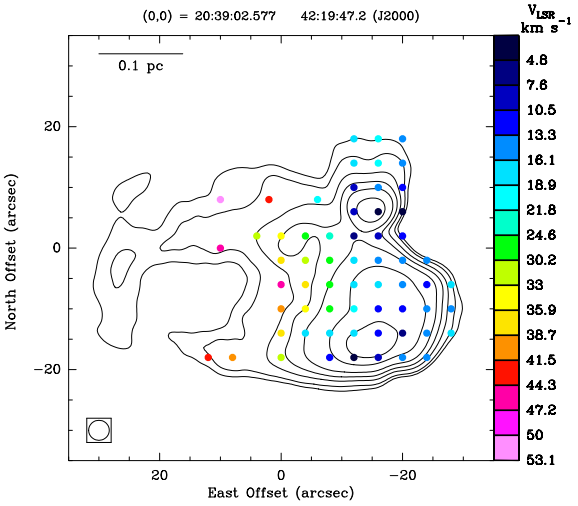

(d) Difference of the absolute velocities of the two fitted Gaussians ($|v_{red}-v_{sys}|-|v_{blue}-v_{sys}|$)

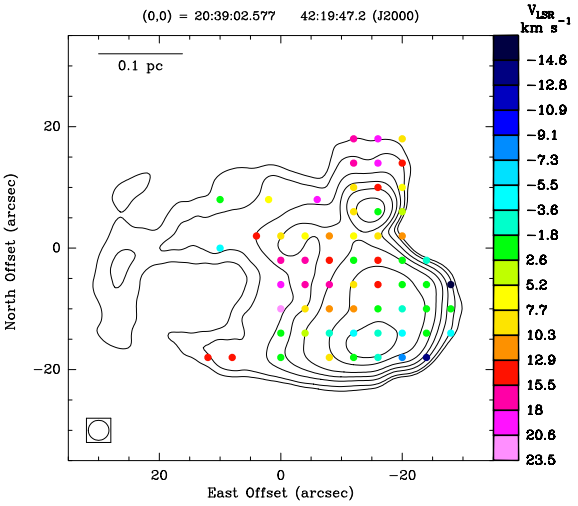

ii) Pure champagne flow: density gradient, no stellar wind, no stellar motion

iii) Champagne flow + stellar wind: density gradient, stellar wind, no stellar motion

iv) Champagne flow + stellar wind + stellar motion: density gradient, stellar wind, stellar motion

In all models, the position of the ionization front is offset from the position of the star. We note that the schematic "hybrid" model proposed in Paper I (champagne flow and bow shock) is similar to (iv), but did not include a stellar wind. These four models make distinguishable predictions for the velocity structure in a cometary H II region and we will compare our results qualitatively with these models.

For the bow shock model (model i), the velocities of the ionized gas at the head of the H II region are similar to the stellar velocity. Since the influence of the stellar motion on the gas is small in the tail, the velocities quickly converge to the systemic velocity of the surrounding material in this region. In the pure champagne flow model (model ii), the velocity of the ionized material at the position of the star is similar to the velocity of the ambient molecular material. Down the tail, the velocity of the ionized gas increases due to the drop in pressure. Including a stellar wind in the champagne flow model (model iii) causes the ionized gas to flow around the stellar wind bubble in a thin shell. The density gradient in the ambient material then leads to large accelerations at the sides of the flow. If additionally the star is moving up the density gradient (model iv), the direction of the flow between the ionization front and the stellar position changes (compared to the pure champagne flow model), being now in the direction of stellar motion (for the four models, compare Figs. 3, 4, 5, and 12 of Arthur & Hoare 2006).

In all cases, the observed morphology and velocity structure will be affected by viewing angle. Zhu et al. (2008) consider viewing angle effects in some detail, in the context of [Ne II] 12.8 μm observations of a sample of compact and UC H II regions. They present schematic position-velocity diagrams, for three different inclinations, for three cases relevant to cometary H II regions: a stellar-wind bow shock H II region (supersonic stellar motion), a stellar-wind pressure-driven H II region (slow stellar motion or ambient density gradient), and a wind-free champagne flow (which they refer to as a "blister" region). In the models with a stellar wind, a cavity is cleared by the wind and the ionized flow is confined to a thin paraboloidal shell. While Zhu et al. (2008) emphasize that their models are qualitative, the schematic position-velocity diagrams (their Figs. 46–48) illustrate kinematic features that are potentially diagnostic.

In particular, for a cometary H II region viewed side-on (e.g., cometary axis in the plane of the sky), two velocity components are expected from a wind-confined ionized flow – one

from the near and one from the far side of the paraboloidal shell (Figs. 46−47 of Zhu et al. 2008). The separation (Δv) between the two velocity components is greatest at the position of the star, and decreases both towards the cometary head and down the tail; at all positions, the two velocity components are symmetric about the velocity of the ambient gas. Notably, for this viewing angle it is not possible to distinguish between the bow-shock and pressure-driven stellar wind cases based on a position-velocity diagram. For intermediate viewing angles, two velocity components are expected near the head, while down the tail one velocity component (side of the shell) becomes dominant (Figs. 46−47 of Zhu et al. 2008). The line-of-sight ionized gas velocities depend both on the precise viewing angle and on the model type. In contrast to the stellar-wind cases, in the wind-free champagne flow the ionized gas fills the "blister" cavity, limited by the ionization front. In this case, a single broad line is expected at all positions (Fig. 48 of Zhu et al. 2008).

In our H66α observations, we clearly detect two separate velocity components in the radio recombination line in the tails of the northern and southern DR 21 H II regions. The two velocity components indicate the presence of strong stellar winds, causing the ionized gas to flow along cone-like shells (with the interior of the cone being filled with low-density gas or completely devoid of material). Thus, the two velocity components of the radio recombination line are emitted by denser gas at the front and the back of the cone. Near the heads of the H II regions, the two Gaussian components are less separated in velocity (Fig. 5.5c), as expected for the Zhu et al. (2008) side-view case. However, our data also exhibit some notable disagreements with the Zhu et al. (2008) schematics: in particular, the velocity separation between the two Gaussian components increases, not decreases, down the tails (Fig. 5.5c). For a champagne flow, we expect increasing velocities along the tail and thus would expect a "broadening" of the position-velocity diagram, as observed in our data. Why this is not seen in the position-velocity diagram of the champagne flow model in Zhu et al. (2008), is not explained in their paper.

5.4.1 Southern H II Region

From the continuum emission peak of the ionized gas down to the end of the tail, the absolute velocities of the ionized gas increase. The champagne flow model fits best to explain this velocity distribution, with the flow of the ionized gas being accelerated down the density gradient of the surrounding material, confirming the tentative result of Paper I. Consistent with Paper I, we find lower velocities than the systemic velocity in the head of the H II region, consistent with a bow shock evoked by the movement of the exciting star through dense material.

We conclude that the velocity structure of the southern H II region is consistent with the

Figure 5.6: H66α moment 1 map of the northern H II region in DR 21. A velocity gradient from the eastern to the western side of the cometary H II region is detected.

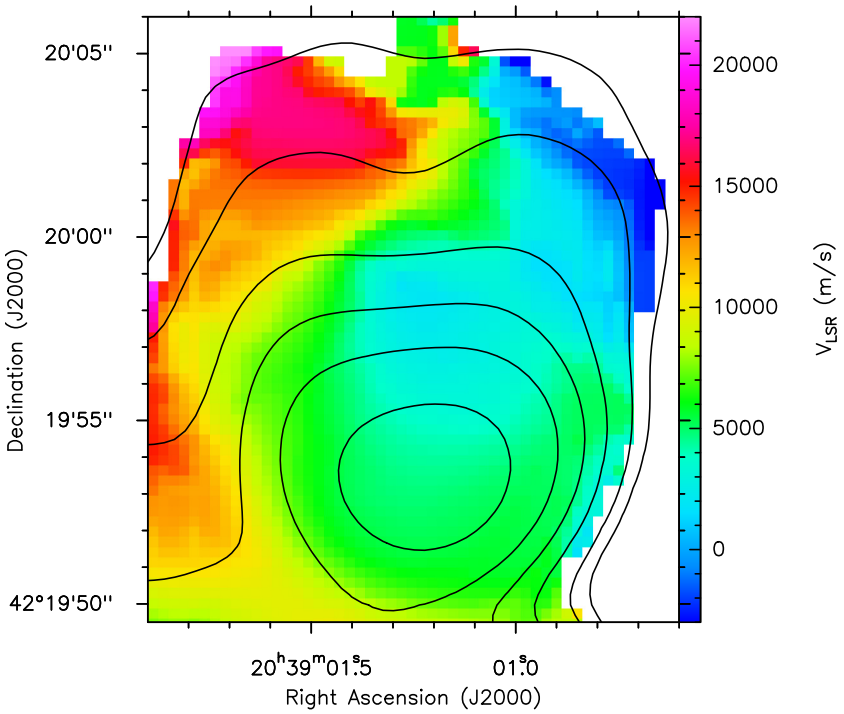

exciting star having a stellar wind and moving through dense material, creating a bow shock in front of the star. The surrounding material likely has a density gradient (see also Section 5.5), which forces the ionized gas on an accelerated flow down the gradient (champagne flow). This velocity structure is best explained by model iv (models G, H, and I of Arthur & Hoare 2006). The cartoon of the "hybrid" model, proposed in Paper I, is consistent with the overall velocity structure of our data but does not explain the two detected velocity components, since it does not include a stellar wind.

If the southern H II region was seen side-on, i.e. with a cometary axis perpendicular to the line-of-sight, we would expect the velocities of the red- and blueshifted Gaussian components to increase symmetrically to the systemic velocity of -1.5 km s^{-1} down the tail and towards the head (as seen in Figs. 46 and 47 of Zhu et al. 2008). This is shown schematically in the left panel of Fig. 5.7 which presents three lines-of-sight through a cometary H II region which is shaped by a bow shock, champagne flow, and stellar wind and viewed side-on. For each line-of-sight, the expected Gaussians of the two velocity components from the front and back of the swept-up shell are presented. Since for this inclination we see the same absolute velocities relative to the systemic velocity (dashed line) at both sides of the shell, their difference ($|v_{red}-v_{sys}|-|v_{blue}-v_{sys}|$)

Figure 5.7: Change in absolute velocity difference relative to systemic velocity across cometary H II region for two different orientations. The kinematics of the cometary H II region are dominated by a bow shock, champagne flow, and strong stellar wind, forming a swept-up shell around the star. The expected Gaussians of the two velocity components at the near and far side of the shell are sketched for three different lines-of-sight. In the case of 90° inclination (w.r.t. the line-of-sight), the two velocity components are emitted at corresponding sides of the shell with the same absolute velocities relative to the systemic velocity (left panel). However, in the case of 75° inclination (w.r.t the line-of-sight), the two components originate from different positions along the shell and thus, the velocity difference to the systemic velocity is not the same for the two components (right panel). The right panel illustrates the velocity structure of the southern H II region, suggesting that the exciting star is moving towards us.

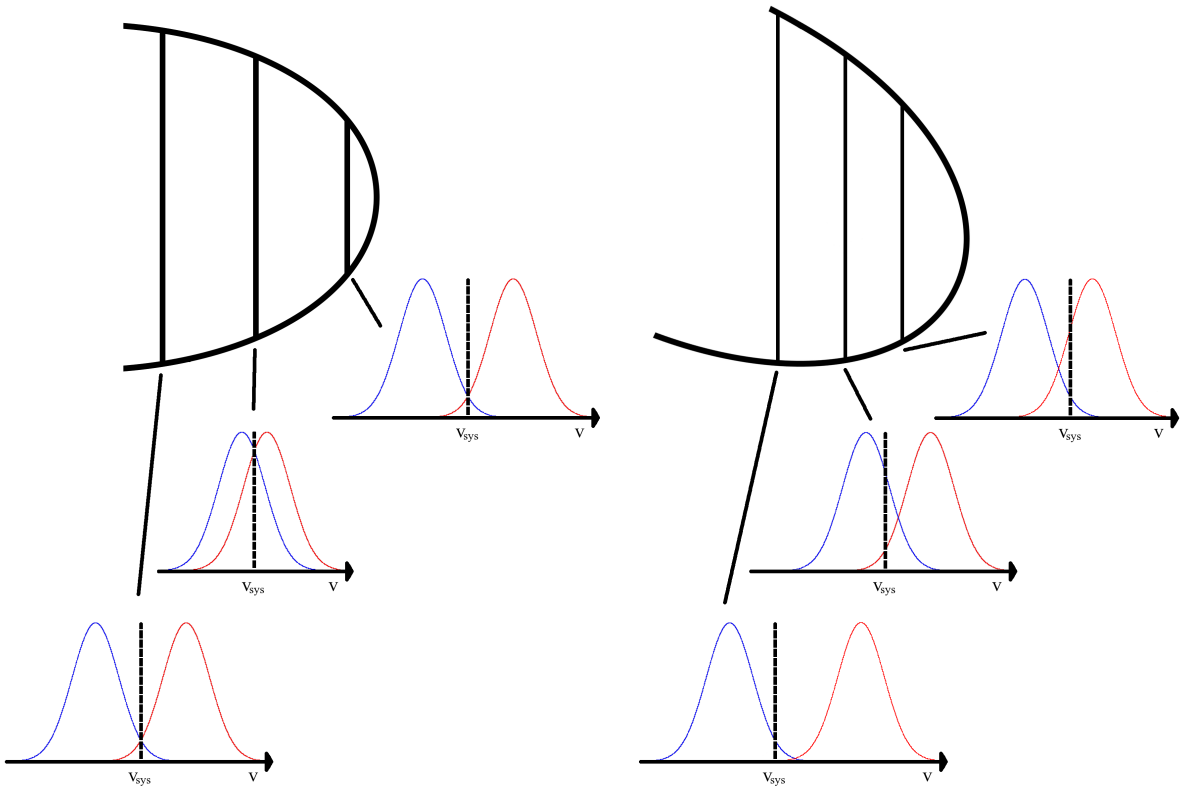

should be roughly zero at each position along the shell. This velocity difference for the two velocity components in the southern H II region is plotted in Fig. 5.5d. We see that the difference is not close to zero at most positions in the H II region. Close to the continuum emission peak of the ionized gas and in the head of the H II region, the velocity difference is slightly negative, i.e. the velocity difference between the blueshifted Gaussian and the systemic velocity is larger than the difference between the redshifted Gaussian and the systemic velocity. Down the champagne flow, the velocity difference is positive at most positions, i.e. the velocity offset of the redshifted Gaussian to the systemic velocity is here larger than the velocity offset of the blueshifted Gaussian. Since, at the head, the blueshifted spectral line seems to be emitted closer to the ionization front than the redshifted spectral line and, in the tail, we observe emission further down the flow for the redshifted Gaussian (i.e. at higher velocities) than for the blueshifted Gaussian, we conclude that the cometary axis of the southern H II region has an angle of $< 90°$ to the line-of-sight. This is shown schematically in the right panel of Fig. 5.7 for a cometary H II region whose cometary axis has an angle of 75° to the line-of-sight. Again, the two velocity components from both sides of the shell are shown for three lines-of-sight which illustrate that the two components are not emitted at corresponding sides of the shell and thus do not show the same absolute velocities relative to the systemic velocity, explaining the non-zero velocity differences ($|v_{red}-v_{sys}|-|v_{blue}-v_{sys}|$). The suggested inclination of the H II region indicates that the exciting star is moving towards us.

5.4.2 Northern H II Region

The absolute velocities of the ionized material in the northern H II region appear to increase from the head to the tail, showing evidence of a champagne flow. The ionized gas velocity at the cometary head is redshifted relative to the systemic velocity of the molecular gas, by up to ~10 km s^{-1} (see also Section 5.3 and Table 5.2). This is evidence for a bow-shock contribution to the velocity structure near the cometary head (consistent with the results of Paper I). We note, however, that the identification of velocity components at the head of the northern H II region is complicated by the superposition of the velocity components from the two H II regions. At positions 16−18 and 23−25, we attempted to fit the spectra with four Gaussians. The quality of the fits was not encouraging due to the low signal-to-noise ratio; thus, we only show the two Gaussian fits for these positions.

The detection of two velocity components indicates the presence of a conical ionized shell, confined by a stellar wind, as for the southern H II region (see also discussion of Zhu et al. 2008, above). In addition, we detected a velocity gradient *across* the ionized flow, from the eastern to

the western side of the northern H II region (Fig. 5.6). A rotating star with a rotating stellar wind might force the ionized gas in the wind swept-up shell to follow the rotation. This interesting possibility warrants further investigation; however, higher spatial resolution data are required to better constrain the velocity structure.

5.5 DR 21 at Infrared and Submillimeter Wavelengths

Figure 5.8: SCUBA 870 μm image of DR 21 with a HPBW of 15″. The contours show the 22 GHz continuum emission with the contour levels corresponding to the contours in Fig. 5.1. The offset between the submillimeter and radio continuum emission peaks is ~0.04 pc.

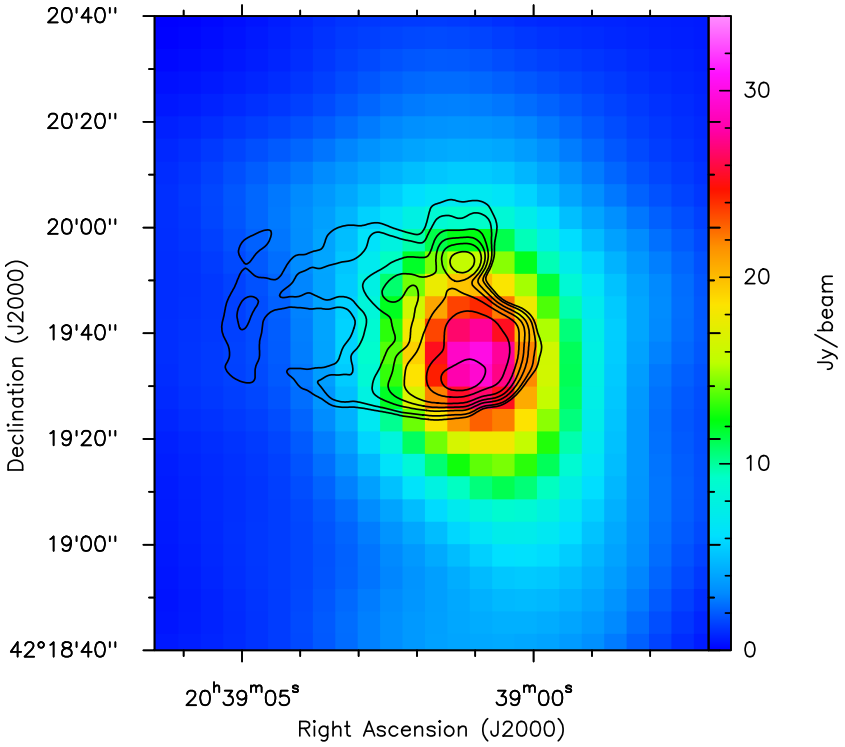

As discussed in Section 5.4, the ionized gas kinematics of the DR 21 H II regions indicate a champagne flow contribution to the cometary tails. Champagne flows require a density gradient in the surrounding medium. Recent large-scale studies of the DR 21 region at (sub)millimeter and midinfrared (MIR) wavelengths provide insight into the interaction of the H II regions with their environment.

Davis et al. (2007) mapped the DR 21 region in 870 μm dust continuum emission with the Submillimeter Common-User Bolometer Array (SCUBA) on the James Clerk Maxwell Telescope (JCMT) (Fig. 5.8). The half power beam width (HPBW) of the SCUBA observations is

Figure 5.9: *Spitzer* IRAC three color image of DR 21 (blue = 3.6 μm, green = 4.5 μm, red = 8.0 μm). The contours show the 22 GHz continuum emission with the contour levels corresponding to the contours in Fig. 5.1. In the upper right corner, a scale of 1 pc is shown.

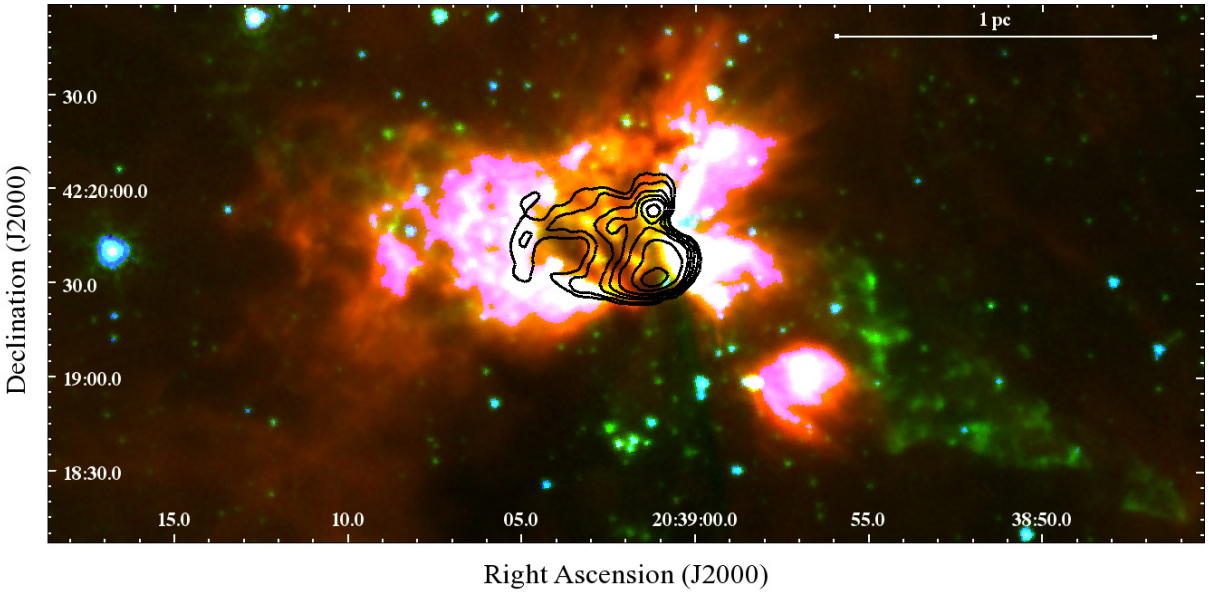

15″. The 870 μm image shows that the head of the southern H II region is embedded in a dust core with a size of ∼0.2 × 0.12 pc (27″ × 16″, Davis et al. 2007; Di Francesco et al. 2008). The peak of the submillimeter emission is slightly offset (by ∼0.04 pc in the north-west direction) from the peak of the ionized emission.

In Schneider et al. (2010), the emission of several molecular lines (^{12}CO(2−1), ^{13}CO(2−1), HCO$^+$(1−0), H^{13}CO$^+$(1−0), $H_2CO(3_{1,2}-2_{1,1})$, C^{34}S (2−1), and N_2H^+(1−0)) was observed with the Institut de Radioastronomie Millimétrique (IRAM) 30 m telescope towards DR 21 with a HPBW between 11″ and 29″. Channel maps of ^{13}CO, H^{13}CO$^+$, and C^{34}S confirm the small velocity dispersion of the molecular gas in DR 21 (their Fig. 7). Velocity-integrated line maps of HCO$^+$ and ^{13}CO show emission of low-density gas from the whole DR 21 region and the associated outflow. In contrast, C^{34}S and N_2H^+ emission, which trace higher density gas, are only observed towards the central part of DR 21, roughly coincident with the SCUBA core. (There is also some weak C^{34}S emission extending to the west.) Neither C^{34}S nor N_2H^+ is detected at the end of the tail of the southern H II region, consistent with a density gradient in the molecular material surrounding the southern H II region with density decreasing from west (cometary head) to east (tail). However, this requires confirmation with molecular line observations at higher spatial resolution.

Figure 5.9 shows a three color composite *Spitzer* Infrared Array Camera (IRAC) image (blue

= 3.6 μm, green = 4.5 μm, and red = 8.0 μm) of DR 21 (Marston et al. 2004). At 4.5 μm (green colors), the large DR 21 outflow is clearly visible, and several *Spitzer*-based analyses have been published (e.g. Smith et al. 2006; Davis et al. 2007). In the northern H II region, the MIR emission peaks at the cometary head. This MIR source is the brightest in the region at 8 μm, and may be the dominant contributor to the infrared luminosity of DR 21 (Marston et al. 2004; Davis et al. 2007, and references therein). In contrast, for the southern H II region, the MIR emission is strongest west of the head and at the end of the cometary tail. The dark dust lane noted by Davis et al. (2007) cuts north-east to south-west across the H II region, and there is also an apparent cavity in the MIR emission at the center of the cometary tail (also recently noted by Zapata et al. 2013).

Interpreting the MIR morphology is complicated by the presence of numerous molecular and atomic emission lines within the broad IRAC bands (e.g. Fig. 1 of Reach et al. 2006). In the *Spitzer* Galactic Legacy Infrared Mid-Plane Survey Extraordinaire (GLIMPSE) of the Galactic Plane, ubiquitous MIR "bubbles" trace the photo-dissociation regions (PDRs) around H II regions, where emission from polycyclic aromatic hydrocarbons (PAHs) likely dominates the flux in the 8 μm band (e.g. Churchwell et al. 2009, and references therein). IRAC images of the high-mass star forming region S255N, which contains a cometary UC H II region, show that bright MIR emission appears to trace the UC H II region surface, consistent with the PDR picture; there is also bright MIR emission at the end of the cometary tail (Cyganowski et al. 2007). However, in the vicinity of extremely energetic H II regions such as M17, dust continuum emission may also contribute significantly to the observed IRAC fluxes, particularly at 8 μm (Povich et al. 2007). Zapata et al. (2013) have recently suggested that the MIR nebulosity in DR 21 is attributable to heating by strong shocks, caused by an explosive event that produced the famous DR 21 outflow. Additional data, e.g. MIR spectroscopy, is needed to constrain the emission mechanism(s) responsible for the complex MIR emission associated with the DR 21 H II regions.

5.6 Conclusions

We have obtained deep H66α radio recombination line observations of the two cometary H II regions in DR 21, with the aim of testing proposed models for cometary H II region kinematics, in particular the "hybrid" bow shock/champagne flow model proposed in Paper I.

Compared to Paper I, our data set recovers weaker emission at the end of the tails of both H II regions which allowed us to extend the "long slit" analysis of Paper I to positions further down

both tails.

Our analysis of the velocities of the cometary heads is consistent with the results of Paper I: we find offsets between the velocities of the ionized gas and the ambient molecular material, indicative of stellar motion as in bow shock models. In the new data, we detect RRL emission with increasing velocities along the tails of the southern and northern H II regions. This velocity structure is consistent with a champagne flow contribution in the tail, as in the hybrid scenario.

The sensitivity of the new data allows us to move beyond "long slit" analysis (which assumes symmetry about the cometary axis) and probe the velocity structure on ∼4″ scales. A detailed analysis of the ionized gas kinematics clearly shows that two velocity components are widespread in both the northern and southern H II regions. To our knowledge, these are the first observations of cometary H II regions in which two velocity components, belonging to the same region, have been detected in RRLs. Intriguingly, in the northern H II region we also find tentative evidence for a velocity gradient *across* the flow of the ionized material, which might indicate a rotation of the flow. Higher spatial resolution data are required to investigate this possibility.

The two velocity components indicate that the ionized gas is likely confined to a thin conical or paraboloidal shell, as predicted by models that include strong stellar winds. Our data suggest that the combined effects of a stellar wind, stellar motion (as in bow shock models) and an ambient density gradient (as in champagne flow models) are necessary to explain the observed ionized gas kinematics. Recent observations of dense gas tracers in the DR 21 region are consistent with the ambient density gradient inferred from the ionized gas kinematics: the cometary head of the southern H II region is embedded in a dense core, while no emission from dense gas tracers is detected towards the eastern end of the cometary tail.

5.A Appendix

Table 5.2: Gaussian fitting results

	Gauss 1			Gauss 2		
Position	Amplitude (mJy)	Velocity (km s^{-1})	FWHM (km s^{-1})	Amplitude (mJy)	Velocity (km s^{-1})	FWHM (km s^{-1})
POS 1	16.0	29.0	37.8			
POS 2	10.9	23.4	32.6			
POS 3[a]	10.2	19.3	43.9	4.6	−26.5	9.9
POS 4[a]	15.8	24.7	24.8	3.4	−28.1	24.7

Table 5.2: Continued.

	Gauss 1			Gauss 2		
Position	Amplitude (mJy)	Velocity (km s^{-1})	FWHM (km s^{-1})	Amplitude (mJy)	Velocity (km s^{-1})	FWHM (km s^{-1})
POS 5[a]	32.1	22.3	26.5	4.3	−19.7	22.6
POS 6	41.3	21.6	28.2	9.9	1.8	34.6
POS 7[a]	2.4	24.1	13.1	2.8	7.1	22.4
POS 8[a]	2.4	25.2	14.0	4.3	5.1	19.9
POS 9[b]	2.7	10.1	24.2	2.9	−4.5	12.5
POS 10	4.8	24.3	17.0	7.7	7.4	24.4
POS 11[b]	3.8	25.4	13.7	9.5	5.0	27.5
POS 12	3.4	13.9	32.1	9.7	−1.0	24.0
POS 13	18.7	11.2	28.3	10.9	2.6	25.9
POS 14	53.9	13.6	23.6	27.1	−0.5	26.5
POS 15	32.5	7.0	26.7	16.0	−4.4	25.1
POS 16	13.3	16.3	28.2	40.9	6.1	26.1
POS 17	151.1	5.7	28.5	69.7	3.4	24.4
POS 18	48.2	6.6	29.0	50.2	2.9	24.3
POS 19[a]	7.4	21.1	21.4	4.3	−11.2	40.3
POS 20[a]	12.8	20.1	28.7	8.6	−13.0	33.1
POS 21[b]	17.4	14.1	39.1	13.5	−11.1	25.5
POS 22[b]	17.2	16.4	34.7	15.2	−7.8	26.3
POS 23	26.2	12.1	27.2	21.7	5.2	34.6
POS 24	44.2	13.0	24.0	41.0	3.4	23.3
POS 25	9.7	16.2	20.4	23.6	4.1	24.8
POS 26	3.0	27.2	23.2			
POS 27[a]	6.1	25.5	28.4	8.1	−12.2	26.9
POS 28[a]	11.1	21.6	29.3	16.5	−8.7	26.1
POS 29[b]	14.0	18.3	27.0	23.9	−7.1	23.9
POS 30	49.0	8.0	33.0	16.2	−9.5	22.8
POS 31	57.7	12.4	25.7	62.5	−1.6	29.0
POS 32	90.1	5.7	27.2	16.1	−7.9	33.8
POS 33	31.0	4.5	24.3	7.7	−10.8	32.2
POS 34	3.4	36.4	20.0			

Table 5.2: Continued.

	Gauss 1			Gauss 2		
Position	Amplitude (mJy)	Velocity (km s^{-1})	FWHM (km s^{-1})	Amplitude (mJy)	Velocity (km s^{-1})	FWHM (km s^{-1})
POS 35[a]	6.3	31.0	20.9	4.6	−14.1	20.7
POS 36[a]	8.9	25.2	24.9	11.3	−11.7	25.4
POS 37	9.0	19.9	25.0	37.2	−7.2	26.7
POS 38	33.0	11.2	27.2	90.6	−5.2	26.3
POS 39	58.4	14.2	23.5	203.0	−3.5	27.6
POS 40	134.6	5.4	27.4	153.5	−8.4	27.2
POS 41	66.3	5.5	22.9	104.4	−7.2	29.2
POS 42	37.9	−2.0	26.1	13.6	−18.4	28.1
POS 43	4.4	29.6	22.0			
POS 44[a]	8.6	29.6	26.0	3.8	−9.4	29.3
POS 45[a]	9.8	19.6	37.5	11.1	−14.3	28.4
POS 46	17.4	18.0	31.6	46.7	−9.0	28.7
POS 47	34.8	14.7	28.6	122.3	−6.0	26.8
POS 48	137.4	4.4	28.2	124.3	−8.2	25.4
POS 49	190.9	2.5	26.3	125.1	−8.9	26.0
POS 50	144.7	5.0	24.0	129.0	−9.7	26.6
POS 51	27.4	7.0	22.7	37.5	−8.5	30.6
POS 52	2.9	27.1	22.3			
POS 53	3.4	25.4	21.0			
POS 54	4.8	24.4	30.4			
POS 55[a]	9.6	17.0	41.7	3.0	−20.8	20.2
POS 56	19.6	9.3	40.5	12.7	−9.5	32.3
POS 57	59.6	5.8	36.1	33.7	−11.3	27.6
POS 58	181.4	5.4	29.9	75.5	−12.8	23.0
POS 59	218.5	2.8	28.0	258.5	−9.4	26.4
POS 60	160.8	−2.0	30.5	222.4	−7.0	29.9
POS 61	90.9	6.1	23.0	158.9	−9.0	28.0
POS 62	22.0	5.5	22.3	21.6	−12.3	27.7
POS 63[a]	1.7	27.6	26.4	2.3	−15.8	15.6
POS 64[a]	5.0	24.7	44.3	2.6	−14.5	11.5

Table 5.2: Continued.

	Gauss 1			Gauss 2		
Position	Amplitude (mJy)	Velocity (km s^{-1})	FWHM (km s^{-1})	Amplitude (mJy)	Velocity (km s^{-1})	FWHM (km s^{-1})
POS 65	5.4	18.6	43.6			
POS 66	12.7	14.8	36.2	2.2	−16.0	17.8
POS 67	31.7	7.5	36.2			
POS 68	43.3	8.1	30.3	46.3	−2.7	27.3
POS 69	121.1	3.0	27.5	80.1	1.0	31.8
POS 70	176.8	2.1	28.1	161.2	−7.7	28.2
POS 71	115.3	1.5	29.6	109.3	−12.6	25.2
POS 72	57.6	−2.2	26.7	33.1	−16.3	22.2

Notes. [(a)] Two velocity components visible. [(b)] Asymmetric line profile indicates two velocity components.

Figure 5.10: Radio recombination line spectra. The red and the blue line show the fitted Gaussians, the dashed black line presents the sum of the two Gaussian fits. The vertical black line marks the systemic molecular gas velocity of −1.5 km s^{-1}.

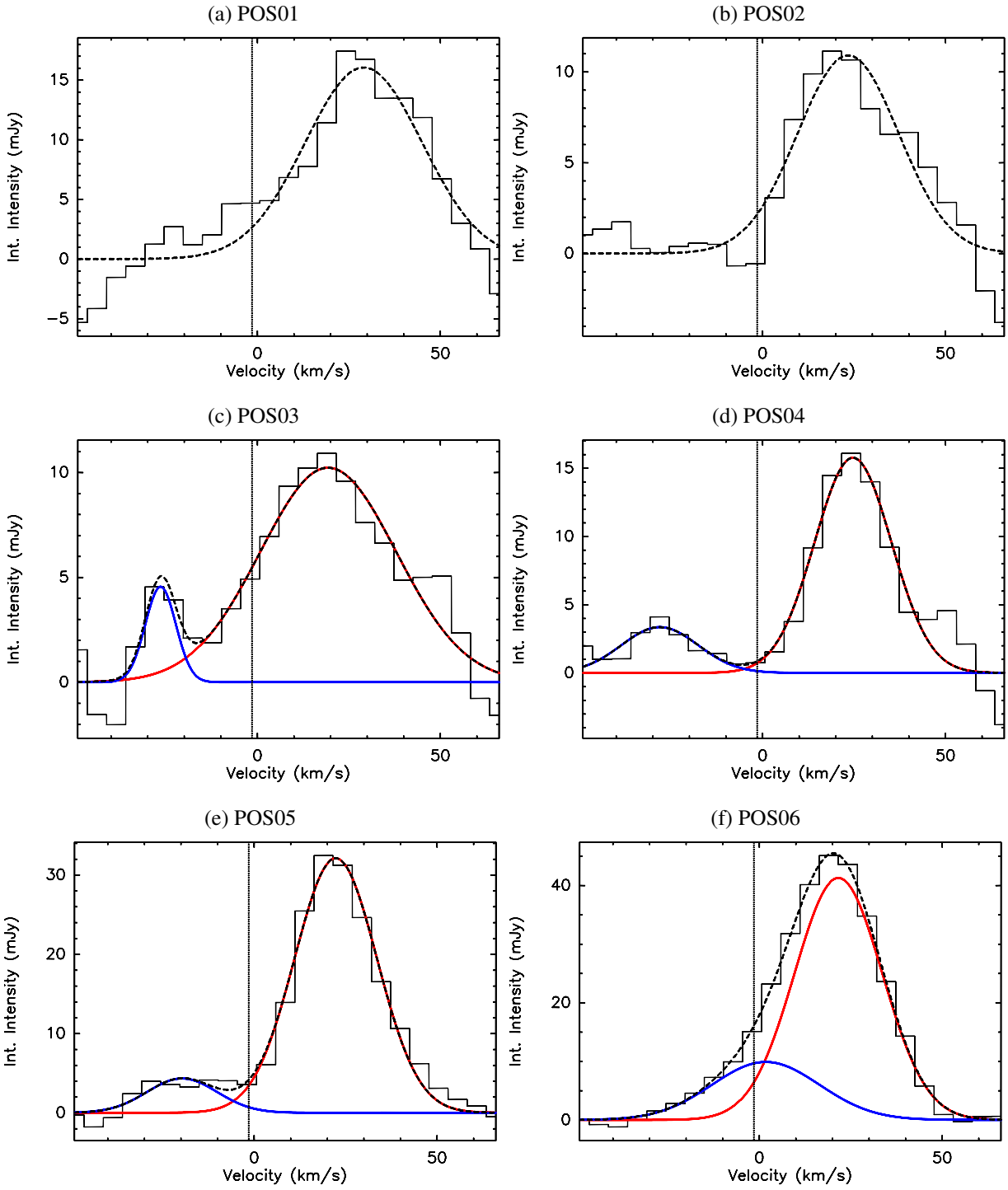

Figure 5.10: Continued.

(a) POS07

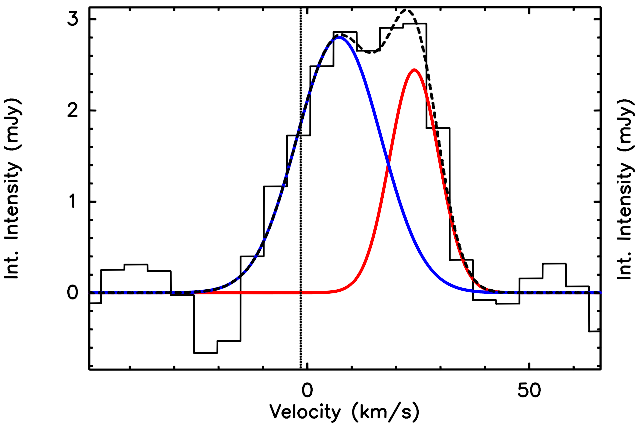

(b) POS08

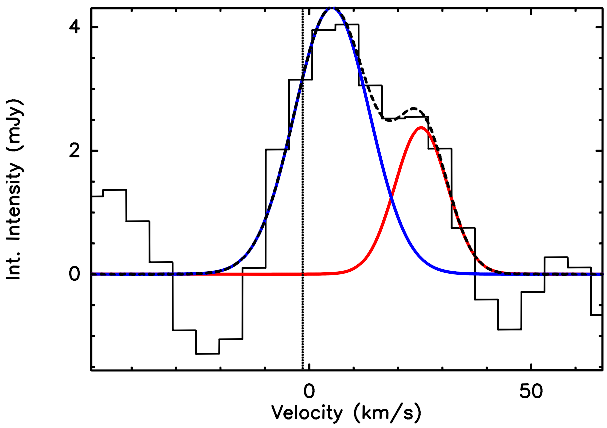

(c) POS09

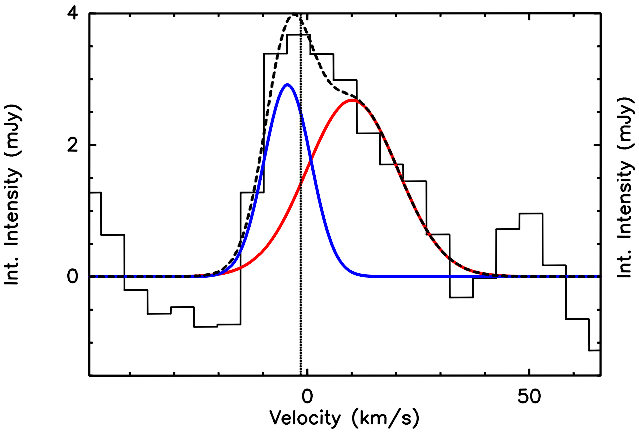

(d) POS10

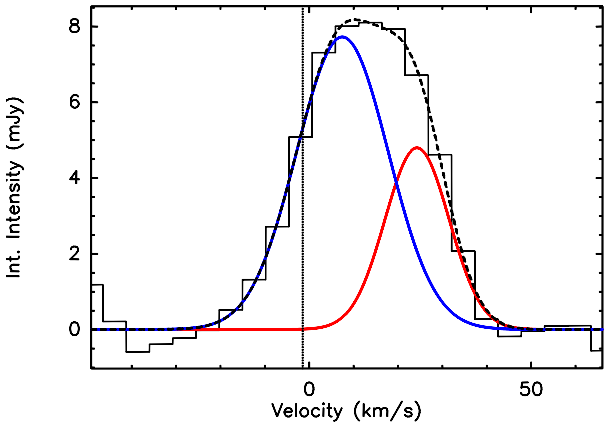

(e) POS11

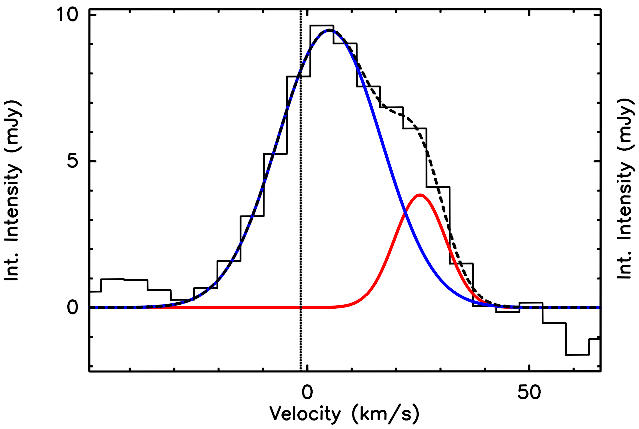

(f) POS12

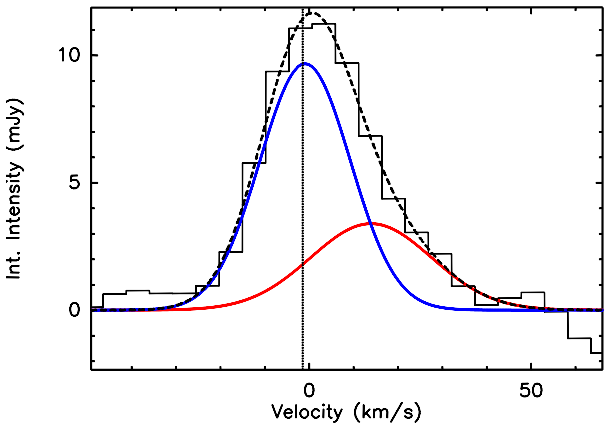

Figure 5.10: Continued.

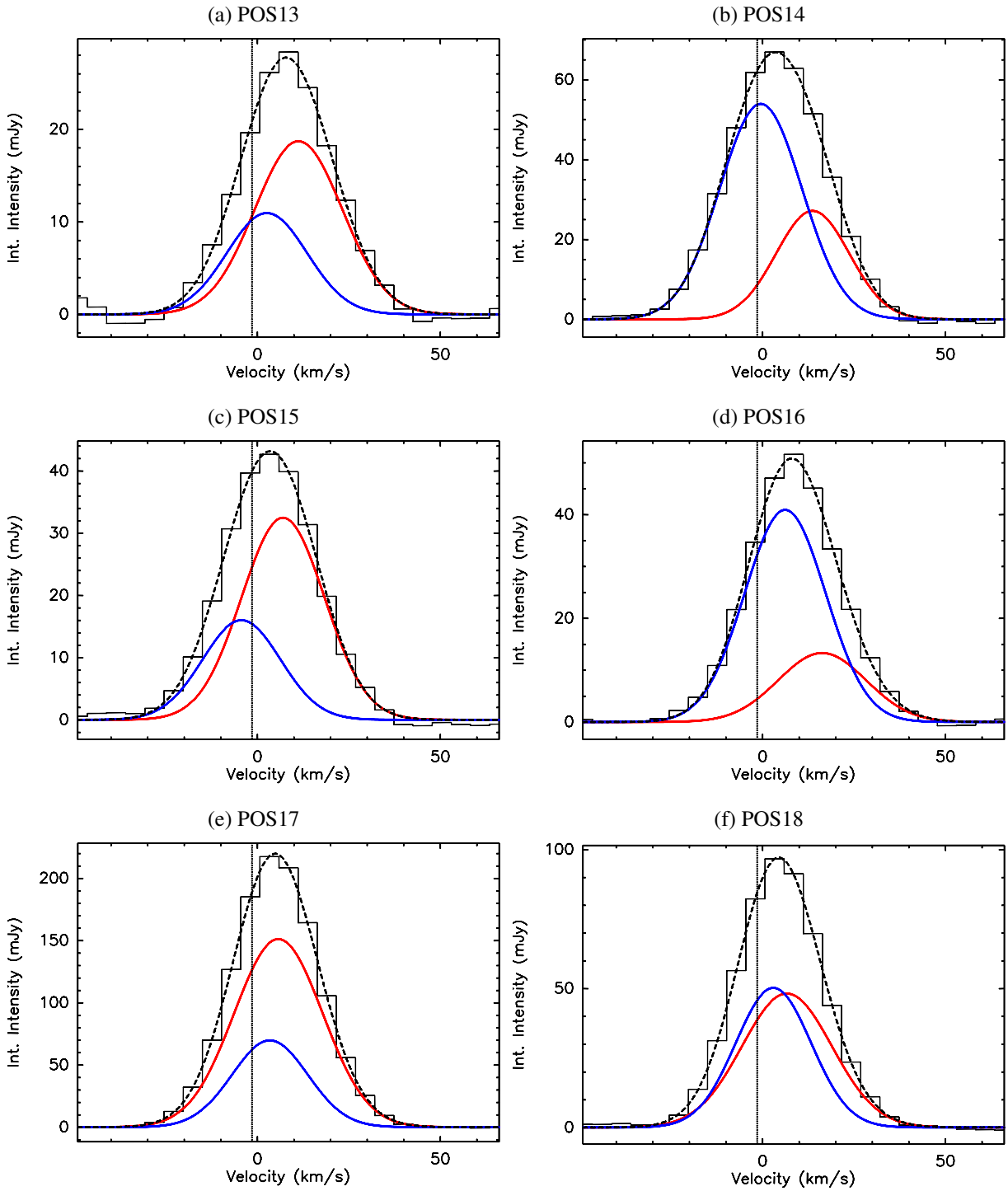

Figure 5.10: Continued.

(a) POS19

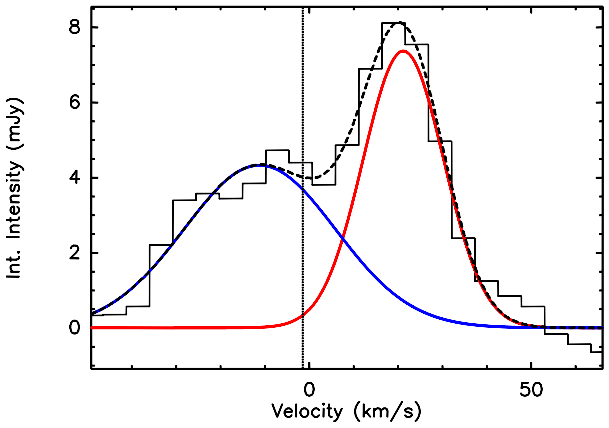

(b) POS20

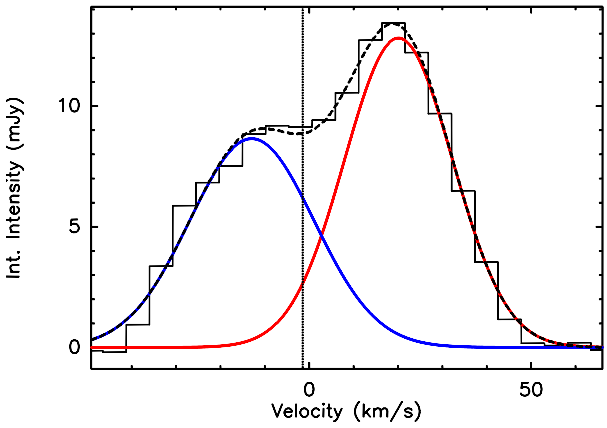

(c) POS21

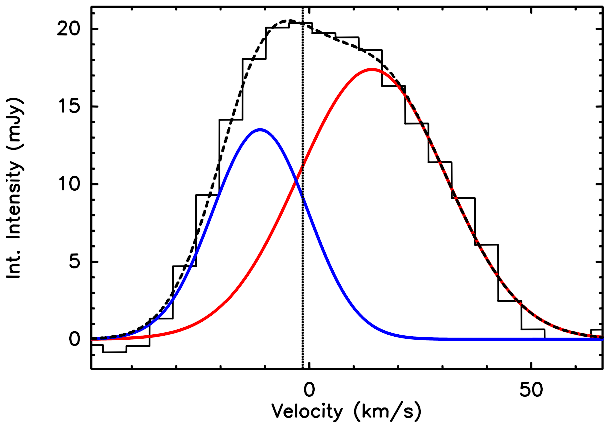

(d) POS22

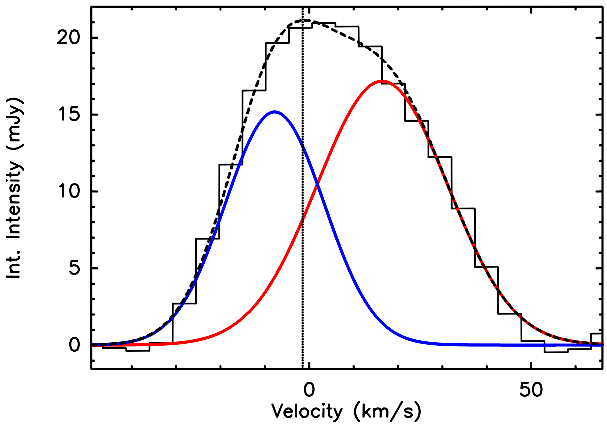

(e) POS23

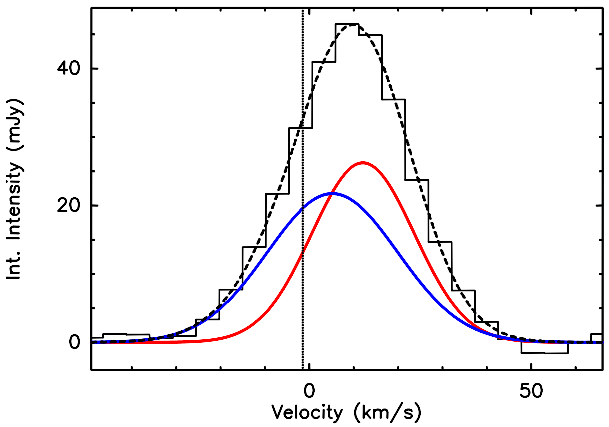

(f) POS24

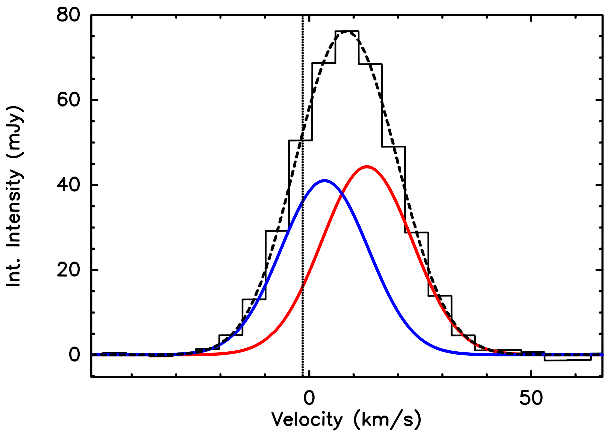

Figure 5.10: Continued.

(a) POS25

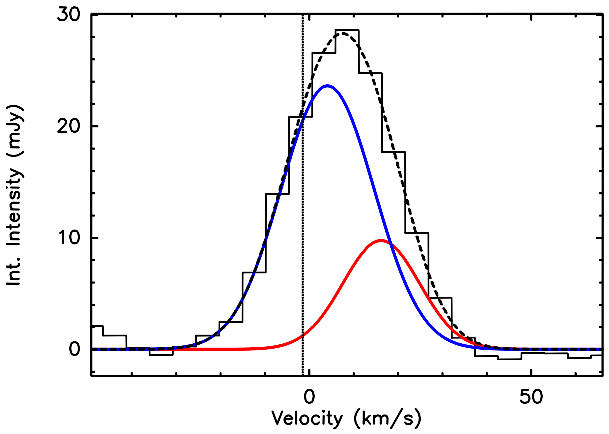

(b) POS26

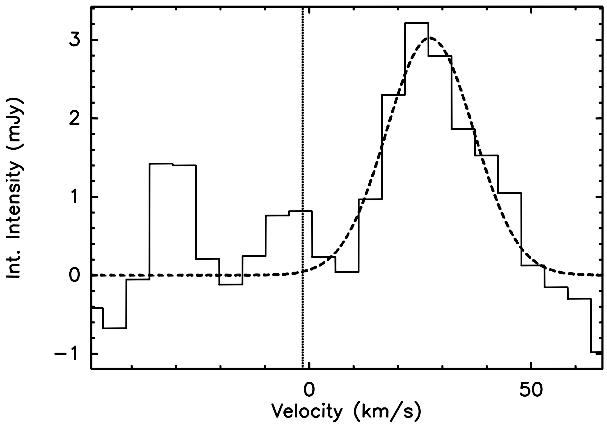

(c) POS27

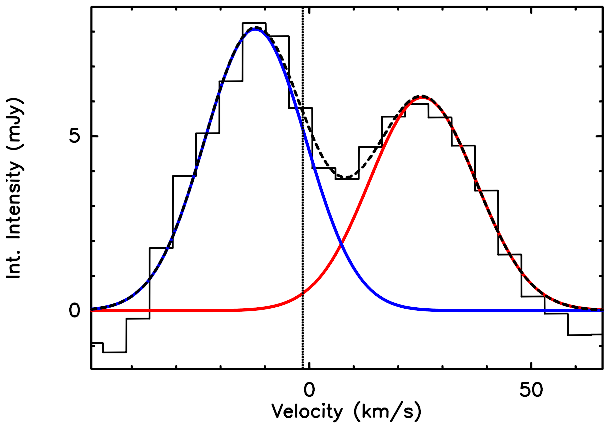

(d) POS28

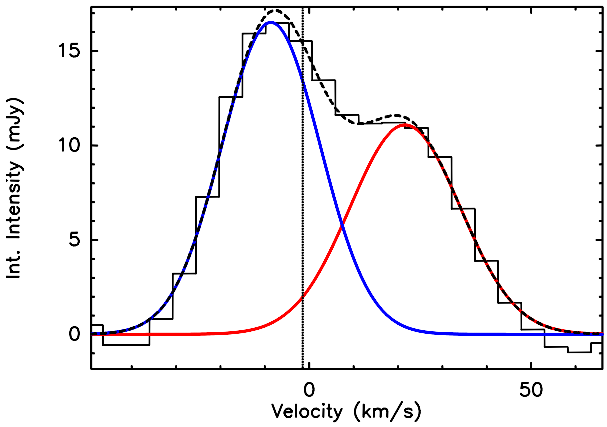

(e) POS29

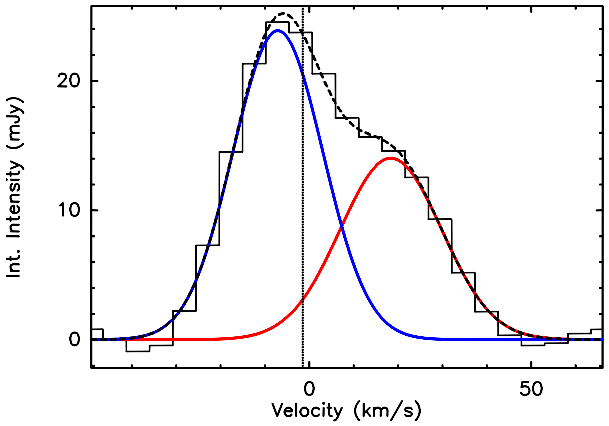

(f) POS30

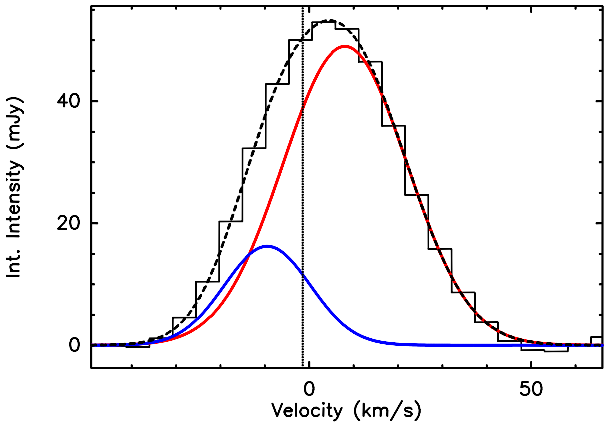

Figure 5.10: Continued.

(a) POS31

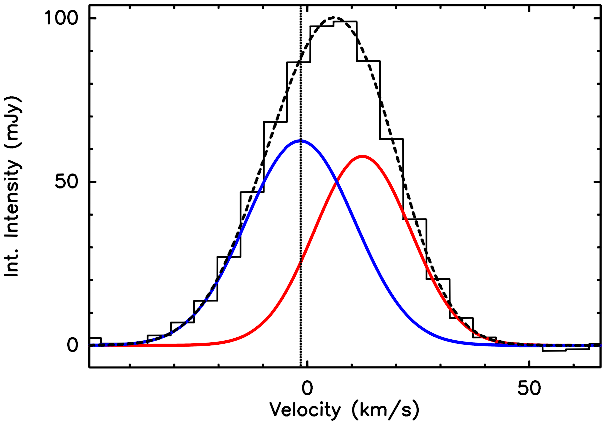

(b) POS32

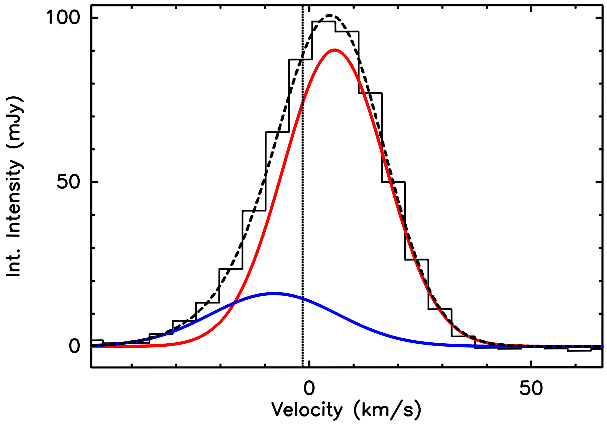

(c) POS33

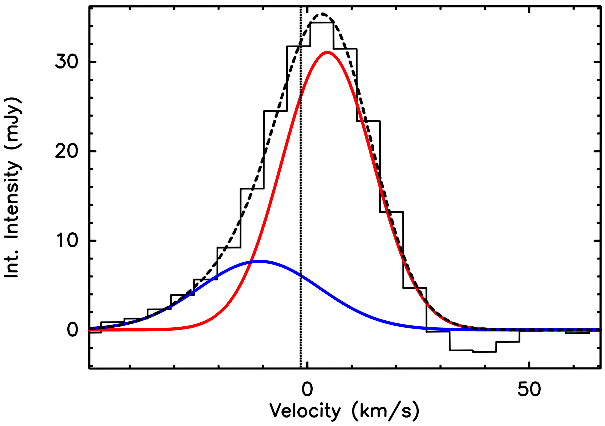

(d) POS34

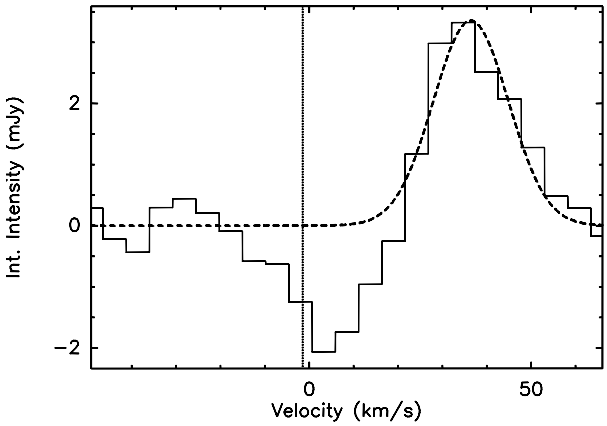

(e) POS35

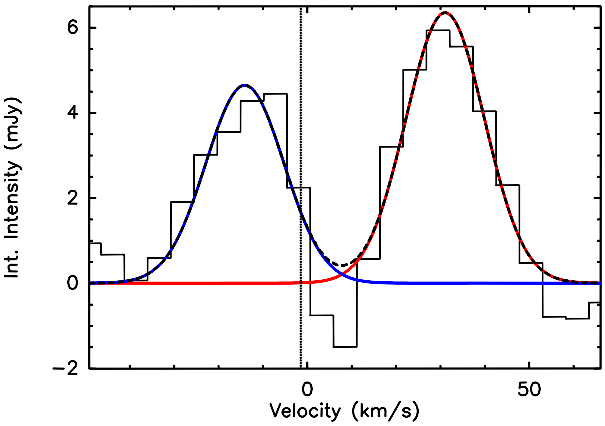

(f) POS36

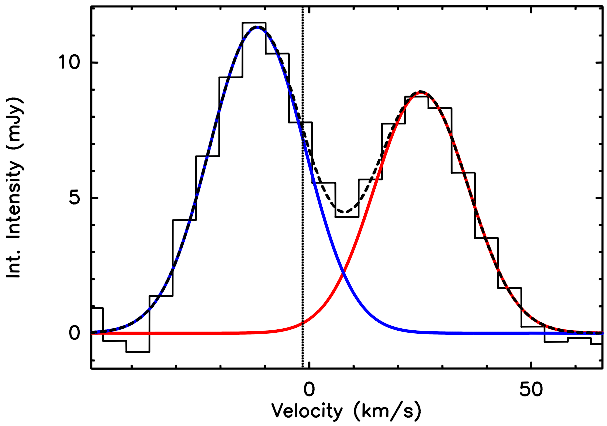

Figure 5.10: Continued.

(a) POS37

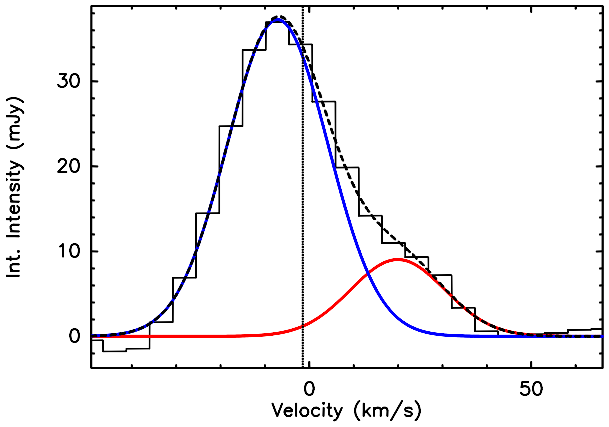

(b) POS38

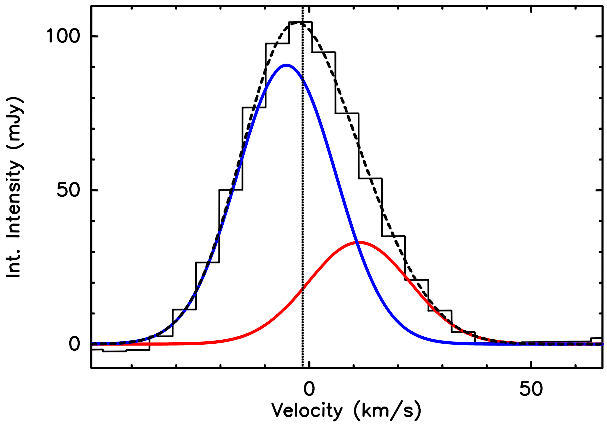

(c) POS39

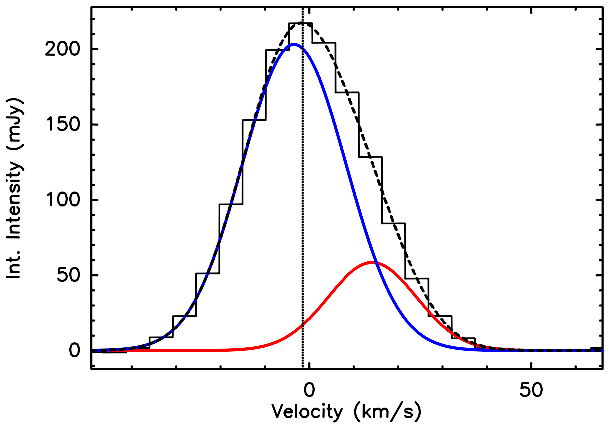

(d) POS40

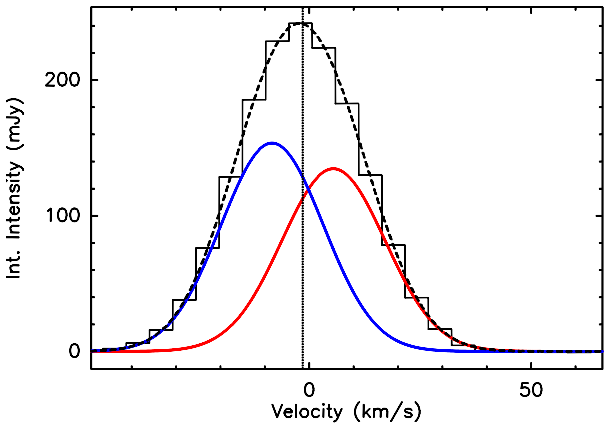

(e) POS41

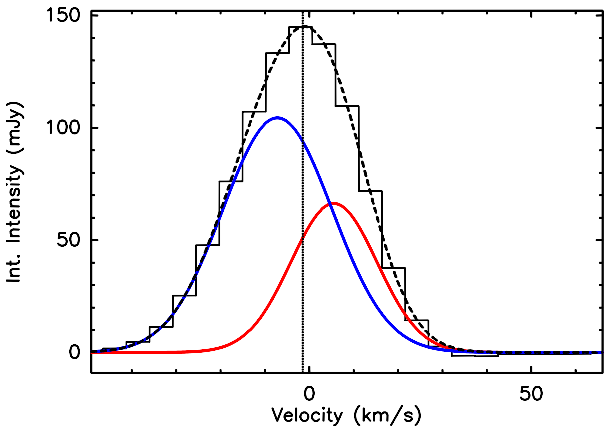

(f) POS42

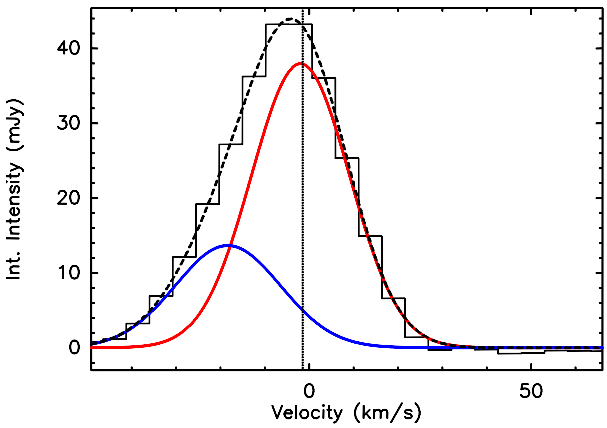

Figure 5.10: Continued.

(a) POS43

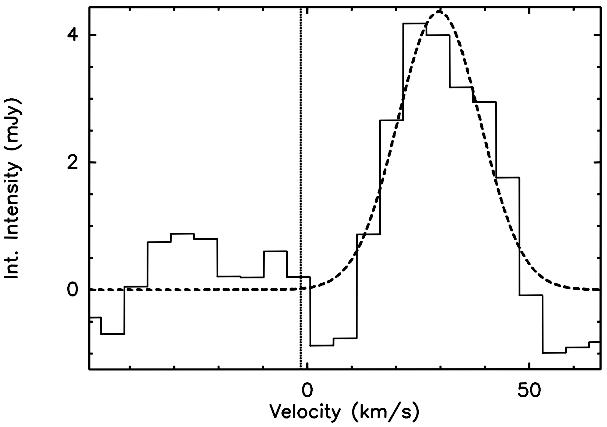

(b) POS44

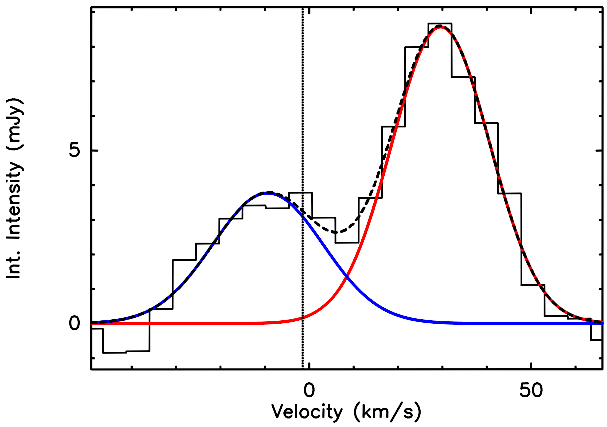

(c) POS45

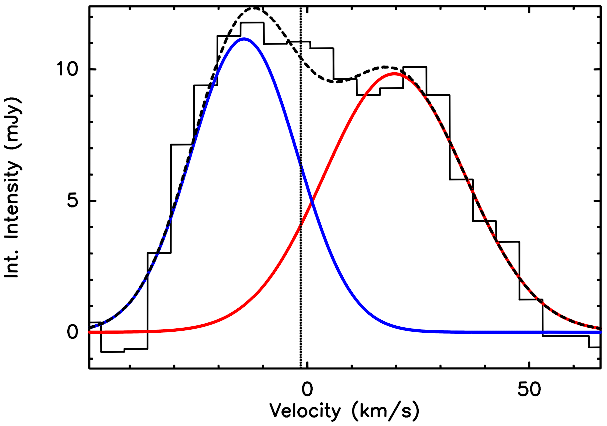

(d) POS46

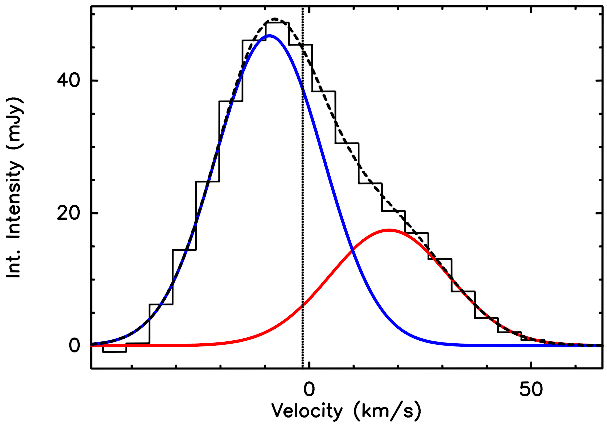

(e) POS47

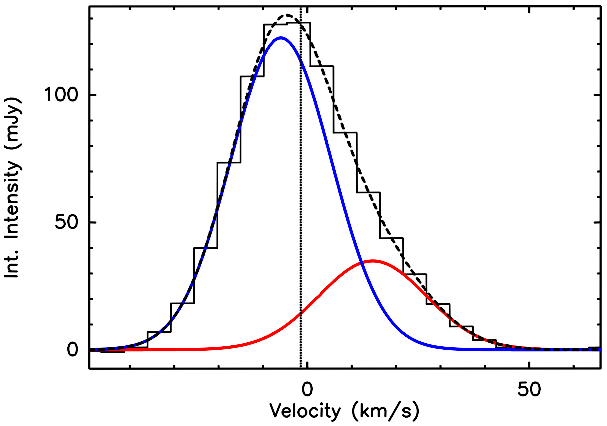

(f) POS48

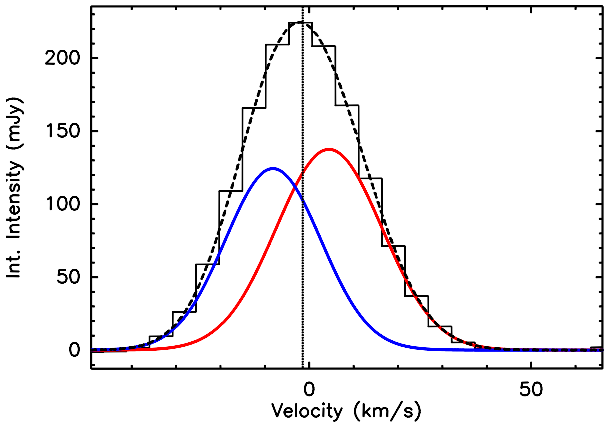

Figure 5.10: Continued.

(a) POS49

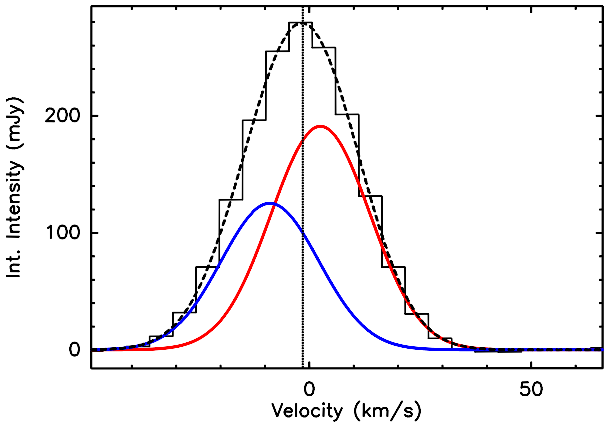

(b) POS50

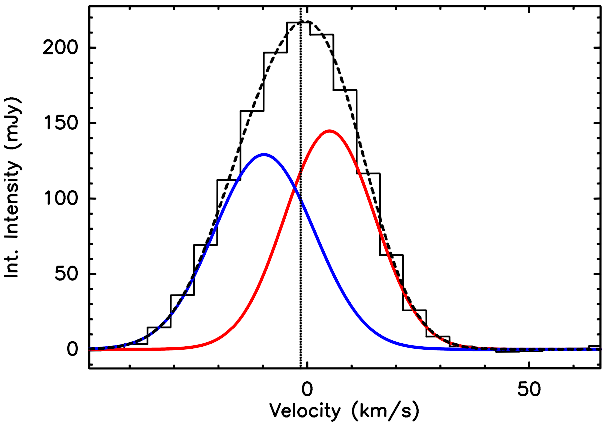

(c) POS51

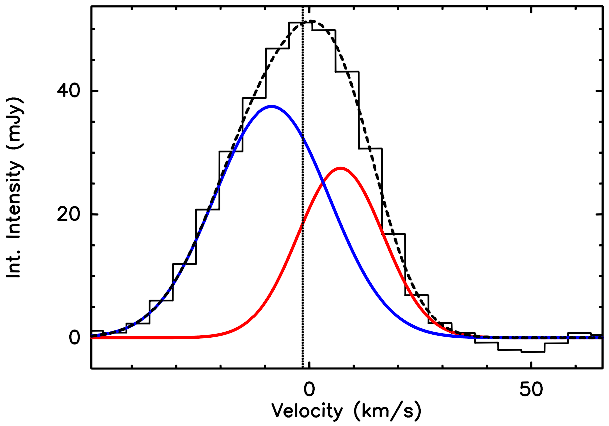

(d) POS52

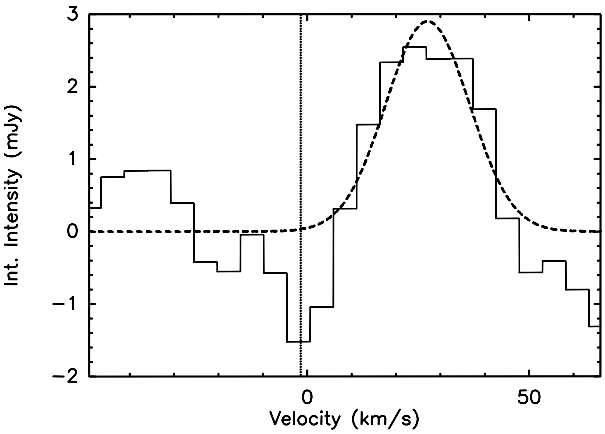

(e) POS53

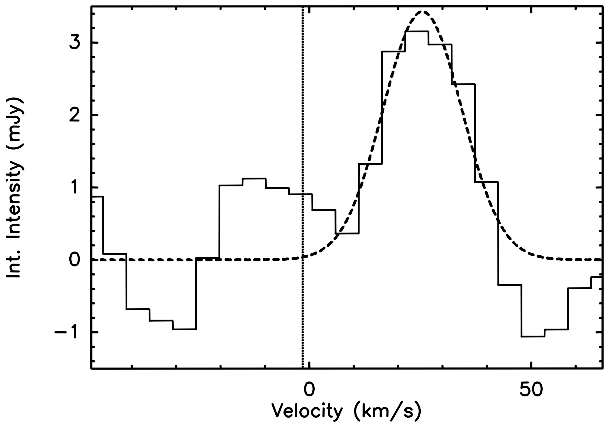

(f) POS54

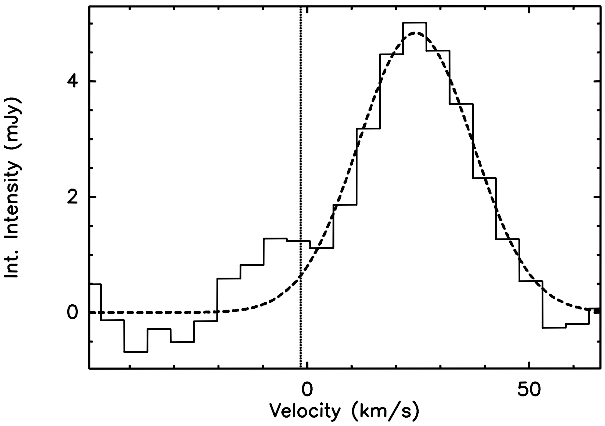

Figure 5.10: Continued.

(a) POS55

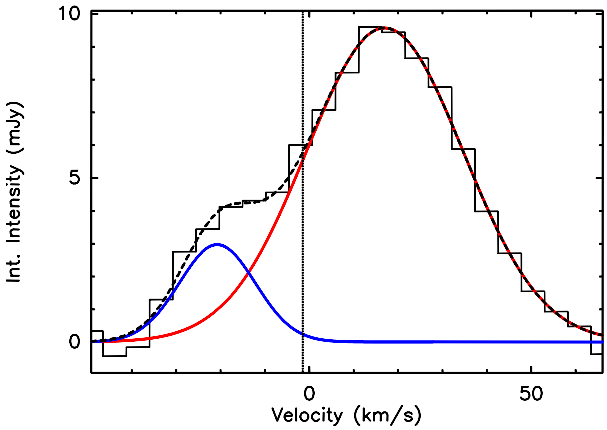

(b) POS56

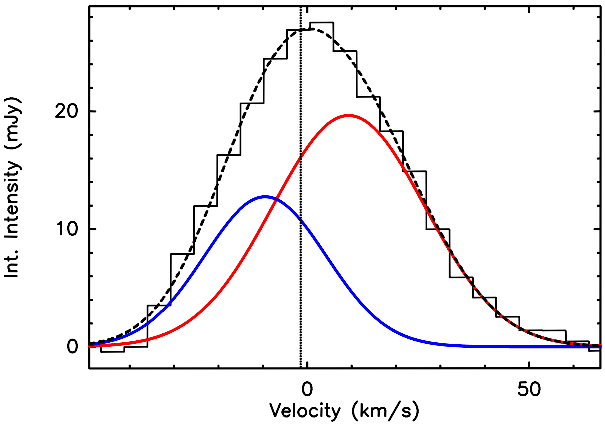

(c) POS57

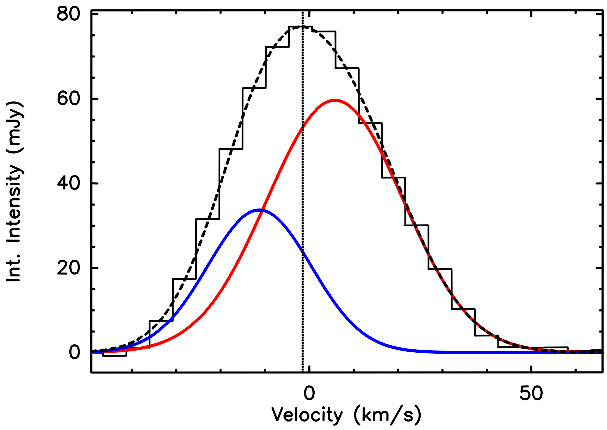

(d) POS58

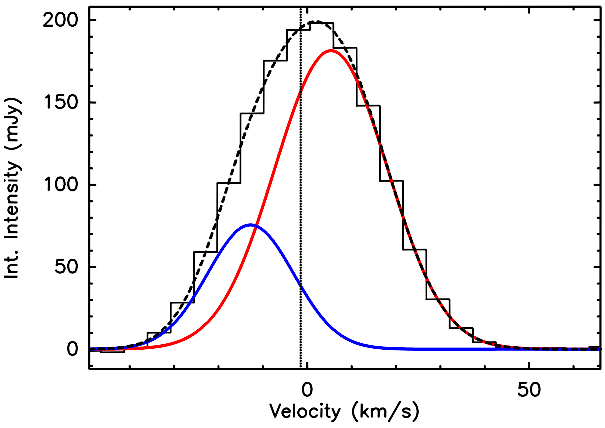

(e) POS59

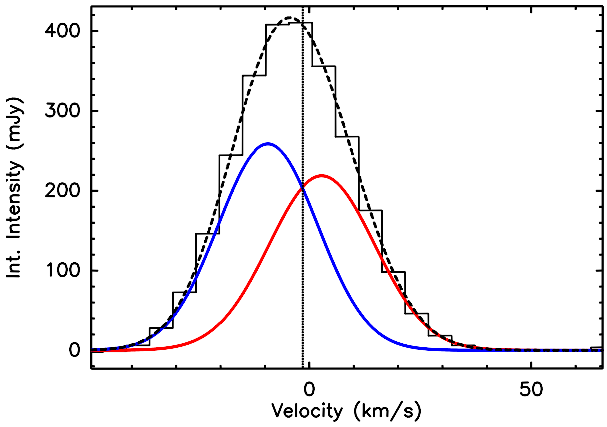

(f) POS60

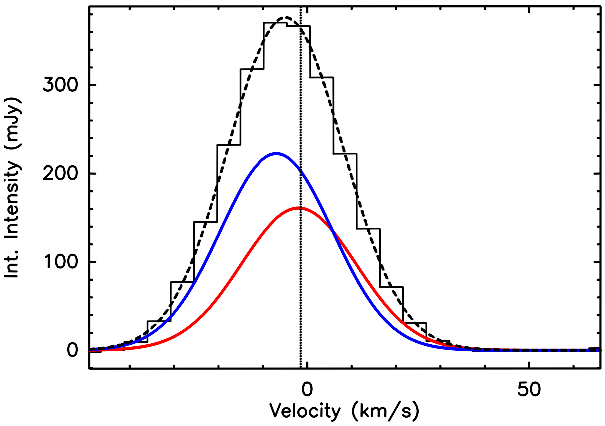

Figure 5.10: Continued.

(a) POS61

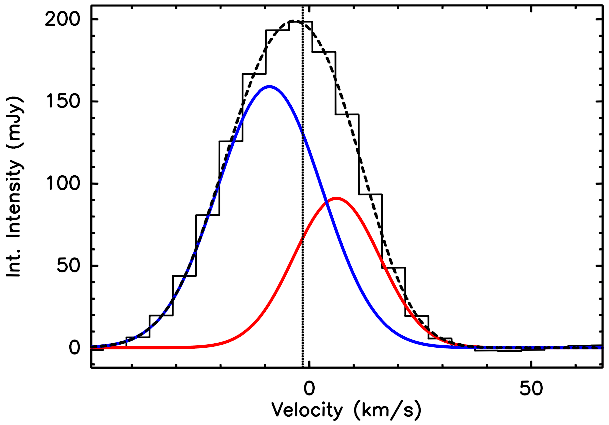

(b) POS62

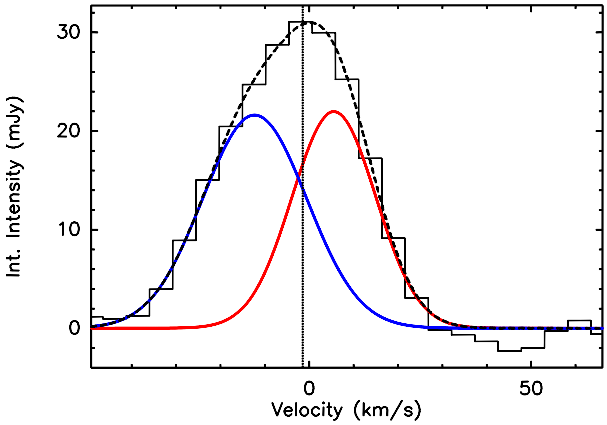

(c) POS63

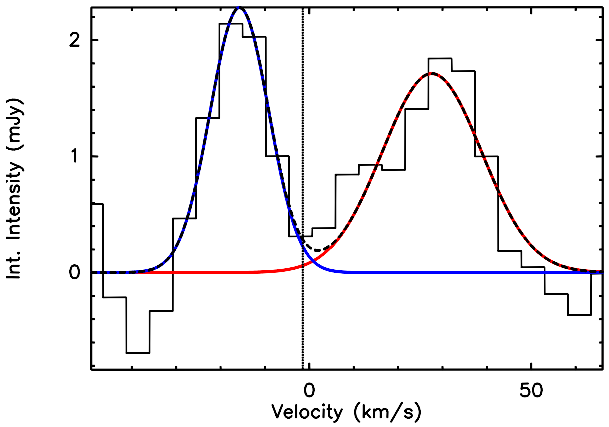

(d) POS64

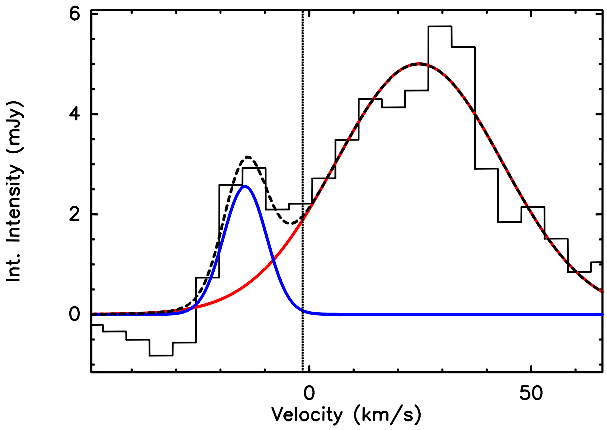

(e) POS65

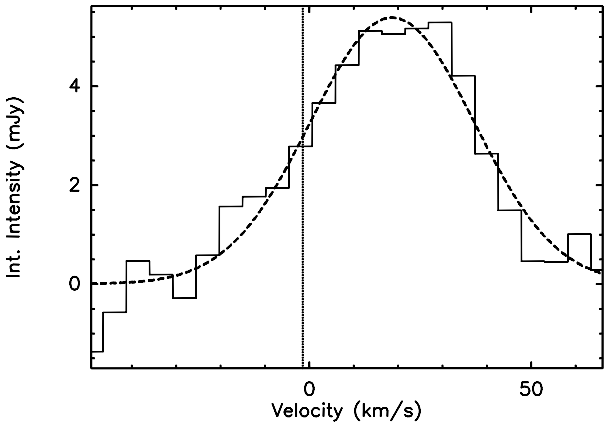

(f) POS66

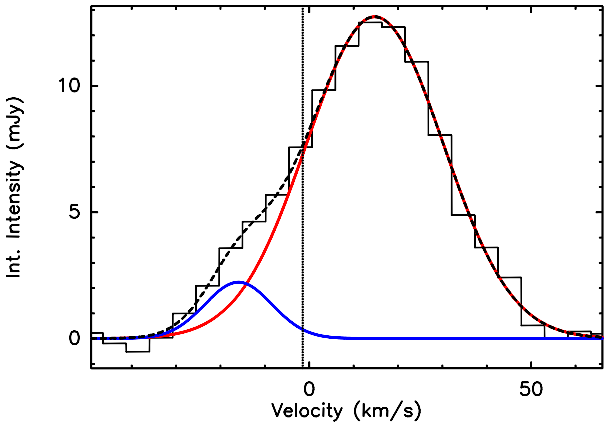

Figure 5.10: Continued.

(a) POS67

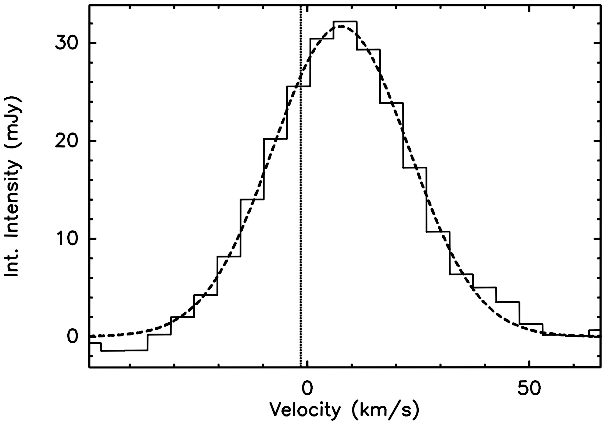

(b) POS68

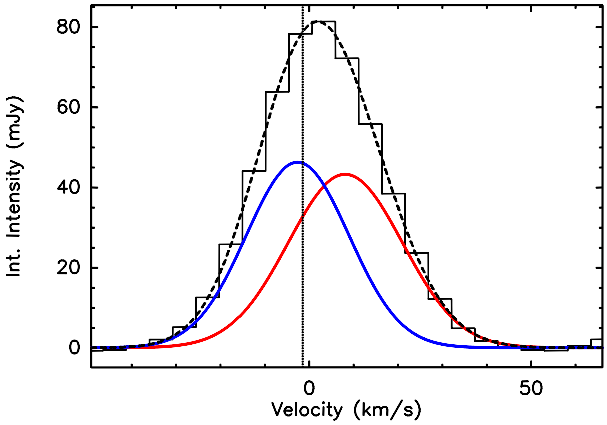

(c) POS69

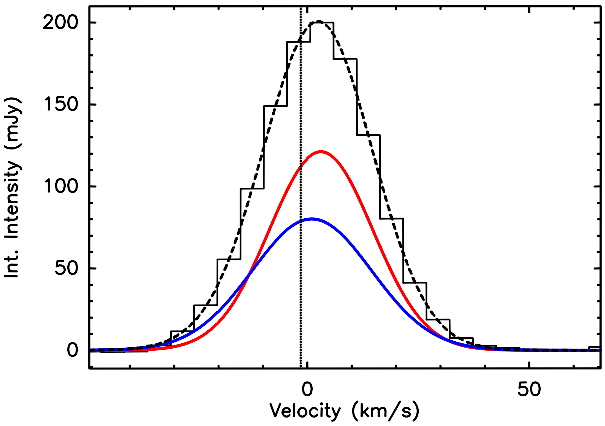

(d) POS70

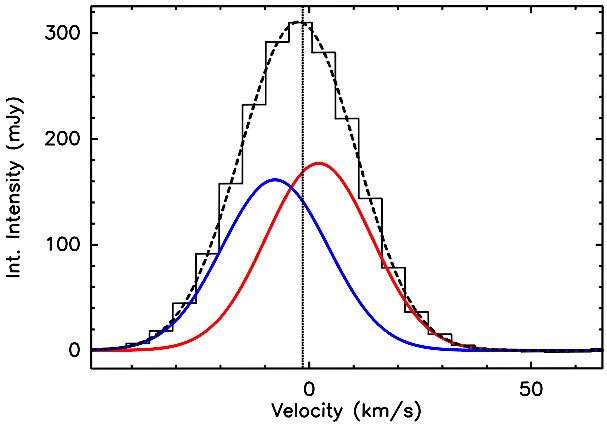

(e) POS71

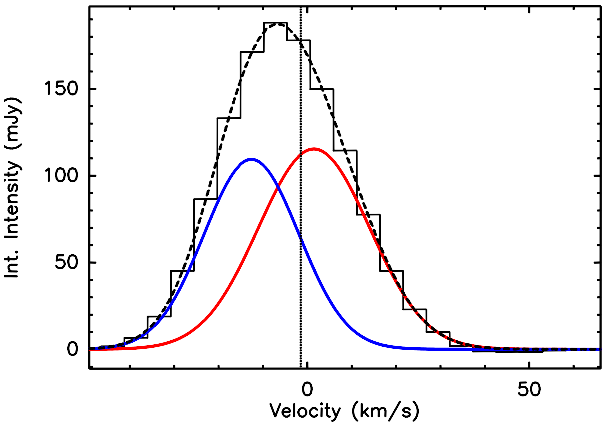

(f) POS72

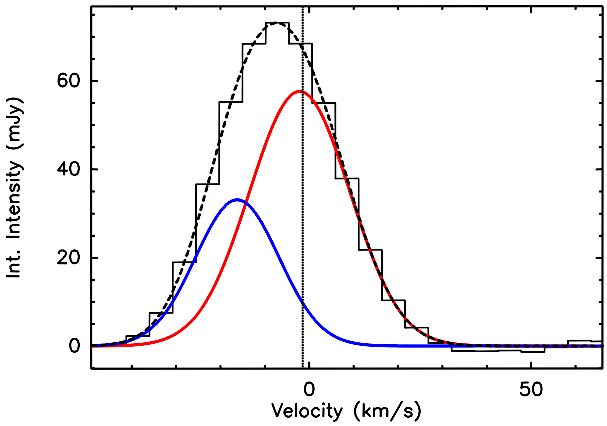

6 Conclusions

For this dissertation, we conducted observations of continuum and spectral line emission, particularly thermal and masing lines, at submillimeter and radio wavelengths. In combination with archival data of infrared continuum observations, we were able to draw a comprehensive picture of the ongoing star formation in the high-mass star forming complex W33, from the prestellar phase to the ultracompact H II region phase (Chapters 2, 3, and 4). The next step in the evolution of star formation is the expansion of the ultracompact H II region into a compact or even larger H II region. During their expansion, the H II regions assume different shapes (spherical, cometary, shell, ...). To understand how cometary H II regions are formed, we studied the two cometary H II regions of DR 21. Analyzing archival radio recombination line observations of this star forming complex, we revealed the velocity structure of the two H II regions.

In the following, our main conclusions will be summarized shortly.

- Trigonometric parallax observations of four water masers in three different clouds of the W33 complex showed that W33 is one connected star forming complex at a distance of 2.4 kpc. This distance locates W33 ~33% closer to us than suggested by the kinematic distance of the complex. This necessitates a revision of the physical properties that were determined for W33 on the basis of the near-kinematic distance. A comparison with the CO observations of Dame et al. (2001) places the W33 complex in the Scutum spiral arm. From the proper motions of the water masers, we inferred the motions of the clouds W33 A and W33 B relative to the most massive cloud W33 Main.

- The W33 complex contains star forming regions at different stages of evolution, from prestellar clouds to H II regions. Since the clouds are located at similar distances and belong to the same complex, a comprehensive chemical study of these clouds along an evolutionary sequence is feasible. We observed the six W33 clouds with the Submillimeter Array

(SMA) and the Atacama Pathfinder Experiment (APEX) telescope, tracing the chemical composition of the clouds on different scales. We determined dust and gas temperatures, column densities, bolometric luminosities, and total masses of the six W33 clouds.

- On smaller scales, the number of complex molecules increases up to the hot core phase, traced by the SMA data. Due to the vicinity of the ionizing radiation in the H II region phase, the complex molecules are probably photo-dissociated and the SMA spectra of the H II region do not resemble the spectra of hot cores anymore.

- However, the spectra observed with the APEX telescope towards the H II region W33 Main show emission of the highest number of complex molecules. Thus, the chemical complexity and diversity on larger scales, traced by the APEX spectra, increases along the evolutionary sequence up to the H II region phase.

- K band high-resolution radio continuum observations of W33 Main with the Karl G. Jansky Very Large Array (JVLA) show strong emission at the center of the dust core W33 Main-Central. Lower-resolution observations at 5 GHz present extended emission with multiple peaks towards all three infrared sources in W33 Main. The K band continuum emission is excited by a star of spectral type B0−O9.5, assuming that the emission is excited by a single ZAMS star.

- Water maser spots at 22 GHz are detected towards W33 Main-Central and W33 Main-North as well as south of W33 Main-Central. A class I methanol maser is detected south-west of W33 Main-Central. However, it is not clear how this maser is powered. The NH_3 emission in W33 Main is not compact enough to be detected in our observations.

- Radio recombination line observations of DR 21 with the Very Large Array (VLA) reveal for the first time the presence of two velocity components towards both cometary H II regions which indicates the presence of stellar winds emptying cavities around the new-born stars. The two observed components probably originate from the near and far sides of the cavities.

- The velocity fields of both H II regions in DR 21 can be explained with a combination of the champagne flow and bow shock models. Thus, the new-born stars are probably moving up a density gradient in the surrounding material. The presence of a density gradient in the southern H II region is supported by observations of dense gas tracers.

7 Outlook

The launch of satellites like the Midcourse Space Experiment (MSX), *Spitzer* or *Herschel* and the installation of bolometer cameras like the Large Array Bolometer Camera at the Atacama Pathfinder Experiment (APEX) telescope, the Submillimetre Common-User Bolometer Array (SCUBA) at the James Clerk Maxwell Telescope (JCMT) or BOLOCAM at the Caltech-Submillimeter-Observatorium (CSO) ushered in a new era of large-scale Galactic plane surveys at infrared and (sub)millimeter wavelengths. These surveys produced a wealth of photometric data from which spectral energy distributions (SEDs) of molecular clouds in a large number of high-mass star forming regions can be constructed. Especially, the *Herschel*/Hi-GAL survey provides the important data points close to the peak of the SEDs. Fitting the SEDs with sophisticated dust emission models yields physical parameters of the high-mass star forming regions like dust temperature and bolometric luminosity as well as dust characteristics. Combining the infrared and submillimeter continuum observations with maser and radio continuum observations allow the sorting of the observed high-mass star forming regions into groups which mirror their evolutionary stages depending on their flux densities at the different wavelengths.

Within the next three years, the BeSSeL survey will determine accurate distances and proper motions of several hundreds of high-mass star forming regions. Accurate distances allow an accurate determination of distance-dependent physical parameters, for example the mass of molecular clouds. Furthermore, knowing the distances of high-mass star forming regions allows a quantitative comparison of their characteristics. Thus, for the first time, we will have a significant sample of high-mass star forming regions with accurate distances and well-characterized evolutionary stages.

Since many molecules of the interstellar medium emit at submillimeter wavelengths, astrochemistry will profit strongly from single dish and interferometer observations in this window.

Chemical composition studies of a statistically significant sample of high-mass star forming regions along the observed evolutionary sequence, from quiescent cold clouds to evolved H II regions, will provide important information about the chemical and physical processes at work while a protostar is formed and evolves into a visible high-mass star. On smallest scales, the recently inaugurated Atacama Large Millimeter/submillimeter Array (ALMA) will play an important role in chemical studies of high-mass star forming regions. Fully operational, ALMA will consist of 54 antennas with a diameter of 12 m and 12 antennas with a diameter of 7 m. The baselines between the antennas will range between 0.15 and 16 km, corresponding to a spatial resolution of 0.02″ at 1 mm. At the distance of W33, this resolution corresponds to a physical scale of ∼50 AU which allows chemical studies of the accretion disks around the protostars. The broad-band receivers at the ALMA antennas will have a frequency coverage of 30−950 GHz with bandwidths of up to 16 GHz. These upgrades in receiver techniques provide the opportunity to trace the emission of molecules over a broad range of excitation temperatures.

These broad bandwidths of newly developed spectrometers at e.g. SMA or ALMA already allow the detection of a "forest" of spectral lines from a large number of molecules and a large range of excitation energies, yielding information about the temperature and density structures in the high-mass star forming regions. Thus, on the analytical side, radiative transfer models have to be expanded into three-dimensional non-LTE radiative transfer codes which will accurately compute the level populations. Undergoing developments in this direction are the ARTIST package which contains the 3D non-LTE radiative transfer code LIME and the Monte-Carlo radiative transfer model RADMC-3D which can treat 1D, 2D, and 3D problems.

In a similar way, chemical modeling has to be improved to include complex grain surface and gas phase reactions to simulate the chemical changes during the evolution of the star forming region on different scales. Here, the wealth of information from observational chemical studies will provide important input for the development of sophisticated chemical models.

8 Acknowledgement

In this section, I would like to acknowledge the people who supported and encouraged me during my studies, especially in the last months of this thesis project. Without them, this dissertation would not have been possible.

First and foremost, I would like to express my deepest gratitude to my advisor Prof. Karl Menten for his guidance and valuable support of my thesis project over the last years and for the liberty to conduct my doctoral research studies in a self-determined way. I would like to thank him for giving me the opportunity to spend one year of the PhD time as a predoctoral fellow at the Center for Astrophysics (CfA) in Cambridge, US. This year made me grow in so many ways that I would have been a different person today without it. I am thankful for his financial support which allowed me to travel to many conferences as well as to the Atacama Pathfinder Experiment (APEX) telescope.

Special gratitude goes to Dr. Mark Reid, my advisor at the CfA, for his warm welcome and constant support during my time in the US. I have greatly benefited from all the things he taught me, in astronomy and beyond. I would like to thank him for providing me with the DR 21 data which became an important part of my dissertation.

Dr. Andreas Brunthaler helped me greatly with the observations, data reduction, and analysis of the Karl G. Jansky Very Large Array (JVLA) data. I am thankful for his advice and constructive feedback, especially on the W33 distance paper and the JVLA chapter of this dissertation.

I am grateful for the constructive comments of my second referee Prof. Uli Klein during several thesis meetings and I would like to thank Prof. Ian Brock and PD Dr. Axel Nothnagel for joining the PhD examination committee.

I feel gratitude for the APEX staff for creating a very nice atmosphere at the base camp and the telescope and for teaching me how to observe.

Extensive discussions with collaborators have been illuminating and I am deeply grateful that they shared their broad knowledge with me. I would like to thank my co-authors for their significant contributions to the submitted and published papers and the anonymous referees of the papers for their time and constructive comments.

I acknowledge financial support of the International Max Planck Research School in Bonn.

I would like to thank my colleagues in the submillimeter group in Bonn and the radio and geoastronomy division at the CfA for the stimulating research atmosphere and the friendly workplace that they created. I am thankful for their support and encouragement.

I would like to offer my special thanks to the people who proof-read my dissertation and gave constructive comments and feedback: Andreas Brunthaler, Nikolas Immer, Tomasz Kaminski, Carsten König, Alexander Kreplin, and Karl Menten.

I would like to show my greatest appreciation to my friends for keeping me sane during the stressful times of the PhD and for all the wonderful distractions over the past years. I have a lot of fun with you guys and I hope we will keep in touch for a long time.

From the people that I met at the CfA, I would like to mention particularly the former predoctoral fellows Sophia Dai, Roberto Galván-Madrid, Alexa Hart, Hau-yu Baobab Liu and his wife Jia-Ling Syu, David Long, Petri Savolainen as well as Vivian U and her husband Charleston Chiang, and the Harvard graduate students Courtney Dressing, Jason Dittmann, Ellie Newton, Sukrit Ranjan, and Katherine Rosenfeld. In addition, many thanks go to Pamela Fox for giving me a home in Cambridge. For his great friendship and our wonderful times in the US, Toledo, Rome, Florence, and Bonn, I am very grateful to Pau Frau. Gràcies.

Special thanks also go to my friends in Bonn: Felipe Alves and his wife Anna Laura Rezende, Elvire de Beck and her husband Matthias Maerker, Timea Csengeri, Talayeh Hezareh and her husband Wolf Dapp, Tomasz Kaminski, Carsten König, Benjamin Magnelli, Aarti Nagarajan, Juan-Pablo Pérez-Beaupuits, Alberto Sanna, Maria Louise Strandet, Anastasia Tsitali, and Zhiyu Zhang. I would like to particularly thank Marcelo de Lima Leal Ferreira for his great friendship and the wonderful year we spent together. Obrigada.

I would like to express my deepest appreciation to my best friend Stefanie Luber. Her friendship over the past 16 years means everything to me. I am very thankful for all the pictures in the last months. They kept me dreaming of a world outside of astronomy. Vielen Dank!

However, the deepest heartfelt gratitude I owe to my family, especially my parents. Without their tremendous moral and mental support I would not be the person I am today. I am very thankful for their constant encouragement and their indispensable advice. This dissertation is dedicated to them. Vielen herzlichen Dank für alles!

9 Bibliography

Anderson, L. D., Zavagno, A., Barlow, M. J., García-Lario, P., & Noriega-Crespo, A. 2012, A&A, 537, A1

Andre, P., Ward-Thompson, D., & Barsony, M. 1993, ApJ, 406, 122

Argon, A. L., Reid, M. J., & Menten, K. M. 2000, ApJS, 129, 159

Arthur, S. J. & Hoare, M. G. 2006, ApJS, 165, 283

Benjamin, R. A., Churchwell, E., Babler, B. L., et al. 2003, PASP, 115, 953

Bergin, E. A. & Tafalla, M. 2007, ARA&A, 45, 339

Beuther, H., Churchwell, E. B., McKee, C. F., & Tan, J. C. 2007, in Protostars and Planets V, ed. B. Reipurth, D. Jewitt, & K. Keil, 165

Beuther, H., Schilke, P., Menten, K. M., et al. 2005, ApJ, 633, 535

Beuther, H., Schilke, P., Sridharan, T. K., et al. 2002, A&A, 383, 892

Beuther, H., Zhang, Q., Bergin, E. A., & Sridharan, T. K. 2009, AJ, 137, 406

Bieging, J. H., Pankonin, V., & Smith, L. F. 1978, A&A, 64, 341

Blitz, L. 1993, in Protostars and Planets III, ed. E. H. Levy & J. I. Lunine, 125–161

Bodenheimer, P., Tenorio-Tagle, G., & Yorke, H. W. 1979, ApJ, 233, 85

Bonnell, I. A. & Bate, M. R. 2006, MNRAS, 370, 488

Bonnell, I. A., Bate, M. R., Clarke, C. J., & Pringle, J. E. 2001, MNRAS, 323, 785

Brogan, C. L., Gelfand, J. D., Gaensler, B. M., Kassim, N. E., & Lazio, T. J. W. 2006, ApJ, 639, L25

Brown, P. D., Charnley, S. B., & Millar, T. J. 1988, MNRAS, 231, 409

Brunthaler, A., Reid, M. J., Menten, K. M., et al. 2011, Astronomische Nachrichten, 332, 461

Burton, W. B. & Gordon, M. A. 1978, A&A, 63, 7

Capps, R. W., Gillett, F. C., & Knacke, R. F. 1978, ApJ, 226, 863

Caswell, J. L. 1998, MNRAS, 297, 215

Charnley, S. B. 1997, ApJ, 481, 396

Charnley, S. B., Tielens, A. G. G. M., & Millar, T. J. 1992, ApJ, 399, L71

Chen, X., Shen, Z.-Q., Li, J.-J., Xu, Y., & He, J.-H. 2010, ApJ, 710, 150

Churchwell, E., Babler, B. L., Meade, M. R., et al. 2009, PASP, 121, 213

Contreras, Y., Schuller, F., Urquhart, J. S., et al. 2013, A&A, 549, A45

Cyganowski, C. J., Brogan, C. L., & Hunter, T. R. 2007, AJ, 134, 346

Cyganowski, C. J., Reid, M. J., Fish, V. L., & Ho, P. T. P. 2003, ApJ, 596, 344

Dame, T. M., Hartmann, D., & Thaddeus, P. 2001, ApJ, 547, 792

Davies, B., Lumsden, S. L., Hoare, M. G., Oudmaijer, R. D., & de Wit, W.-J. 2010, MNRAS, 402, 1504

Davis, C. J., Kumar, M. S. N., Sandell, G., et al. 2007, MNRAS, 374, 29

Dent, W. R. F., Matthews, H. E., & Ward-Thompson, D. 1998, MNRAS, 301, 1049

Di Francesco, J., Johnstone, D., Kirk, H., MacKenzie, T., & Ledwosinska, E. 2008, ApJS, 175, 277

Dickel, H. R., Goss, W. M., Rots, A. H., & Blount, H. M. 1986, A&A, 162, 221

Downes, D. & Rinehart, R. 1966, ApJ, 144, 937

Dyck, H. M. & Simon, T. 1977, ApJ, 211, 421

Egan, M. P., Shipman, R. F., Price, S. D., et al. 1998, ApJ, 494, L199

Elmegreen, B. G. & Lada, C. J. 1977, ApJ, 214, 725

Faúndez, S., Bronfman, L., Garay, G., et al. 2004, A&A, 426, 97

Fey, A. L., Gordon, D., Jacobs, C. S., & et al. 2009, IERS Technical Note, 35, 1

Galván-Madrid, R., Zhang, Q., Keto, E., et al. 2010, ApJ, 725, 17

Garden, R., Geballe, T. R., Gatley, I., & Nadeau, D. 1986, MNRAS, 220, 203

Garden, R. P. & Carlstrom, J. E. 1992, ApJ, 392, 602

Garden, R. P., Geballe, T. R., Gatley, I., & Nadeau, D. 1991, ApJ, 366, 474

Gardner, F. F. & Whiteoak, J. B. 1972, Astrophys. Lett., 12, 107

Gardner, F. F., Wilson, T. L., & Thomasson, P. 1975, Astrophys. Lett., 16, 29

Gaume, R. A., Fey, A. L., & Claussen, M. J. 1994, ApJ, 432, 648

Genzel, R. & Downes, D. 1977, A&AS, 30, 145

Goldsmith, P. F. & Langer, W. D. 1999, ApJ, 517, 209

Goldsmith, P. F. & Mao, X.-J. 1983, ApJ, 265, 791

Goss, W. M., Matthews, H. E., & Winnberg, A. 1978, A&A, 65, 307

Green, J. A., Caswell, J. L., Fuller, G. A., et al. 2010, MNRAS, 409, 913

Güsten, R., Nyman, L. Å., Schilke, P., et al. 2006, A&A, 454, L13

Harris, S. 1973, MNRAS, 162, 5P

Haschick, A. D. & Ho, P. T. P. 1983, ApJ, 267, 638

Haschick, A. D., Menten, K. M., & Baan, W. A. 1990, ApJ, 354, 556

Ho, P. T. P., Klein, R. I., & Haschick, A. D. 1986, ApJ, 305, 714

Hoare, M. G., Kurtz, S. E., Lizano, S., Keto, E., & Hofner, P. 2007, in Protostars and Planets V, ed. B. Reipurth, D. Jewitt, & K. Keil, 181

Hoare, M. G., Purcell, C. R., Churchwell, E. B., et al. 2012, PASP, 124, 939

Hollenbach, D., Johnstone, D., Lizano, S., & Shu, F. 1994, ApJ, 428, 654

Immer, K., Brunthaler, A., Reid, M. J., et al. 2011, ApJS, 194, 25

Immer, K., Reid, M. J., Menten, K. M., Brunthaler, A., & Dame, T. M. 2013, A&A, 553, A117

Israel, F. P. 1978, A&A, 70, 769

Jaeger, S. 2008, in Astronomical Society of the Pacific Conference Series, Vol. 394, Astronomical Data Analysis Software and Systems XVII, ed. R. W. Argyle, P. S. Bunclark, & J. R. Lewis, 623

Jaffe, D. T., Guesten, R., & Downes, D. 1981, ApJ, 250, 621

Johnstone, D., Hollenbach, D., & Bally, J. 1998, ApJ, 499, 758

Kahn, F. D. 1974, A&A, 37, 149

Kauffmann, J. & Pillai, T. 2010, ApJ, 723, L7

Keto, E. R. & Ho, P. T. P. 1989, ApJ, 347, 349

Kettenis, M., van Langevelde, H. J., Reynolds, C., & Cotton, B. 2006, in Astronomical Society of the Pacific Conference Series, Vol. 351, Astronomical Data Analysis Software and Systems XV, ed. C. Gabriel, C. Arviset, D. Ponz, & S. Enrique, 497

Kraus, S., Hofmann, K.-H., Menten, K. M., et al. 2010, Nature, 466, 339

Kroupa, P. 2001, MNRAS, 322, 231

Kurtz, S. 2005, in IAU Symposium, Vol. 227, Massive Star Birth: A Crossroads of Astrophysics, ed. R. Cesaroni, M. Felli, E. Churchwell, & M. Walmsley, 111–119

Kurtz, S., Cesaroni, R., Churchwell, E., Hofner, P., & Walmsley, C. M. 2000, Protostars and Planets IV, 299

Lada, C. J. 1987, in IAU Symposium, Vol. 115, Star Forming Regions, ed. M. Peimbert & J. Jugaku, 1–17

Lada, C. J., Blitz, L., Reid, M. J., & Moran, J. M. 1981, ApJ, 243, 769

Langer, W. D., van Dishoeck, E. F., Bergin, E. A., et al. 2000, Protostars and Planets IV, 29

Longmore, S. N., Burton, M. G., Barnes, P. J., et al. 2007, MNRAS, 379, 535

Mac Low, M.-M., van Buren, D., Wood, D. O. S., & Churchwell, E. 1991, ApJ, 369, 395

MacLaren, I., Richardson, K. M., & Wolfendale, A. W. 1988, ApJ, 333, 821

Maret, S., Hily-Blant, P., Pety, J., Bardeau, S., & Reynier, E. 2011, A&A, 526, A47

Marston, A. P., Reach, W. T., Noriega-Crespo, A., et al. 2004, ApJS, 154, 333

Martin-Pintado, J., Bachiller, R., & Fuente, A. 1992, A&A, 254, 315

McKee, C. F. & Ostriker, E. C. 2007, ARA&A, 45, 565

Menten, K. 1991, in Astronomical Society of the Pacific Conference Series, Vol. 16, Atoms, Ions and Molecules: New Results in Spectral Line Astrophysics, ed. A. D. Haschick & P. T. P. Ho, 119

Menten, K. M., Walmsley, C. M., Henkel, C., & Wilson, T. L. 1986, A&A, 157, 318

Molinari, S., Swinyard, B., Bally, J., et al. 2010, PASP, 122, 314

Müller, H. S. P., Thorwirth, S., Roth, D. A., & Winnewisser, G. 2001, A&A, 370, L49

Panagia, N. 1973, ApJ, 78, 929

Panagia, N. & Walmsley, C. M. 1978, A&A, 70, 411

Perault, M., Omont, A., Simon, G., et al. 1996, A&A, 315, L165

Pickett, H. M., Poynter, R. L., Cohen, E. A., et al. 1998, J. Quant. Spec. Radiat. Transf., 60, 883

Povich, M. S., Stone, J. M., Churchwell, E., et al. 2007, ApJ, 660, 346

Price, S. D., Egan, M. P., Carey, S. J., Mizuno, D. R., & Kuchar, T. A. 2001, AJ, 121, 2819

Purcell, C. R., Longmore, S. N., Walsh, A. J., et al. 2012, MNRAS, 426, 1972

Reach, W. T., Rho, J., Tappe, A., et al. 2006, AJ, 131, 1479

Reid, M. J. & Ho, P. T. P. 1985, ApJ, 288, L17

Reid, M. J., Menten, K. M., Brunthaler, A., et al. 2009a, ApJ, 693, 397

Reid, M. J., Menten, K. M., Zheng, X. W., et al. 2009b, ApJ, 700, 137

Remijan, A. J., Markwick-Kemper, A., & ALMA Working Group on Spectral Line Frequencies. 2007, in Bulletin of the American Astronomical Society, Vol. 39, American Astronomical Society Meeting Abstracts, 132

Rengarajan, T. N. & Ho, P. T. P. 1996, ApJ, 465, 363

Roelfsema, P. R., Goss, W. M., & Geballe, T. R. 1989, A&A, 222, 247

Rohlfs, K. & Wilson, T. L. 2004, Tools of radio astronomy (Springer)

Roy, A., Ade, P. A. R., Bock, J. J., et al. 2011, ApJ, 727, 114

Rygl, K. L. J., Brunthaler, A., Sanna, A., et al. 2012, A&A, 539, A79

Salpeter, E. E. 1955, ApJ, 121, 161

Sanna, A., Reid, M. J., Moscadelli, L., et al. 2009, ApJ, 706, 464

Sato, M., Hirota, T., Reid, M. J., et al. 2010a, PASJ, 62, 287

Sato, M., Reid, M. J., Brunthaler, A., & Menten, K. M. 2010b, ApJ, 720, 1055

Schneider, N., Csengeri, T., Bontemps, S., et al. 2010, A&A, 520, A49

Schuller, F., Menten, K. M., Contreras, Y., et al. 2009, A&A, 504, 415

Shu, F. H., Adams, F. C., & Lizano, S. 1987, ARA&A, 25, 23

Smith, H. A., Hora, J. L., Marengo, M., & Pipher, J. L. 2006, ApJ, 645, 1264

Sridharan, T. K., Beuther, H., Schilke, P., Menten, K. M., & Wyrowski, F. 2002, ApJ, 566, 931

Stier, M. T., Fazio, G. G., Roberge, W. G., et al. 1982, ApJS, 48, 127

Stier, M. T., Jaffe, D. T., Rengarajan, T. N., et al. 1984, ApJ, 283, 573

Stutzki, J. & Guesten, R. 1990, ApJ, 356, 513

Thompson, A. R., Moran, J. M., & Swenson, Jr., G. W. 2001, Interferometry and Synthesis in Radio Astronomy, 2nd Edition

Tielens, A. G. G. M. 2005, The Physics and Chemistry of the Interstellar Medium (Cambridge Univ. Press)

Tielens, A. G. G. M., Tokunaga, A. T., Geballe, T. R., & Baas, F. 1991, ApJ, 381, 181

Turner, B. E. & Matthews, H. E. 1984, ApJ, 277, 164

Urquhart, J. S., Busfield, A. L., Hoare, M. G., et al. 2008, A&A, 487, 253

van Buren, D. & Mac Low, M.-M. 1992, ApJ, 394, 534

van der Tak, F. F. S. & Menten, K. M. 2005, A&A, 437, 947

van Dishoeck, E. F. & Blake, G. A. 1998, ARA&A, 36, 317

Walsh, A. J., Burton, M. G., Hyland, A. R., & Robinson, G. 1998, MNRAS, 301, 640

Westerhout, G. 1958, Bull. Astron. Inst. Netherlands, 14, 215

Wienen, M., Wyrowski, F., Schuller, F., et al. 2012, A&A, 544, A146

Williams, D. A. 1993, Physical and Chemical Processes on Dust, ed. T. J. Millar & D. A. Williams, 143

Williams, J. P., Blitz, L., & McKee, C. F. 2000, Protostars and Planets IV, 97

Wilson, T. L., Batria, W., & Pauls, T. A. 1982, A&A, 110, L20

Wolfire, M. G. & Cassinelli, J. P. 1987, ApJ, 319, 850

Wood, D. O. S. & Churchwell, E. 1989, ApJS, 69, 831

Wynn-Williams, C. G., Beichman, C. A., & Downes, D. 1981, AJ, 86, 565

Wynn-Williams, C. G., Werner, M. W., & Wilson, W. J. 1974, ApJ, 187, 41

Xu, Y., Reid, M. J., Zheng, X. W., & Menten, K. M. 2006, Science, 311, 54

Yorke, H. W., Tenorio-Tagle, G., & Bodenheimer, P. 1983, A&A, 127, 313

Zapata, L. A., Schmid-Burgk, J., Perez-Goytia, N., et al. 2013, ArXiv e-prints

Zhu, Q.-F., Lacy, J. H., Jaffe, D. T., Richter, M. J., & Greathouse, T. K. 2005, ApJ, 631, 381

Zhu, Q.-F., Lacy, J. H., Jaffe, D. T., Richter, M. J., & Greathouse, T. K. 2008, ApJS, 177, 584

Zinnecker, H. & Yorke, H. W. 2007, ARA&A, 45, 481